Tuning Fluorescence Sensing and Heterogeneous Catalytic Activities of Highly Stable Metal-Organic Frameworks through Linker Design

A Dissertation
Submitted in Partial Fulfilment of the
Requirements for the Degree of
Doctor of Philosophy
by

Mr. Aniruddha Das

Department of Chemistry
Indian Institute of Technology Guwahati
Guwahati-781039
India

March 2020

TH-2604_156122006

CERTIFICATE

This is to certify that the work presented in this thesis tilted as, **"Tuning Fluorescence Sensing and Heterogeneous Catalytic Activities of Highly Stable Metal-Organic Frameworks through Linker Design"** submitted to the Indian Institute of Technology Guwahati by Aniruddha Das, was worked out by the candidate at the Indian Institute of Technology Guwahati, under my supervision.

Dr. Shyam Prosad Biswas **Date:**

(thesis supervisor)

Associate Professor,

Department of Chemistry,

Indian Institute of Technology Guwahati,

Guwahati, Assam, India, 781039

TH-2604_156122006

CANDIDATE'S DECLEARATION

I hereby declared that my work on this thesis tilted as, **"Tuning Fluorescence Sensing and Heterogeneous Catalytic Activities of Highly Stable Metal-Organic Frameworks through Linker Design"** submitted for the award of degree of ***Doctor of Philosophy*** in Chemistry to the Indian Institute of Technology Guwahati.

Aniruddha Das **Date:**

Indian Institute of Technology Guwahati,

Guwahati, Assam, 781039, India

TH-2604_156122006

Dedicated to My Beloved Parents

Acknowledgement

Foremost, I would like to express my sincere gratitude to my thesis supervisor ***Dr. Shyam Prosad Biswas*** *for the continuous support of my Ph.D study and research, for his patience, motivation, passion, and immense knowledge. His guidance helped me in all the time of research and writing of this thesis. I will remember his guidance as well as cool behavior throughout my life. I could not have imagined having a better supervisor and mentor for my Ph.D study.*

Beside my supervisor, I extend my sincere thanks to Dr. Vishal Trivedi and his student Mr. Banesh Sooram for their continuous support to my research work.

TH-2604_156122006

My sincere thanks also goes to Dr. Amarajothi Dhakshinamoorthy and his student Dr. Nagaraj Anbu for their unbelievable support to my research work from their group and leading my work on diverse exciting projects.

I extend my deep sincere gratitude to Dr. Helge Reinsch for his continuous support to the theoretical calculations and analyses of MOFs.

I would also like to acknowledge my doctoral committee members Prof. Gopal Das, Prof. Vadivelu Manivannan and Dr. Kingsuk Mahata for their valuable time and suggestions throughout my PhD journey.

I would like to thank IIT Guwahati for the fellowship. I am also thankful to IIT Guwahati, Department of Chemistry and Central Instruments Facilities for providing research and instrumental facilities. I am remained very much thankful to scientific staffs of CIF and department of chemistry.

I have also extended my sincere thanks to my laboratory senior Dr. Amlan Buragohain, Dr. Rana Dalapati, Dr. Mostakim SK and Dr. Kaustuv Banerjee who have supported all the time during my Ph.D. course. I would show my sincere gratitude and special thanks to Dr. Mostakim SK for his unexpected supports to my Ph.D. research work. I thank my fellow labmates in IIT Guwahati: Mr. Soutick Nandi, Mr. Chiranjib Gogoi, Mr. Masud Alam and Mr. Subhrajyoti Ghosh for the stimulating discussions, for we were working together, and for all the fun we have had in the last five years. I thank to our past project fellow, Mr. Sourik Das, Ms. Ankita Mandal.

I would like express my love and thanks to my all friends Ranjan Manna, Tousif Hossain, Munendra Pal Singh, Biswajit Nayak, Asik Kumar Das, Milan Maji, Souvik Mondal and my departmental juniors: Abhijit Mandal and Sudip Shit, who have supported me. Their encouragements and advices make easier of my Ph.D. research life and realize my dream to reality. I would also extend my sincere thanks to all of my seniors, friends for their supports.

I wish to show my love and thanks to Babli for being with me.

I wish to show my love to my didi Mrs. Anima Das Manna, my dada Mr. Anirban Das and Mr. Animesh Das, my jiju Mr. Gouranga Manna, my boudi Mrs. Ananya Samanta Das and Piyali Sarkar Das, my cousins, liite mama Avinandan, Riju, little kakai Aaban and Sana who are always present with me by showing their love and inspiration. Their

TH-2604_156122006

motivation and encouragement were always appreciated and their pride is deeply emotive. I am always grateful to this world for giving me this beautiful life.

Last but not the least, I would like to express my heartiest love to my parents for believing in me and supporting me. I would express my sincere respect to my parents and to My BABA Late Madan Mohan Das and my MAA Mrs. Shyamali Das. Today my father wherever he is, would be the happiest person when I am very close to achieve the doctorate degree.

Aniruddha Das

TH-2604_156122006

Chapter 4

TH-2604_156122006

Thesis Title: **Tuning Fluorescence Sensing and Heterogeneous Catalytic Activities of Highly Stable Metal-Organic Frameworks through Linker Design**

Name of the Candidate: Mr. Aniruddha Das

Registration Number: 156122006

Thesis Supervisor: Dr. Shyam Prosad Biswas

Department: Chemistry

Institute: Indian Institute of Technology Guwahati, Guwahati, Assam, 781039, India.

Thesis Overview:

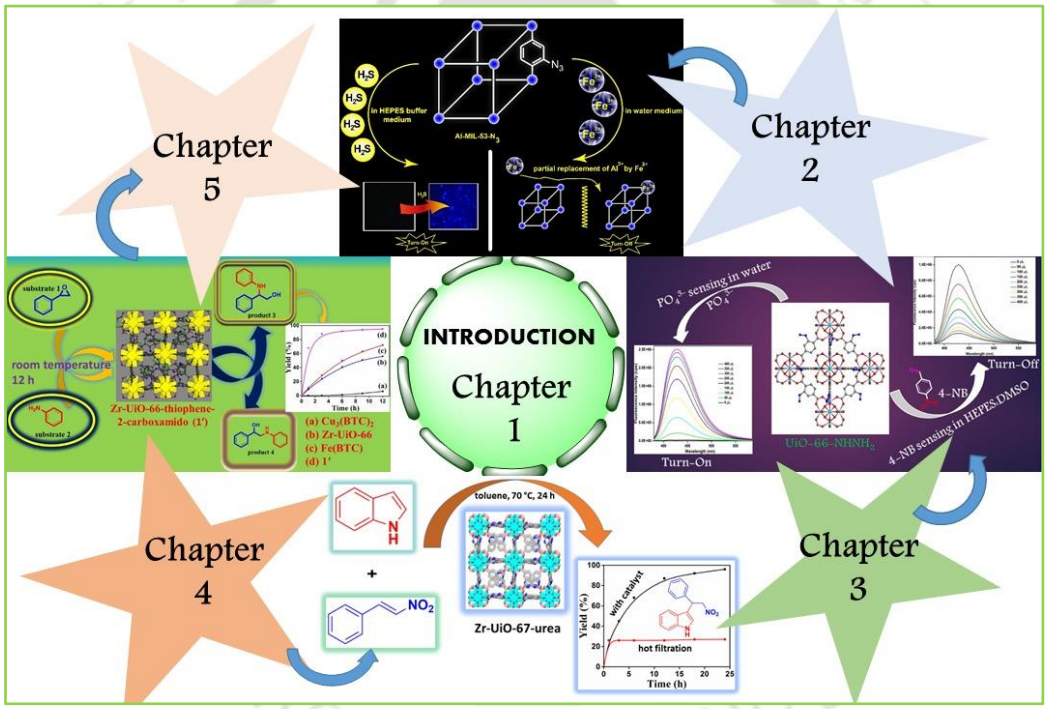

Chapter 1: Chapter 1 focuses on the literature study, design, and synthetic strategies of dicarboxylate linker based metal-organic frameworks (MOFs) and their various applications such as gas storage, fluorometric detection of toxic chemicals and roles in heterogeneous catalysis. MOFs are an emerging class of crystalline porous materials constructed from metal nodes (also known as secondary building units, or SBUs) and organic linkers. Among all the rapidly growing organic-inorganic hybrid solids, MOFs are unique materials, since they bear excellent crystallinity, huge surface areas and tunable pore apertures. They are highly promising materials in chemical and material science, not only for their versatile structural

TH-2604_156122006

topology but also for their thermal and hydrolytic stability, tunable functionality in different applications, including gas storage and purification, chemical sensing, photoluminescence, molecular-based magnetism, drug delivery, biomedicine and catalysis. The ditopic carboxylate based linker and high valent metal ions (Zr^{4+}, Hf^{4+}, Al^{3+}, Cr^{3+}, *etc.*) produce MOFs with high physicochemical stability. Applying the concept of isoreticular chemistry, MOFs can be achieved with predetermined topology. The variation of functional groups at linker body makes MOFs highly potential candidates for various applications like gas adsorption, chemical sensing, proton conductivity, drug delivery, heterogeneous catalysis, photocatalysis, *etc*. Post-synthetic modification (PSM) of MOFs provide many advantages whereas a pre-synthetic strategy has some limitations such as instability of newly formed functional groups under the synthesis conditions of MOFs because of the bulkiness of side chain. Among various synthetic methods, solvo/hydrothermal processes are the most widely used methods for synthesis of MOFs. Generally, amide solvents (like DMF, DEF, DMA, NMP, *etc*.) are used for the MOF synthesis because these solvents can easily deprotonate the carboxylate proton and help the linker to bind with metal. Variation of reaction temperature, time, nature,and amount of modulator can vary the crystallinity, pore size, BET surface area and gas adsorption capacity of resulting MOFs. Motivated by the exceptional characteristics of MOFs, enormous number of MOFs have been synthesized for the study of their utility for gas storage and separation, fluorometric detection of metal cations and anions, small organic molecules, in light-emitting devices and as heterogeneous synergistic catalysts for various organic transformation reactions.

Chapter 2: Chapter 2 describes the solvothermal synthesis and characterization of an Al(III) metal-organic framework (MOF) called Al-MIL-53-N_3 (**1**). Material **1** was synthesized using $Al(NO_3)_3{\cdot}9H_2O$ and $H_2BDC\text{-}N_3$ ($H_2BDC\text{-}N_3$ = 2-azido-1,4-benzenedicarboxylic acid) linker in a DMF/water (DMF = *N*, *N*-dimethylformamide) mixture at 80 °C in a sealed tube. Phase purity of material **1** was checked by X-ray powder diffraction (XRPD), Fourier transform infrared (FT-IR) spectroscopy, and thermogravimetric (TG) analysis. TG analysis suggests that **1** is highly stable up to 300 °C under air atmosphere. The activated **1** (called **1′**) showed a very fast fluorescence response to H_2S (turn-on) (Figure 1) and the fold increment was ~76 (Figure 2). Compound **1′** can detect Fe(III) ions (turn-off) (Figure 3) in an aqueous medium with ~90% quenching efficiency (Figure 4). The LOD values for H_2S and Fe(III) ion in water were 90.47 nM and 0.03 μM, respectively. High selectivity was observed for both H_2S and Fe(III) even in the presence of other potentially intrusive analytes. In the presence of H_2S, the azide moiety of linker molecule converts to amine and results in turn-on fluorescence. On the

TH-2604_156122006

other hand, the partial replacement of framework Al(III) ions by Fe(III) can be assigned for the selective detection behavior to Fe(III) ions, which results in turn-off fluorescence. Material **1′** can detect H_2S in human blood plasma (HBP) and sulfide ions in real water samples. Comound **1′**-loaded J774A.1 macrophage cells responded to intracellular H_2S to exhibit strong blue fluorescence, confirming its suitability to detect H_2S inside the cells.

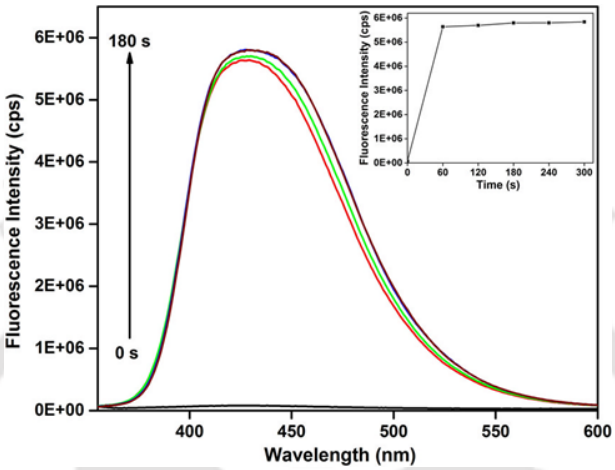

Figure 1. Change in fluorescence intensity of **1′** (in aqueous medium) upon the addition of Na_2S at a regular time interval till 300 s. Inset: change in fluorescence intensity at 425 nm as a function of time (λ_{ex} = 315 nm).

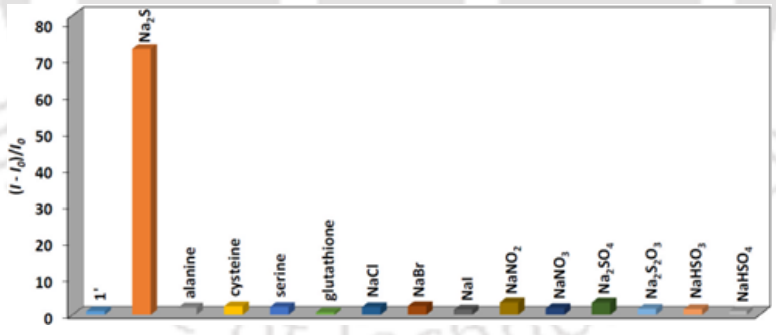

Figure 2. Fluorescence responses of **1′** (in aqueous medium) towards the addition of various analytes (10 equiv. per $–N_3$ group).

TH-2604_156122006

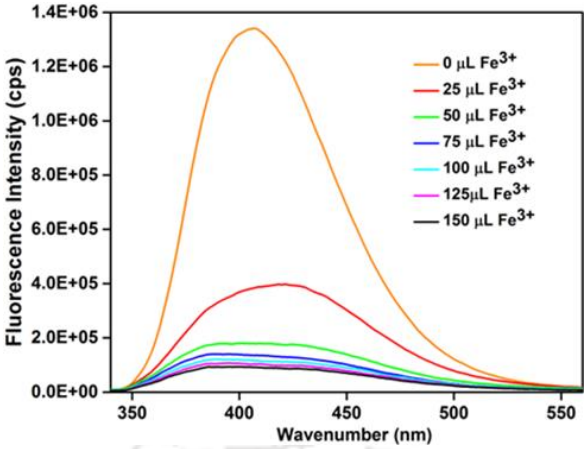

Figure 3. Quenching of the fluorescence intensity of **1′** by incremental addition of 2 mM Fe(III) solution to a 3 mL stable suspension of **1′** in water (λ_{ex} = 315 nm).

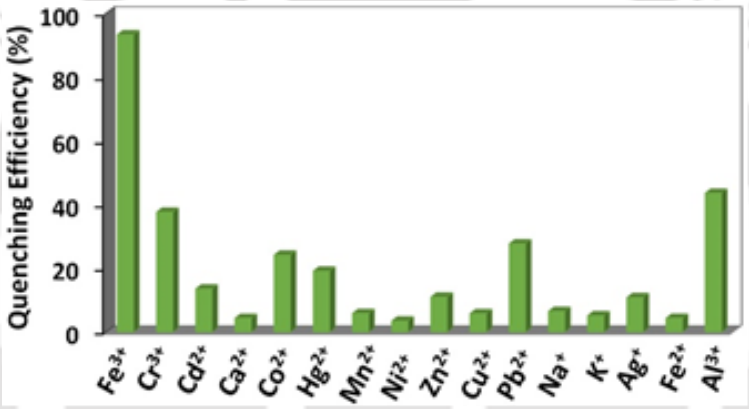

Figure 4. Fluorescence quenching efficiencies upon the addition of 150 μL of different metal ions (2 mM) to a 3 mL suspension of **1′**.

Chapter 3: Chapter 3 presents the successful synthesis, characterization, and sensing application of hydrazine functionalized Zr(IV)-based UiO-66 metal-organic framework (MOF) called Zr-UiO-66-N_2H_3 (**2**). The guest-free material **2′** showed selective and sensitive fluorimetric detection (turn-on) of phosphate (PO_4^{3-}) anions in HEPES buffer (10 mM, pH = 7.4) and aqueous medium (Figure 5). Other competitive analytes did not show any considerable fluorescence response whereas PO_4^{3-} showed ~120 fold increment in fluorescence response (Figure 6). It could also fluorimetrically detect (turn-off) 4-nitrobenzaldehyde (4-NB) in a HEPES : DMSO (9 : 1, v/v) medium with high selectivity and sensitivity (Figure 7). The quenching efficiency in presence of 4-NB is above 90% (Figure 8). The selectivity for both analytes is retained in the presence of other potentially competitive analytes. The detection limit for PO_4^{3-} ion in water is 0.196 μM, which is far below the PO_4^{3-} level present in the aqueous environment. MOF **2′** can detect intracellular phosphate and it also has the capacity to

TH-2604_156122006

exhibit differences in the intracellular phosphate level. Furthermore, the probe is capable of sensing PO_4^{3-} ions in real samples such as tap water, lake water, human urine and human blood serum. The sensitivity of the probe for sensing 4-NB is very high (detection limit = 4.7 μM). The possible mechanisms for sensing PO_4^{3-} ions and 4-NB have been explored in detail by experimental techniques.

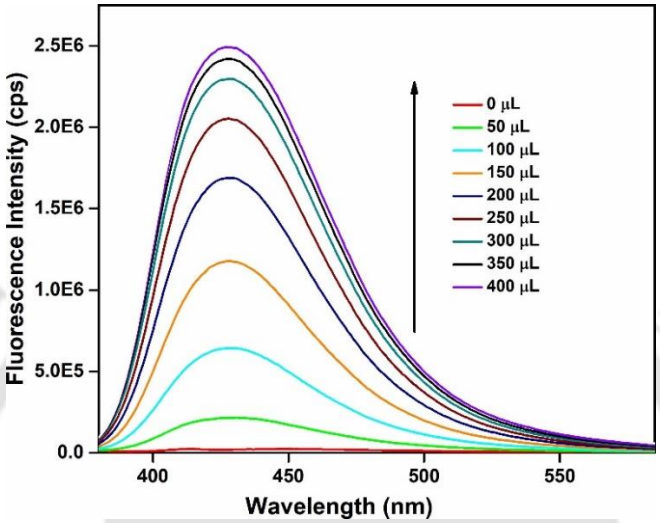

Figure 5. Enhancement of the fluorescence intensity of **2′** (0.87 mM) upon gradual addition of 400 μL of 2 mM aqueous solution of PO_4^{3-} ion (λ_{ex} = 360 nm, λ_{em} = 430 nm).

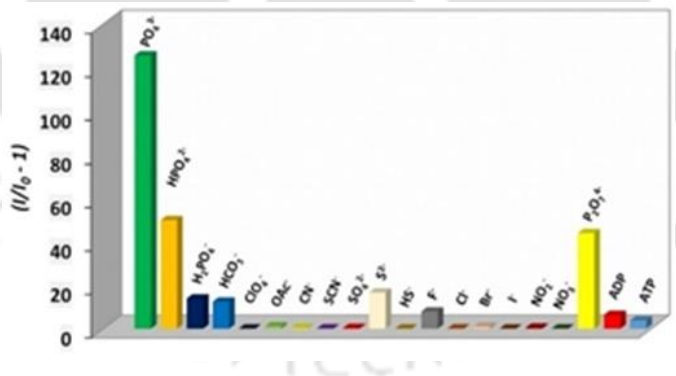

Figure 6. Change in the fluorescence intensity of the suspension of **2′** (0.87 mM) upon the addition of 400 μL of 2 mM aqueous solutions of various anions (λ_{ex} = 360 nm, λ_{em} = 430 nm).

TH-2604_156122006

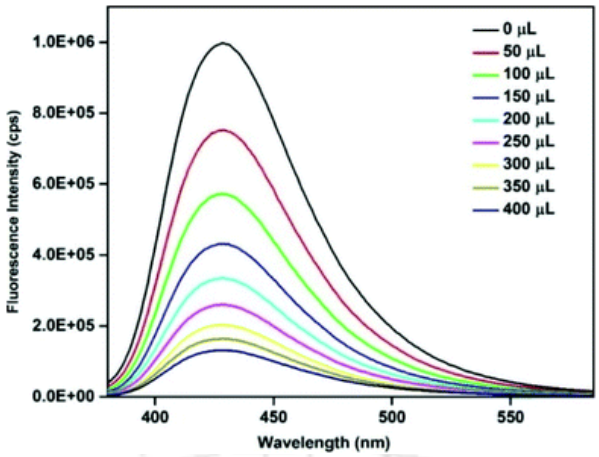

Figure 7. Quenching of the fluorescence intensity of **2′** (0.87 mM) by incremental addition of 400 µL of 50 mM 4-NB solution to a 3 mL stable suspension of **2′** in HEPES/DMSO (9:1, v/v) (λ_{ex} = 360 nm, λ_{em} = 430 nm).

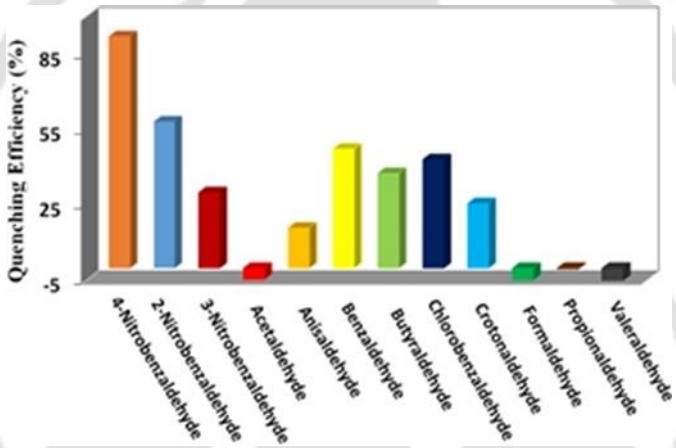

Figure 8. Fluorescence quenching efficiencies of different aldehydes towards **2′** (0.87 mM) in DMSO/HEPES (9:1, v/v) mixture. The fluorescence spectra were collected after the addition of 400 µL of 50 mM aldehyde solutions (λ_{ex} = 360 nm, λ_{em} = 430 nm).

Chapter 4: In this chapter, a new Zr(IV)-based UiO-67 metal-organic framework (**3**) was prepared with urea-functionalized biphenyl-4,4′-dicarboxylic acid (BPDC-urea) as the linker using conventional solvothermal technique and thoroughly characterized using XRPD (Figure 9), FT-IR spectroscopy, TG, and N_2 sorption analyses. The activated form of **3** (called **3′**) exhibited great BET surface area in spite of having a large functional moiety (urea) in the linker side. The activated form of this material (**3′**) was successfully employed for the Friedel–Crafts alkylation of indole with β-nitrostyrene to achieve 97% yield in toluene at 70 °C for 24 h. Furthermore, the catalyst was used for four cycles, with no significant loss in its activity, and the reaction was heterogeneous. Figure 10 shows that the activity of **3′** is comparable to UiO-67-$(NH_2)_2$, whereas the activity is 2-fold higher compared to the parent UiO-67.

TH-2604_156122006

Further, the activity of the BPDC-urea linker was nearly 2-fold higher than that of $ZrCl_4$ (Figure 10), suggesting the crucial role played by the urea moiety than the metal node. In addition, the catalyst (**3′**) exhibited a broad substrate scope, allowing the preparation of a series of compounds with moderate to high yields under the optimized reaction conditions. The roles of metal salt and linker in the catalysis have also been studied separately, and the mechanism (scheme 1) for the catalysis has been clarified.

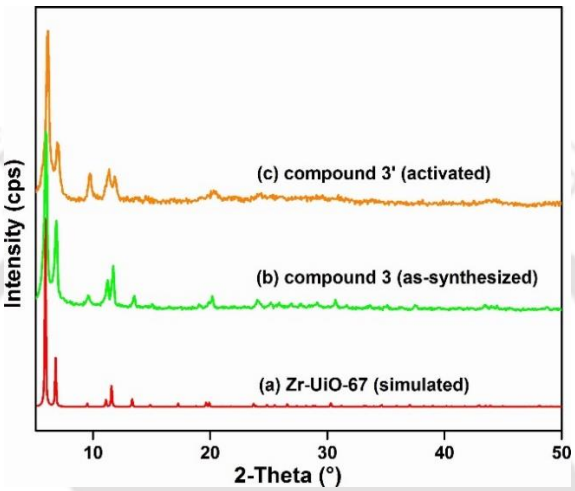

Figure 9. XRPD patterns of (a) simulated Zr-UiO-67 and (b) as-synthesized (experimental) **3** and (c) activated **3′**.

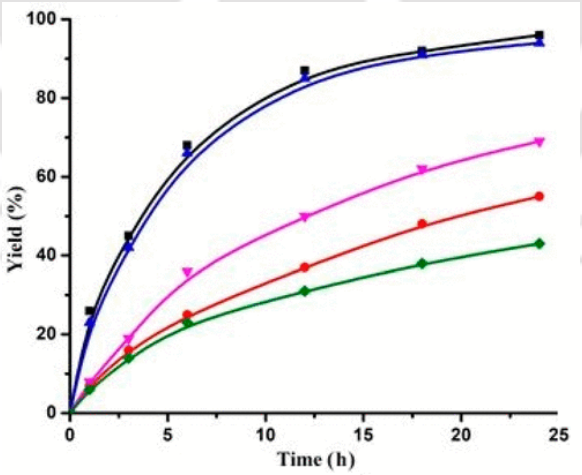

Figure 10. Time conversion plots for the Friedel-Crafts alkylation reaction between indole and β-nitrostyrene using (■) UiO-67-urea (**3′**), (▲) UiO-67-$(NH_2)_2$, (▼) BPDC-urea linker, (●) UiO-67 and (♦) $ZrCl_4$.

TH-2604_156122006

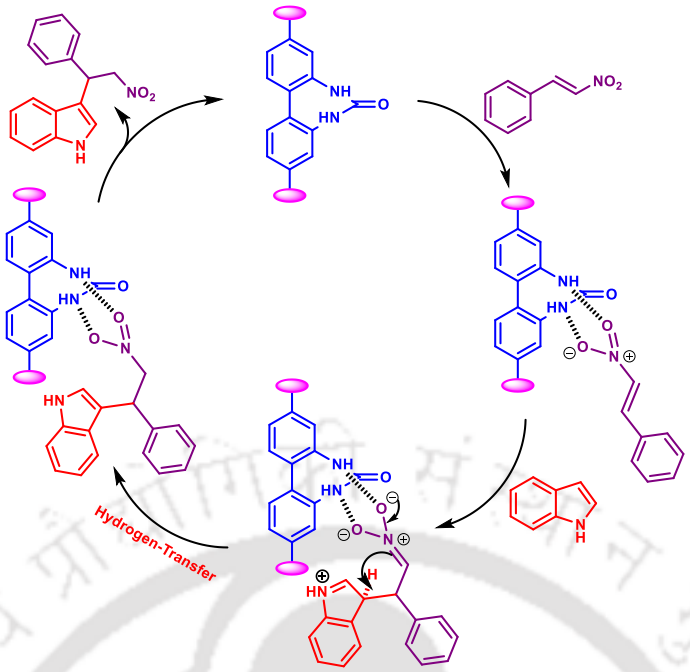

Scheme 1. A possible mechanism for the Friedel-Crafts alkylation of indole with β-nitrostyrene catalyzed by **3′**.

Chapter 5: In this work, a new thiophene-2-carboxamide-functionalized Zr-UiO-66 MOF (**4**) was synthesized by employing a traditional solvothermal procedure. Figure 11 shows that material **4** has very good crystallinity and it preserves its structural framework even after activation procedure. Compound **4** displayed high thermal (up to 340 °C under an Ar atmosphere) and chemical stability (in water, 1 M HCl, and acetic acid). The nitrogen physisorption measurement with the activated form of **4** (denoted **4′**) exhibited a BET surface area of 781 m^2/g despite attachment of a bulky side chain with the linker molecule. Compound **4′** was able to catalyze the ring-opening reaction of epoxides with amines, heterogeneously. Catalyst **4′** exhibited significant yields as well as broad substrate scope in the ring-opening of epoxides utilizing amines. It also displayed better catalytic performance in comparison to known MOF catalysts such as $Cu_3(BTC)_2$, Fe(BTC) (BTC: 1, 3, 5-benzenetricarboxylate) and Zr-UiO-66 (Figure 12). Control experiments were performed with the corresponding free linker, Zr(IV) salt and without catalyst **4′**, confirming the exclusive role of **4′** in the catalytic reaction (Figure 12). The reusability characteristics of catalyst **4′** was established for up to five consecutive catalytic cycles. The synthesis and characterization of material **4** and **4′** and mechanism (scheme 2) of the catalysis reaction were studied elaborately.

TH-2604_156122006

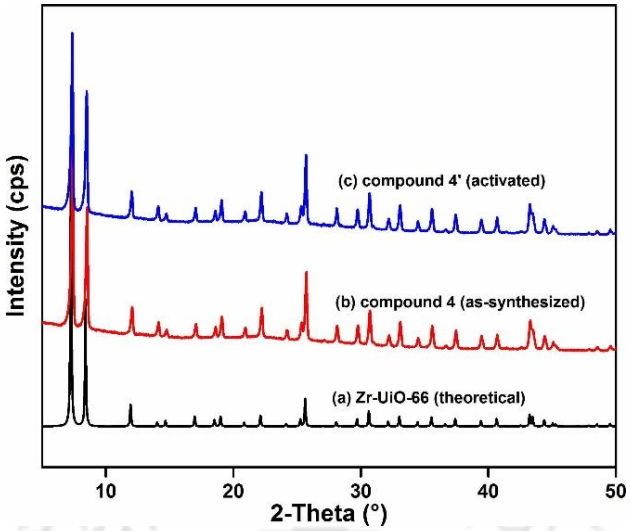

Figure 11. XRPD patterns of (a) Zr(IV) based UiO-66 (theoretical), (b) **4** (experimental) and (c) **4′** (experimental).

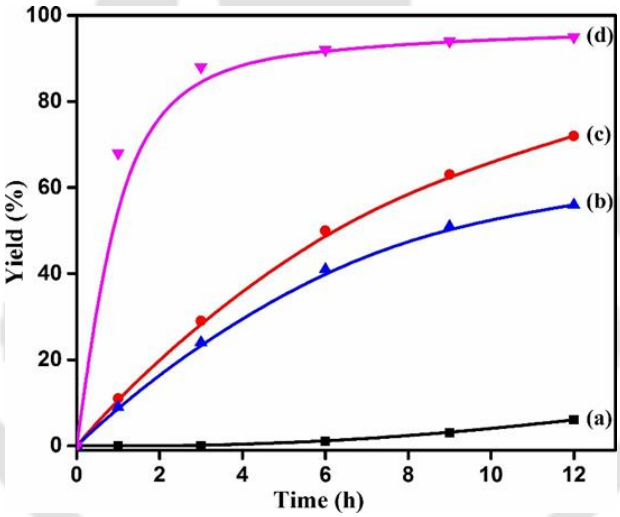

Figure 12. Time-conversion plot for ring-opening of substrate **1** by substrate **2** using different MOFs as solid heterogeneous catalysts: (a) $Cu_3(BTC)_2$, (b) Zr-UiO-66, (c) Fe(BTC) and (d) **4′**.

TH-2604_156122006

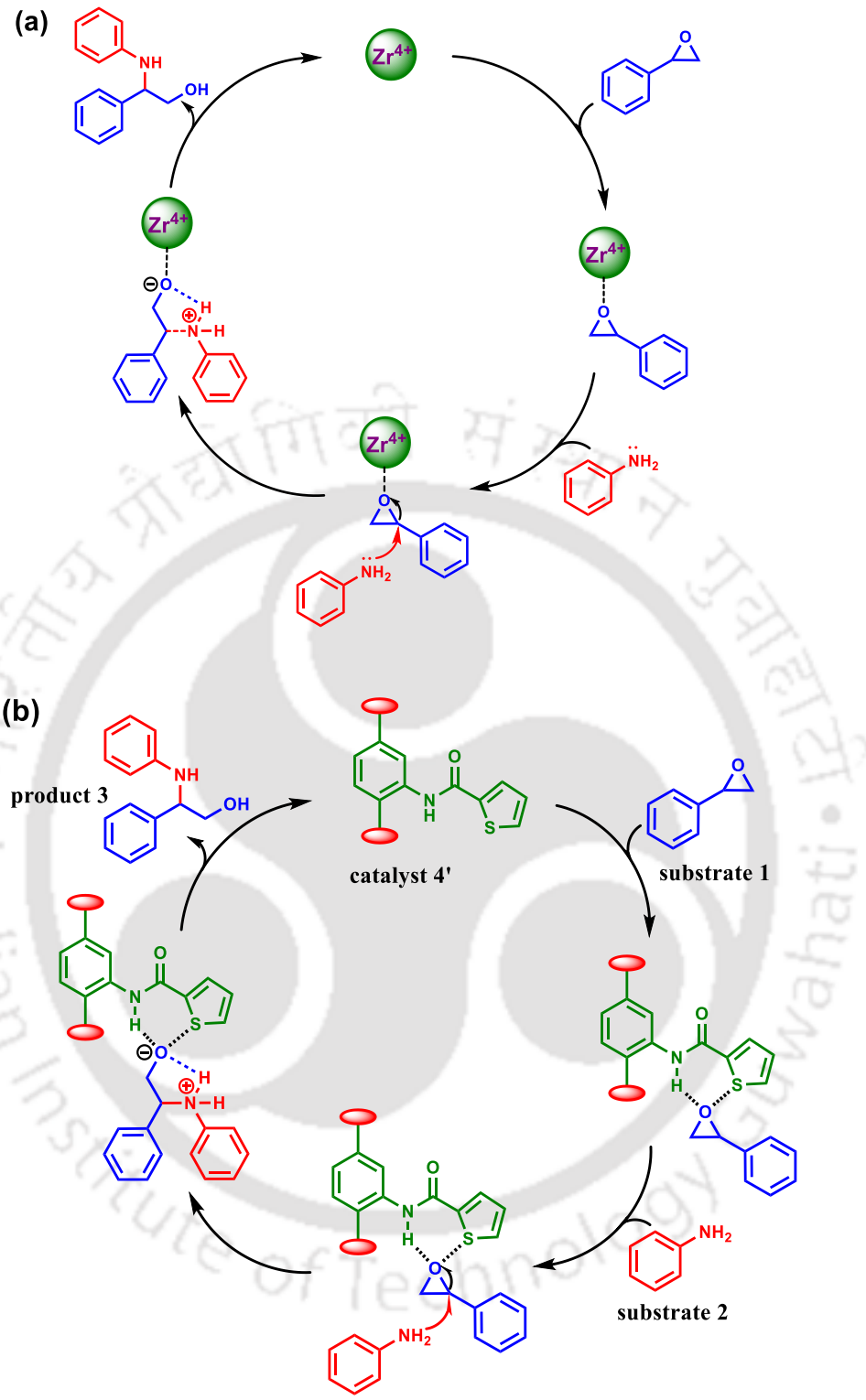

Scheme 2. A possible mechanism for the ring-opening of substrate **1** by substrate **2** through (a) metal sites (Zr^{4+}) and (b) thiophene-2-carboxamido linker in **4′**.

TH-2604_156122006

Ph.D. Thesis
Chapter 1

Tuning Fluorescence Sensing and Heterogeneous Catalytic Activities of Highly Stable Metal-Organic Frameworks through Linker Design

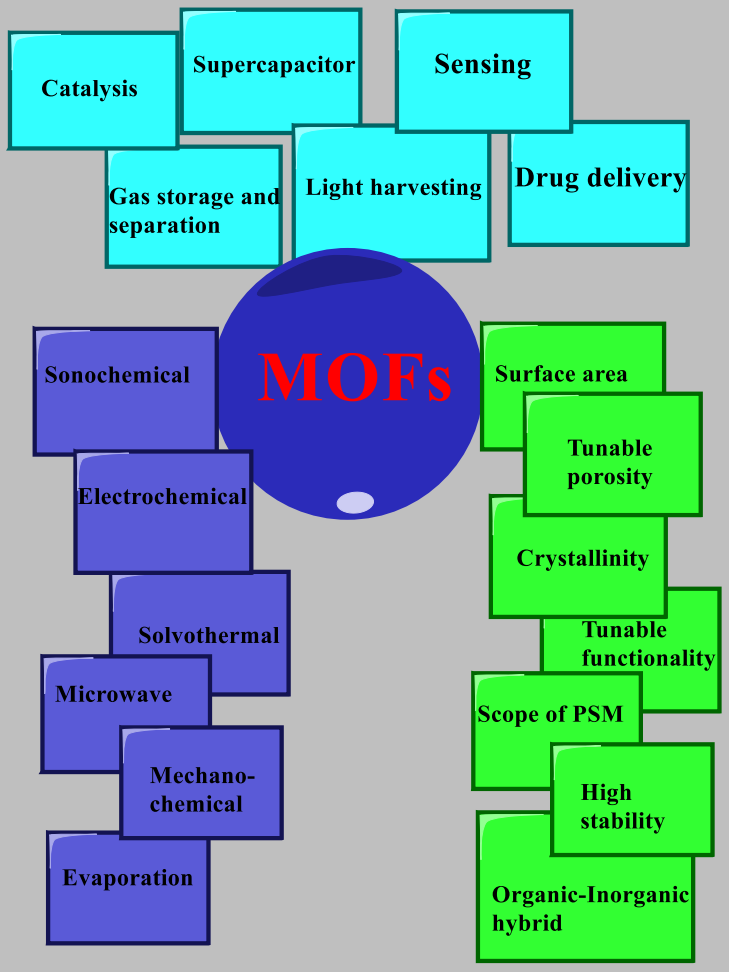

TH-2604_156122006

Chapter 1

1.1 Introduction

Coordination compounds are molecules that contain one or more metal centers bound with linkers (atoms, ions, or molecules that donate electrons to the metal center). The nearby linker molecules communicate with the central metal ion through the coordinate bond (dative covalent bond). German alchemist Andreas Libavius first discovered the blue colored $[Cu(NH_3)_4]^{2+}$ as the first coordination compound in the year of 1597. It was absolutely an inorganic coordination compound.[1] At the beginning of the 18th century, another coordination compound called Prussian blue having molecular formula of $KFe[Fe(CN)_6]$ was discovered.[2] Another example of coordination compound is potassium hexachloroplatinate(IV) dianion, which was prepared in the year of 1760.[3] The systematic and continuous progress of coordination chemistry is considered with the incomplete discovery of ammoniacal solutions of cobalt chloride by the French chemist B. M. Tassaert in 1798 and subsequently orange crystals of $CoCl_3 \cdot 6NH_3$ was achieved by other scientists.[1] Gradually, chain theory (1869) by the Swedish chemist Christian Wilhelm Blomstrand and coordination theory (1893) by the Alsatian-born Swiss chemist Alfred Werner were well established.[4, 5] Werner first found the basis of how to assign the coordination number and oxidation state of transition metal complexes and achieved Nobel Prize in the year of 1913 for his exceptional contribution in coordination theory.[6]

Molecular chemistry is the chemistry of compounds where the interactions are found to occur between atoms.[7] Supramolecular chemistry is the analogous chemistry where interactions are found to occur between molecules. The interactions of chemical systems are built with a discrete number of units and involve non-covalent weaker interactions such as hydrogen bonding, electrostatic interactions, intermolecular forces, π-π interactions and Van der Waals forces.[7] Supramolecular chemistry has become more sophisticated in 1987 with researchers such as Donald J. Cram, Jean-Marie Lehn and Charles J. Pedersen when they were awarded Nobel Prize for their contribution in 'host-guest' chemistry, in which a particular host selectively binds a specific guest.[8]

One of the most rapidly developing areas of coordination chemistry is supramolecular coordination chemistry (SCC). SCC involves discrete systems in which judiciously selected metal centers undergo self-assembly with linkers holding various binding sites oriented with specific angularity to generate a finite supramolecular complex.[9]

Another emerging field of coordination chemistry is metal-organic frameworks (MOFs).[10] MOFs are comprised of infinite networks of metal centers or inorganic clusters bridged by simple organic linkers through metal−linker coordination bonds.[11] The term 'MOF' was first coined by Omar Yaghi in 1995.[12] MOFs, as described by Yaghi et al., are formed by anchoring metal-containing units or secondary-building units (SBUs) with organic linkers by coordination, yielding open frameworks that show the exceptional features of permanent porosity, rigid structure, large surface area, and pore volume.[13] The porosity is a consequence of long organic linkers that deliberate sufficient storage space and various adsorption sites within MOFs along with the capability to systematically vary and functionalize their pore structure.[11]

In the year of 1989, Robson and co-workers have shown that 4,4′,4″,4‴-tetracyanotetraphenylmethane linker can gain a tetrahedral geometry upon binding with Cu(I) centers.[14] This was a critical material because after that the mode of thinking for linker diversity was increased from cyanide to nitrile to pyridyl-based donors.[10] Four years after, Fujita and co-workers showed an assembly of square grids observed as colorless crystals and characterized as $[Cd(4,4'\text{-bpy})_2(NO_3)_2]$ (bpy = bipyridine), when $Cd(NO_3)_2$ was treated with 4,4′-bipyridine in 1:2 ratio in aqueous ethanol.[15] The field then inspireed the use of polytopic donors. Around the year of 1995, Kitagawa and co-workers discovered new porous materials with permanent microporosity based on pyridyl linkers.[16] After that, Yaghi and co-workers created the carboxylate based coordination polymers showing reversible gas adsorption properties and implemented the name "metal−organic framework". According to IUPAC: "Metal-Organic Framework, abbreviated to MOF, is a Coordination Polymer (or Coordination Network) with an open framework containing potential voids."[17]

In the history of MOFs, MOF-5 ($Zn_4O(BDC)_3$, BDC = terephthalate) is one of the first porous MOFs. This material was discovered by Yaghi and co-workers in the year of 1999.[18] Before the discovery of MOF-5, zeolites were known to be the most essential porous materials, which were discovered in 1756 and held the record for the highest porous material over one hundred years.[19] MOF-5 has three times greater internal surface area compared to that of zeolite.[20, 21] After the discovery of MOF-5, several popular MOFs such as MIL-101(Cr/Fe/Al),[22, 23] UiO-66(Zr/Hf),[24, 25] MIL-53(Al/Fe/Cr),[26] MIL-100(Fe/Cr/Al),[27] PCN-5(Ni),[28] PCN-6(Cu),[29] PCN-13(Zn)[30] and HKUST-1 with high porosity and low pressure gas

sorption ability[31, 32] were discovered. Afterwards, MOF-74(Zn) with low pressure adsorption of CO_2[33] and several isostructural analogs of Mg-MOF-74 termed as IRMOF-74-I to IRMOF-74-XI, with large pore apertures to accommodate protein,[34] were the few well-known members of MOF family. In the year of 2012, NU-109E and NU-110E MOFs having highest experimental Brunauer-Emmett-Teller (BET) surface area of any porous material reported to date (7010 and 7140 $m^2 g^{-1}$) were discovered.[35]

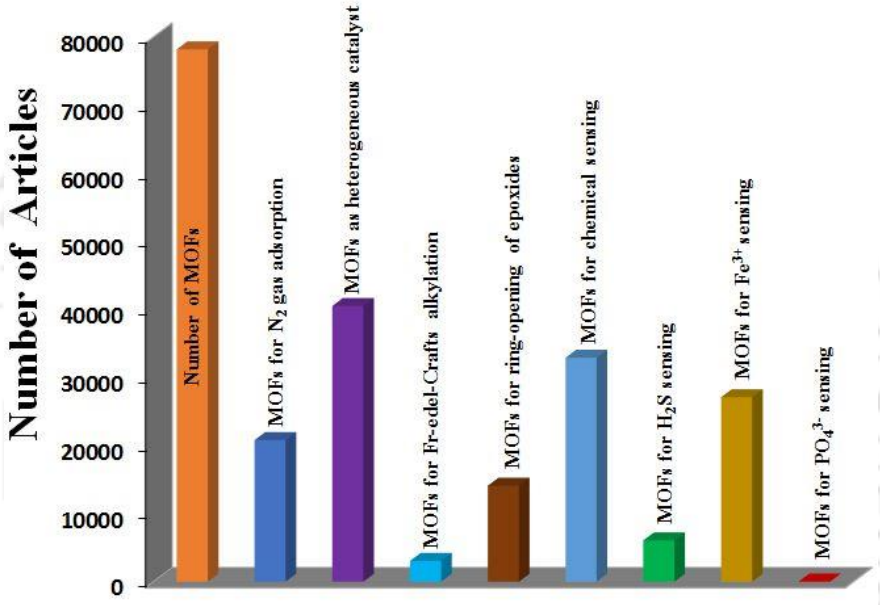

Figure 1.1 Growth in research interest of metal organic frameworks (MOFs) and their various applications. Based on Google Scholar data, retrieved on 4th February, 2020. Google Scholar search term: Metal-Organic Framework, Metal-Organic Framework for N_2 gas adsorption, Metal-Organic Framework as heterogeneous catalyst, Metal-Organic Framework for Friedel-Crafts alkylation, Metal-Organic Framework for ring opening of epoxide, Metal-Organic Framework for chemical sensing, Metal-Organic Framework for H_2S sensing, Metal-Organic Framework for Fe(III) sensing, Metal-Organic Framework for tri-phosphate sensing. Custom range: since 1995 up to 2020.

1.2 Design and Synthesis Principles of MOFs

The name MOF itself says that there are two types of components: one is inorganic metal part and another is an organic linker part. The metal part can form a metal cluster and binds with linkers, or metal ions itself can bind with linkers and form 1D, 2D, or 3D MOF structure

depending upon the oxidation and coordination number of metal ion and restrictive environment of linkers.[36] Mostly, MOFs are reported constructing from transition metal ions or clusters because of variable oxidation state and flexible coordination environment of transition metals.[37, 38] Now-a-days, many MOFs are reported from the lanthanide series also.[39] The coordination geometry around the metal ions or clusters and binding sites of linkers decide the structure of the resulted frameworks or MOFs.[40-42]

The lengths, geometries, and functional groups of designed linker molecules typically customize the structure and properties of MOFs. The linker molecules can be anionic, neutral, and cationic (Figure 1.2).[43] Anionic, as well as neutral linkers, can form stable MOFs, especially with high valent metals, because the accumulation of electron is very high in the case of anionic linkers, which can bind tightly with the high valent metals.[44] The cationic linker is very reluctant to form MOFs due to their very low electron density.[44] On the other hand, the linker could be mono-dentate or multi-dentate. Multi-dentate linkers can form an extended 3D framework, whereas mono-dentate linkers form only 1D framework due to their small size and restricted coordination number.[45, 46] Typically, linker molecules can be classified as (a) ditopic, (b) tritopic, (c) tetratopic, (d) hexatopic, (e) octatopic, (f) mixed desymmetrized and (g) metallo and N-heterocyclic linkers.[13] Again, linkers can have smaller chain lengths, or these can be long-chain flexible in nature. The rigid linker molecules form high thermally as well as chemically stable MOFs but the flexible ones form less stable MOFs.[13, 47]

The inorganic nodes also dictate MOF structures and properties.[38] The transition metals have coordination numbers ranging from 2-10, which allows different arrangements of coordinated linkers and construction of a variety of MOF structures. Metal ions or clusters can form several possible geometries like linear, bent, triangular, tetrahedral, square planar, square pyramidal, and octahedral depending upon coordination number and coordination environment.[48-53] During earlier stages of MOF synthesis, divalent metals like Zn^{2+} and Cu^{2+} were widely used.[54] Latter, more or less all the metal cations in the Periodic Table, including some radioactive ones, have been used as inorganic nodes to construct MOFs. The metals used for MOF synthesis are monovalent (Cu^{+}, Ag^{+}, etc.), divalent (Mg^{2+}, Mn^{2+}, Fe^{2+}, Co^{2+}, Ni^{2+}, Cu^{2+}, Zn^{2+}, Cd^{2+}, etc.), trivalent (Al^{3+}, Sc^{3+}, V^{3+}, Cr^{3+}, Fe^{3+}, Ga^{3+}, In^{3+}, lanthanides^{3+}, etc.), or tetravalent (Ti^{4+}, Zr^{4+}, Hf^{4+}, Ce^{4+}) metal cations.[38] Despite the numerous advantages,

applications of these monovalent or divalent metal-based MOFs are ultimately limited due to their instability under harsh conditions. Therefore, researchers have turned their efforts to construct high thermally and chemically stable trivalent (Al^{3+}, Cr^{3+}, Fe^{3+}) and especially, tetravalent (Zr^{4+}, Hf^{4+}) metal-based MOFs.[38]

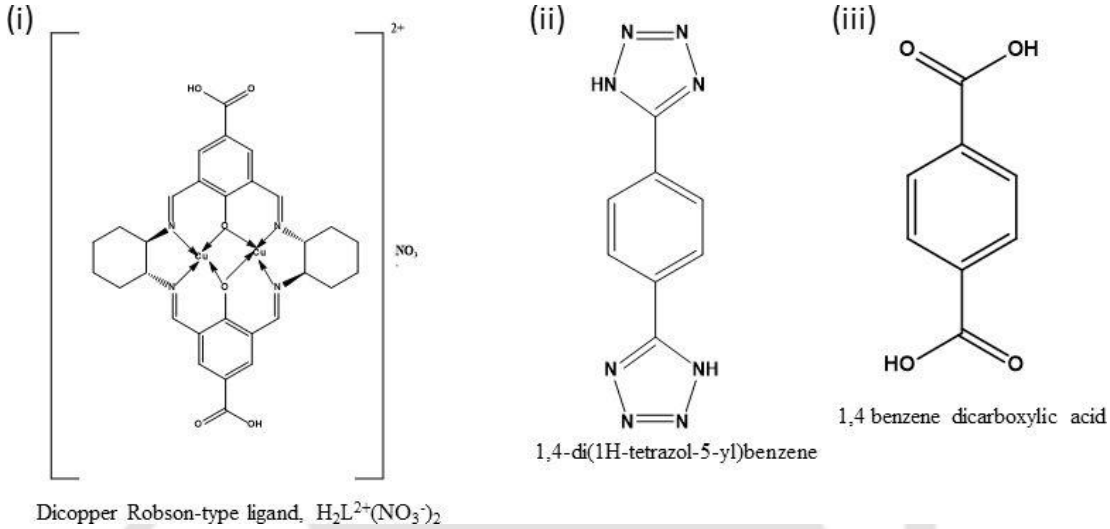

Figure 1.2 Example of cationic, neutral and anionic linkers for construction of various MOFs.

1.3 Network Geometry and Secondary Building Units of MOFs

In coordination polymers, the molecular building units are formed by the strong interactions like ionic, covalent, H-bonding, etc. which help to the formation of extended structures.[55-57] These types of communications lead to the creation of new porous polymers in which typically metal ions are used to interact with the carboxylate-based linkers to make porous MOF materials (examples: MOF-5, UiO-66, Cr-MIL-101, etc.).[58-60] In the design and synthesis of MOF materials, two different strategies have been used for the study of exact structures and properties, which are: (a) Node and Spacer and (b) Secondary Building Units (SBUs).

1.3.1 Node and Spacer Strategy

The extended structures of MOFs consist of inorganic metal ions and organic polytopic linkers. In this strategy, the metal ions are termed as 'Node' and organic linkers as 'Spacer'.[61] Various metal nodes and organic spacers are utilized during the synthesis of MOF materials. The spacers may have different topologies (e.g., square, tetrahedral, octahedral, etc.). Several

combinations of organic spacers with various metal nodes lead to the formation of MOF materials with diverse topologies (Figure1.3).[62]

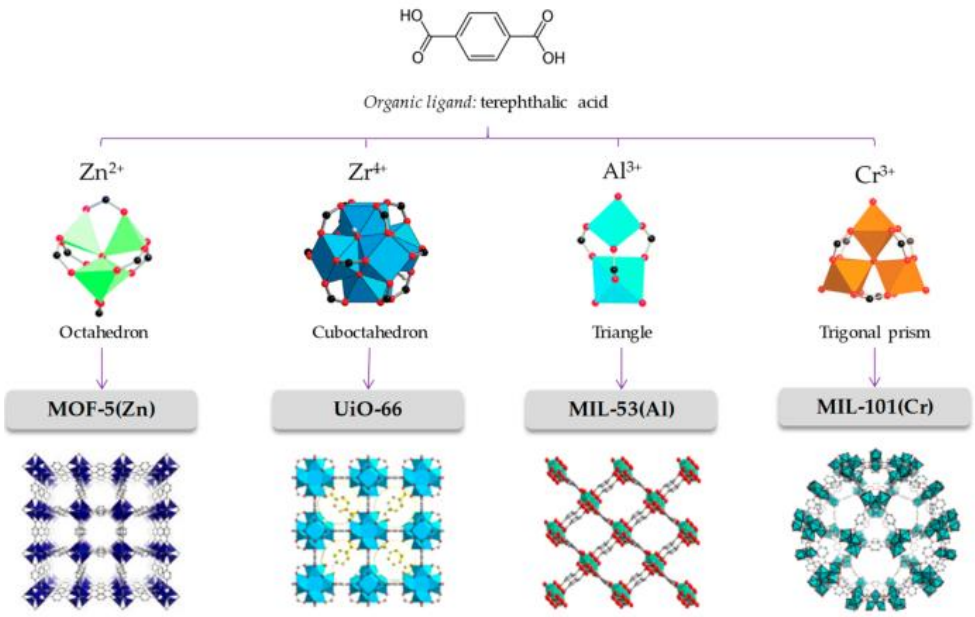

Figure 1.3 The node-and-spacer approach to prepare MOFs. The adequate selection of the organic linker (linear in the case of terephthalic acid) and connection geometry of the metal cluster lead to the desired topology. Each framework topology has its characteristic pore size and available surface. Reproduced with permission from ref. 63. Copyright 2019 MDPI.

1.3.2 SBU Strategy

The most common term, 'secondary building unit (SBU)' has been used in the zeolites chemistry, where the SBUs refer to a compact structural motif, which occurs in various tetrahedral frameworks.[53, 64] Secondary building units (SBUs) are set of building or cluster units in molecular level in which linker coordination modes and metal coordination environments can be utilized in the transformation of these fragments into prolonged porous networks using polytopic linkers. In the field of MOF materials, Yaghi and co-workers have introduced the 'secondary building units (SBU)' strategy for the construction of porous framework materials.[44, 65] These SBUs are formed by the coordination sites of the metal nodes and coordination modes of the organic spacers.[65] Moreover, these SBUs build well-defined coordination structures, which are systematic in the framework structures.[53] Figure 1.4 shows

examples of SBUs of different MOFs: MOF-5 has $OZn_4(\text{-}COO)_6$, UiO-66 has $Zr_6O_4(OH)_4(\text{-}COO)_6$, MIL-53 has $AlO_4(OH)_2(\text{-}COO)_6$ SBUs.[53, 66]

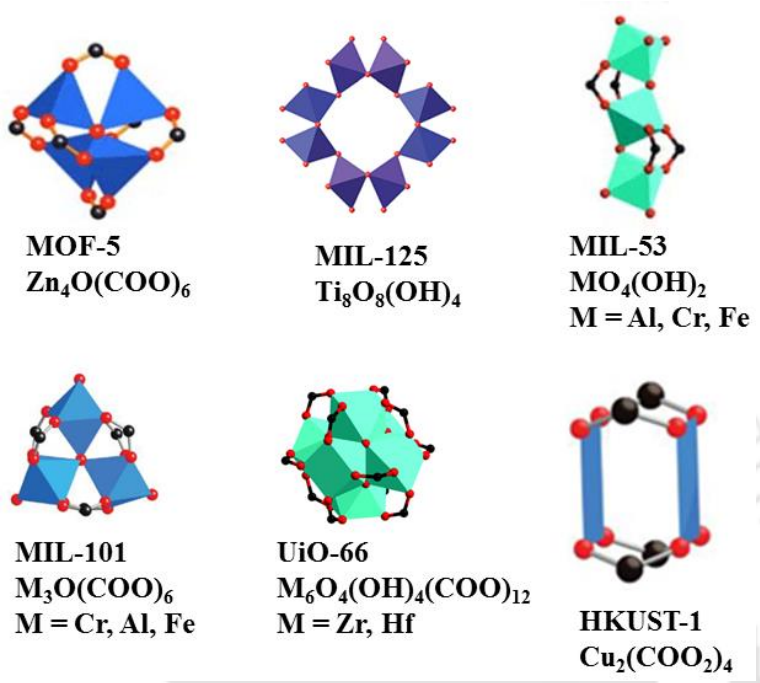

Figure 1.4 Graphic illustration of common SBUs within MOFs.

1.4 Stability and Rigidity of MOFs

The stability of MOFs generally means chemical, thermal and mechanical stability. Chemically stable MOFs have high demand because of their various applications in many chemical environment, e.g., moisture, solvents, acids, bases and aqueous solutions containing coordinating anions.[67] The thermal and mechanical stability of MOFs usually correlate with their ability to preserve structural integrity upon exposure to heat, vacuum or pressure treatment.[67]

To address the issue of stability of MOFs, Pearson's hard soft acid-base (HSAB) theory can be considered. High-valent metals with high charge density (hard acids) (Zr^{4+}, Cr^{3+}, Al^{3+}, Fe^{3+}, etc.) and 'O' donor linkers (hard bases) are required to form MOFs with strong coordination bonding, thus usually presenting excellent chemical stability.[67] These high-valent metal ions need more linkers to balance the charges during coordination with carboxylate linkers. This can lead to a high connection number of metal clusters and further enhance the stability of the resultant MOFs. For example, Cr-MIL-101, Cr-MIL-53, UiO, MIL-125 and PCN series MOFs

are exceptionally stable in acid and alkali.[68] On the other hand, even with the same metal cluster and framework topology, the chemical stability of some MOFs decreases with the lengthening of the linker and the enlargement of pore size (as observed in UiO-66 series, SUMOF-7 series, etc.).[24, 69]

Low-valent metal ions, including Zn^{2+}, Co^{2+}, Ni^{2+}, Fe^{2+} and Ag^{+}, can be considered as soft acids to construct highly stable MOFs with suitable N-containing linkers (soft bases). In general, the higher the pKa of the N-donor linkers, the more stable the resultant MOFs under humid conditions.[67] For example, the reaction between the pyrazol-type linker (1,3,5-tris(1H-pyrazol-4-yl)benzene, H_3BTP) and Ni^{2+}ions resulted in an ultrastable framework, $Ni_3(BTP)_2$.[70]

Modulated synthesis strategy is highly efficient in regulating the size of Zr-MOFs from nanosize to large single crystals for easy single-crystal X-ray diffraction.[71] Note that high-valent metal-containing MOFs with remarkable chemical stability include not only carboxylate-based MOFs but also those with phosphonate and phenolate-based frameworks. The relatively high pKa of the phenolate linkers can afford stronger M–O bonds with Zr^{4+} ions in comparison to carboxylate linkers and forms highly stable MOFs.[71]

Sometimes, MOFs containing mixed-metals display improved stability as compared to single-metal MOFs. There may be several reasons for this: (i) formation of stronger coordination bonds compared to pristine bonds, (ii) enhancement of the inertness of metal clusters and (iii) improvement of surface hydrophobicity.[72, 73] Therefore, the design principle toward the synthesis of stable MOFs considers mixed-metal MOF strategy where the replacement of existing metal ions occurs with more inert metals. For example, the partial replacement of Zn by Ni metal ions in MOF-5 increases the hydrostability of the MOF.[72]

To enhance the stability of MOFs toward moisture, hydrophobic properties of MOFs need to be enhanced by incorporating hydrophobic binding groups to the linkers or by creating them around the metal nodes. The water repellent functional groups around the metal clusters can efficiently protect the weak coordination bonds from the attack by water molecules as nucleophiles and enhance the MOF stability in an aqueous system. To prove the effectiveness of hydrophobic linkers, a methyl group modified MOF-5 was synthesized and it was more stable compared to pristine MOF-5 in water.[60]

Thermodynamic factors are mainly related to the metal-linker coordination bond strength.[67] The coordination bond strength might be predicted by Pearson's hard soft acid-base (HSAB) theory. In the de novo synthesis of MOFs, ligands with relatively high pKa (e.g., azoles) efficiently produce robust frameworks with low-valent metal ions, whereas linkers with relatively low pKa (e.g., carboxylic acids) tend to bind with high-valent metal ions to give stable structures.[74]

1.5 Isoreticular Chemistry in Design of MOFs

Isoreticular chemistry is a powerful principle to design new MOFs with predetermined topology. It is the chemistry which showed the impact of design and study of new structural and functional MOF materials using the organic linkers of different sizes but having a common or same symmetry with the desirable framework topology.[75] This concept discovered new MOFs with new functionality and produces better and expected results for gas storage and separation, chemical sensing and catalysis, etc.[76] In real case, it is hard to predict the topology of a predesigned system especially when it is a more complex system (for example, polytopic linkers). At the same time, the other factors like temperature, solvent and substrate composition/concentration remain untold, which would also affect the product crystallinity and morphology. Once the synthesis of the SBU is established, it could be used to direct the assembly of ordered frameworks with rigid organic linkers. Thus, it becomes quite easy to predict the chemistry of the yielded crystalline materials or MOFs. This approach was first established by Yaghi and co-workers as “reticular synthesis”, which has triggered systematic investigation of diverse properties of MOFs with pore metrics varied and functionalized.[77, 78] The first MOF based on isoreticular chemistry was discovered in 2002 by Yaghi and co-workers.[78] Till date, an enormous number of MOFs have been reported based this concept.[79, 80] The isoreticular chemistry developed the idea that a predesigned MOF can be achieved for a target application by changing the length of linker molecules and functional groups (Figure 1.5). Many scientists are still working on MOFs follow this chemistry, as there is wide scope to design and synthesis of new functional MOF materials.

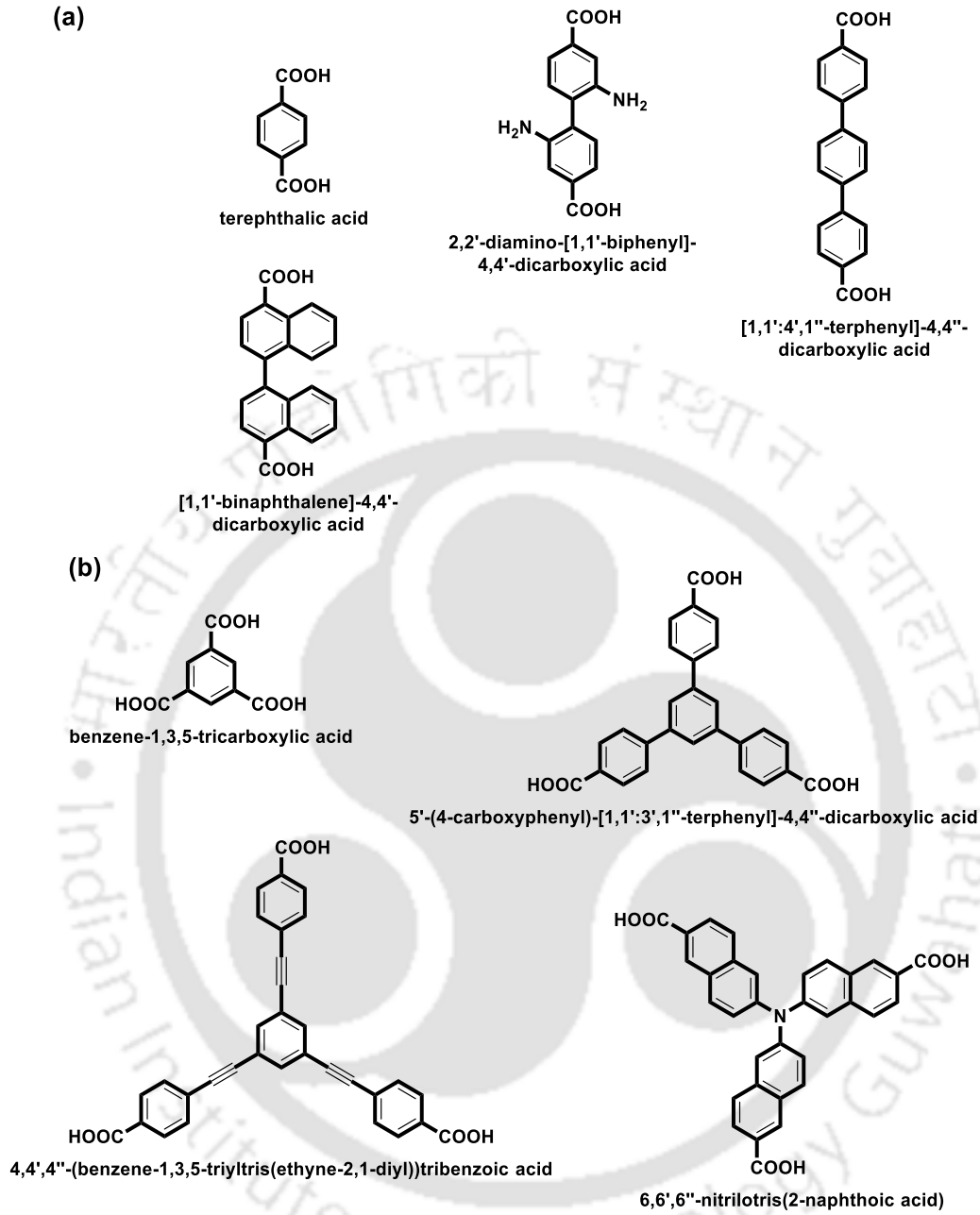

Figure 1.5 Type (a) and (b) linkers form $Zr_6O_4(OH)_4^{12+}$ and dicopper paddlewheel SBUs, respectively. Here, linker type (a) and (b) separately can be used for MOF synthesis following the isoreticular chemistry.

1.6 Linker Design to Construct MOFs

MOFs are formed from metal clusters or SBUs and linkers. The SBUs are constructed from metal ions *in situ* in reaction system whereas, the linkers used for the formation of MOFs are pre-designed as well as pre-formed.[78] The geometry and connectivity of linker molecules decide the framework topology of MOFs.[75] The organic units (linkers/bridging ligands) are carboxylates or other organic anions such as phosphonate, sulfonate and heterocyclic compounds.[81, 82] The length, shape, functional group and metal/linker ratio dictate the pore size, shape, surface area and activity of MOFs for a pre-determined application.[13] For a particular selected use of MOFs towards gas storage, sensing, catalysis and proton conductivity, etc., the choice of a proper linker is highly desirable because it controls the inherent properties of MOFs. Therefore, based on topology or symmetry, linkers are classified in different categorized such as ditopic, tritopic, tetratopic, hexatopic, octatopic, mixed, desymmetrized, metallo, and N-heterocyclic linkers.[13] This thesis highlights the synthesis of MOFs with ditopic carboxylate based linkers with a specific focus on tuning the topology and functionality for different applications like gas storage, sensing of toxic chemicals and heterogeneous catalysis.

1.6.1 Ditopic Carboxylate Linkers

In chemistry, ditopic resembles chemistry of a compound that has two sites at which another mixture can form a complex. In MOF chemistry, the use and chemistry of ditopic linkers are well established because of their easy accessibility and noticeable structures in combination with a variety of SBUs. Generally, the twisted angle of linear dicarboxylates plays a decisive role in defining both the dimensionality and topology of the final network structure. While introducing various bulkiness can influence the dihedral angle, but linker length might not necessarily be a requirement for topological control. It should be pointed out that dihedral angle does not guarantee that the two carboxylates are perpendicular to each other. The reaction between zinc nitrate [$Zn(NO_3)_2$] and ditopic linker terephthalate (BDC) (Figure 1.6) produces crystalline MOF-5 [$Zn_4O(BDC)_3$] under solvothermal conditions.[18] In the crystal, the octahedral $Zn_4O(CO_2)_6$ cluster is the SBUs. It has been proved that the structure of MOF-5 is three dimensional (3D) network.[18] The ditopic linkers can have different lengths, but the same topology can connect the same SBUs and form different materials with same network

topology. While the replacement of this BDC linker with functionalized or un-functionalized BDC, BPDC, TPDC, NDC, PDC and HPDC (all are ditopic linkers) (Figure 1.6) produce MOFs (IRMOFs) of same framework topology with MOF-5.[83] This successful utilization of SBUs and ditopic linkers of different lengths not only gives new functionalized (–Br, $–NH_2$, $–OC_3H_7$, OC_5H_{11}, $–C_2H_4$ and $–C_4H_4$) porous materials but also demonstrates how a particular predicted MOF structure can be achieved carrying expanded pores.[84]

Metal ions with high corrosion resistant power and high affinity towards carboxylates are desirable for the synthesis of highly stable MOFs.[85] Zr(IV) is readily available on earth in the form of its mineral zircon. In the year of 2008, a new MOF called UiO-66 (UiO = University of Oslo) was reported for the first time with exceptional features like high BET surface area, hydrothermal stability and chemical stability, application towards a specific target analytes, etc.[24] This MOF was synthesized utilizing $ZrCl_4$ and BDC linker (Figure 1.6) in DMF solvent under solvothermal conditions. Its 3D framework contains octahedral as well as tetrahedral cages. The regular octahedral cages can be expanded by expanding the length of the linker molecules. For example, when BPDC and TPDC (Figure 1.6) linkers were used instead of BDC, UiO-67 and UiO-68 MOFs were produced, respectively, with higher unit cell parameters but having the same framework topology as UiO-66.[24] Till date, several functionalized UiO-66, UiO-67 and UiO-68 MOFs have been reported for gas adsorption, gas storage and separation, chemical sensing, catalysis, proton conductivity and bio-related applications. Recently, along with Zr(IV), Hf(IV)-based UiO-n (n = 66, 67, and 68) series, MOFs have been also reported with better performances as compared to that of Zr(IV)-based UiO-n MOFs. Due to their high chemical stability, the UiO MOFs are used for various applications via PSM techniques.[86-88]

Another interesting MOF called MIL-53 was reported using ditopic BDC (Figure 1.6) linker and trivalent metal salts (Al^{3+}, Cr^{3+}, Fe^{3+}, V^{3+}).[89-92] The MIL-53 MOF comprises infinite chains (having trans geometry) of corner-sharing $[AlO_4(OH)_2]$ octahedra in its structural framework.[93] These octahedra share their corners through the bridging hydroxyl groups. The cross-linking of the adjacent infinite chains through the BDC linkers causes the formation of 3D framework structure of MIL-53 compound.

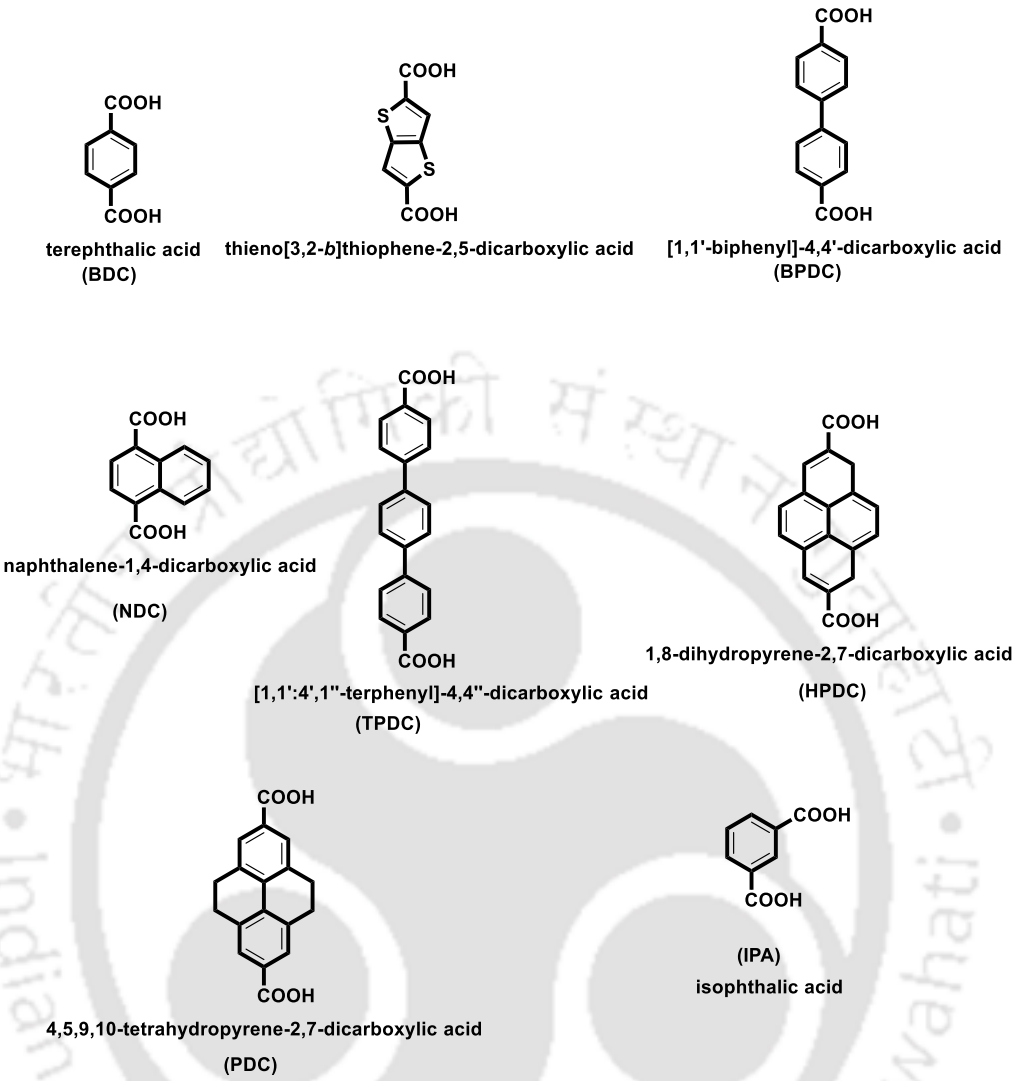

Figure 1.6 Examples of ditopic carboxylate based linkers.

1.6.2 Tritopic Carboxylate Linkers

HKUST-1 is one of the famous MOFs with **tbu** topology built with tritopic carboxylate linker.[54] The dicopper paddle-wheel SBU as node and 1,3,5-benzenetricarboxylate (BTC) (Figure 1.7) as a linker form this MOF.[54] Other isoreticular MOFs were synthesized by employing elongated tritopic linkers such as PCN-HTB (PCN = porous coordination polymer) with 4,4′,4″-(1,3,4,6,7,9,9-heptaazaphenalene-2,5,8-triyl)tribenzoate (HTB) as linker and PCN-6′ with 4,4′,4″-s-triazine-2,4,6-triyl-tribenzoate (TATB) (Figure 1.7) as linker.[94]

The structure of MIL-100(Cr), assembled from the $Cr_3O(CO_2)_6$ cluster and tritopic linker BTC (Figure 1.7), was successfully determined by the combination of simulation and XRPD

studies.[95] The network of MIL-100 contains two types of mesoporous cages with available cage diameters being 25 and 29 Å. The smaller cages consist of pentagonal windows and the larger cages include both pentagonal and hexagonal windows (apertures of pentagonal and hexagonal windows are 4.8 and 8.6 Å). After the discovery of MIL-100 (Cr), its isostructural MOFs, MIL-100(M) (M = Fe^{3+}, Al^{3+}, and V^{3+}) were prepared by replacing the metals in the inorganic SBUs.[96-98] These MOFs showed superior hydrothermal stability and have found extensive applications in adsorption/separation (gas, vapor, and liquid), heterogeneous catalysis and drug delivery, etc.

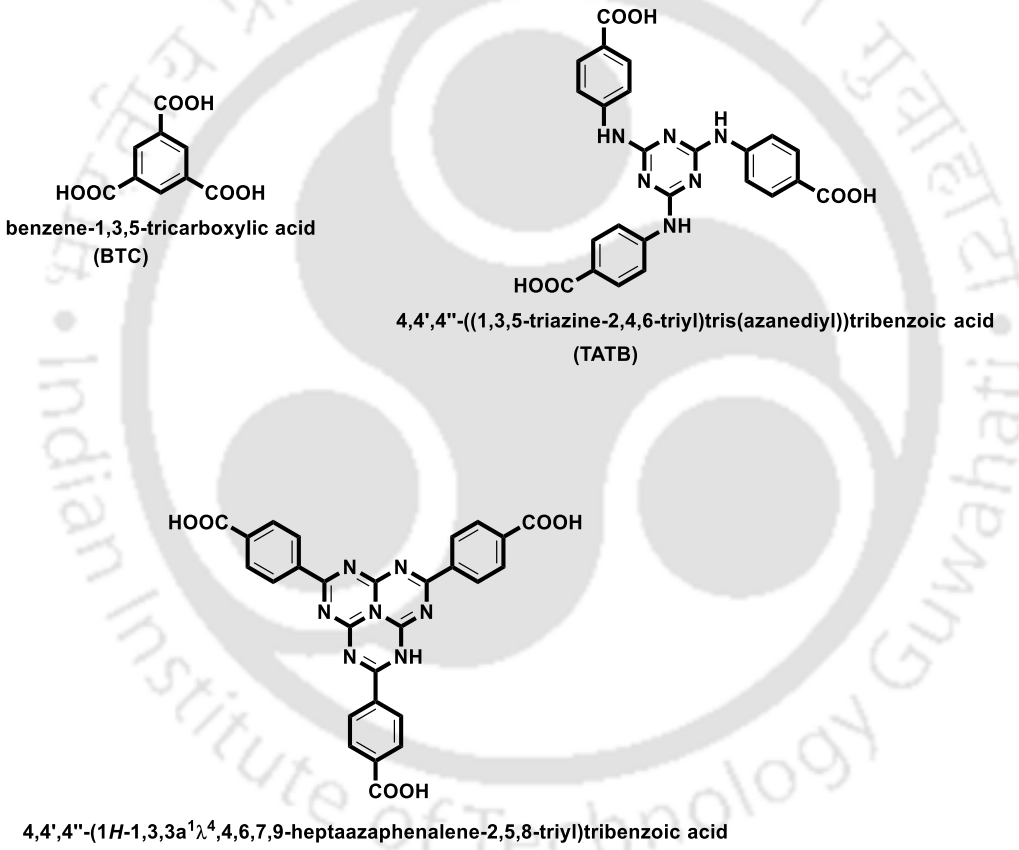

Figure 1.7 Examples of tritopic carboxylate based linkers.

1.6.3 Tetratopic carboxylate linkers

Tetratopic carboxylate linkers are very interesting building units in MOF chemistry and have gained growing attention in recent years for MOFs, especially having tetrahedral geometry. First, the tetrahedral linker has a full T_d symmetry, which is the highest symmetry

in a linker that can be achieved through organic synthesis. High-symmetry building units are always preferred in MOF construction, as they facilitate the packing process of repetitive units during the assembly of crystalline materials. Second, the tetrahedral linker may adopt the symmetry of any T_d subgroup and generates diversity in MOF structures. Third, the tetrahedral linker is an inherently 3D, fully extended structure. Once incorporated into a framework, wide channels and large pores will be provided to maximize the exposure of the framework struts and eliminate the "dead space". In other words, MOFs with exceptionally large porosities can be constructed with tetrahedral building units and symmetrically compatible SBUs.[13]

UHM-8 and UHM-9 are two MOFs which are formed by copper ions and linear tetracarboxylate linker (5,5'-(1,4-phenylenebis(ethyne-2,1-diyl))diisophthalic acid) (Figure 1.8) under different reaction conditions. UHM-8 and UHM-9 have **fof** and **sxt** net system, respectively.[99]

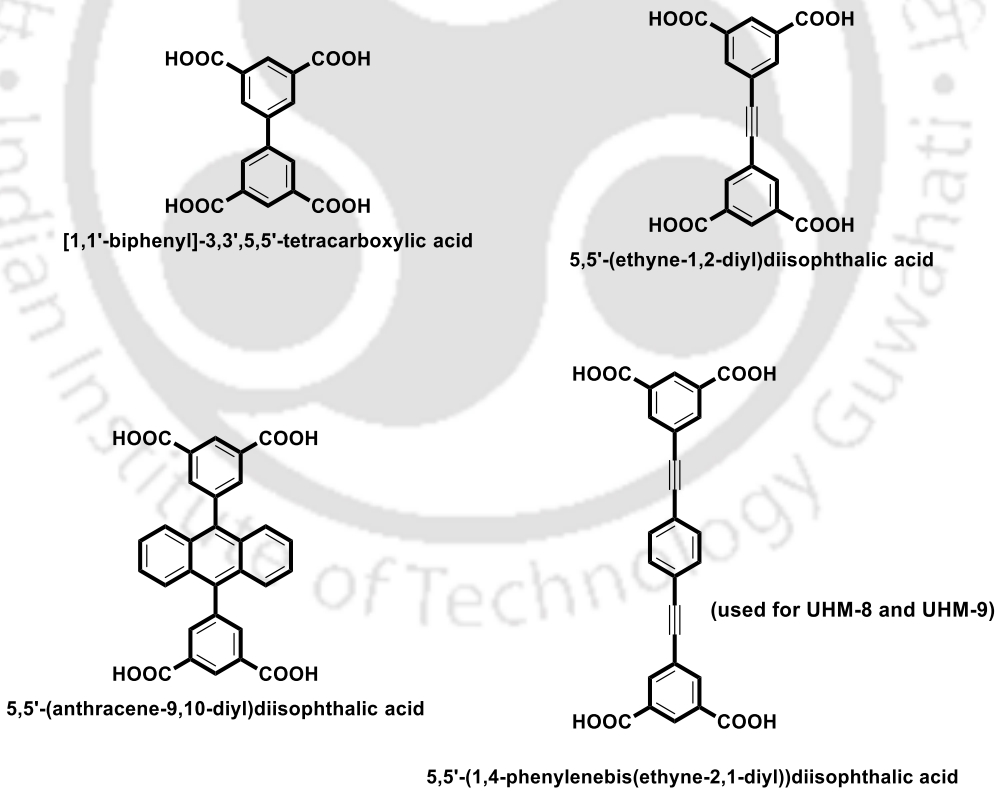

Figure 1.8 Examples of tetratopic carboxylate based linkers.

1.6.4 Hexatopic carboxylate linkers

The 5,5′,5″-[1,3,5-Benzenetriyltris(carbonylimino)]tris-1,3-benzenedicarboxylate (BTEI), a semi-rigid hexatopic linker with C_3 symmetry (Figure 1.9), was used to construct a MOF with a (3,24)-network topology, where nanometre-sized SBBs (cuboctahedra) have been incorporated into a cubic close packing arrangement, leading to superoctahedral and supertetrahedral cavities. This (3,24)-connected **rht** topology has been utilized progressively in the practice of isoreticular chemistry, where higher surface areas have been achieved through expansion of the organic linker.[100] A series of isoreticular (3,24)-connected mesoporous MOFs (PCN-61, -66, -69 and -610) were accumulated from dicopper paddle-wheel units and corresponding hexatopic linkers.[100, 101]

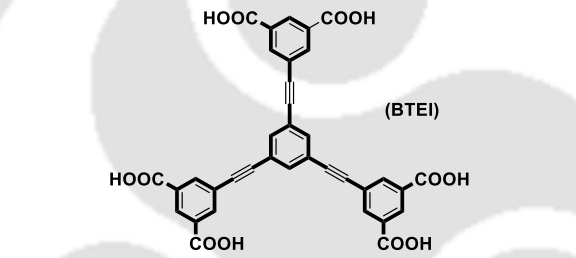

5,5',5''-(benzene-1,3,5-triyltris(ethyne-2,1-diyl))triisophthalic acid

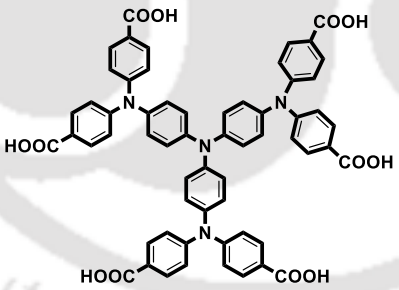

4,4',4'',4''',4'''',4'''''-((nitrilotris(benzene-4,1-diyl))tris(azanetriyl))hexabenzoic ac

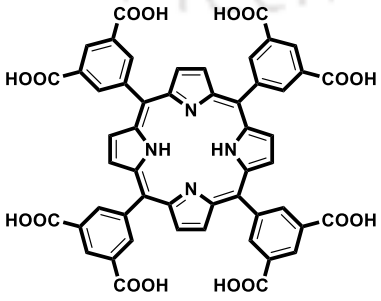

5,5',5'',5'''-(porphyrin-5,10,15,20-tetrayl)tetraisophthalic acid

Figure 1.9 Examples of hexatopic carboxylate based linkers.

1.6.5 Octatopic carboxylate linkers

Only very few MOFs with octatopic carboxylate linkers are reported because of the difficulty in the linker synthesis. The linkers with long arms tend to form interpenetrated structures during the formation of frameworks. Previously reported MOFs constructed from octacarboxylate linkers showed that polytopic linkers might effectively avoid interpenetration probably due to the high connectivity.[13] The octatopic linker (Figure 1.10) and zinc metal form the microporous MOF UTSA-33, where each metal cluster and organic linker can be regarded as 4- and 8-connected nodes respectively and they are linked together to form a noninterpenetrated 4,8-connected network with **flu** topology.[102] The moderate pore size of framework is suitable for selective adsorption of acetylene, ethylene and ethane over methane.

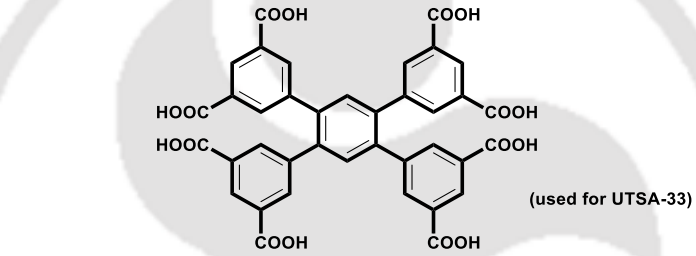

4',5'-bis(3,5-dicarboxyphenyl)-[1,1':2',1''-terphenyl]-3,3'',5,5''-tetracarboxylic acid

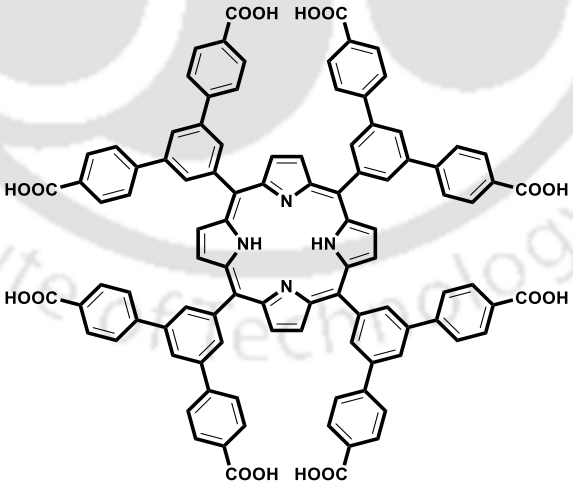

5',5'''',5''''''',5'''''''''-(porphyrin-5,10,15,20-tetrayl)tetrakis(([1,1':3',1''-terphenyl]-4,4''-dicarboxylic acid))

Figure 1.10 Examples of octatopic carboxylate based linkers.

1.7 Functionalization of Linkers

MOFs can be synthesized in an infinite number of structures allowing for the targeted synthesis with tailored pore sizes and functional group based applications. Following the principle of isoreticular chemistry, the linker used during MOF synthesis can be functionalized by adding a variety of substituents to the backbone of linker molecules.[103-105] However, these methods have limitations because the formation of a particular topology of a MOF is prone to delicate change of reaction conditions, geometry, chemical and electronic nature of linker. The limitation in pre-synthetic linker functionalization encourages developing a new toolbox for the modification of functional groups of MOFs after they have been synthesized. This newly developed principle is called "post-synthetic modification or PSM".[86, 88] The PSM method allows MOF to be functionalised at linker sides without altering the structural topology, crystallinity and porosity.

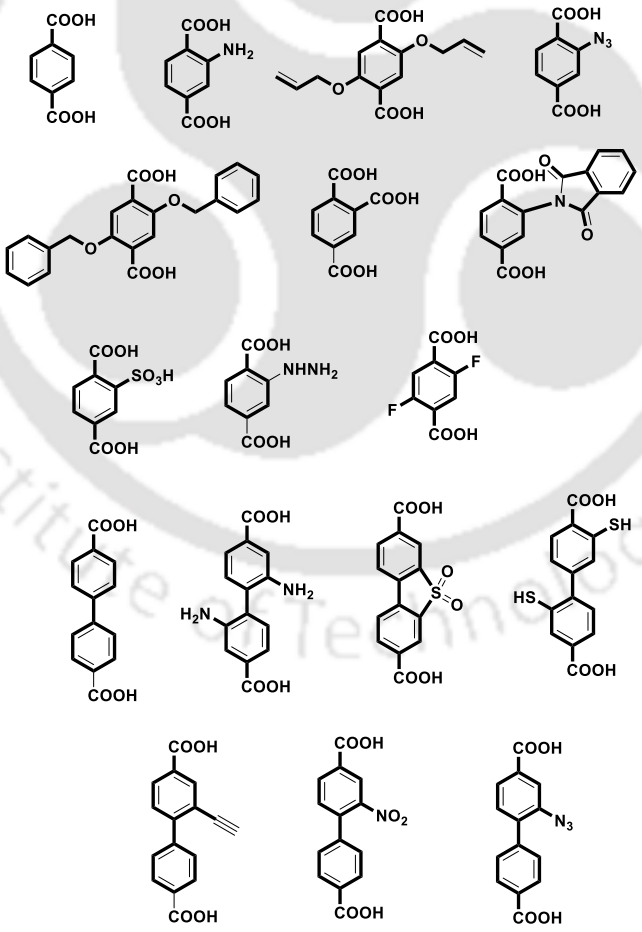

Figure 1.11 Examples of pre-functionalized linkers for preparing isoreticular structures.

1.7.1 Pre-Synthetic Linker Functionalisation

The trademark of MOFs is their undying porosity, which is regularly found in MOFs constructed from metal clusters. These clusters are often formed in situ, whereas the linkers are generally pre-formed. The geometry and connectivity of a linker dictate the structure of the resulting MOF. Variations of linker geometry, length, ratio and functional group can alter the size, shape and internal surface property of a MOF for targeted applications.[13] It is highly desirable to develop functional MOFs for selective guest molecule storage/separation, sensing and catalysis. The technique to make the linker functionalized before the MOF synthesis is known as 'pre-synthetic linker functionalization'.[106] Some MOFs suffer from the disadvantage of relatively low stability, which would restrict their practical applications. Hence, the side functional groups, which will be added to the linker, should be chosen in such a way that they do not hamper the formation of targeted MOF as well as its physicochemical stability. Usually, the amino, azide, urea, carbazole, hydrazinyl or bipyridine substituents (Figure 1.11) are preferred as functional groups because these functionalities are suitable for CO_2 adsorption, heterogeneous catalysis as well as toxic chemical sensing due to their specific chemical character.[107-111] Moreover, they provide further scope for the formation of a new coordinate or covalent bond of the as-synthesized MOF by performing the PSM technique.

The use of protected functionalities is highly desirable in the pre-synthetic linker functionalization strategy because they are highly compatible with the conditions for MOF synthesis. Advantages can be taken by adding some analytes, which can react with the protected functionalities in sensing purposes. Also, PSM can be performed to take advantage of the protected functionalities by the deprotection of the same. Few examples of pre-synthetically functionalized MOFs which have been utilized for gas adsorption are amine-functionalized TEPA-MIL-101,[112] triazole functionalized FJI-H14,[113] IRMOF-74-III-$(CH_2NH_2)_2$ MOFs,[114] thiadiazole functionalised ZJNU-40,[115] UiO-66-X (X = NO_2, NH_2, Cl, Br, I, Br_2),[116] etc. Examples of pre-synthetically functionalized MOFs successfully used for sensing of toxic chemicals and ions *via* fluorescence method are NH_2-UiO-66,[117] pyrazinyl functionalized HBU-18,[118] hydroxyl functionalized Tb based MOF,[119] and NH_2-MIL-125(Ti)[120], etc. Examples of MOFs which are pre-synthetically functionalized and employed for various catalysis are urea functionalized PCN-56-UM[108], UiO-66(Hf)-SO_3H,[121] MOF-5-NH_2,[122] UiO-67-NH_2,[123], etc. Although highly stable MOFs are being reported still, it is quite

challenging to synthesize physicochemically stable, functionalized new MOF materials for various applications like guest molecules storage, toxic chemical sensing *via* fluorescence method and heterogeneous catalysis.

1.7.2 Post-Synthetic Linker Functionalisation

As discussed in the pre-synthetic linker functionalization section, the linker can be functionalized before synthesis of a targeted MOF; hence, the MOF can be utilized for various applications like chemical sensing, catalysis, drug delivery, proton conductivity, etc. PSM, which was first proposed by Hoskins and Robson[124] in 1990 and officially introduced by Wang and Cohen,[125] is defined as the chemical modification of a framework after it has been synthesized (Figure 1.12). Mainly, the pre-synthetic approach has some limitations such as instability of newly formed functional group under the synthesis conditions of MOFs because of the bulkiness of side chain.[126] The major PSM strategies for functionalizing MOFs include covalent and coordinate covalent modification. Covalent modification describes the chemical modification of the organic linker component of the MOF. In 2007, Wang and Cohen performed the first detailed study of PSM by modifying the amino groups of IRMOF-3 with acetic anhydride to generate a MOF that contained methyl amide substituents, termed IRMOF-3–AM1 (AM = amide).[125] In contrast to covalent modification, coordinate covalent modification involves changes in the coordination environment of the SBUs inside the framework that does not change the overall SBU or the framework topology. There are two common tactics for coordinate covalent modification. In the first picture, coordinating linkers, such as alkylamine or pyridines, can be hosted into the framework to bind to the metal nodes of the SBUs where unsaturated metal sites are present. In the second common picture, the organic linker of the MOF may have metal-binding groups (e.g., –OH) that do not show any role in the framework structure, and hereafter can be metallated in a PSM manner.[125] For example, Lin and coworkers prepared a MOF from Cd^{2+} and a corresponding linker. They obtained a structure with free, uncoordinated hydroxyl groups that could be metallated with $Ti(O^iPr)$.[127] Therefore, PSM technique offerings an attractive way to functionalized linker after synthesis of MOF without hampering the topology of the framework (Figure 1.12).

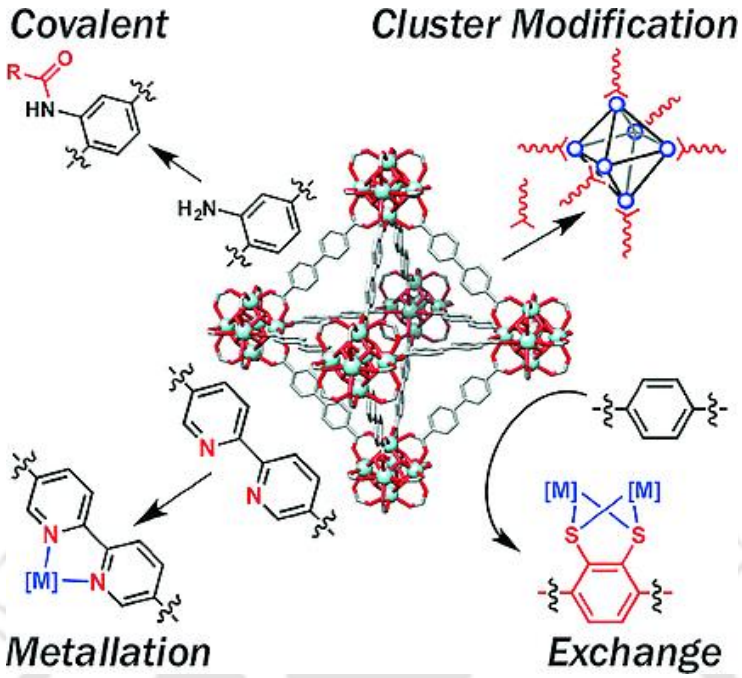

Figure 1.12 An overview of the various techniques for modification and the functionalities that can be incorporated into zirconium MOFs to facilitate different applications. Reproduced with permission from ref. 128. Copyright 2016 John Wiley & Sons.

1.8 Synthetic Protocols

For the synthesis of MOFs, several synthetic procedures are followed. Every synthetic method differs in its temperature, pressure and time. Hence, they produce MOFs with different particle size, pore size, distribution of particle sizes and morphologies. Therefore, every synthetic method has a unique role in creating MOFs with different properties. Among various ways, the most commonly applied methods are solvothermal/hydrothermal synthesis, microwave synthesis, electrochemical synthesis, mechano chemical synthesis, sonochemical synthesis,and slow evaporation method.

1.8.1 Solvothermal/Hydrothermal Synthesis

According to Rabenau, a solvothermal synthesis procedure is a reaction in which the reaction occurs in a tightly closed vessel at autogenous pressure above the boiling point of the solvent used.[129] Usually, Teflon-lined stainless autoclaves (Figure 1.13) are used and polar solvents having high boiling points are chosen (DMF, DMA, DEF, NMP, DMSO, etc.). In solvothermal synthesis, sometimes a sealed glass or Pyrex tube is used instead of autoclave.

When water is used as a solvent for the synthesis of MOFs, it is called hydrothermal synthesis. To attain a large crystals or highly crystalline powder samples of MOFs, a gap between the concentration of reactants and critical nucleation concentration should be in such a way that the critical nucleation concertation must exceed the concentration of reactants.[130] This can be achieved by varying the temperature or evaporating the solvent. Thus, solvothermal synthesis allows for precise control over the size, shape distribution and crystallinity of MOFs. Sometimes, a mixture of solvents is used for synthesis. The use of mixed solvent systems offers good solubility of the starting materials and this technique can tune the polarity of solution. This technique helps to achieve good quality crystals of MOFs.[131] Example of MOFs synthesized solvothermally are MOF-5, UiO-n, MIL-53 (Al, Cr, Fe), CAU-10, etc.[24, 26, 90, 102, 132]

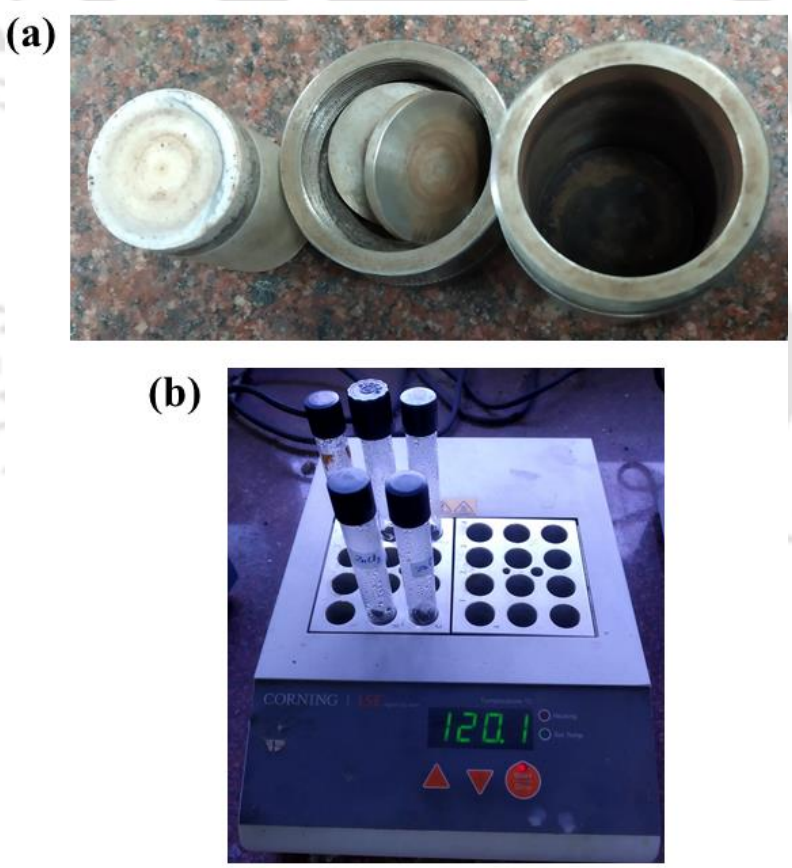

Figure 1.13 Digital images of the different parts of a (a) Teflon-lined steel autoclave and (b) sealed tube used in solvo/hydrothermal reaction for the synthesis of MOF materials.

1.8.2 Microwave Synthesis

Apart from solvothermal synthesis procedure, microwave synthesis is a useful synthetic procedure in which very high energy heat is produced during the synthesis of MOFs.[133] In this method, a microwave reaction tube is used and polar solvents like DMF, DEF, DMA, etc. are used (Figure 1.14). The technique can produce excellent crystalline products within maximum 1 h whereas, the other synthetic strategies require over 24 h.[130] In microwave synthesis strategy, excellent quality crystalline products or crystals have been achieved due to the higher nucleation rate. Mainly, this strategy is used to produce nano sized MOF particles with high purity, homogeneous morphology and uniform distributions of products. In a microwave, electromagnetic radiation is converted to thermal energy. When electromagnetic energy is applied, the dipoles of the precursors in the reaction vessel rotate themselves and align with the electromagnetic energy. Consequently, the collisions between reactant molecules occur and kinetic energy or heat of the reactant molecules is increased.[134] The advantages of this method are energy and cost-effectiveness. Examples of MOFs synthesized by this method are IRMOF-1, IRMOF-2, IRMOF-3, Cr-MIL-101, etc.[135, 136]

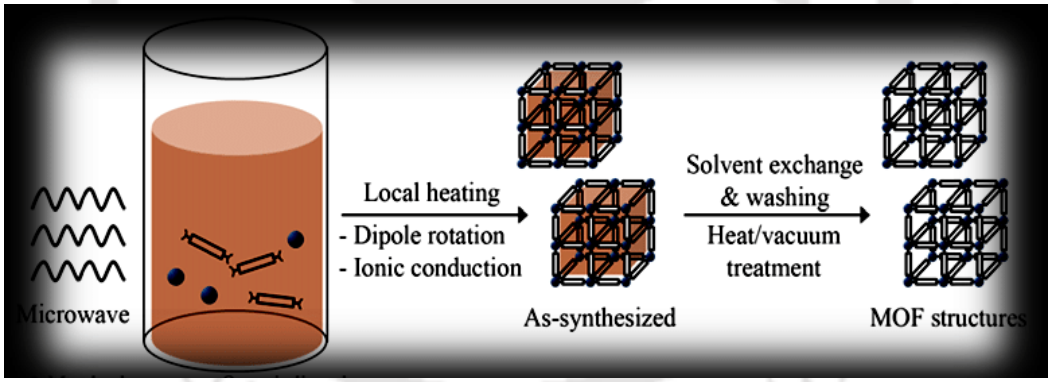

Figure 1.14 Microwave-assisted solvothermal synthesis of MOFs. Reproduced with permission from ref. 130. Copyright 2013 Springer.

1.8.3 Electrochemical Synthesis

An electrochemical set up for MOF synthesis contains battery cell, cathode and anode plates into an electrochemical bath containing metal ions and organic linkers.[130] Here, the metal ions are supplied by the anodic dissolution to the electrochemical bath (reaction medium) which reacts with organic linkers to produce MOFs. Metal deposition on the cathode is avoided by

using protic solvents. Microcrystalline powders can be prepared by this synthesis method. Examples of few MOFs, which were synthesized by these methods, are HKUST-1, Al-MIL-100, Al-MIL-53 and Al-MIL-53-NH_2.[137]

1.8.4 Mechanochemical Synthesis

This is a solvent-free synthesis technique.[138] Here, mechanical forces are applied during the grinding of a mixture of the metal salt and organic linkers in a mechanical ball mill. As a result of mechanical grinding, the intramolecular bonds between the starting materials are broken and new bonds are formed to construct MOFs. Sometimes, liquid assisted grinding is also performed to accelerate the rate of mechanochemical reactions. The main advantages of this method are non-requirement of solvents, short reaction time and room temperature synthesis. The examples of MOFs synthesized by this method are MOF-5 and HKUST-1.[138, 139]

1.8.5 Sonochemical Synthesis

The word ‘sono' means ultrasound and the chemical reaction where the ultrasound of considerable energy is employed to perform a chemical reaction is called sonochemical reaction. This process of MOF synthesis is an efficient and eco-friendly method. In this process, the starting materials are taken in a reaction tube and allowed to sonicate. After the reaction, the crystalline products are filtered and dried. In this technique, the crystallization time decreases because the ultrasound enhances the chemical or physical changes through a process called ‘cavitation’. During the process, bubbles are created and destroyed due to the ultrasound energy. The destruction of bubbles releases power having a temperature of 400 K and pressure more than 1000 bar. This energy is enough to synthesize MOFs.[140] Few examples of MOFs synthesized by this method are MOF-5, PCN-6 and IRMOF-10.[130, 141]

1.8.6 Slow Evaporation Method

Another method for MOF synthesis is the slow evaporation method. In this method, the solvents evaporate or diffuse slowly at room temperature.[134] The metal salts and linkers used in this method are highly soluble in the reacting solvents. As the solvents start to diffuse or evaporate, the nucleation rate becomes faster. The main drawback of this method is the requirement of a longer time compared to the other methods of MOF synthesis. Examples of

MOFs which were synthesized by this technique are $[Ca_2Co(pzdc)_2(NO_3)_2(H_2O)_8]_n \cdot 2nH_2O$, $[Sr_2Co(pzdc)_2(H_2O)_{10}]_n \cdot 2nCl$, $[Ba_2Co(pzdc)_2(H_2O)_{10}]_n \cdot 2nCl$, etc.[142]

1.9 Effect of Reaction Parameters

The size, shape and coordination geometry of MOFs can be controlled by varying the compositional parameters such as solvents, molar ratio and pH as well as the process parameters like temperature, pressure and period of a reaction. Mainly, these parameters affect the nucleation rate, rate of deprotonation and mode of coordination of linkers with metals. Hence, the chemistry of MOF varies upon change of reaction parameters.

1.9.1 Role of Solvent

The choice of proper solvent in a chemical reaction during the synthesis of MOFs has a high impact on the determination of the structure and coordination geometry of MOFs. Although the very systematic choice of exact solvent in a particular reaction of MOF synthesis is still not very clear, many studies showed that every solvent can have a different role to form the different coordination environments of the crystal structures of MOFs. The solvent molecules can behave as coordination molecules with metal or remain as a guest molecule in the final lattice structure. The solvent can behave as a structure directing agent or can act as a medium for crystal growth, which means that the extent of deprotonation of carboxylates depends on the choice of solvents. For example, DMF, DMA and DEF can produce different crystal systems keeping other conditions of reactions unchanged. The amide solvent is converted to its corresponding amine at higher reaction temperature and thus can deprotonate the carboxylates in different extents.[134]

Solvents with different sizes may lead to the formation of crystals having different structures. The pore size of MOFs can be varied with the size of solvents. Solvent assisted variation in the pore volume of MOFs were also found. As the size of the solvents is increased in the order DMA < NMP < DMI [*N*,*N*-dimethylacetamide (DMA), *N*-methyl pyrrolidinone (NMP) and 1,3-dimethyl-2-imidazolidinone (DMI)], the size of the pore volumes are also increased to the same order with increasing the size of the solvent.[143] Hence, template effect of different solvents may lead to the formation of new structures with different pore size, shape or even different bond connectivity because these solvent molecules behave like structure directing agents during the self-assembly process.[134]

1.9.2 Effect of Temperature

The solvothermal synthesis of MOFs has some serious advantages over other conventional and non-conventional synthesis procedures. The probability of the formation of right quality crystals is higher in the solvothermal synthesis method because the reactions are carried out in a closed system at high temperature and pressure. Sometimes, the solvothermal procedures are necessary for MOF synthesis when the reactant molecules are not readily soluble in the solvent systems.

Succinic acid is widely used for MOF synthesis to investigate the effect of temperature during solvothermal synthesis because of its flexibility and different modes of coordination with varying reaction temperature. A comparative study was carried out to check the impact of temperature where succinic acid has been used as a linker and holmium (Ho(III)) has been used as the metal. G. E. Narda and his group prepared two Ho(III) succinate coordination polymers by hydrothermal and non-solvothermal methods.[134, 144] These two compounds have different dimensionality, which affects their thermal stability as well as magnetic property. It was found that the hydrothermally synthesized compound has higher thermal stability compared to the compound synthesized at room temperature. Also, the higher temperature is more useful to synthesize a highly stable open framework with empty channels instead of polymeric layers formed under mild conditions.[134] Although, many reports showed higher reaction temperature favors the generation of higher dimensional MOFs, it is not the case where every synthesis would maintain the concept.

1.9.3 Effect of Modulator

Modulators are used during the synthesis of MOFs as they can control the crystal growth of MOFs during the synthesis by fine-tuning the reaction kinetics. Majority of research involved in the synthesis of MOFs like MILs and UiOs uses various modulators. Commonly used modulators are acetic acid (AA), benzoic acid (BA), hydrochloric acid, formic acid (FA), trifluoroacetic acid (TFA), water and proline. The modulators have several effects on various features of MOFs like crystallinity, yield, morphology, pore size, defects, porosity, stability and gas separation performance. It is believed that modulators play two critical roles during the synthesis of UiO (Zr/Hf) MOFs: (i) to facilitate the growth of crystals *via* the formation

of $Zr_6O_4(OH)_4$ SBUs and (ii) to slow down the crystal growth to avoid the fast precipitation of amorphous products.[145, 146]

To establish the relation of the role of modulator with synthetic conditions and product performances, many types of research were carried out where MOFs were synthesized by varying the modulator parameter (acidity, amount), synthetic conditions and the performances of products were checked. Zhao et al. synthesized Zr and Hf MOFs in a modulated hydrothermal synthesis (MHT) using fumarate as a linker and three carboxylic acid based modulators varying in their pKa values.[147] They have compared the crystallinity, yield, morphology, defect concentration, surface area, pore size and gas uptake of the resultant MOFs. It was found that the modulation mechanism is involved in the synthesis and they modeled the optimal molar ratio of the modulator with respect to linker versus pKa of modulators and linkers. It is believed that the carboxylic acid groups of modulators bind with metals, which modulates crystal growth during the crystallization process. To get more insights about the role of modulators in modulated solvothermal process, they used three different modulators having three different pKa values: TFA (0.3) > FA (3.74) > AA (4.76). From XRPD data, they concluded that for a particular modulator, the crystallinity of a MOF would be highest at an optimal modulator ratio with respect to the linker. For different modulators, the maximum crystallinity was found to decrease with optimal molar ratio (indicating the relative amount of modulator used) from AA (70), FA (53) to TFA (13). It is consistent with the increasing acidity of the modulators. Taking both the acidity (TFA > FA > AA) and amount (TFA < FA < AA) of the modulators into consideration, it is suggested that increasing modulator acidity and decreasing its amount have an equivalent effect in affecting the crystallinity of resultant MOFs.

Besides crystallinity, yield is another important factor that is also affected by the amount and acidity of the modulator. Based on literature survey, it can be mentioned that for a more acidic modulator, the yield will be least at its optimal ratio with respect to the linker.[147] Thermal stability is another factor that depends upon the acidity of the modulator. With enhancing the acidity of the modulator used, the thermal stability of the MOF increases.[147] The enhancement of the acidic nature of the modulator leads to the formation of MOFs with higher BET surface area and higher porosity.[147]

1.9.4 Effect of pH

Slight changes in acidity or basicity in reaction medium has a remarkable influence on the crystallization process and growth of organic-inorganic hybrid materials. With the change in pH values, the extent of deprotonation and sometimes generation of –OH groups favor the linking between the organic linker and metal ion. Some interesting works regarding the influence of pH on MOF synthesis have been studied by many research groups. Zhang et al. showed that 1,3-adamantane acetic acid (H_2ADA) linker produces three different neutral polymeric complexes, $[Co(HADA)_2(BPP)]$, $[Co(ADA)(BPP)(CH_3OH)]$ and $[Co_2(ADA)_2(BPP)]$ with different compositions and dimensionalities upon reaction with one cobalt salt at pH values of 5, 6 and 7 respectively.[148] Hence, depending upon the pH of the reaction medium, the same carboxylic acid linker binds with the same metal ion through different coordination modes. As a result, different MOFs are formed due to change in pH.

1.10 Applications of MOFs

Metal-organic frameworks (MOFs) are an emerging class of porous materials created by the assembly of inorganic connectors and organic linkers. They have potential applications in fields such as gas storage as well as separation, sensing, catalysis and drug delivery due to their properties such as flexibility, porosity, high surface area and functionality. This study is based on fluorescence sensing and heterogeneous catalytic activity of MOFs.

1.10.1 Fluorescence Sensing

Luminescence is the process in which light is produced by the absorption of energy.[149] Luminescence covers two basic terms called fluorescence and phosphorescence, depending upon multiplicity of spin state during the radiative relaxation process.[149] During fluorescence, the light emits between energy states having same spin multiplicity and the process generally persists for maximum ~10 ns.[150] Fluorescence can arise from direct organic linkers upon excitation (particularly from the highly conjugated linkers), metal-centered emission (Figure 1.15) (widely observed in lanthanide MOFs through the so-called antenna effect) and charge-transfer such as ligand-to-metal charge transfer (LMCT) (Figure 1.15) and metal-to-ligand charge transfer (MLCT) (Figure 1.15).[150] Furthermore, fluorescence in MOFs is sometimes observed from the guest molecules residing inside the MOFs (Figure 1.15).[150] When

fluorescence is weakened or quenched upon the absorption of the analyte, it is known as the 'turn-off'[151] mechanism. When the enhancement of fluorescence occurs, it is described as a 'turn-on'[152] mechanism.

In the last few decades, environmental pollution has become a severe issue for the ecosystem as well as human health with increasing population and industrial development. Many types of pollutants, e.g., water and air pollution of various heavy metals, toxic anions, organic compounds, noxious gases, nitroaromatic explosives (NAEs), nerve agents and other poisonous compounds, are associated with health risks.[86, 153-155] Even some biologically essential metal ions, anions or other compounds affect human health and environment badly when they are present in excess or deficient. Among these Fe(III), H_2S, PO_4^{3-} and 4-NB are some biologically relevant species which are harmful to human health and ecosystem when they are present in excess.[156-159] Hence, detection of these undesired chemicals from wastewater or biological systems to protect human health and environment are essential and meaningful research topics.

In the past decades, for the detection of these analytes, numerous methods have been developed, including electrochemistry, ion chromatography, atomic absorption spectrometry, spectrophotometry, etc.[160] However, the low sensitivity, poor recyclability, narrow detection range, complicated operation and time-consuming procedures make these methods not always suitable. Therefore, fluorometric methods for sensing have gained considerable attention in the scientific community over these techniques due to their fast response time, easy handling techniques and detection of even trace amounts of analytes in both solid and liquid phases. In the fluorescence method, no reference is required. Additionally, with fluorescence, it is possible to perform remote monitoring. An advantage of fluorescence spectroscopy is that different assays can be designed based on various aspects of the fluorescence output (lifetime, intensity, anisotropy and energy transfer). Therefore, fluorescence techniques are envisioned as the most critical future detection method for chemical sensing.[161, 162]

MOFs are chosen as probes for the detection of undesired species in wastewater and biological systems because of their numerous advantages such as high crystalline nature, diverse and easily modifiable structures and topology, permanent porosity, systematically tunable band gaps and electronic structures. Most notably, high surface area and justifiable pores within MOFs provide natural habitats for guest molecules.[163] The capture of guest

molecules within the pores increases the chances of guest-host interactions (Figure 1.15). Besides, functional groups within the framework in the linkers and open metal sites further promote preferred analyte binding for selective detection (Figure 1.15).[164, 165] Finally, compared to amorphous materials, the highly ordered crystalline nature of MOFs allows them for precise and easy communication for the detection of analytes. All these unique characteristics may be responsible for sensitive detection. Overall, MOFs have great potentials as a novel class of sensitive materials. Table 1.1 shows few examples of MOF based chemical sensing in current research.

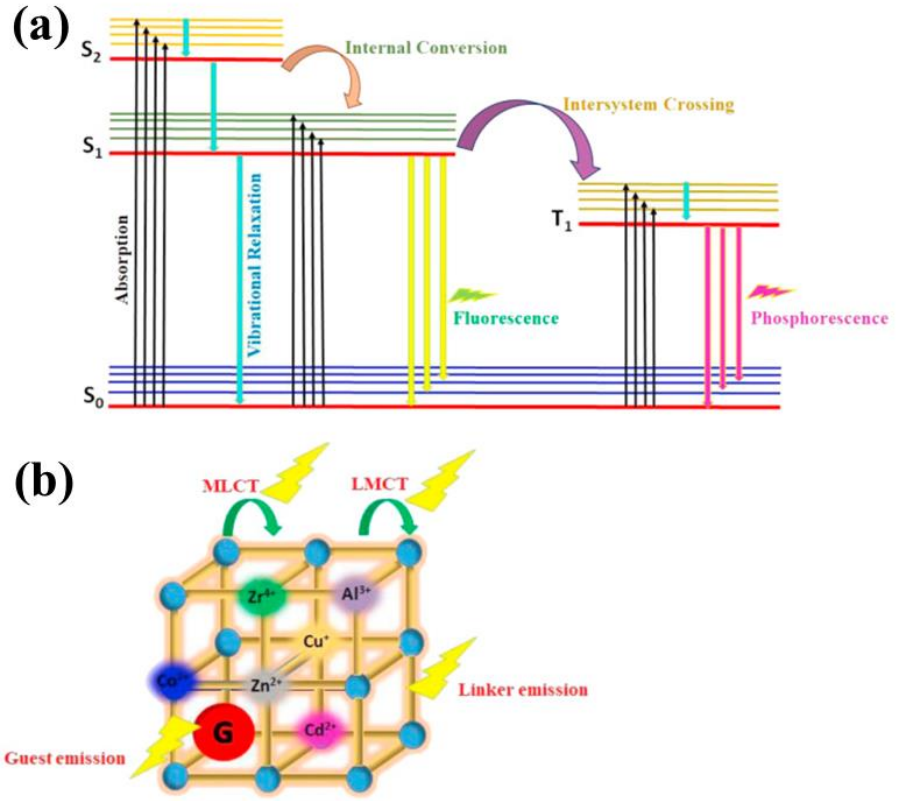

Figure 1.15 (a) Schematic illustration of the electronic states involved in the luminescence of a coordination complex (brief overview of Jablonski Diagram) and (b) Schematic representation of various modes of luminescence in MOFs where inorganic metal clusters (multi- color spheres) are linked by functional organic linkers (orange rods) with an inclusion of guest molecules (red sphere). Reproduced with permission from ref. 166. Copyright 2019 Elsevier.

Table 1.1 Summary of various reported MOFs towards chemical sensing using fluorescence technique.

MOF	Analyte	Sensing Mechanism	Ref.
$[EuL[(H_2O)_{1.35}(DMF)_{0.65}]\cdot 1.9DMF]_n$	PO_4^{3-}	interactions between PO_4^{3-} and MOF	167
UiO-66-NH_2	PO_4^{3-}	binding of PO_4^3 with Zr	168
Tb@Zn-MOF	PO_4^{3-}	coordination between Tb and PO_4^{3-}	169
NH_2-MIL-88(Fe)	As(v)	coordination of arsenate to metal centers	170
Tb-ADP-Bipy	CN^-	extended π-conjugation caused by cyanide	171
NTU-9-NS	Fe^{3+}	UV-Vis competitive adsorption, electron transfer	172
BUT-14 and BUT-15	Fe^{3+}	PET	173
PCN-224	Hg^{2+}	complex formation	174
$[Cd_5Cl_6(L)(HL)_2]\cdot 7H_2O$	picric acid	energy and electron transfer, electrostatic interactions	153
TMU-31, TMU-32	nitroaromatic	hydrogen bonds and π−π stacking interactions	175
CAU-10-N_3	H_2S	reduction of azide	176
Eu^{3+}/Cu^{2+}@UiO-66-$(COOH)_2$	H_2S	Cu_2S formation	177
[Zn(L)(2,2′-bpy)]	$^1O_2$	[4 + 2] cycloaddition	178
$[Hf_6O_4(OH)_4(C_8H_5BO_6)_6]\cdot 25H_2O\cdot 4DMF$	peroxynitrite	Baeyer−Villiger oxidation	179
UiO-66-DNSCl	biothiol	reaction based	180
Abtz–CdI_2–MOF	dopamine	redox reaction	181
UiO-67-bpydc	H^+ or pH sensing	H^+ binds with N atom in the bipyridine	182
$[(ZnCl_2)_2$ Py-TPE]	VOC	host-guest binding	183

$[Zr_6O_4(OH)_4(C_{16}H_7NO_6)_6]$	hydrazine	reaction based	184
Tb@UiO-66-$(COOH)_2NH_2$	tetrachloro-benzoquinoe	inner filter effect	185
DNA@MOF	Hg^{2+} and I^-	host-guest binding	186
FJU56a	NH_3	coordination between NH_3 and metal	187
Al-MIL-53-N_2H_3	HCHO	PET off	154
Zr-MOF:Eu^{3+}	bilirubin	FRET	188

1.10.1.1 Fe(III) Sensing

Iron is the most abundant transition metals in cellular systems and it takes part in lots of crucial biological processes such as oxygen metabolism, electron transfer and transcriptional regulation.[189, 190] Yet, an excess amount of Fe^{3+} ions causes severe diseases like cancer, Alzheimer's disease and Parkinson's disease.[191, 192] Hence, the detection of Fe^{3+} ions has attracted intense attention. For this purpose, chemosensors with high sensitivity and selectivity are excitedly anticipated. There are various types of probes for the detection of Fe^{3+} ions based on different mechanisms like replacement of metal ion,[193] PET (photoinduced electron transfer),[194] energy transfer,[195] interaction between Fe^{3+} and heteroatom of the linker,[195] etc. MOFs as chemosensors for the sensing of Fe^{3+} is generally considered as one of the best promising materials because of their unique features like highly robust nature, tunable pore and functionality, recyclability and high sensitivity. MOFs based chemosensors follow several kinds of mechanisms for the sensing of Fe^{3+} ions.[196, 197] The structure/formula, type of fluorescence responses, proposed mechanism, limit of detection, sensing medium, etc. are displayed to get a clear and visual picture of the MOF based Fe^{3+} sensing. In the present study, using a fluorometric sensing strategy, Fe^{3+} detection has been carried out in aqueous medium in the presence of various completive analytes with a good limit of detection value.

1.10.1.2 H_2S Sensing

Hydrogen sulfide (H_2S) is a colorless, highly flammable gas with a characteristic smell of rotten eggs.[198] The primary sources of its production are natural gas drilling and refining, wastewater treatment, coke ovens, tanneries, etc. H_2S plays crucial roles in physiological and

pathophysiological responses. In recent years, H_2S has been discovered as an essential biological molecule in organisms.[199] Abnormal levels of H_2S cause various diseases, including cardiac ischemia disease, hypertension, atherosclerosis, diabetes, tumor, etc.[199] Therefore, the selective and sensitive detection of H_2S in environmental samples as well as a biological system is highly required.[199] In this perspective, the development of new methods for sensing H_2S has attracted tremendous attention. The methods to detect H_2S include colorimetry, electrochemical precipitation, metal-induced sulfide precipitation, gas chromatography, high-performance liquid chromatography-mass spectrometry and sulfide precipitation.[199] Recently, fluorescent probes have been considered a practical tool for H_2S detection. The H_2S fluorescent probes are designed by some approaches, such as sulfide-induced precipitation of quantum dots,[200] reduction of azide and nitro group to amines,[201] substitution reaction,[202] nucleophilic reactions,[203] high adsorptions of S^{2-} to Cu^{2+},[204] and the reaction with the unsaturated double bond.[205] This study focuses on turn-on detection of H_2S in aqueous medium as well as *in vitro* system and the sensor showed excellent limit of detection value.

1.10.1.3 Phosphate Sensing

Phosphates play central roles in the building of the most fundamental molecules in living organisms such as DNA and RNA. Phosphates are also significant constituents of membrane lipids (in the form of phospholipids). They are involved in many biological processes including skeletal development and bone integrity, energy metabolism, cell sensing and regulation of protein synthesis.[158, 206] Along with the fast growth of modern agriculture and industry, phosphate has been found to be used in a large quantity, which is inevitably released into the aqueous environment. Accordingly, excess of phosphate ions (PO_4^{3-}) in water lead to eutrophication and result in the reduction or elimination of dissolved oxygen, resulting in a negative effect on the water ecosystem.[158, 207] Thus, the detection of phosphate in water as well as in cellular medium has a significant impact. Many probes have been reported for fluorescence-based phosphate sensing and they have followed the different mechanisms such as reaction-based,[208] coordination of PO_4^{3-} with metal, energy transfer,[209] proton snatching,[209] etc. However, the fluorescence sensors based on MOFs are still rare. Hence, herein, MOF based fluorescent sensors with high sensitivity have been developed.

1.10.1.4 4-Nitrobenzaldehyde Sensing

Aldehydes are essential for the production of synthetic resins, synthetic dyes, flavorings, perfumes and other chemicals.[210] They are widely used as antiseptics and preservatives in many situations.[210] As a result, aldehydes are regularly released to the environment. Hence, their presence needs to be examined.[211] 4-Nitro benzaldehyde (4-NB) is a side product upon decomposition of the drug chloramphenicol, which is used for eye drop preparation and treatment of typhoid disease.[212] The toxicities of this side product towards bone-marrow cells are also very dangerous. Therefore, *in vitro* and in *vivo* detection of 4-NB has a significant impact on protecting human health from several diseases like cancer. The existing methods to monitor the presence of aldehydes in the environment are colorimetric measurements, electrochemical, gas chromatography and fluorescence techniques.[210] One common approach to detect the aldehyde is to isolate the product after the reaction of an aldehyde with aromatic hydrazine. The covalent bond formation is monitored by changes in optical properties such as fluorescence spectra.[211] MOFs can be a much more useful sensor for the detection of aldehyde compounds, especially 4-NB *via* the shift of its fluorescence. Hence, in this study, we have focused on the fluorometric detection of the toxic hazards 4-NB with a considerable limit of detection value.

1.10.2 Heterogeneous Catalysis

Currently, people are becoming increasingly concerned with the growing energy shortage and environmental pollution. A sustainable development model that integrates considerations of economic viability and ecological integrity must be developed. Improving catalytic efficiencies, reducing waste, and using environmentally friendly reagents are the critical factors of green chemistry.[213] The problem associated with energy consumption could be minimized by performing chemical reactions in the presence of catalysts. The Swedish chemist Berzelius first coined the term "catalysis" in 1835. Still, a suitable definition was presented after many years by Ostwald who wrote in 1894: "catalysis is the acceleration of a slow chemical process by the presence of a foreign material".[214] Homogeneous catalysis is a powerful synthetic tool to make the reaction faster and get a better yield of products. However, the disadvantages of homogeneous catalysts are related to the reusability of catalysts, difficulty of separation from products, etc. Heterogeneous catalysis is one of the vital solutions

of our developed society, as many chemical processes can be brought about cost-effectively using heterogeneous catalysts.[215] Heterogeneous catalysis takes place at the surface of a solid. Therefore, materials with a large surface area, i.e., fine powders of porous solids, make better results than large single crystals.[214] From a sustainable chemistry viewpoint, heterogeneous catalysis reactions are better efficient and environmentally friendly chemical synthesis methods as compared to homogeneous catalysis.[213]

The possible compositions and structures of MOFs are nearly infinite, as demonstrated by a large number of metal nodes and functional linkers that can be used in their fabrication.[213] In particular, compared with other porous materials, homochiral MOFs for asymmetric catalysis can be synthesized easily using enantiotropic linkers. Other main features of MOFs include their large surface areas and pore volumes, which enable active guest species to be introduced into the pores/cages/channels and allow substrates to access the internal active sites. These multifunctional MOFs can be categorized by the type of active center as follows: (i) open metal centers and functional organic linkers in the MOF structure, (ii) active guest sites in the pores and active sites in the MOF structure and (iii) bimetallic nanoparticles (NPs) on MOF supports. Thus, the combination of different types of MOF active sites such as metal nodes, functional organic linkers and guest species in the pores, makes MOFs promising multifunctional materials for heterogeneous catalysis for many organic transformation reactions.[216] In this study, the applications of MOFs with multiple active sites in organic catalysis reactions (Friedel-Crafts alkylation and ring-opening of epoxides by amine) are discussed. Table 1.2 shows examples of MOF based heterogeneous catalysts which have been utilized for different organic reactions.

Table 1.2 Summary of various reported MOFs utilized as heterogeneous catalysts for different organic reactions.

MOF	Catalysis reaction	Active Center (Metal/Linker)	Ref.
MIL-101(Cr)-NH_2	cycloaddition of CO_2 and epoxides	Cr metal and linker	217
Pd@MIL-101(Cr)-NH_2	Suzuki–Miyaura cross-coupling	Pd	218
Ce_{53}/Zr-CAU-24	reduction of NO	Ce	219
PCN-124	Knoevenagel condensation	Cu^{2+}, pyridine, and amide	220
$Cu_3(btc)_2$	Beckmann rearrangement	Cu^{2+}	221
$[Cu_2L_2Cl_2]H_2O$	Biginelli reaction	linker	222
MIL-53(Al-Li)	Friedel–Crafts alkylation	Li and Al	89
TMU-18 and TMU-19	ring-opening of epoxides	linker	223
(Ti)MIL-125/NH_2-MIL-125(Ti)	H_2O_2 generation and catalytic oxidative desulfurization	Ti	224
NH_2-UiO-66(Zr)	photocatalytic CO_2 reduction	Zr, linker	225
$Yb_6(BDC)_7(OH)_4(H_2O)_4$	conversion of glucose into 5-hydroxymethylfurfural	bridging hydroxyls and Yb	226
MIL-100(Fe, Ni)	Prins condensation of β-pinene and paraformaldehyde	Ni	227
Ti_3–BPDC–CoH	cascade reduction of N-heteroarenes	Ti, Co	228
(*R*)-ZnMOF-4	the ring-opening reaction of *meso*-epoxides	Zn and linker	229
MOF-808	hydrolysis of dipeptides	Zr_6O_8 cluster	230
VUiO-66	gas-phase oxidative dehydrogenation of cyclohexene	vanadium metal	231

1.10.2.1 Friedel-Crafts Alkylation

The Friedel-Crafts alkylation of aromatic compounds is a significant C-C bond formation reaction.[232, 233] Many Lewis acids, including BF_3, $BeCl_2$, $TiCl_4$, $SbCl_5$, or $SnCl_4$, have been used as catalysts for the Friedel-Crafts alkylation.[234] Furthermore, strong Brønsted acids such as sulfuric acid, hydrofluoric acid or super acids like $HF{\bullet}SbF_5$ and $HSO_3F{\bullet}SbF_5$ have also been introduced to speed up this transformation.[234] Since stoichiometric or super stoichiometric amounts of a Lewis acid or Brønsted acid and toxic alkyl halides have to be utilized to achieve massive amounts of salt side products, the need for the development of Friedel-Crafts alkylation using only catalytic amounts of a metal or acid catalyst would be highly desirable.[234] Beyond this, the use of activated double bonds and styrenes/nitro styrenes would be even more efficient as no side products are to be expected. Nitro-substituted substrates can be activated towards nucleophilic addition during Friedel-Crafts alkylation using hydrogen bond donating catalyst (Figure 1.16).[235, 236] The development of efficient Friedel–Crafts alkylations of arenes and heteroarenes using only catalytic amounts of a hydrogen bond donating catalyst has gained much attention over the last decade.[232, 236-238] The new catalytic approaches are favored over classical Friedel–Crafts conditions as benzyl-, propargyl- and allyl alcohols or styrenes/nitro styrenes, can be used instead of toxic benzyl halides.[239-241] Additionally, only low catalyst loadings are needed to provide a wide range of products. This study will describe the Friedel-Crafts alkylation of indole using β-nitrostyrene and environmentally gentle substrates, which can be applied as an approach towards greener processes.

TH-2604_156122006

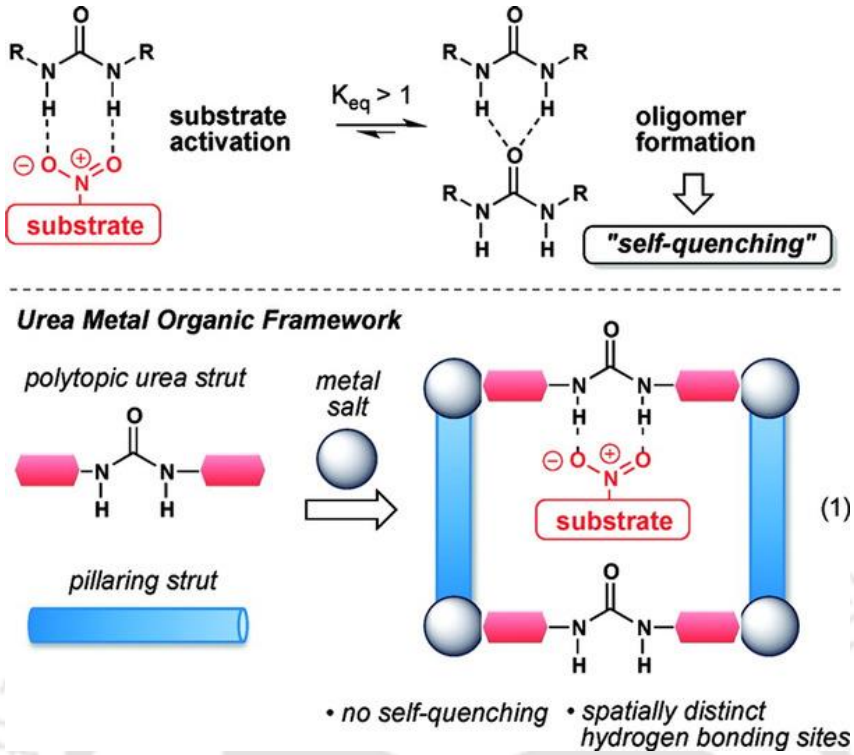

Figure 1.16 The synthetic substrate activation and self-quenching of urea functionalities in homogeneous catalysis (top) and the representation of MOF strategy (bottom). Reproduced with permission from ref. 235. Copyright 2012 American Chemical Society.

1.10.2.2 Ring Opening of Epoxides

Epoxides are one of the most useful synthetic intermediates in pharmaceuticals, fine chemicals and biologically active compounds preparation.[242] Ring-opening of epoxides mainly occurr due to the electronic character of the heterocyclic moiety as well as their ring strain. The inherent ring strain of ~27 kcal/mol associated with the three-membered heterocycle provides sufficient driving force for the ring-opening event.[243] Ring-opening reactions can proceed by either S_N2 or S_N1 mechanisms, depending on the structural features of the epoxides and reaction conditions. When an asymmetric epoxide is reacted under primary conditions, ring-opening occurs by S_N2 mechanism and in acidic conditions (Scheme 1.1), ring-opening proceeds via S_N1 mechanism.[242, 244] β-Amino alcohol is a biologically active natural or synthetic product via ring opening of an epoxide.[245] Various Lewis acids such as $Y(NO_3)_3{\cdot}6H_2O$, $ZrCl_4$, $Sc(OTf)_3$, SmI_2, $RuCl_3$ and $NbCl_5$ have been studied for this class of reactions.[245] Milder and improved reaction conditions are also required to achieve the

desired product. Due to the toxicity of metals, a better catalyst is still anticipated for the nucleophilic ring-opening of epoxides by various amines to afford the corresponding β-amino alcohols. In this thesis, we will describe the application of Zr(IV)-based MOF as a synergistic catalyst for this purpose using different substrates.

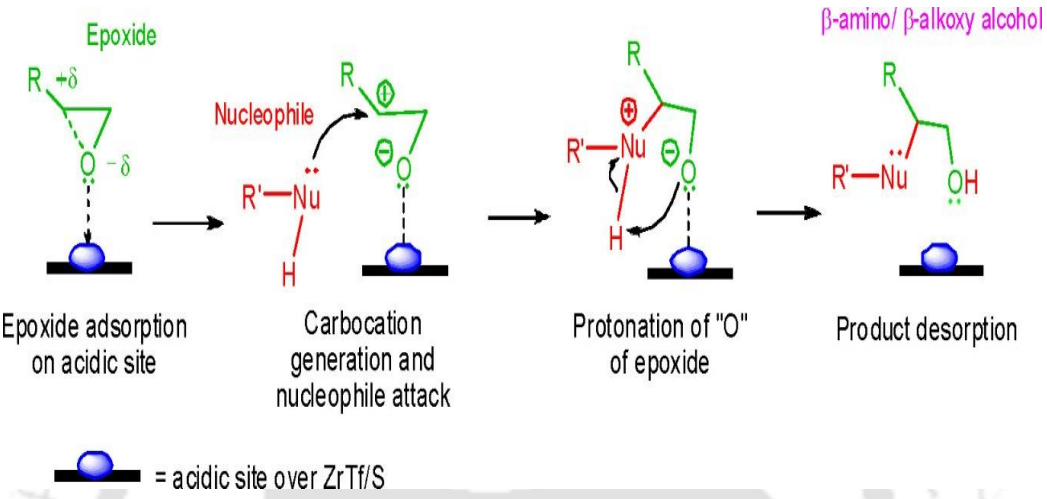

Scheme 1.1 Plausible reaction pathway of epoxide ring-opening reaction in the presence of an acidic catalyst (over ZrTf/S). Reproduced with permission from ref. 244. Copyright 2017 Elsevier.

1.11 Objectives and Motivations of the Study

MOFs are an emerging class of porous materials created by the association of inorganic clusters and organic linkers. Due to their high surface area, tunable porosity and functionality, they are highly useful in various fields such as gas storage as well as separation, chemical sensing, heterogeneous catalysis, drug delivery, etc. However, MOFs should be highly stable under aqueous, acid and basic media as well as high temperature and pressure for their practical and real-life applications. Yet, most of the reported MOFs have low survival in the above mentioned operational environments. This disadvantage considerably obstructs MOFs' practical applications. Therefore, the preparation and implementation of stable MOFs have attracted immense attention.

At the initial stage of MOF exploration, the main objective was to synthesize frameworks holding the highest BET surface area and the largest pore volume. In recent times, substantial

efforts have been dedicated to the design of highly stable structures, allowing various applications like fluorescence sensing and heterogeneous catalysis under harsh conditions. The general purposes of this research are to investigate the synthesis, complete characterization of functionalized, highly stable MOFs and their successful utilization towards chemical sensing via the fluorescence methods and usage of these MOFs as heterogeneous solid catalysts for organic transformation reactions. This study focuses on the design and synthesis of functionalized MOFs based on the carboxylic acid linkers. The carboxylate based linkers have been used for MOF synthesis because the carboxylates can chelate with metal clusters and lock them into rigid structures. Thus, they provide rigid MOFs with definite geometry. High valent metals like Zr^{4+}, Al^{3+}, etc. are used to achieve highly stable (hydrolytic, thermal and chemical) MOFs. This study covers developments of highly stable MOFs as well as their fluorescence sensing and catalytic applications via linker design. The linkers are functionalized with proper choice of functional groups to utilize the MOFs for desired fluorometric and catalytic applications. Hence, development of some highly stable MOFs will have great impacts in modern science, since they can make the chemical reactions faster and enable the detection of toxic chemicals existing in the environment.

1.12 References

1. E. C. Constable, *Chemistry*, 2019, **1**, 126–163.
2. F. Grandjean, L. Samain and G. J. Long, *Dalton Trans.*, 2016, **45**, 18018-18044.
3. D. P. Graddon, *An introduction to co-ordination chemistry : International series of monographs in inorganic chemistry*, Pergamon Press Ltd., London, 1961.
4. A. Werner, *Z. Anorg. Chem.*, 1893, **3**, 267–330.
5. G. B. Kauffman, *ACS Symp. Ser.*, 1994, **565**, 2-33.
6. K. Bowman-James, *Acc. Chem. Res.*, 2005, **38**, 671-678.
7. P. H. Dinolfo and J. T. Hupp, *Chem. Mater.*, 2001, **13**, 3113-3125.
8. F. Huang and E. V. Anslyn, *Chem. Rev.*, 2015, **115**, 6999−7000.
9. R. Adam, M. Mon, R. Greco, L. H. G. Kalinke, A. Vidal-Moya, A. Fernandez, R. E. P. Winpenny, A. Doménech-Carbó, A. Leyva-Pérez, D. Armentano, E. Pardo and J. Ferrando-Soria, *J. Am. Chem. Soc.*, 2019, **141**, 10350−10360.

10. T. R. Cook, Y.-R. Zheng and P. J. Stang, *Chem Rev.*, 2013, **113**, 734–777.
11. H. Furukawa, K. E. Cordova, M. O'Keeffe and O. M. Yaghi, *Science*, 2013, **341**, 1230444-1123056.
12. O. M. Yaghi, G. Li and H. Li, *Nature*, 1995, **378**, 703–706.
13. W. Lu, Z. Wei, Z.-Y. Gu, T.-F. Liu, J. Park, J. Park, J. Tian, M. Zhang, Q. Zhang, T. Gentle, M. Bosch and H.-C. Zhou, *Chem.Soc.Rev.*, 2014, **43**, 5561-5593.
14. B. F. Hoskins and R. Robson, *J. Am. Chem. Soc.*, 1989, **111**, 5962-5964.
15. M. Fujita, Y. J. Kwon, S. Washizu and K. Ogura, *J. Am. Chem. Soc.*, 1994, **116**, 1151-1152.
16. M. Kondo, T. Yoshitomi, H. Matsuzaka, S. Kitagawa and K. Seki, 1997, **36**, 1725-1727.
17. S. R. Batten, N. R. Champness, X.-M. Chen, J. Garcia-Martinez, S. Kitagawa, L. Öhrström, M. O'Keeffe, M. P. Suh and J. Reedijk, *Pure Appl. Chem.*, 2013, **85**, 1715–1724.
18. H. Li, M. Eddaoudi, M. O'Keeffe and O. M. Yaghi, *Nature*, 1999, **402**, 276–279.
19. M. E. Davis, *Ind. Eng. Chem. Res.*, 1991, **30**, 1675-1683.
20. Q.-H. Xia, S.-C. Shen, J. Song, S. Kawi and K. Hidajat, *J. Catal.*, 2003, **219**, 74-84.
21. D. J. Tranchemontagne, J. R. Hunt and O. M. Yaghi, *Tetrahedron*, 2008, **64**, 8553–8557.
22. G. Férey, C. Mellot-Draznieks, C. Serre, F. Millange, J. Dutour, S. Surblé and I. A. Margiolaki, *Science*, 2005, **309**, 2040–2042.
23. X. Xia, Y. Xu, Y. Chen, Y. Liu, Y. Lu and L. Shao, *Appl. Catal., A*, 2018, **559**, 138-145.
24. J. H. Cavka, S. Jakobsen, U. Olsbye, N. Guillou, C. Lamberti, S. Bordiga and K. P. Lillerud, *J. Am. Chem. Soc.*, 2008, **130**, 13850–13851.
25. Z. Hu, A. Nalaparaju, Y. Peng, J. Jiang and D. Zhao, *Inorg. Chem.*, 2016, **55**, 1134-1141.
26. S. Biswas, T. Ahnfeldt and N. Stock, *Inorg. Chem.*, 2011, **50**, 9518-9526.
27. P. Horcajada, S. Surblé, C. Serre, D. Y. Hong, Y. K. Seo, J. S. Chang, J. M. Grenèche, I. Margiolaki and G. Férey, *Chem. Commun.*, 2007, **27**, 2820–2822.

28. C. J. Kepert, T. J. Prior and M. J. Rosseinsky, *J. Am. Chem. Soc.*, 2000, **122**, 5158–5168.
29. D. F. Sun, Y. X. Ke, D. J. Collins, G. A. Lorigan and H. C. Zhou, *Inorg. Chem.*, 2007, **46**, 2725–2734.
30. S. Q. Ma, X. S. Wang, C. D. Collier, E. S. Manis and H. C. Zhou, *Inorg. Chem.*, 2007, **46**, 8499–8501.
31. I. Senkovska and S. Kaskel, *Microporous Mesoporous Mater.*, 2008, **112**, 108–115.
32. K.-S. Lin, A. K. Adhikari, C.-N. Ku, C.-L. Chiang and H. Kuo, *Int. J. Hydrogen Energy*, 2012, **37**, 13865-13871.
33. J. A. Mason, K. Sumida, Z. R. Herm, R. Krishna and J. R. Long, *Energy Environ. Sci.*, 2014, **4**, 3030-3040.
34. H. Deng, S. Grunder, K. E. Cordova, C. Valente, H. Furukawa, M. Hmadeh, F. Gándara, A. C. Whalley, Z. Liu, S. Asahina, H. Kazumori, M. O'Keeffe, O. Terasaki, J. F. Stoddart and O. M. Yaghi, *SCIENCE*, 2012, **336**, 1018-1023.
35. O. K. Farha, I. Eryazici, N. C. Jeong, B. G. Hauser, C. E. Wilmer, A. A. Sarjeant, R. Q. Snurr, S. T. Nguyen, A. O. Yazaydın and J. T. Hupp, *J. Am. Chem. Soc.*, 2012, **134**, 15016−15021.
36. Z.-J. Lin, J. Lü, M. Hong and R. Cao, *Chem. Soc. Rev.*, 2014, **43**, 5867-5895.
37. J. Calbo, M. J. Golomb and A. Walsh, *J. Mater. Chem. A*, 2019, **7**, 16571-16597.
38. S. Yuan, J.-S. Qin, C. T. Lollar and H.-C. Zhou, *ACS Cent. Sci.*, 2018, **4**, 440-450.
39. J.-Y. Wang, Y. Shi, D.-L. Tao and Q.-B. Bo, *CrystEngComm*, 2019, **21**, 6591-6603.
40. L. Carlucci, G. Ciani, P. Macchi and D. M. Proserpio, *Chem. Commun.*, 1998, **0**, 1837–1838.
41. B. Moulton and M. J. Zaworotko, *Chem. Rev.*, 2001, **101**, 1629–1658.
42. O. M. Yaghi, M. O'Keeffe, N. W. Ockwig, H. K. Chae, M. Eddaoudi and J. Kim, *Nature* 2003, **423**, 705–714.
43. S. Kitagawa, R. Kitaura and S. Noro, *Angew. Chem., Int. Ed.*, 2004, **43**, 2334-2375.
44. M. Eddaoudi, D. B. Moler, H. L. Li, B. L. Chen, T. M. Reineke, M. O'Keeffe and O. M. Yaghi, *Acc. Chem. Res.*, 2001, **34**, 319-330.
45. H.-Y. Yu, L. Xu, D. Wang, Q. Wei, J. Pan, Z.-Z. Xu and Z.-L. Ma, *Inorg. Chem. Commun.*, 2019, DOI: 10.1016/j.inoche.2019.107713.

46. J. M. Moreno, A. Velty, U. Díaz and A. Corma, *Chem. Sci.*, 2019, **10**, 2053–2066.
47. S. Abednatanzi, P. G.Derakhshandeh, H. Depauw, F.-X. r. Coudert, H. Vrielinck, P. V. D. Voort and K. Leus, *Chem. Soc. Rev.*, 2019, **48**, 2535-2565.
48. D. Sun, D. J. Collins, Y. Ke, J.-L. Zuo and H.-C. Zhou, *Chem.–Eur. J.*, 2006, **12**, 3768–3776.
49. N. Stock and S. Biswas, *Chem. Rev.*, 2012, **112**, 933–969.
50. Z. R. Pan, H. G. Zheng, T. W. Wang, Y. Song, Y. Z. Li, Z. J. Guo and S. R. Batten, *Inorg. Chem.*, 2008, **47**, 4481-4489.
51. H. Abourahma, B. Moulton, V. Kravtsov and M. J. Zaworotko, *J. Am. Chem. Soc.*, 2002, **124**, 9990-9991.
52. K. Shen, M. Zhang and H. Zheng, *CrystEngComm*, 2015, **17**, 981–991.
53. M. J. Kalmutzki, N. Hanikel and O. M. Yaghi, *Sci. Adv.*, 2018, **4**, 9180-9195.
54. S. S.-Y. Chui, S. M.-F. Lo, J. P. H. Charmant, A. G. Orpen and I. D. A. Williams, *Science*, 1999, **283**, 1148−1150.
55. L. Applegarth, A. E. Goeta and J. W. Steed, *Chem. Commun.*, 2005, **0**, 2405–2406.
56. S.-Q. Zang, Y.-J. Fan, J.-B. Li, H.-W. Hou and T. C. W. Mak, *Cryst. Growth Des.*, 2011, **11**, 3395–3405.
57. P. Blondeau, A. v. d. Lee and M. Barboiu, *Inorg. Chem.*, 2005, **44**, 5649−5653.
58. S. Friebe, B. Geppert, F. Steinbach and J. Caro, *ACS Appl. Mater. Interfaces*, 2017, **9**, 12878−12885.
59. K. Leng, Y. Sun, X. Li, S. Sun and W. Xu, *Cryst. Growth Des.*, 2016, **16**, 1168-1171.
60. J. Yang, A. Grzech, F. M. Mulder and T. J. Dingemans, *Chem. Commun.*, 2011, **47**, 5244-5246.
61. D. M. Shin, I. S. Lee, Y. K. Chung and M. S. Lah, *Chem. Commun.*, 2003, **0**, 1036–1037.
62. R. Haldar and T. K. Maji, *CrystEngComm*, 2013, **15**, 9276-9295.
63. P. Rocío-Bautista, I. Taima-Mancera, J. Pasán and V. Pino, *Separations*, 2019, **6**, 33-53.
64. C. Li, M. Moliner and A. Corma, *Angew. Chem., Int. Ed.*, 2018, **57**, 15330-15353.
65. D. J. Tranchemontagne, J. L. Mendoza-Corte´s, M. O'Keeffe and O. M. Yaghi, *Chem. Soc. Rev.*, 2009, **38**, 1257–1283.

66. M. R. DeStefano, T. Islamoglu, S. J. Garibay, J. T. Hupp and O. K. Farha, *Chem. Mater.*, 2017, **29**, 1357−1361.
67. M. Ding, X. Cai and H.-L. Jiang, *Chem. Sci.*, 2019, **10**, 10209–10230.
68. K. Leus, T. Bogaerts, J. D. Decker, H. Depauw, K. Hendrickx, H. Vrielinck, V. V. Speybroeck and P. V. D. Voort, *Microporous Mesoporous Mater.*, 2016, **226**, 110–116.
69. Q. Yao, A. B. Gómez, V. P. J. Su, Y. Yun, H. Zheng, H. Chen, L. Liu, H. N. Abdelhamid, B. Martín-Matute and X. Zou, *Chem. Mater.*, 2015, **27**, 5332–5339.
70. V. Colombo, S. Galli, H. J. Choi, G. D. Han, A. Maspero, G. Palmisano, N. Masciocchi and J. R. Long, *Chem. Sci.*, 2011, **2**, 1311–1319.
71. A. Schaate, P. Roy, A. Godt, J. Lippke, F. Waltz, M. Wiebcke and P. Behrens, *Chem.–Eur. J.*, 2011, **17**, 6643–6651.
72. H. Li, W. Shi, K. Zhao, H. Li, Y. Bing and P. Cheng, *Inorg. Chem.*, 2012, **51**, 9200–9207.
73. X.-W. Zhu, X.-P. Zhou and D. Li, *Chem. Commun.*, 2016, **52**, 6513–6516.
74. N. C. Burtch, H. Jasuja and K. S. Walton, *Chem. Rev.*, 2014, **114**, 10575–10612.
75. G. E. M. Schukraft, S. A. Jr., B. L. Dick and S. M. Cohen, *Chem. Commun.*, 2017, **53**, 10684-10687.
76. Z. Chen, S. L. Hanna, L. R. Redfern, D. Alezi, T. Islamoglu and O. K. Farha, *Coord. Chem. Rev.*, 2019, **386**, 32–49.
77. M. Eddaoudi, D. B. Moler, H. L. Li, B. L. Chen, T. M. Reineke, M. O'Keeffe and O. M. Yaghi, *Acc. Chem. Res.*, 2001, **34**, 319–330.
78. M. Eddaoudi, J. Kim, N. Rosi, D. Vodak, J. Wachter, M. O'Keeffe and O. M. Yaghi, *Science*, 2002, **295**, 469–472.
79. D. Q. Yuan, D. Zhao, D. F. Sun and H. C. Zhou, *Angew. Chem., Int. Ed.*, 2010, **49**, 5357–5361.
80. J. Liu, B. Lukose, O. Shekhah, H. K. Arslan, P. Weidler, H. Gliemann, S. Bräse, S. Grosjean, A. Godt, X. Feng, K. Müllen, I.-B. Magdau, T. Heine and C. Wöll, *Sci. Rep.*, 2012, **2**, 921.
81. Y. Bai, Y. Dou, L.-H. Xie, W. Rutledge, J.-R. Li and H.-C. Zhou, *Chem. Soc. Rev.*, 2016, **45**, 2327-2236.

82. A. Schoedel, M. Li, D. Li, M. l. O'Keeffe and O. M. Yaghi, *Chem. Rev.*, 2016, **116**, 12466−12535.

83. M. O'Keeffe, *Chem. Soc. Rev.*, 2009, **38**, 1215–1217.

84. A. G. Wong-Foy, A. J. Matzger and O. M. Yaghi, *J. Am. Chem. Soc.*, 2006, **128**, 3494–3495.

85. W. B. Blumenthal, *The chemical behavior of zirconium*, D. Van Nostrand Company, Princeton, NJ, 1958.

86. R. Dalapati and S. Biswas, *Sens. Actuators, B*, 2017, **239**, 759-767.

87. H. A. Hamzah, T. S. Crickmore, D. Rixson and A. D. Burrows, *Dalton Trans.*, 2018, **47**, 14491-14496.

88. B. Li, B. Gui, G. Hu, D. Yuan and C. Wang, *Inorg. Chem.*, 2015, **54**, 5139-5141.

89. E. Rahmani and M. Rahmani, *Ind. Eng. Chem. Res.*, 2018, **57**, 169-178.

90. M. A. Ghasemzadeh, B. Mirhosseini-Eshkevari and M. H. Abdollahi-Basir, *Appl Organometal Chem.*, 2019, **33**, 4679-4686.

91. A. Ghoufi, K. Benhamed, L. Boukli-Hacene and G. Maurin, *ACS Cent. Sci.*, 2017, **3**, 394-398.

92. D. I. Kolokolov, H. Jobic, A. G. Stepanov, M. Plazanet, M. Zbiri, J. Ollivier, V. Guillerm, T. Devic, C. Serre and G. Férey, *Eur. Phys. J. Special Topics*, 2010, **189**, 263–271.

93. S. Biswas, D. E. P. Vanpoucke, T. Verstraelen, M. Vandichel, S. Couck, K. Leus, Y.-Y. Liu, M.Waroquier, V. V. Speybroeck, J. F. M. Denayer and P. V. D. Voort, *J. Phys. Chem. C*, 2013, **117**, 22784−22796.

94. S. Ma, D. Sun, M. Ambrogio, J. A. Fillinger, S. Parkin and H.-C. Zhou, *J. Am. Chem. Soc.*, 2007, **129**, 1858–1859.

95. G. Férey, C. Serre, C. Mellot-Draznieks, F. Millange, S. Surblé, J. Dutour and I. Margiolaki, *Angew. Chem., Int. Ed.*, 2004, **43**, 6296–6301.

96. P. Horcajada, S. Surble, C. Serre, D.-Y. Hong, Y.-K. Seo, J.-S. Chang, J.-M. Greneche, I. Margiolaki and G. Ferey, *Chem. Commun.*, 2007, 2820–2822.

97. C. Volkringer, D. Popov, T. Loiseau, G. R. Férey, M. Burghammer, C. Riekel, M. Haouas and F. Taulelle, *Chem. Mater.*, 2009, **21**, 5695–5697.

98. A. Lieb, H. Leclerc, T. Devic, C. Serre, I. Margiolaki, F. Mahjoubi, J. S. Lee, A. Vimont, M. Daturi and J.-S. Chang, *Microporous Mesoporous Mater.*, 2012, **157**, 18–23.

99. D. Frahm, F. Hoffmann and M. Fröba, *Cryst. Growth Des.*, 2014, **14**, 1719−1725.

100. D. Zhao, D. Yuan, D. Sun and H.-C. Zhou, *J. Am. Chem. Soc.*, 2009, **131**, 9186–9188.

101. D. Yuan, D. Zhao and H.-C. Zhou, *Inorg. Chem.*, 2011, **50**, 10528–10530.

102. Y. He, Z. Zhang, S. Xiang, F. R. Fronczek, R. Krishna and B. Chen, *Chem.–Eur. J.*, 2012, **18**, 613–619.

103. O. Karagiaridi, W. Bury, A. A. Sarjeant, J. T. Hupp and O. K. Farha, *J. Visualized Exp.*, 2014, **91**, 52094-52102.

104. Y. Zhang, X. Yang and H.-C. Zhou, *Polyhedron*, 2018, **154**, 189-201.

105. X. Meng, B. Gui, D. Yuan, M. Zeller and C. Wang, *Sci. Adv.*, 2016, 1600480-1601600.

106. O. M. Yaghi, M. J. Kalmutzki and C. S. Diercks, *Introduction to Reticular Chemistry: Metal-Organic Frameworks and Covalent Organic Frameworks*, John Wiley & Sons, 2019.

107. S. Ganguly, P. Pachfule, S. Bala, A. Goswami, S. Bhattacharya and R. Mondal, *Inorg. Chem.*, 2013, **52**, 3588-3590.

108. H. Zhang, X.-W. Gao, L. Wang, X. Zhao, Q.-Y. Li and X.-J. Wang, *CrystEngComm*, 2019, **21**, 1358-1362.

109. N. Xu, Q. Zhang and G. Zhang, *Dalton Trans.*, 2019, **48**, 2683-2691.

110. R. Dalapati, S. Nandi, H. Reinsch, B. K. Bhunia, B. B. Mandal, N. Stock and S. Biswas, *CrystEngComm*, 2018, **20**, 4194-4201.

111. K. Manna, T. Zhang, F. X. Greene and W. Lin, *J. Am. Chem. Soc.*, 2015, **137**, 2665-2673.

112. X. Wang, H. Li and X.-J. Hou, *J. Phys. Chem. C*, 2012, **116**, 19814-19821.

113. L. Liang, C. Liu, F. Jiang, Q. Chen, L. Zhang, H. Xue, H.-L. Jiang, J. Qian, D. Yuan and M. Hong, *Nat. Commun.*, 2017, **8**, 1233-1242.

114. R. W. Flaig, T. M. O. Popp, A. M. Fracaroli, E. A. Kapustin, M. J. Kalmutzki, R. M. Altamimi, F. Fathieh, J. A. Reimer and O. M. Yaghi, *J. Am. Chem. Soc.*, 2017, **139**, 12125−12128.

115. C. Song, Y. He, B. Li, Y. Ling, H. Wang, Y. Feng, R. Krishna and B. Chen, *Chem. Commun.*, 2014, **50**, 12105-12108.

116. M.-B. Kim, K.-M. Kim, T.-H. Kim, T.-U. Yoon, E.-J. Kim, J.-H. Kim and Y.-S. Bae, *Chem. Eng. J.*, 2018, **339**, 223-229.

117. M. E. DMello, N. G. Sundaram, A. Singh, A. K. Singh and S. B. Kalidindi, *Chem. Commun.*, 2019, **55**, 349-352.

118. J.-M. Liu, J.-X. Hou, J. Liu, X. Jing, L.-J. Li and J.-L. Du, *J. Mater. Chem. C*, 2019, **7**, 11851-11857.

119. S. Pal and P. K. Bharadwaj, *Cryst. Growth Des.*, 2016, **16**, 5852−5858.

120. P. George and P. Chowdhury, *Microporous Mesoporous Mater.*, 2019, **288**, 1095912-1095926.

121. S. S. R. Gupta and M. L. Kantam, *Catal. Commun.*, 2019, **124**, 62-66.

122. W. Kleist, F. Jutz, M. Maciejewski and A. Baiker, *Eur. J. Inorg. Chem.*, 2009, **2009**, 3552–3561.

123. A. M. Rasero-Almansa, A. Corma, M. Iglesias and F. Sanchez, *ChemCatChem*, 2014, **6**, 3426–3433.

124. B. F. Hoskins and R. Robson, *J. Am. Chem. Soc.*, 1990, **112**, 1546–1554.

125. Z. Wang and S. M. Cohen, *J. Am. Chem. Soc.*, 2007, **129**, 12368–12369.

126. K. K. Tanabe and S. M. Cohen, *Chem. Soc. Rev.*, 2011, **40**, 498–519.

127. C.-D. Wu, A. Hu, L. Zhang and W. Lin, *J. Am. Chem. Soc.*, 2005, **127**, 8940–8941.

128. R. J. Marshall and R. S. Forgan, *Eur. J. Inorg. Chem.*, 2016, **2016**, 4310-4331.

129. A. Rabenau, *Angew. Chem. Int. Ed. Engl.*, 1985, **24**, 1026-1040.

130. Y.-R. Lee, J. Kim and W.-S. Ahn, *Korean J. Chem. Eng.*, 2013, **30**, 1667-1680.

131. S. Bo, M. Fadda, A. Castiglione, G. Ciccone, A. D. Francesco, D. Fedele, A. Guggino, M. P. Caprino, S. Ferrara, M. V. Boggio, G. Mengozzi, E. Ghigo, M. Maccario and F. Broglio, *Int. J. Obes.*, 2015, **39**, 1689–1695.

132. C. Serre, F. Millange, C. Thouvenot, M. Noguès, G. Marsolier, D. Louër and G. Fe´rey, *J. Am. Chem. Soc.*, 2002, **124**, 13519–13526.

133. J. Klinowski, F. A. A. Paz, P. Silva and J. Rocha, *Dalton Trans.*, 2011, **40**, 321-330.

134. R. Seetharaj, P. V. Vandana, P. Arya and S. Mathew, *Arabian J. Chem.*, 2019, **12**, 295–315.

135. Y. Liu, J. Hu, Y. Li, Y. T. Shang, J. Q. Wang, Y. Zhang and Z. L. Wang, *Electrophoresis*, 2017, **38**, 2521-2529.

136. Z. Ni and R. I. Masel, *J. Am. Chem. Soc.*, 2006, **128**, 12394-12395.

137. A. M. Joaristi, J. Juan-Alcañiz, P. Serra-Crespo, F. Kapteijn and J. Gascon, *Cryst. Growth Des.*, 2012, **12**, 3489-3498.

138. M. Klimakow, P. Klobes, A. F. Thünemann, K. Rademann and F. Emmerling, *Chem. Mater.*, 2010, **22**, 5216-5221.

139. D. Lv, Y. Chen, Y. Li, R. Shi, H. Wu, X. Sun, J. Xiao, H. Xi, Q. Xia and Z. Li, *J. Chem. Eng. Data*, 2017, **62**, 2030-2036.

140. K. S. Suslick, D. A. Hammerton and R. E. Cline, *J. Am. Chem. Soc.*, 1986, **108**, 5641-5642.

141. W.-J. Son, J. Kim, J. Kim and W.-S. Ahn, *Chem. Commun.*, 2008, **0**, 6336-6338.

142. S. Zhang, X. Liu, Q. Yang, Q. Wei, G. Xie and S. Chen, *CrystEngComm*, 2015, **17**, 3312-3324.

143. Y.-C. He, J. Guo, H.-M. Zhang, J.-F. Ma and Y.-Y. Liu, *CrystEngComm*, 2014, **16**, 5450-5457.

144. M. C. Bernini, E. V. Brusau, G. E. Narda, G. E. Echeverria, C. G. Pozzi, G. Punte and C. W. Lehmann, *Eur. J. Inorg. Chem.*, 2007, **2007**, 684-693.

145. A.Schaate, P. Roy, A. Godt, J. Lippke, F. Waltz, M. Wiebcke and P. Behrens, *Chem. - Eur. J.*, 2011, **17**, 6643-6651.

146. Z. Hu, Y. Peng, Z. Kang, Y. Qian and D. Zhao, *Inorg. Chem.*, 2015, **54**, 4862−4868.

147. Z. Hu, I. Castano, S. Wang, Y. Wang, Y. Peng, Y. Qian, C. Chi, X. Wang and D. Zhao, *Cryst. Growth Des.*, 2016, **16**, 2295−2301.

148. W.-H. Zhang, Y.-Y. Wang, E. K. Lermontova, G.-P. Yang, B. Liu, J.-C. Jin, Z. Dong and Q.-Z. Shi, *Cryst. Growth Des.*, 2010, **10**, 76-84.

149. S. N. Iyer, N. Behary, V. Nierstrasz, J. Guan and G. Chen, *Sci. Rep.*, 2019, **9**, 8696-8700.

150. Y. Cui, Y. Yue, G.Qian and B. Chen, *Chem. Rev.*, 2012, **112**, 1126–1162.

151. X. Li, L. Yang, L. Zhao, X. L. Wang, K. Z. Shao and Z. M. Su, *Cryst. Growth Des.*, 2016, **16**, 4374–4382.

152. M. Zhang, G. X. Feng, Z. G. Song, Y. P. Zhou, H. Y. Chao, D. Yuan, T. T. Y. Tan, Z. Guo, Z. Hu, B. Z. Tang, B. Liu and D. Zhao, *J. Am. Chem. Soc.*, 2014, **136**, 7241–7244.

153. A. Buragohain, M. Yousufuddin, M. Sarma and S. Biswas, *Cryst. Growth Des.*, 2016, **16**, 842-851.

154. S. Nandi, E. Sharma, V. Trivedi and S. Biswas, *Inorg. Chem.*, 2018, **57**, 15149-15157.

155. M. SK, M. R. U. Z. Khan, A. Das, S. Nandi, V. Trivedi and S. Biswas, *Dalton Trans.*, 2019, **48**, 12615-12621.

156. C. Gogoi, M. Yousufuddin and S. Biswas, *Dalton Trans.*, 2019, **48**, 1766-1773.

157. Z. Li, N. Wang, Z. Lin, J. Wang, W. Liu, K. Sun, Y. Q. Fu and Z. Wang, *ACS Appl. Mater. Interfaces*, 2016, **8**, 20962-20968.

158. S. Zhao, J. Xiao, T. Zheng, M. Liu, H. Wu and Z. Liu, *ACS Omega*, 2019, **4**, 16378-16384.

159. L. Luo, C. Gu, M. Li, X. Zheng and F. Zheng, *J. Pharm. Biomed. Anal.*, 2018, **156**, 307-312.

160. R.-Z. Wu, X. Yang, L.-W. Zhang and P.-P. Zhou, *Dalton Trans.*, 2017, **46**, 9859–9867.

161. Y. Cao, R.-C. Qian, D.-W. Li and Y.-T. Long, *Chem. Commun.*, 2015, **51**, 17584-17587.

162. O. A. Savchuk, O. F. Silvestre, R. M. R. Adão and J. B. Nieder, *Sci. Rep.*, 2019, **9**, 7535-7545.

163. X. Fang, B. Zong and S. Mao, *Nano-Micro Lett.*, 2018, **10**, 1-19.

164. L. E. Kreno, K. Leong, O. K. Farha, M. Allendorf, R. P. V. Duyne and J. T. Hupp, *Chem. Rev.*, 2012, **212**, 1105–1125.

165. F. A. A. Paz, J. Klinowski, S. M. F. Vilela, J. P. C. Tome´, J. A. S. Cavaleiro and J. Rocha, *Chem. Soc. Rev.*, 2012, **41**, 1088–1110.

166. M. Pamei and A. Puzari, *Nano-Struct. Nano-Objects*, 2019, **19**, 100364-100386.

167. Y. Cheng, H. Zhang, B. Yang, J. Wu, Y. Wang, B. Ding, J. Huo and Y. Li, *Dalton Trans.*, 2018, **47**, 12273-12283.

168. J. Yang, Y. Dai, X. Zhu, Z. Wang, Y. Li, Q. Zhuang, J. Shi and J. Gu, *J. Mater. Chem. A*, 2015, **3**, 7445-7452.

169. G. Ji, X. Gao, T. Zheng, W. Guan, H. Liu and Z. Liu, *Inorg. Chem.*, 2018, **57**, 10525−10532.

170. D. Xie, Y. Ma, Y. Gu, H. Zhou, H. Zhang, G. Wang, Y. Zhang and H. Zhao, *J. Mater. Chem. A*, 2017, **5**, 23794-23804.

171. L. Wang, S. Wang and Y. Chen, *Microchim. Acta*, 2017, **184**, 4597–4602.

172. H. Xu, J. Gao, X. Qian, J. Wang, H. He, Y. Cui, Y. Yang, Z. Wang and G. Qian, *J. Mater. Chem. A*, 2016, **4**, 10900-10905.

173. W. Yan, C. Zhang, S. Chen, L. Han and H. Zheng, *ACS Appl. Mater. Interfaces*, 2017, **9**, 1629-1634.

174. J. Yang, Z. Wang, Y. Li, Q. Zhuang, W. Zhao and J. Gu, *RSC Adv.*, 2016, **6**, 69807-69814.

175. A. A. Tehrani, L. Esrafili, S. Abedi, A. Morsali, L. Carlucci, D. M. Proserpio, J. Wang, P. C. Junk and T. Liu, *Inorg. Chem.*, 2017, **56**, 1446-1454.

176. S. Nandi, H. Reinsch, S. Banesh, N. Stock, V. Trivedi and S. Biswas, *Dalton Trans.*, 2017, **46**, 12856–12864.

177. X. Zhang, Q. Hu, T. Xia, J. Zhang, Y. Yang, Y. Cui, B. Chen and G. Qian, *ACS Appl. Mater. Interfaces*, 2016, **8**, 32259-32265.

178. R. Dalapati, S. Nandi, K. V. Hecke and S. Biswas, *Cryst. Growth Des.*, 2019, **19**, 6388−6397.

179. M. SK, S. Nandi, R. K. Singh, V. Trivedi and S. Biswas, *Inorg. Chem.*, 2018, **57**, 10128-10136.

180. S. Sharma and S. K. Ghosh, *ACS Omega*, 2018, **3**, 254−258.

181. Y. Cheng, J. Wu, C. Guo, X.-G. Li, B. Ding and Y. Li, *J. Mater. Chem. B*, 2017, **5**, 2524-2535.

182. S.-H. Wu, S. Wang, W.-L. Fang, X.-F. Guo and H. Wang, *Anal. Methods*, 2019, **11**, 36-43.

183. S. L. Jackson, A. Rananaware, C. Rix, S. V. Bhosale and K. Latham, *Cryst. Growth Des.*, 2016, **16**, 3067−3071.

184. M. SK, M. R. U. Z. Khan, A. Das, S. Nandi, V. Trivedi and S. Biswas, *Dalton Trans.*, 2019, **48**, 12615-12621.

185. X.-M. Du, Q. Wang, Q. Liu, D. Ning, B. Zhao, Y. Li and W.-J. Ruan, *J. Mater. Chem. C*, 2019, **7**, 8626-8633.

186. P. Wu, Y. Liu, Y. Liu, J. Wang, Y. Li, W. Liu and J. Wang, *Inorg. Chem.*, 2015, **54**, 11046−11048.

187. J. Zhang, J. Ouyang, Y. Ye, Z. Li, Q. Lin, T. Chen, Z. Zhang and S. Xiang, *ACS Appl. Mater. Interfaces*, 2018, **10**, 27465−27471.

188. C. Xia, Y. Xu, M.-M. Cao, Y.-P. Liu, J.-F. Xia, D.-Y. Jiang, G.-H. Zhou, R.-J. Xie, D.-F. Zhang and H.-L. Li, *Talanta*, 2020, **212**, 1207952-1207959.

189. J. Li, Q. Wang, Z. Guo, H. Ma, Y. Zhang, B. Wang, D. Bin and Q. Wei, *Sci. Rep.*, 2016, **6**, 23558-23565.

190. K. Ghosh and S. Rathi, *RSC Adv.*, 2014, **4**, 48516-48521.

191. Q. Chen, Y. Chen, Y. Zhang, F. Wang, H. Yu, C. Zhang, Z. Jiang and W. Luo, *BMC Neurosci.*, 2019, **20**, 1-8.

192. O. Weinreb, T. Amit and M. B. H. Youdim, *Nutr. Aging*, 2012, **1**, 27–39.

193. H. Li, Y. He, Q. Li, S. Li, Z. Yi, Z. Xu and Y. Wang, *RSC Adv.* , 2017, **7**, 50035–50039.

194. L. Jin, C. Liu, N. An, Q. Zhang, J. Wang, L. Zhao and Y. Lu, *RSC Adv.*, 2016, **6**, 58394-58400.

195. X. Li, J.Tang, H. Liu, K. Gao, X. Meng, J. Wu and H. Hou, *Chem. Asian J.*, 2019, **14**, 3721 –3727.

196. H. Chen, P. Fan, X. Tu, H. Min, X.Yu, X. Li, J.-L. Zeng, S. Zhang and P. Cheng, *Chem. Asian J.*, 2019, **14**, 3611–3619.

197. C.-H. Chen, X.-S. Wang, L. Li, Y.-B. Huang and R. Cao, *Dalton Trans.*, 2018, **47**, 3452-3458.

198. K. S. Yoo, S. D. Han, H. G. Moon, S.-J. Yoon and C.-Y. Kang, *Sensors*, 2015, **15**, 15468-15477.

199. S. Peng, T. Zhong, T. Guo, D. Shu, D. Meng, H. Liu and D. Guo, *New J. Chem.*, 2018, **42**, 5185-5192.

200. K. E. Marusak, Y. Feng, C. F. Eben, S. T. Payne, Y. Cao, L. You and S. Zauscher, *RSC Adv.*, 2016, **6**, 76158–76166.

201. A. Buragohain and S. Biswas, *CrystEngComm*, 2016, **18**, 4374-4381.

202. T. Saha, D. Kand and P. Talukdar, *RSC Adv.*, 2015, **5**, 1438-1446.

203. C. Liu, J. Pan, S. Li, Y. Zhao, L. Y. Wu, C. E. Berkman, A. R. Whorton and M. Xian, *Angew. Chem. Int. Ed.*, 2011, **50**, 10327 –10329.

204. H. Li, *Anal. Chim. Acta*, 2018, **1010**, 69-75.

205. H. Li, X. Feng, Y. Guo, D. Chen, R. Li, X. Ren, X. Jiang, Y. Dong and B. Wang, *Sci. Rep.*, 2014, **4**, 4366-4370.

206. Q. Wang, Y. Tan, N. Wang, Z. Lu and W. Wang, *Spectrochim. Acta, Part A*, 2018, **201**, 216-222.

207. A. V. Kolliopoulos, D. K. Kampouris and C. E. Banks, *Anal. Chem.*, 2015, **87**, 4269–4274.

208. R. Liu, X.Tang, Y. Wang, J. Han, H. Zhang, C. Li, W. Zhang, L. Ni and H. Li, *Tetrahedron*, 2017, **73**, 5229-5238.

209. G. W. Lee, N. Singh and D. O. Jang, *Tetrahedron Lett.*, 2008, **49**, 1952–1956.

210. O. Dilek and S. L. Bane, *Chemosensors*, 2016, **4**, 1-8.

211. M. Vogel, A. Buldt and U. Karst, *Fresenius J. Anal. Chem.*, 200, **366**, 781–791.

212. G. M. J. B. V. Henegouwen, *J. Photochem. Photobiol., B*, 1991, **10**, 183 —210.

213. P. Sudarsanam, R. Zhong, S. V. d. Bosch, S. M. Coman, V. I. Parvulescu and B. F. Sels, *Chem. Soc. Rev.*, 2018, **47**, 8349-8402.

214. E. Roduner, *Chem. Soc. Rev.*, 2014, **43**, 8226-8239.

215. M. Liu, J. Wu and H. Hou, *Chem. Eur. J*, 2019, **25**, 2935-2948.

216. Y.-B. Huang, J. Liang, X.-S. Wang and R. Cao, *Chem. Soc. Rev.*, 2017, **46**, 126-157.

217. D. Ma, B. Li, K. Liu, X. Zhang, W. Zou, Y. Yang, G. Li, Z. Shi and S. Feng, *J. Mater. Chem. A*, 2015, **3**, 23136-23142.

218. F. Carson, V. Pascanu, A. B. Gómez, Y. Zhang, A. E. Platero-Prats, X. Zou and B. Martín-Matute, 2015, **21**, 10896-10902.

219. S. Smolders, J. Jacobsen, N. Stock and D. D. Vos, *Catal. Sci. Technol.*, 2020, **10**, 337-341.

220. J. Park, J. R. Li, Y. P. Chen, J. M. Yu, A. A. Yakovenko, Z. Y. U. Wang, L. B. Sun, P. B. Balbuena and H. C. Zhou, *Chem. Commun.*, 2012, **48**, 9995–9997.

221. M. Opanasenko, M. Shamzhy, M. Lamač and J. Čejka, *Catal. Today*, 2013, **204**, 94–100.

222. M. Wang, M. H. Xie, C. D. Wu and Y. G. Wang, *Chem.Commun.*, 2009, **0**, 2396–2398.

223. A. A. Tehrani, S. Abedi, A. Morsali, J. Wang and P. C. Junk, *J. Mater. Chem. A*, 2015, **3**, 20408–20415.

224. X. Liao, W. Wei, Y. Zhou, M. Zhang, Y. Cai, H. Liu, Y. Yao, S. Lu and Q. Hao, *Catal. Sci. Technol.*, 2020, DOI: 10.1039/C9CY02318F

225. Y. Fu, J. Wu, R. Du, K. Guo, R. Ma, F. Zhang, W. Zhu and M. Fan, *RSC Adv.*, 2019, **9**, 37733–37738.

226. D. L. Burnett, R. Oozeerally, R. Pertiwi, T. W. Chamberlain, N. Cherkasov, G. J. Clarkson, Y. K. Krisnandi, V. Degirmenci and R. I. Walton, *Chem. Commun.*, 2019, **55**, 11446-11449.

227. M. Giménez-Marqués, A. Santiago-Portillo, S. Navalón, M. Álvaro, V. Briois, F. Nouar, H. Garcia and C. Serre, *J. Mater. Chem. A*, 2019, **7**, 20285-20292.

228. X. Feng, Y. Song, J. S. Chen, Z. Li, E. Y. Chen, M. Kaufmann, C. Wang and W. Lin, *Chem. Sci.*, 2019, **10**, 2193-2198.

229. K. Tanaka, M. Kinoshita, J. Kayahara, Y. Uebayashi, K. Nakaji, M. Morawiak and Z. Urbanczyk-Lipkowska, *RSC Adv.*, 2018, **8**, 28139-28146.

230. H. G. T. Ly, G. Fu, A. Kondinski, B. Bueken, D. D. Vos and T. N. Parac-Vogt, *J. Am. Chem. Soc.*, 2018, **140**, 6325-6335.

231. H. G. T. Nguyen, N. M. Schweitzer, C.-Y. Chang, T. L. Drake, M. C. So, P. C. Stair, O. K. Farha, J. T. Hupp and S. T. Nguyen, *ACS Catal.*, 2014, **4**, 2496-2500.

232. D. Roca-López, E. Marqués-López, A. Alcaine, P. Merinoa and R. P. Herrera, *Org. Biomol. Chem.*, 2014, **12**, 4503-4510.

233. J.-L. Zhao, L. Liu, Y. Sui, Y.-L. Liu, D. Wang and Y.-J. Chen, *Org. Lett.*, 2006, **8**, 6127-6130.

234. M. Rueping and B. J. Nachtsheim, *Beilstein J. Org. Chem.*, 2010, **6**, 6.

235. J. M. Roberts, B. M. Fini, A. A. Sarjeant, O. K. Farha, J. T. Hupp and K. A. Scheidt, *J. Am. Chem. Soc.*, 2012, **134**, 3334-3337.

236. P. C. Rao and S. Mandal, *Chem. - Asian J.*, 2019, **14**, 4087-4102.

237. P. C. Rao and S. Mandal, *ChemCatChem.*, 2017, **9**, 1172-1176.

238. D. Markad and S. K. Mandal, *ACS Catal.*, 2019, **9**, 3165-3173.

239. R. Connon and P. J. Guiry, *Eur. J. Org. Chem.*, 2019, **2019**, 5950-5954.

240. J.-H. Li, W.-J. Liu and D.-L. Yin, *Synth. Commun.*, 2004, **34**, 3161–3165.

241. X.-W. Dong, T. Liu, Y.-Z. Hu, X.-Y. Liu and C.-M. Che, *Chem. Commun.* , 2013, **49**, 7681-7683.

242. E. J. Corey, S. Shibata and R. K. Bakshi, *J. Org. Chem.* , 1988, **53**, 2861–2863.

243. M. Fallah-Mehrjardi, A. R. Kiasat and K. Niknam, *J. Iran. Chem. Soc.*, 2018, **15**, 2033–2081.

244. K. N.Tayade, L. Wang, S. Shang, W. Dai, M. Mishra and S. Gao, *Chin. J. Catal.*, 2017, **38**, 758-766.

245. S. Bansal, Y. Kumar, P. Pippal, D. K. Das, P. Pramanik and P. P. Singh, *New J. Chem.*, 2017, **41**, 2668-2671.

Ph.D. Thesis
Chapter 2

Extraordinary Sensitivity for H_2S and Fe(III) Sensing in Aqueous Medium by Al-MIL-53-N_3 Metal–Organic Framework: *in vitro* and *in vivo* Applications of H_2S Sensing

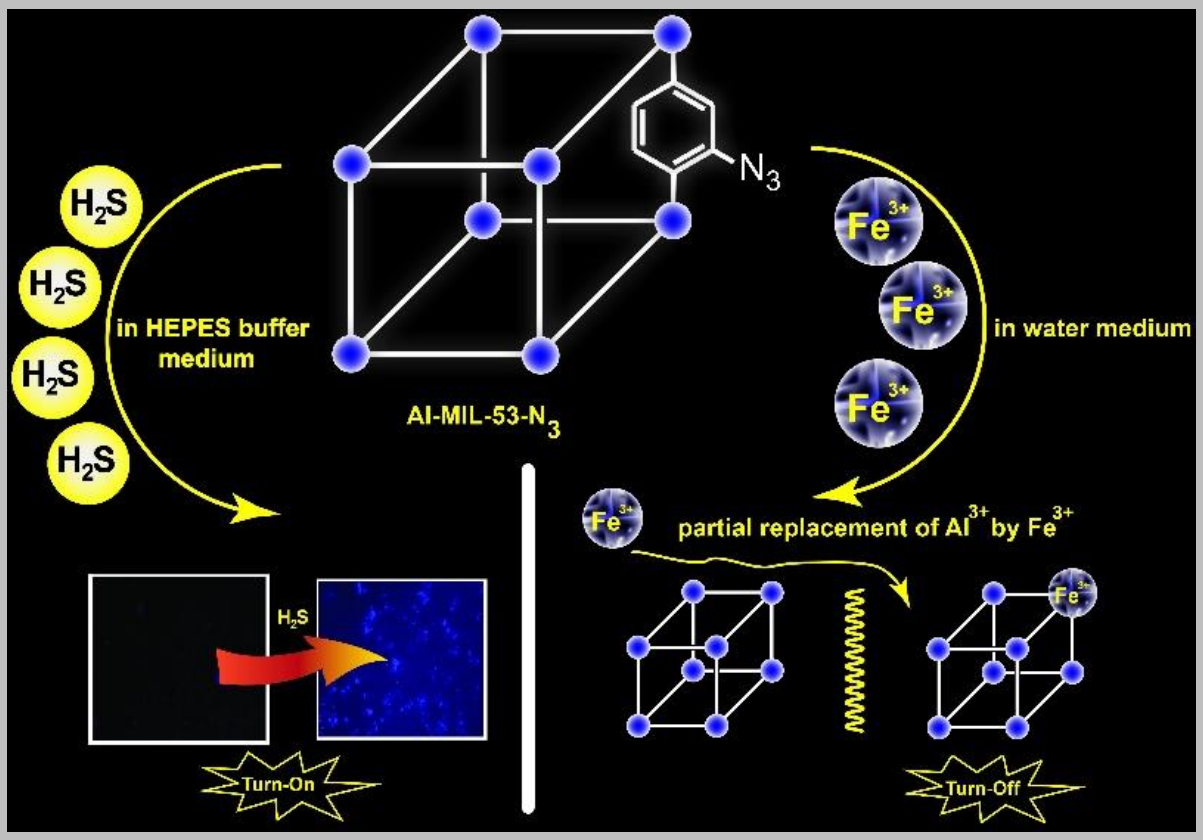

Chapter 2

2.1 Introduction

MOFs with various potential applications have become a very popular research topic in chemistry and materials science during the last two decades. These promising applications encompass chemical sensing,[1] heterogeneous catalysis,[2] gas storage[3] and separation[4] as well as drug delivery[5]. Large surface areas and pore volumes as well as organic linkers having strong π-conjugation make MOFs promising candidates for chemical and biosensing. Among the large family of MOFs, those incorporating Al(III) as framework metal ions exhibit low toxicity, biocompatibility as well as exceptional thermal and chemical stability. Endowed with these additional important features, Al(III) MOFs hold great potentials for practical chemical and biosensing processes.[6] In general, MOFs have been shown to act as chemical and biosensors for nitroaromatic explosives, pesticides, antibiotics, metal ions, small organic molecules, anions, biomolecules, biological signalling molecules (H_2S, CO and NO), etc.[7] On the other hand, the utility of comparatively less number of Al(III) MOFs has been demonstrated in the literature for chemical and biosensing applications.[8-12]

Hydrogen sulfide (H_2S) occurs as a colorless, toxic gas. It can penetrate within living animals, most often through inhalation.[13] This gas can emanate from various industries like mining, smelting, petrochemical and natural gas production, as well as industries associated with the production of organophosphate pesticides, sulfur dyes, paints, animal glues, etc.[13] The effects of exposure to high level (100 ppm or higher) of H_2S can be serious and life-threating.[14] It may affect the respiratory system, brain, liver and pancreas, causing convulsion, breathing difficulty, rapid unconsciousness, coma and death.[15] It can also result in various diseases, including liver cirrhosis, Alzheimer's disease, diabetes and Down's syndrome.[13] In sharp contrast, H_2S present in the cardiovascular system of mammals helps to lower blood pressure.[16] It is also associated with several pathological and physiological processes like vasorelaxation, neuroprotection, angiogenesis, cardioprotection and control of inflammation.[17] Due to the above-mentioned important features, the design and development of new sensors for H_2S are highly demanding.

Fe(III) is one of the crucial ions present in human blood.[18] It is widely found in the structures of several proteins and enzymes, and plays vital roles in many biological processes like oxygen metabolism, muscle and brain function, formation of hemoglobin, synthesis of DNA and RNA, and oxygen metabolism.[19] Both the deficiency and excess of

TH-2604_156122006

Fe(III) ion can hamper cellular homeostasis and cause several biological malfunctions. Therefore, the preparation of new sensors for Fe(III) ion is still a challenging target.

The use of fluorescence spectroscopy has attracted intense interests over other detection methods in recent years due to its simplicity, low cost, rapid response, great selectivity and sensitivity, ability to be operated in both solution and solid media, easy portability, etc.[20] Thus far, numerous literature reports have appeared, which have demonstrated the ability of different MOF compounds to act as sensors for H_2S[9, 21-25] as well as Fe(III) ion[8, 19, 26, 27]. However, so far, there is no report on a single, dual-functional MOF which can selectively sense H_2S and Fe(III) ion independently in solution phase. In the literature, only one Al(III) MOF (namely Al-MIL-53) has been utilized for Fe(III)[8] sensing and two Al(III) MOFs (namely Al-MIL-101-N_3 and CAU-10-N_3) containing azide functional groups have been reported to detect of H_2S selectively.[9, 23] In this report, we present a new Al(III) MOF (called **1′**) having azide functionality, which shows unprecedented sensitivity in the sensing of H_2S and Fe(III) ion in aqueous medium (Scheme 2.1). As compared to the previously reported MOF based fluorescent probes, the detection limits of the presented compound for H_2S and Fe(III) ions in the aqueous medium are relatively lower. The MOF compound has been utilized for the sensing of H_2S in human blood plasma (HBP), living cells as well as environmental samples.

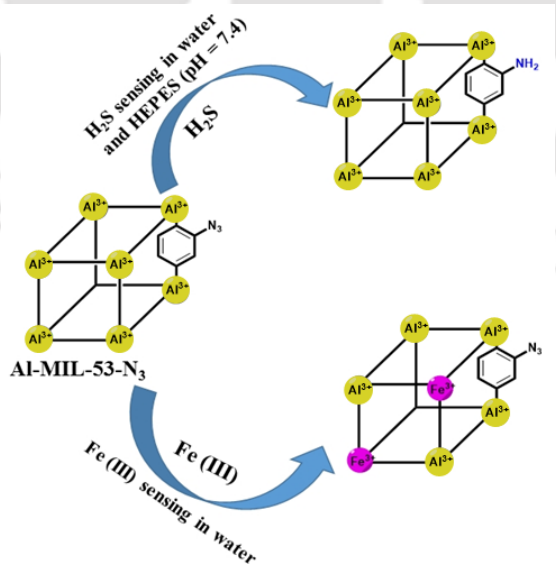

Scheme 2.1 Schematic representation displaying the sensing properties of **1′** towards H_2S in aqueous and HEPES medium through fluorescence *turn-on* and Fe(III) in aqueous medium through *turn-off* mechanisms.

TH-2604_156122006

2.2 Experimental

2.2.1 Materials and General Methods

The linker $H_2BDC\text{-}N_3$ was synthesized by following the previously reported procedure.[28] All others chemicals were commercially available and they were used without any further purification. Milli-Q water was used as a medium in all the fluorescence sensing experiments. Fourier transform infrared spectroscopy was performed in the region 400-4000 cm^{-1} with the Perkin Elmer Spectrum Two FT-IR spectrometer. The following indications were used to characterize the absorption bands: very strong (vs), strong (s), medium (m), weak (m), weak (w), shoulder (sh) and broad (br). Thermogravimetric analyses (TGA) were performed using a SDT Q600 thermogravimetric analyzer in the temperature range 25-700 °C under argon atmosphere at a heating rate of 10 °C min^{-1}. X-ray powder diffraction (XRPD) patterns were measured with a Bruker D2 Phaser X-ray diffractometer (30 kV, 10 mA) using Cu-Kα (λ = 1.5406 Å) radiation. Energy dispersive X-ray (EDX) analyses were carried out with a Hitachi S3400 N EDX (EDX = electron diffraction spectroscopy) instrument. An Agilent 6520 Q-TOF high-resolution mass spectrometer (HR-MS) was employed to collect the mass spectra. The ^{1}H-NMR spectra were recorded on a Bruker AM 600 spectrometer. Before recording the ^{1}H-NMR spectra, 10 mg of **1′** was suspended in 500 µL of DMSO-d_6 and 30 µL of HF (48%) was added to it for digesting the MOF. Na_2S solution was added to **1′** (10 mg), filtered off and the recovered solid was also digested by adding 30 µL of HF (48%) in 500 µL of DMSO-d_6. Before recording the HR-MS spectra, un-treated or Na_2S-treated **1′** (10 mg each) was independently digested by adding 100 µL of HF (48%) to 1.0 mL of methanol. After separation of the organic phase by filtration, it was diluted with methanol. The resulting solution was used for the HR-MS analysis. The Field Emission - Scanning Electron Microscopy (FE-SEM) images were collected with a Zeiss (Zemini) scanning electron microscope. Nitrogen sorption isotherms were recorded on a Quantachrome Autosorb iQMP gas sorption analyzer. The CO_2 adsorption isotherms up to 1 bar were measured using a Quantachrome iSorb-HP gas sorption analyzer at 25 °C. Fluorescence emission studies were performed using a HORIBA JOBIN YVON Fluoromax-4 spectrofluorometer. Edinburgh Instrument Life-Spec II equipment was used to measure the fluorescence lifetimes by employing time-correlated single-photon counting (TCSPC) procedure. The compound was heated at 100 °C for 24 h before the sorption experiments.

TH-2604_156122006

2.2.2 Synthesis of MOF and Activation of 1

2.2.2.1 Synthesis of [Al(OH)(BDC-N_3)]1.2H_2O·0.3DMF (Al-MIL-N_3, 1)

A mixture of $Al(NO_3)_3·9H_2O$ (80 mg, 0.21 mmol), H_2BDC-N_3 linker (44 mg, 0.21 mmol), DMF (DMF = *N*,*N*-dimethylformamide) (1 mL) and water (2 mL) was placed in a Pyrex tube. After sonicating the reaction mixture for 5 min, the tube was sealed and heated in an aluminum block heater at 80 °C for 24 h. The brownish precipitate was filtered off, and washed consecutively with DMF (2 × 2 mL), water (2 × 2 mL) and acetone (3 × 3 mL). The material was dried in a conventional oven at 60 °C for 5 h. The yield was 60 mg (0.21 mmol, 96 %). FT-IR (KBr, cm^{-1}): 3439 (br), 2929 (w), 2855 (w), 2125 (s), 1706 (m), 1651 (s), 1611 (s), 1496 (s), 1426 (s), 1381 (m), 1280 (s), 1091 (m), 1016 (m), 772 (s), 658 (m), 597 (s), 489 (s).

2.2.2.2 Activation of 1

50 mg of as-synthesized **1** was placed in a Teflon-lined stainless steel autoclave and 15 mL of methanol was added to it. Then, this mixture was heated in a conventional oven at 80 °C for 48 h during which time methanol was discarded and fresh methanol was added after 24 h. After cooling down to room temperature, the material was collected by vacuum filtration and dried in air. Afterwards, the compound was heated at 100 °C under dynamic vacuum for 24 h. The activated for was denoted by **1′**.

2.2.3 Preparation of a Suspension of 1′ for Fluorescence Sensing Experiments

For Fe(III) sensing experiments, 2 mg of **1′** was placed in a 5 mL glass vial and 3 mL of water was added to it. The mixture was sonicated for 1 h. For H_2S sensing experiments, 0.5 mg of **1′** (2.007 µmol of azide functional group) was placed in a 5 mL glass vial and 2 mL of water or HEPES buffer (4-(2-hydroxyethyl)-1-piperazineethanesulfonic acid) (10 mM, pH = 7.4) was added to it. This mixture was sonicated for 1 h. All the suspensions were kept undisturbed under ambient conditions for 3 days in order to get a stable suspension of **1′** for the fluorescence sensing studies. These suspensions were excited at a wavelength (λ_{ex}) of 315 nm and all the fluorescence spectra were recorded in the range of 360-600 nm

TH-2604_156122006

2.2.4 Fe(III) Sensing Experiments in Water

100 μL of the suspension of **1′** from the stock suspension was placed in a quartz cuvette and 2900 μL of water was added to it in order to make a suspension having a total volume of 3 mL. Afterwards, 2 mM of Fe(III) solution was added to the cuvette in an incremental manner (up to 150 μL). The quenching efficiency (η) was calculated using the formula: $\eta = (1-I/I_0) \times 100$ %, where I_0 initial fluorescence intensity of the suspension of **1′** and I is the fluorescence intensity after addition of the analyte.

2.2.5 H_2S Sensing Experiments in Water and HEPES Buffer

For investigating the effect of reaction time on the H_2S sensing properties, aqueous solution of Na_2S (10 equiv. per azide functional group) was added to the suspension of **1′**. After the Na_2S addition, the fluorescence spectra were recorded at a regular time interval of 1 min till the attainment of saturation point. We have also conducted similar types of experiments by replacing Na_2S with other intrusive analytes such as alanine, glutathione, cysteine, serine, NaBr, $NaNO_2$, NaCl, NaI, NaSCN, Na_2SO_4, $NaNO_3$, $NaHSO_4$, $NaHSO_3$, $Na_2S_2O_3$ and Na_2SO_3. To check the selectivity of **1′** towards Na_2S in the existence of different intrusive species, the interfering analyte (10 equiv. per azide group) was added to the suspension of **1′**, followed by the addition of Na_2S (10 equiv. per azide group). After 3 min of addition of these analytes, the fluorescence spectra were recorded. For investigating the influence of Na_2S concentration on the sensing behavior, 0 to 10 equiv. of Na_2S solution were added to the suspension of **1′**. After the addition of each equiv. of Na_2S solution, the fluorescence spectra were collected. The fold increment was calculated by using the formula: fold increment = I/I_0.

2.2.6 H_2S Sensing Experiments in HBP and Sulfide Sensing Experiments in Real Water Samples

We have carried out the H_2S detection experiments in HBP in a similar way as reported formerly by us.[22]

We have collected three dissimilar types of water samples. They include mineral, tap and lake water (brought from Tihor lake of IIT Guwahati, India). The water samples were distributed in nine microcentrifuge tubes so that three tubes contain samples of one type.

TH-2604_156122006

Then, known amount of Na_2S was spiked into every water sample so that the final concentrations of Na_2S in three tubes having samples of one kind become 100, 200 and 300 μM. Later, the suspension of **1′** in water was treated with 100 μL of each Na_2S-spiked water sample. We have measured the fluorescence spectrum of the dispersion of the probe after 4 min of addition of Na_2S-spiked water sample.

2.2.7 Culture of Macrophage Cells and Cell Viability Assay

For the culture and maintenance of the macrophage J774A.1 cells, we have followed our previously reported protocol.[29]

For conducting the live-cell imaging experiments, our recently published procedure was followed.[22] In brief, twenty thousand macrophage J774A.1 cells were loaded with 25 μM probe and incubated cells were washed with PBS to remove excess probe attached to cell surface or present in extracellular medium. Cells were incubated with 5 μM Na_2S for 15 min to produce H_2S inside the cells. Cells were washed with PBS and cellular morphology was observed in bright light and fluorescence signal was detected in blue channel (λ_{ex} = 381 nm; λ_{em} = 435 nm) using Cytell cell imaging system (GE Healthcare).

2.3 Results and Discussion

2.3.1 Preparation and Activation Procedure

Initially, attempts were made for the synthesis of **1** by following the previously reported procedure for un-functionalized Al-MIL-53 compound by Loiseau et al.[30, 31] However, the azide group attached with the BDC-N_3 linker was removed at such as a high reaction temperature (220 °C).[30] The synthesis method for **1** was optimized after performing several solvothermal reactions with different aluminium salts ($Al(NO_3)_3{\cdot}9H_2O$, $AlCl_3{\cdot}6H_2O$, $Al(ClO_4)_3{\cdot}9H_2O$, $Al_2(SO_4)_3{\cdot}18H_2O$) in various polar solvents/solvent mixtures (DMF, DMA, DEF, H_2O, DMF/H_2O, DMA/H_2O and DEF/H_2O; DMA = *N*,*N*-dimethylacetamide, DEF = *N*,*N*-diethylformamide). The reaction temperature and time were also varied. The optimized synthesis conditions were established when a mixture containing $Al(NO_3)_3{\cdot}9H_2O$ and H_2BDC-N_3 linker in 1:1 molar ratio was heated at 80 °C for 24 h in DMF/H_2O (1:1, v/v) mixture. At reaction temperatures higher than 80 °C, the removal of the azide group attached with the BDC-N_3 linker occurred. Under the optimum reaction

TH-2604_156122006

conditions, Al-MIL-53-N_3 (**1**) was synthesized with very high crystallinity (Figure 2.1). As shown in Figure 2.2, the FE-SEM images display that the compound crystallized as a homogeneous crystalline phase.

For removing the guest molecules entrapped inside the pores of **1**, a two-step activation procedure was performed. In the first step, the guest molecules (DMF and H_2O) were exchanged by the volatile and easily removable methanol molecules by heating the as-synthesized compound at 80 °C for 48 h. In the second step, the compound obtained after the methanol-exchange procedure was heated at 100 °C under high vacuum over 24 h. In this way, the activated form of **1′** was obtained. It is worthy to mention that any degassing temperature higher than 100 °C resulted in the elimination of the azide functional groups from the framework BDC-N_3 linkers. Due to this phenomenon, the complete removal of the guest DMF molecules from the pores was not possible to accomplish.

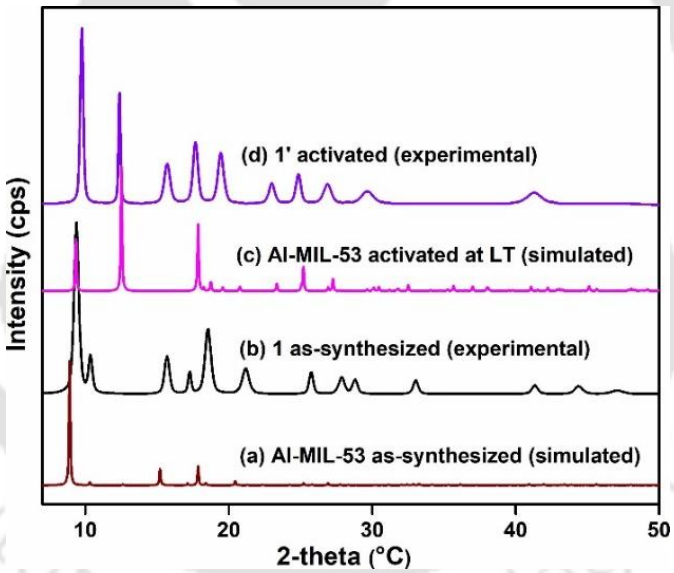

Figure 2.1 XRPD patterns (a) Al-MIL-53-as-synthesized (simulated), (b) compound **1** (experimental), (c) Al-MIL-53-thermally activated at LT (LT = Low Temperature) and (d) compound **1′** (experimental).

TH-2604_156122006

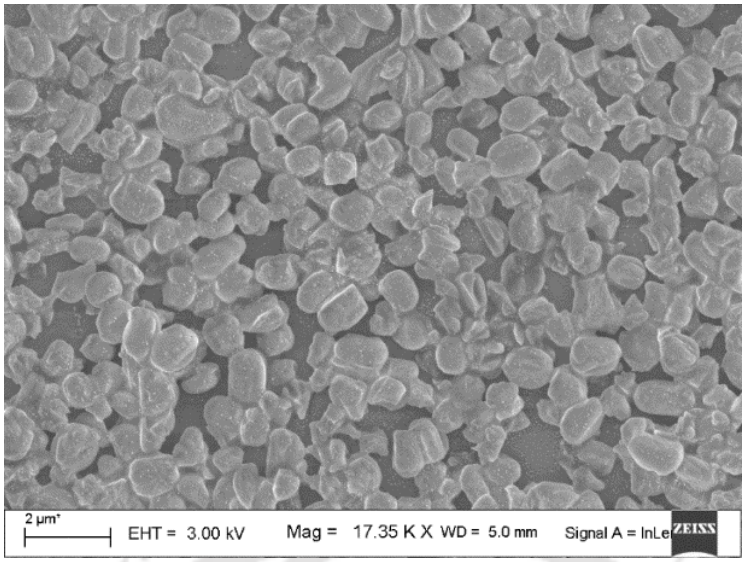

Figure 2.2 FE-SEM images of **1′**

2.3.2 Structure Description

The XRPD pattern (Figure 2.1) of **1** proves that it is isostructural with the un-functionalized Al-MIL-53 MOF.[30] According to the description by Loiseau *et al.*, Al-MIL-53 comprises infinite chains (having *trans* geometry) of corner sharing $[AlO_4(OH)_2]$ octahedra in its structural framework. These octahedra share their corners through the bridging hydroxyl groups. The cross-linking of the adjacent infinite chains through the 1,4-benzenedicarboxylate (BDC) linkers causes formation of the three-dimensional framework structure of the Al-MIL-53 compound (Figure 2.3). For the title compound, the azide-functionalized BDC molecules serve as the framework linkers instead of un-functionalized BDC linkers. One-dimensional rhombic shaped channels are present in the structural framework. At ambient conditions, these channels are occupied by the guest molecules such as unreacted linkers and solvents. The narrow-pore form (having monoclinic crystal system) of the Al-MIL-53 framework structure can change to its large pore-form (having orthorhombic crystal system). This phenomenon has been termed as the "breathing behavior".[31] This property depends not only on the temperature but also on the type of guest molecules.

TH-2604_156122006

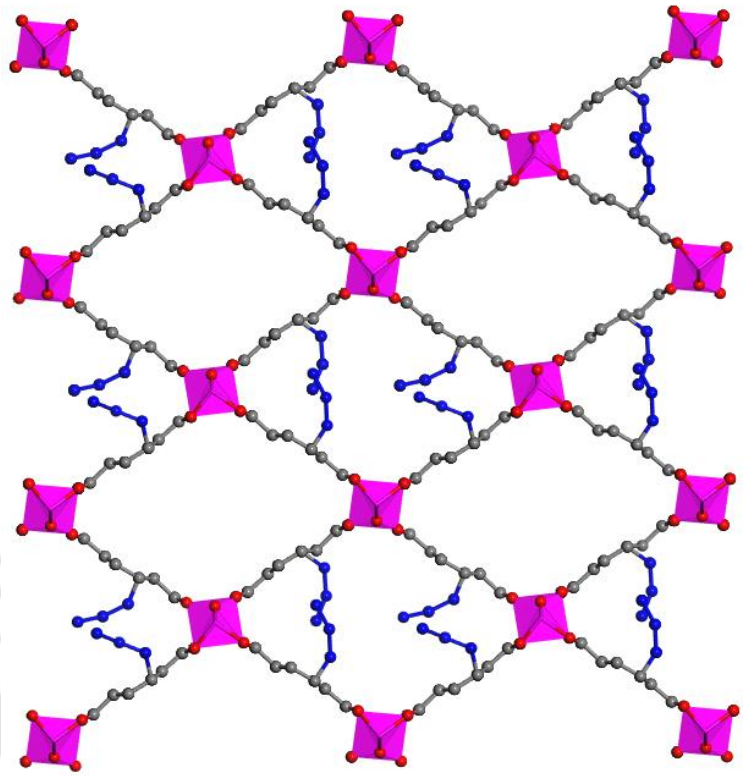

Figure 2.3 Structure of the large-pore form of the Al-MIL-53-N_3 framework. Color codes: Al, violet octahedra; C, grey; O, red; N, blue. The structure of **1** was modelled and drawn by using the Materials Studio (version 5.0, Accelrys Inc., San Diego, 2009) software package.

2.3.3 Infrared Spectroscopy

As we have expected, the FT-IR spectra (Figure 2.4) of the samples of **1** and **1′** are very similar. In the IR spectra of both **1** and **1′**, the strong absorption peaks at *ca.* 1610 and 1425 cm^{-1} are attributable to the asymmetric and symmetric stretching vibrations for the coordinated $–CO_2$ group of the BDC-N_3 linkers in the framework structure, respectively.[30] The azide group gives rise to strong absorption peak at 2125 cm^{-1} in the IR spectra of both **1** and **1′**.[32] A strong absorption peak at 1670 cm^{-1} is present in the IR spectrum of **1** for the carbonyl stretching vibration of guest DMF molecules.

TH-2604_156122006

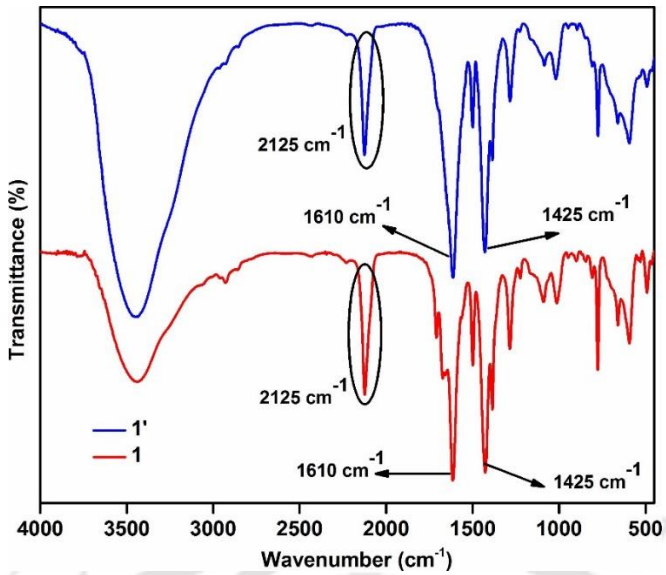

Figure 2.4 FT-IR spectra of as-synthesized **1** (red) and thermally activated (blue) **1′**. The absorption band for the $–N_3$ group is high-lighted by the black ovals.

2.3.4 Thermal Stability

Thermogravimetric (TG) analyses were conducted with **1** and **1′** for checking their thermal stability. The TG traces (Figure 2.5) disclosed that the MOF compound is thermally stable up to 300 °C in air atmosphere. It is worthy to notice that the Al-MIL-53-N_3 compound has lower thermal stability as compared to the previously reported pristine and functionalized Al-MIL-53-X (X = -F, -Cl, -Br, -NO_2, -CH_3, -NH_2, -$(OH)_2$, -F_2) compounds.[75, 76, 82, 83]

Before the decomposition temperature, two weight loss steps are observed in the TG trace of **1** due to the removal of guest molecules (H_2O and DMF) from the 1D channels. In the range of 25-150 °C, the first weight loss of 7.5 wt% can be accounted for the removal of 1.2 occluded water molecules per formula unit (calcd.: 7.3 wt%). The second weight loss of 6.9 wt% in the range of 150-200 °C takes place due to the elimination of 0.3 guest DMF molecule per formula unit (calcd.: 7.4 wt%). After 300 °C, structural decomposition begins because of the loss of BDC-N_3 linkers from the framework structure of **1**. In the TG curve of **1′**, the first weight loss step is observed for the removal of adsorbed water molecules. The second weight loss step indicates that the DMF molecules are still present inside the channels due to the incomplete activation of the compound. Our efforts for the

TH-2604_156122006

removal of DMF molecules at higher temperatures (>100 °C) led to the detachment of the $–N_3$ groups from the framework linkers.

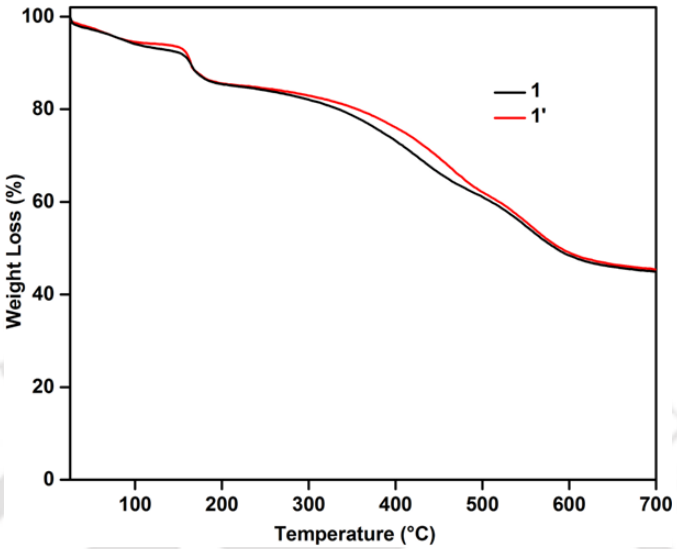

Figure 2.5 TG curves of as-synthesized **1** (black) and thermally activated **1′** (red) recorded in an argon atmosphere in the temperature range of 25-700 °C with a heating rate of 10 °C min^{-1}.

2.3.5 Gas Sorption Properties

The N_2 adsorption experiments were conducted with **1′** to check its permanent porosity. It can be seen from Figure 2.6a that the N_2 adsorption isotherms of the compound have type-I shape. The BET surface area observed for **1′** is 628 m^2 g^{-1} and the micropore volume of the compound at p/p_0 = 0.5 corresponds to 0.34 cm^3 g^{-1} (Table 2.1). These values are comparable with those of the formerly published, functionalized and non-functionalized Al-MIL-53 compounds.[30, 31, 33, 34]

The CO_2 sorption features of **1′** were investigated at 25 °C up to 1 bar. In the pressure range from 0 to 1 bar, the compound displayed CO_2 adsorption isotherm (Figure 2.6b) having type-I behavior. The Al-MIL-53-N_3 compound exhibited CO_2 uptake capacity of 7.2 wt% at 1 bar. This value falls within the range of CO_2 uptake values of the existing, parent and functionalized Al-MIL-53 and Cr-MIL-53 compounds at 25 °C and 1 bar.[35-37]

TH-2604_156122006

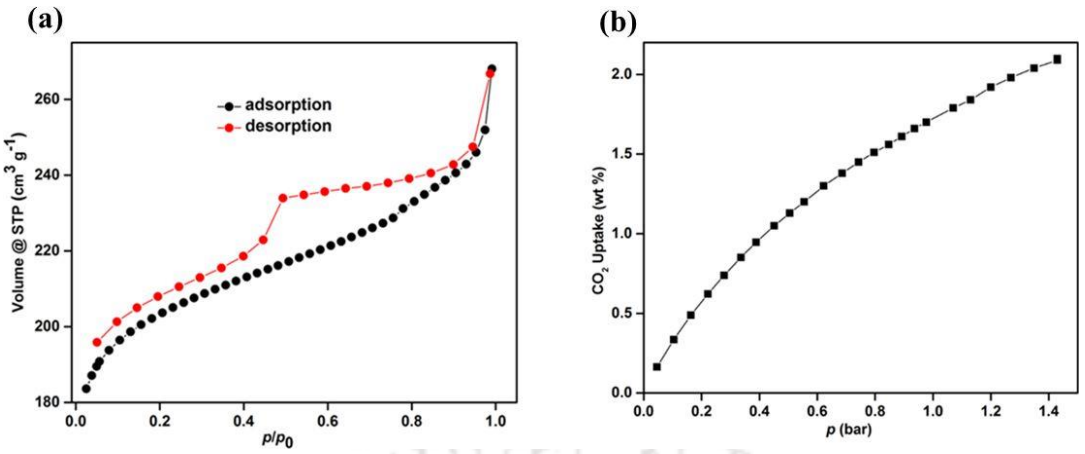

Figure 2.6 (a) N_2 adsorption (black circles) and desorption (red circles) isotherms of **1′** measured at –196 °C. (b) CO_2 adsorption isotherms of **1′** measured at 25 °C.

Table 2.1 Micropore volumes (at $p/p_0 = 0.5$) of the Al-MIL-53-X compounds determined from N_2 adsorption isotherms.

Sl. No.	Compound	Micropore volume ($cm^3\ g^{-1}$)	Ref.
1.	Al-MIL-53-N_3	0.34	this work
2.	Al- MIL-53	0.54	31
3.	Al-MIL-53-Cl	0.32	31
4.	Al-MIL-53-Br	0.14	31
5.	Al-MIL-53-CH_3	0.32	31
6.	Al-MIL-53-NO_2	0.34	31
8.	Al-MIL-53-$(OH)_2$	0.04	31
9.	Al-MIL-53-NH_2	0.44	31
10.	Al-MIL-53-F	0.48	38
11.	Al-MIL-53-F_2	0.16	39

TH-2604_156122006

2.3.6 H_2S Sensing in Water and HEPES Buffer

So far, a large number of small organic molecules containing the $–N_3$ group have been shown to act as fluorescent probes for the selective sensing of H_2S.[40, 41] In case of these reaction-based H_2S sensors, the azide-functionalized molecules having weak fluorescence intensity are converted to their corresponding amine derivatives, which show strong fluorescence intensity. Recently, we and other research groups have exploited the possibility of utilizing the azide-functionalized MOF compounds as fluorescent *turn-on* probes for the in vivo and in vitro detection of H_2S. Ghosh and co-workers prepared the Zr-UiO-66-N_3 compound by post-synthetic modification of the corresponding amino-functionalized material.[25] They have employed the MOF compound having azide groups for the sensing of both extracellular and intracellular H_2S. Our group has demonstrated the H_2S sensing potential of the Ce-UiO-66-N_3 compound in simulated biological medium.[21] Along the same line, the IRMOF-3 and Al-MIL-101 compounds possessing $–N_3$ groups (both compounds prepared by post-synthetic modification approach) in their structural frameworks were used for the sensing of H_2S with extraordinary sensitivity.[23, 24] Especially, the limit of detection (LOD) value of Al-MIL-101-N_3 for H_2S in HBSS buffer medium was as low as 100 nM under laser excitation.[23] Very recently, we have reported the H_2S sensing properties of the Al(III) MOF called CAU-10-N_3.[9] The MOF compound exhibited unprecedented sensitivity (LOD = 2.65 μM) towards the detection of in vivo and in vitro H_2S. The biocompatibility of the Al(III) based MOF makes them ideal candidates for bio-imaging and drug delivery.[42] All the above-stated facts encouraged us to examine the detection ability of the Al-MIL-53-N_3 material for H_2S. The fluorescence sensing experiments for H_2S was accomplished in water as well as in HEPES buffer (pH = 7.4, 10 mM).

To investigate the H_2S sensing ability, we have added 10 equiv. of Na_2S per $–N_3$ group to the suspension of **1′** in water and HEPES buffer separately. After the addition of Na_2S, we have recorded the fluorescence spectra at a regular interval of time (60 s). The fluorescence intensity of the Al-MIL-53-N_3 probe increased rapidly with time upon the addition of Na_2S. The saturation in the fluorescence intensity was achieved within 3 and 6 min in water and HEPES buffer, respectively (Figure 2.7 and Figure 2.8). At the saturation time, 76- and 5-fold enhancements in the fluorescence intensity of the compound were observed in water and HEPES buffer respectively. The response time of **1′** in water is

TH-2604_156122006

comparable with the previous reports on MOF type H_2S sensors (Table 2.2).[9, 22, 24, 25] The increment of fluorescence intensity (at saturation point) upon the addition of H_2S in aqueous medium is higher than any MOF based H_2S sensor reported till date.[43-46] Since the response time and *n*-fold enhancement in fluorescence intensity of the probe is better in water as compared to HEPES buffer, we have performed all the subsequent fluorescence sensing experiments in the aqueous medium. The quick response and very large increment in fluorescence emission intensity in water after Na_2S addition indicate that the MOF material can be applied as a highly promising fluorescent probe for the real-life detection of H_2S.

The suitability of a H_2S sensor for the on-site application requires high selectivity for H_2S over other intrusive species. To elucidate the selectivity, we have chosen few biological molecules (like alanine, serine, cysteine and glutathione) and anions (like NaCl, NaBr, NaI, $NaNO_2$ and $NaNO_3$, Na_2SO_4, $Na_2S_2O_3$, $NaHSO_3$ and $NaHSO_4$), which might interfere with Na_2S. After 3 min of addition of these analytes (10 equiv. per $–N_3$ group) separately to the aqueous suspension of the compound, the fluorescence spectra were measured. The results show that the addition of these competitive analytes led to negligible change in the fluorescence intensity of **1′** (Figure 2.9 and Figure 2.10). In this way, the high selectivity of the Al-MIL-53-N_3 probe towards H_2S is confirmed.

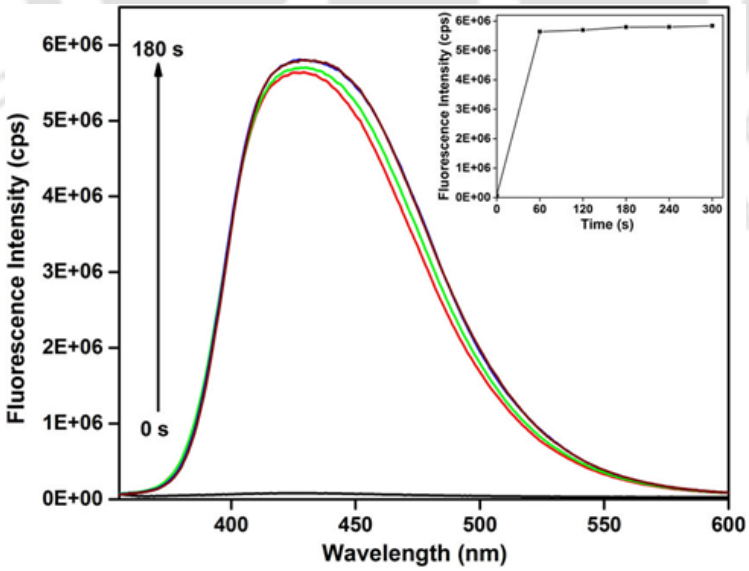

Figure 2.7 Change in the fluorescence intensity of **1′** (in aqueous medium) upon the addition of Na_2S at a regular time interval until 300 s. Inset: Change in fluorescence intensity at 425 nm as a function of time.

TH-2604_156122006

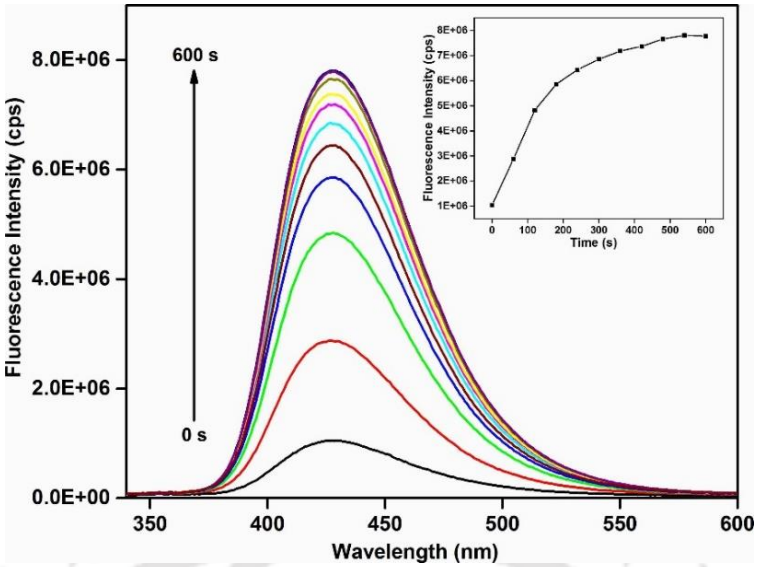

Figure 2.8 Fluorescence *turn-on* response of **1′** (in HEPES buffer) towards the addition of Na_2S at a regular time interval (60 s) up to 600 s. Inset: time-dependence of fluorescence intensity at 425 nm.

Table 2.2 Comparison of the repose time, detection limit and analyte used for H_2S detection for MOFs reported till date.

Sl. No.	MOF	Response Time (s)	Detection Limit	Medium Used	Analyte	Ref.
1.	Al-MIL-53-N_3	180	90.47 nM	H_2O	Na_2S	this work
2.	CAU-10-N_3	420	2.65 µM	HEPES buffer	Na_2S	47
3.	Ce-UiO-66-N_3	760	12.20 µM	HEPES buffer	NaSH	21
4.	Ce-UiO-66-NO_2	760	34.84 µM	HEPES buffer	NaSH	21
5.	Zr-DUT-52-$(NO_2)_2$	3300	20.00 µM	HEPES buffer	Na_2S	48
6.	Zr-UiO-66-N_3	180	118.00 µM	HEPES buffer	Na_2S	49
7.	Zr-UiO-66-NO_2	≈ 460	188.00 µM	HEPES buffer	Na_2S	50
8.	IRMOF-3-N_3	< 120	28.30 µM	HEPES buffer	NaSH	51

TH-2604_156122006

9.	MN-ZIF-90	-	-	PBS buffer	-	52
10.	Al-TCPP-Cu	-	-	BBS buffer	-	53
11.	Al-MIL-101-N_3	-	100 µM	DMSO; HBSS buffer	Na_2S	54
12.	Eu^{3+}/Cu^{2+}@UiO-66-$(COOH)_2$	30	5.45 µM	borate buffer	NaSH	55
13.	Tb^{3+}@Cu-MOF	120	1.20 µM	HEPES buffer	Na_2S	56

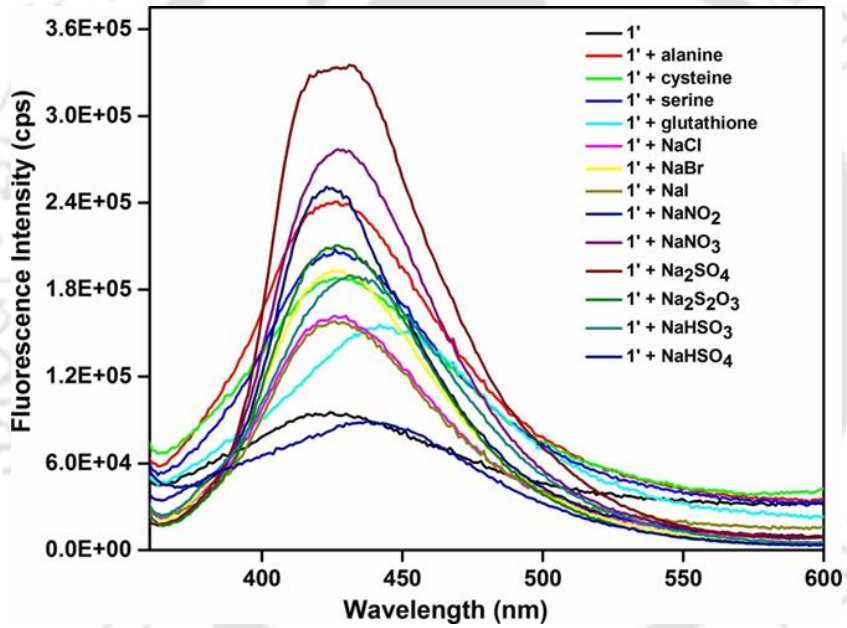

Figure 2.9 Fluorescence response spectra of **1′** in presence of different analytes in water.

TH-2604_156122006

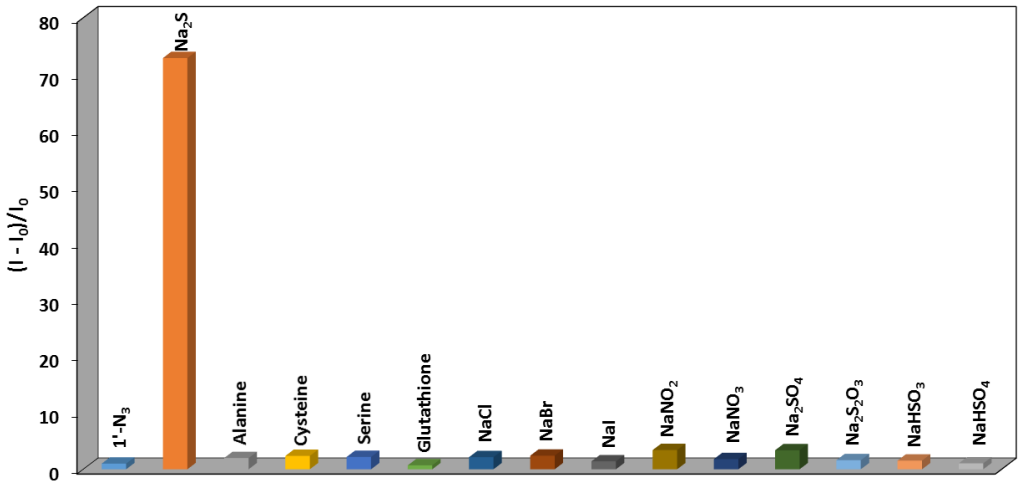

Figure 2.10 Fluorescence responses of **1′** (in aqueous medium) towards the addition of various analytes (10 equiv. per $–N_3$ group).

It is very important for the practical application of an efficient H_2S sensor that it responds towards H_2S even in the presence of potentially disturbing biomolecules and anions. To check the selectivity, the interfering analytes (10 equiv. per $–N_3$ group) were added first to the aqueous dispersion of **1′** and subsequently Na_2S (10 equiv. per $–N_3$ group) was added to the suspension. The fluorescence spectra were recorded after 3 min of Na_2S addition. As shown in Figure 2.11 and Figure 2.12, the MOF probe can recognize H_2S very effectively, even in the presence of the interfering species.

We have examined the influence of Na_2S concentration on the fluorescence response of probe **1′**. For this purpose, fluorescence titration experiments were carried out upon the gradual (0 to 10 equiv.) addition of Na_2S to the aqueous suspension of probe. The fluorescence intensity increased after every addition and there was 76-fold increment in the fluorescence intensity after the addition of 10 equiv. of Na_2S (Figure 2.13). The limit of detection (LOD) was calculated by performing fluorescence titration experiment using less-concentrated (0.01 mM) solution of Na_2S. The plot of fluorescence intensity against the concentration of Na_2S exhibits a linear curve (Figure 2.14). The slope of the curve was found to be 9.32×10^7. The LOD was calculated using the equation: $LOD = 3S_b/S$, where S denotes the slope of the curve and S_b is the standard deviation for repetitive measurements of the aqueous suspension in the absence of the probe. The estimated LOD in aqueous medium was 90.47 nM. The H_2S concentration in the biological systems ranges from nanomolar to milimolar levels.[57] Thus, the probe might be able to detect H_2S present

TH-2604_156122006

in the biological medium. The LOD of the Al-MIL-53-N_3 compound in the aqueous medium is lower than any other existing MOF type of H_2S sensors (Table 2.2). The XRPD experiments (Figure 2.15) unambiguously verify that the framework structure of the compound was preserved after the sensing of H_2S.

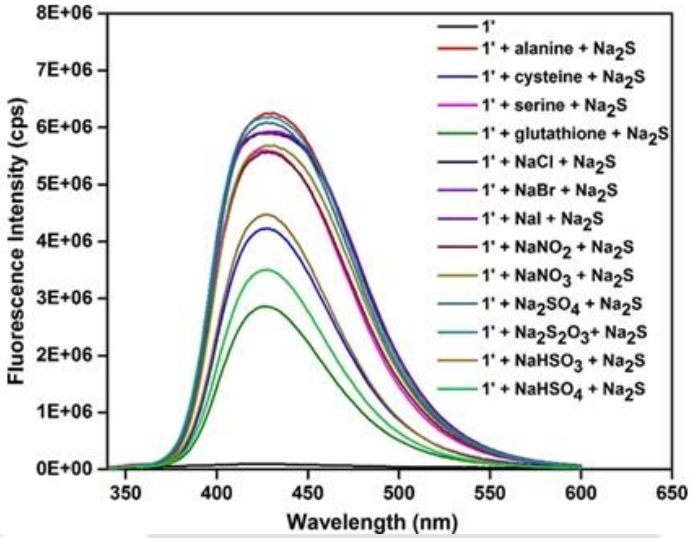

Figure 2.11 Fluorescence response spectra of **1′** towards Na_2S in presence of other interfering analytes in water.

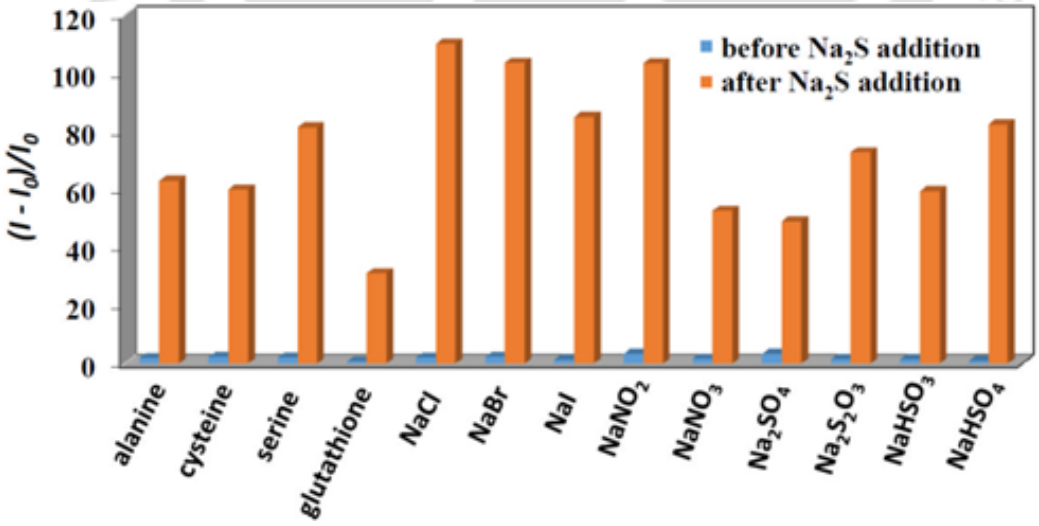

Figure 2.12 Fluorescence responses of **1′** (in aqueous medium) towards the addition of different competing analytes (blue), followed by the addition of Na_2S (orange).

TH-2604_156122006

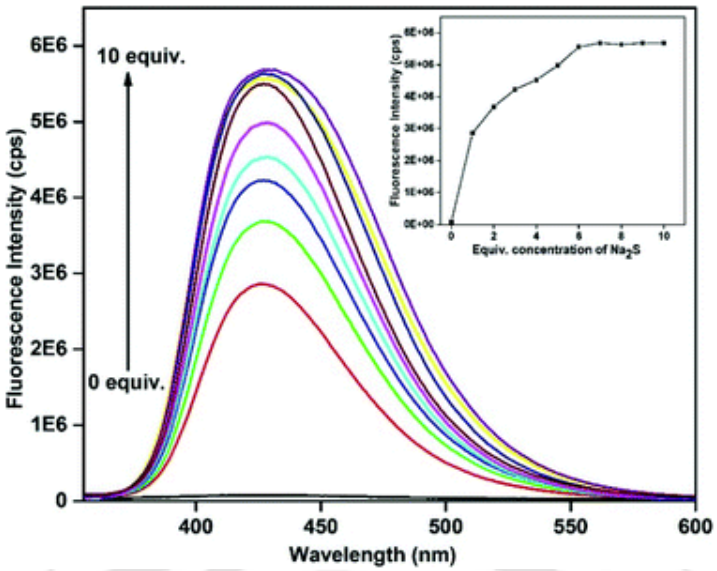

Figure 2.13 Change in the fluorescence intensity of **1′** (in aqueous medium) with increasing concentration of Na_2S (up to 10 equiv.).

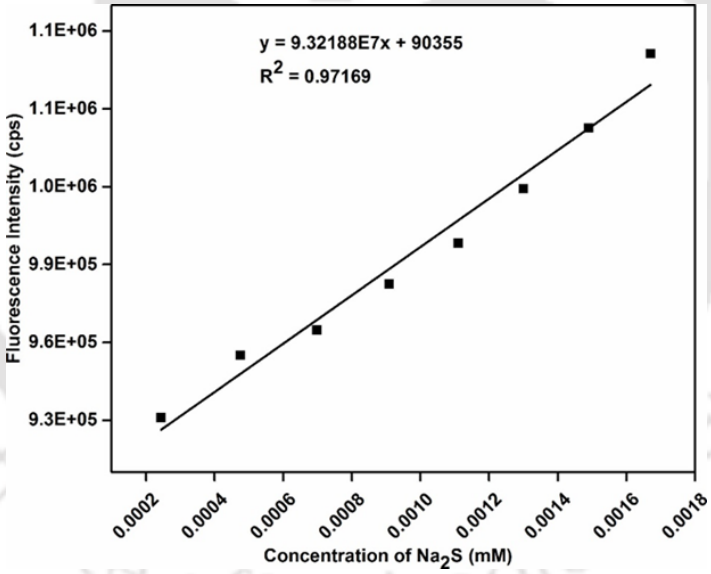

Figure 2.14 Change in the fluorescence intensity of **1′** in aqueous suspension as a function of Na_2S concentration.

TH-2604_156122006

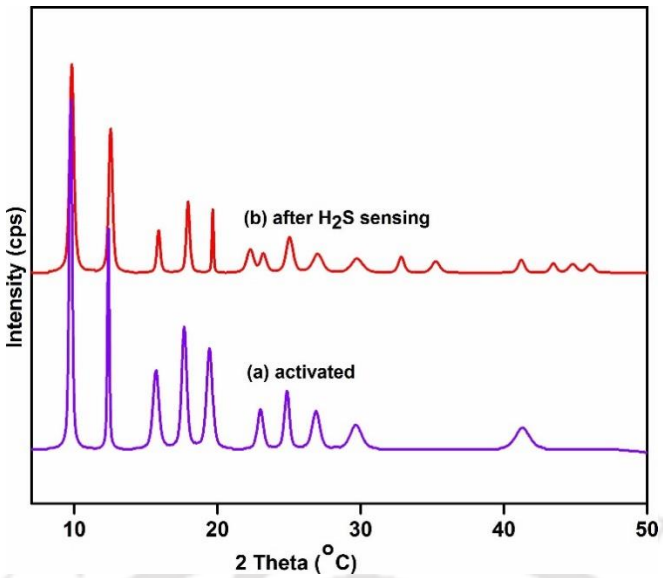

Figure 2.15 XRPD patterns of **1** in different forms: (a) before and (b) after sensing of H_2S in water medium.

2.3.7 Mechanism for H_2S Sensing in the Aqueous Medium

We have performed control experiments for H_2S sensing with the analogous Al-MIL-53 MOF (without any attached functional group) in aqueous medium. The experiment showed fluorescent *turn-off* responses when Al-MIL-53 was treated with Na_2S (Figure 2.16). These results indicated that not the main Al-MIL-53 framework rather the azide moiety was responsible for the *turn-on* response when **1′** was treated with Na_2S.

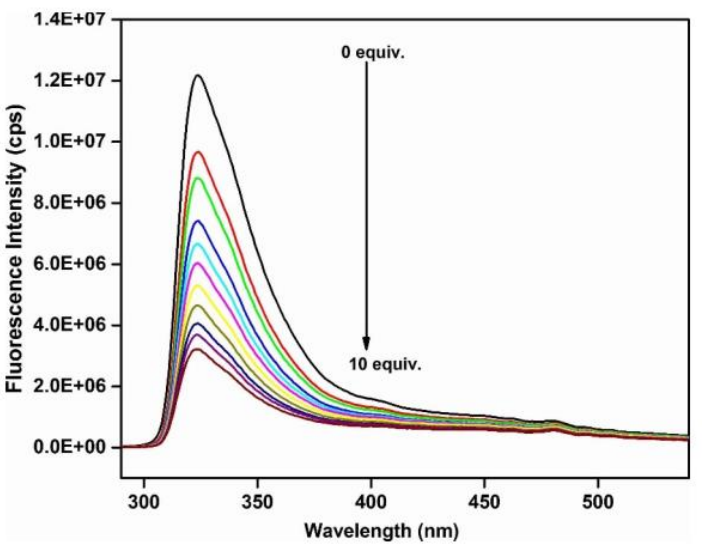

Figure 2.16 Change in fluorescence intensity of unfunctionalized-Al-MIL-53 (in aqueous medium) with increasing concentration of Na_2S (up to 10 equiv.).

TH-2604_156122006

Various experimental techniques such as mass spectrometry, FT-IR and NMR spectroscopic analyses were utilized in order to establish the H_2S sensing mechanism by the Al-MIL-53-N_3 probe. FT-IR spectrum was recorded after treatment of **1'** with H_2S. The Na_2S-treated probe did not contain any peak (at 2125 cm^{-1}) for the attached $–N_3$ functionality in its IR spectrum (Figure 2.17). It becomes evident from the IR analysis that the grafted $–N_3$ group has undergone reaction with Na_2S. The digested sample of **1'** (without reaction with Na_2S) showed an intense peak at m/z = 206.1883 in its mass spectrum (Figure 2.18). This peak can be assigned to $(M{-}H)^-$ ion, where M denotes the mass of $H_2BDC\text{-}N_3$ linker. The mass spectrum of the Na_2S-treated probe was also measured after digestion. In this mass spectrum (Figure 2.19), an intense peak at m/z = 181.0206 was observed. This peak can be accounted for the $(M{-}H)^-$ ion of the reduced form of $H_2BDC\text{-}N_3$, i.e. $H_2BDC\text{-}NH_2$ linker. The absence of any peak (at m/z = 206.1883) for the $H_2BDC\text{-}N_3$ linker in the mass spectrum of the digested sample of Na_2S-treated **1'** indicates that the grafted $–N_3$ groups have been completely converted (by reduction mechanism) to the $–NH_2$ functionalities in presence of Na_2S. The H_2S sensing mechanism by **1'** was further supported by the ^1H NMR experiments (Figure 2.20). The peaks at 7.89, 8.32 and 8.48 ppm for non-treated **1'** can be assigned to the three non-equivalent aromatic protons of the $H_2BDC\text{-}N_3$ linker. For Na_2S-treated **1'**, the appearance of a new peak at 10.07 ppm is observed in combination with the peaks (at 7.40, 7.84 and 7.99 ppm) for the three non-equivalent aromatic protons, which are shifted towards the upfield region. This newly observed peak can be ascribed to the protons for the $–NH_3^+$ group attached with the protonated form of $H_2BDC\text{-}NH_2$ linker.[25] The upfield shift of the peaks for the three aromatic protons occurs owing to the conversion of the electron-withdrawing $–N_3$ groups to the electron-donating $–NH_2$ groups. The outcomes of IR, mass and NMR analyses clearly confirm that the framework BDC-N_3 linker is fully converted (through reduction process) to the BDC-NH_2 linker during the H_2S sensing event.

TH-2604_156122006

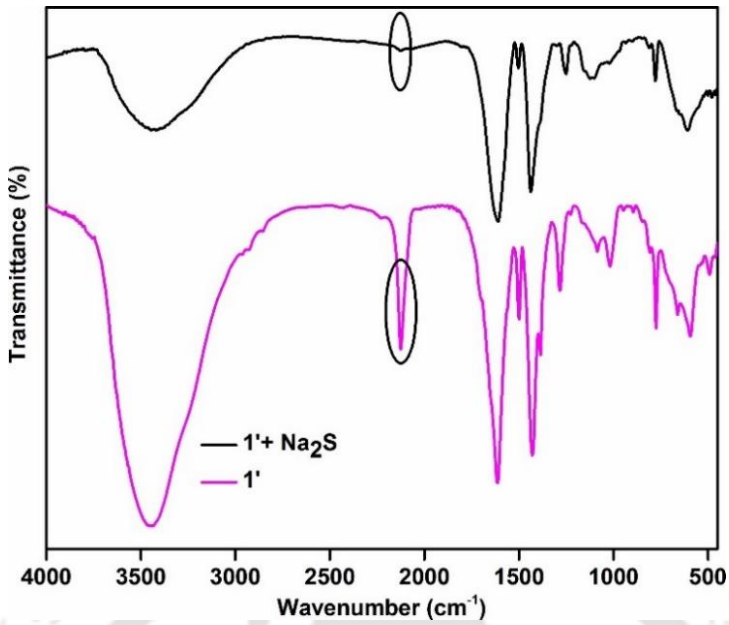

Figure 2.17 FT-IR spectra of **1'** (a) before and (b) after treatment with Na_2S. The absorption band for the $–N_3$ group is high-lighted by the black ovals.

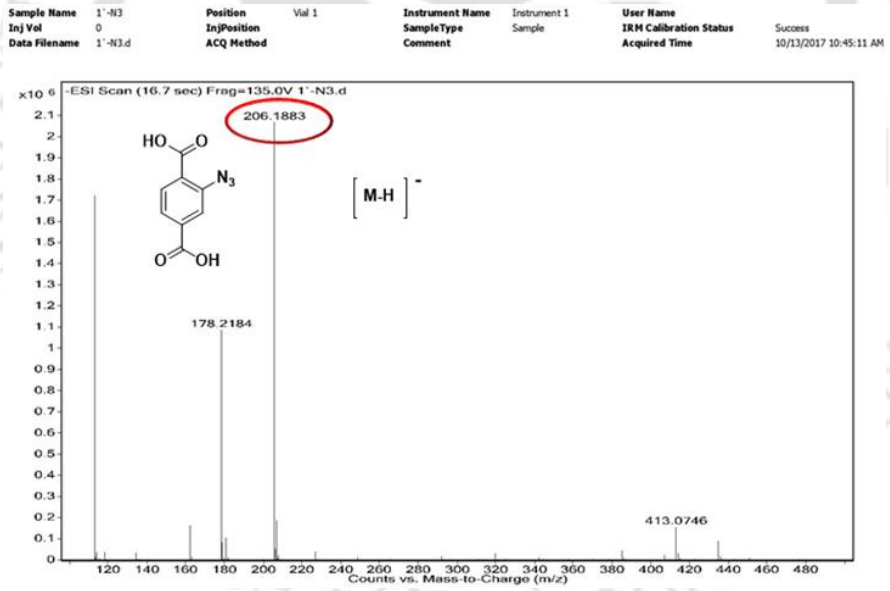

Figure 2.18 HR-MS spectrum of **1′** after digestion in MeOH/HF. The spectrum shows m/z (negative ion mode) peak at 206.1883 (negative ion mode), which corresponds to $(M-H)^-$ ion (M = mass of $H_2BDC\text{-}N_3$ linker).

TH-2604_156122006

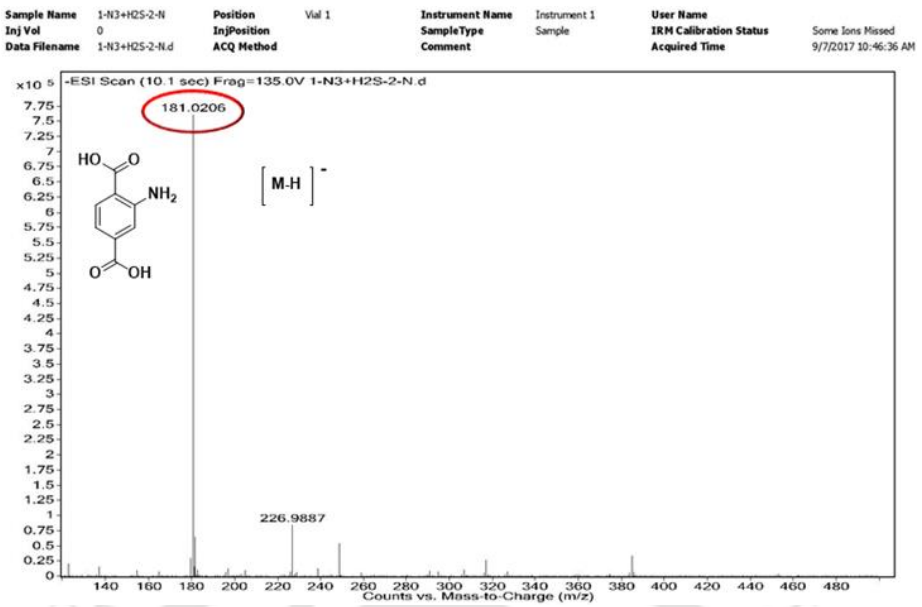

Figure 2.19 HR-MS spectrum of Na_2S-treated **1′** after digestion in MeOH/HF. The spectrum shows m/z (negative ion mode) peak at 181.0206 which correspond to $(M-H)^-$ ion of reduced $H_2BDC\text{-}N_3$ i.e. $H_2BDC\text{-}NH_2$ linker.

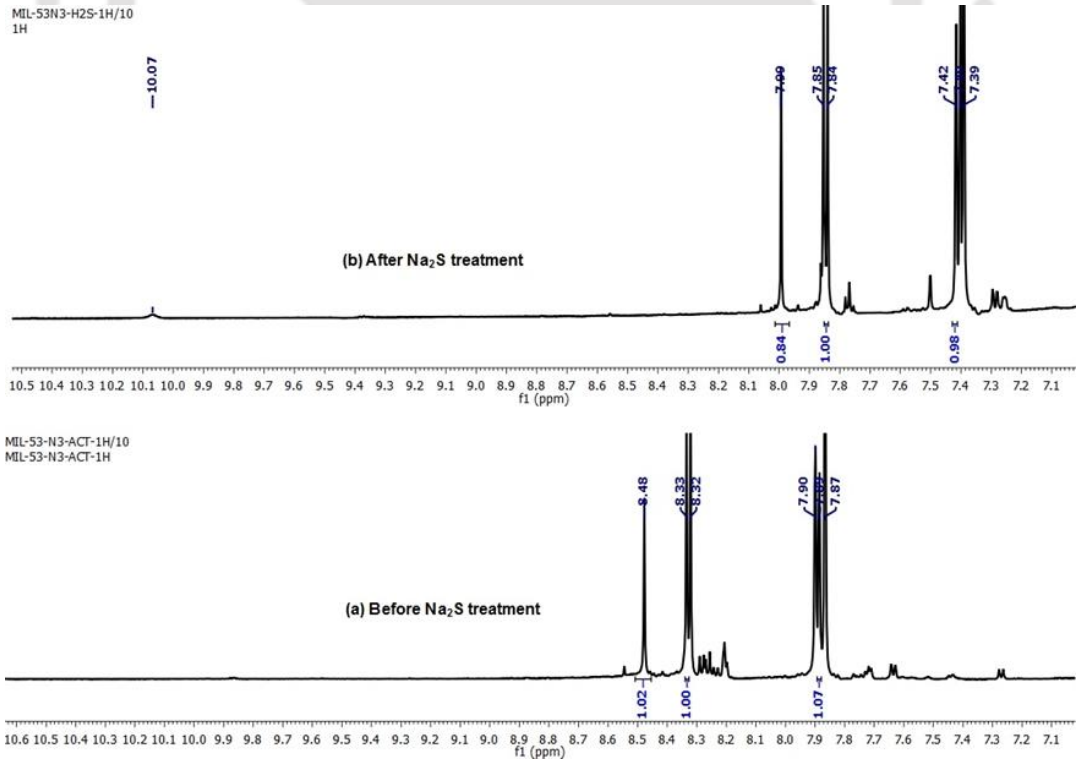

Figure 2.20 ^1H NMR spectra of (a) **1′** and (b) Na_2S-treated **1′** after digestion in DMSO-d_6/HF. In the spectrum of Na_2S-treated **1′**, a new peak appears at 10.07 ppm, which can be

TH-2604_156122006

assigned to the protons for the–NH_3^+ group attached with the protonated form of H_2BDC-NH_2 linker.

2.3.8 H_2S Sensing in HBP

Since the Al-MIL-53-N_3 compound exhibited fast response and extraordinary sensitivity for the recognition of H_2S in aqueous medium, we subsequently decided to employ the probe in a relatively complicated sensing medium such as HBP. For fulfilling this purpose in practice, the internal standard addition technique was utilized. The HEPES suspension of **1′** was treated with Na_2S-spiked HBP samples having four different concentrations (0.0, 0.5, 5.0, 50.0 μM). Upon continuing addition of Na_2S-spiked HBP to the suspension of **1'** in HEPES buffer, gradual enhancement in the fluorescence intensity was observed (Figure 2.21). It becomes unequivocal from these results that that probe **1′** can detect H_2S in HBP.

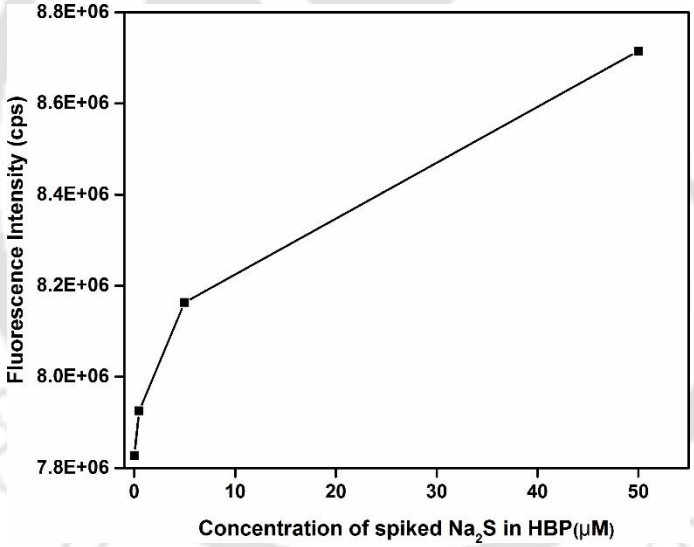

Figure 2.21 Fluorescence response of **1′** in presence of Na_2S-spiked human blood plasma.

2.3.9 H_2S Sensing in Living Cells

Compound **1′** showed very fast and outstanding sensitivity for the sensing of extracellular H_2S in the aqueous medium. Inspired by these features of the probe, we decided to check its capability to recognize intracellular H_2S through live-cell imaging study. The cellular imaging investigation was carried out in J774A.1 macrophage cells. The probe (25 μM) was internalized into the macrophage cells and then the cells were treated with Na_2S solution (5 μM). This process generates the intracellular H_2S. When

TH-2604_156122006

observed in bright field, the untreated cells exhibited good morphology (Figure 2.22a). For these cells, no fluorescence was noticed in the blue channel (Figure 2.22b). After loading the cells with the probe only, decent morphology and very weak background fluorescence were observed in the bright field and blue channel, respectively (Figure 2.22c-d). Very interestingly, the probe-loaded cells exhibited bright blue fluorescence signal after incubation with Na_2S (Figure 2.22f). The observation of these cells in the bright field also revealed good morphology (Figure 2.22e). Based on the above observations, it can be deduced that the Al-MIL-53-N_3 probe is capable for recognizing intracellular H_2S.

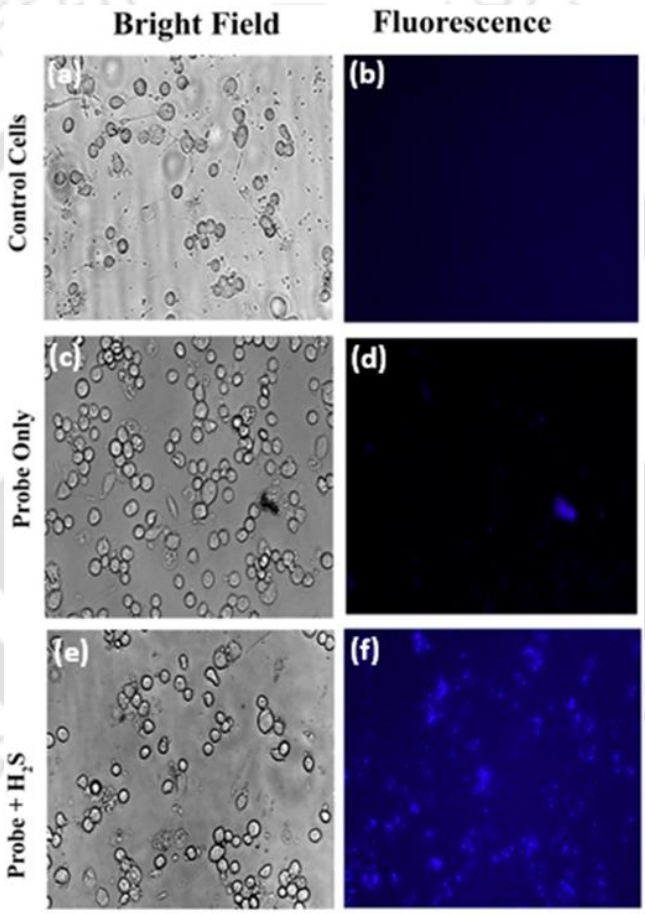

Figure 2.22 Intracellular fluorescence behaviour of **1′** exposed to H_2S (produced by Na_2S treatment) in macrophage J774A.1 cells: the cells were incubated overnight with [(c) and (e)] and without probe (a). The cells exposed to Na_2S showed bright fluorescence (f) or negligible basal fluorescence (d). The cells without **1′** display no background fluorescence (b). The **1′**-treated cells show no morphological abnormalities. Cell imaging in HEK 293 cells: the cells were seeded in 96 well plates. The procedure was similar to the cell imaging in J774A.1 cells. The fluorescence images and bright field images were collected from

TH-2604_156122006

randomly chosen fields. The cells exposed to Na_2S show bright fluorescence (l) as compared to the only probe-treated cells (j).

2.3.10 Sulfide Sensing in Real Water Samples

The ability of **1′** to detect sulphide was examined in three types of real water samples: tap, mineral and lake water. The nine water samples consisted of three samples of the same type. These water samples were spiked with Na_2S solutions having specified concentrations. The tap, mineral and lake water were spiked with known concentration of Na_2S. The MOF was suspended in milli-Q water. Then, the fluorescence spectra of MOF suspension were recorded. Afterward, a definite volume of Na_2S-spiked water was added to the MOF suspension inside the cuvette and the fluorescence spectra were recorded. The same experiment was performed thrice for every concentration of spiked Na_2S. From the obtained data and following formula, % of recovery = (concentration of Na_2S spiked × 100)/ concentration of Na_2S observed. For calculating the observed concentration of Na_2S, the LOD curve was considered as reference. After the spike-and-recovery experiment, the concentrations of Na_2S found as well as the recovery percentages in the real water samples are summarized in Table 2.3. In case of all the samples, the recovery percentages for Na_2S fall in the range of 95-105%. In addition, the RSD (RSD = SD/mean value × 100; SD = standard deviation) values range from 0.81 to 5.01. Thus, good percent of recovery and low RSD values were obtained after the analysis of sulphide concentration in different types of environmental water samples. Therefore, it can be inferred that the Al-MIL-53-N_3 compound is suitable for analyzing sulfide concentration in real water samples.

Table 2.3 Detection performance of H_2S in water samples by **1′**.

Na_2S Spiked (nM)	Mineral Water		Tap Water		Lake Water	
	Na_2S Found[a] (nM)	Recovery (%)	Na_2S Found[a] (nM)	Recovery (%)	Na_2S Found[a] (nM)	Recovery (%)
100	98.01±	98.01	105.43±	105.43	98.70±	98.70

TH-2604_156122006

	0.81		2.47		2.07	
200	192.00± 3.74	96.00	191.90± 2.96	95.95	189.62± 1.58	94.81
300	288.09± 5.01	96.03	287.04± 1.08	95.68	290.31± 3.63	96.77

[a] Na_2S found ± RSD (n = 3)

2.3.11 Detection of Fe(III) Ion in Aqueous Medium

Fe(III) ion is a very good fluorescence quencher, which can easily capture electron density from electron-rich species.[58-60] The un-functionalized Al-MIL-53 compound has been formerly studied for the sensing of Fe(III) ion.[8] It has been shown that the Al(III) ions of the Al-MIL-53 compound are partially replaced by the Fe(III) ions, without affecting the structural robustness of the framework. Based on this cation-exchange process, the MOF compound displayed fluorescent *turn-off* behavior in the presence of Fe(III) ions. Considering the fact that the electron-withdrawing $–N_3$ groups might affect the Fe(III) sensing characteristics, we have studied the performance of the Al-MIL-53-N_3 compound for the fluorescence sensing of Fe(III) ions in aqueous medium.

For investigating the fluorescence sensing ability of **1′**, we have performed fluorescence titration experiments, in which we have gradually added 2 mM aqueous solutions of nitrate salts of different metal ions (Na^+, K^+, Ag^+, Co^{2+}, Ni^{2+}, Cu^{2+}, Zn^{2+}, Cd^{2+}, Hg^{2+}, Al^{3+}, Cr^{3+} and Fe^{3+}) to the aqueous dispersion of the compound. After the every addition (25 µL), the fluorescence spectra were recorded. After the addition of 150 µL of 2 mM Fe(III) solution, there was considerable decrease in the fluorescence intensity of **1′** (Figure 2.23a). On the contrary, the fluorescence intensity changed slightly upon the addition of the rest of metal ions. For Fe(III) ion, the fluorescence quenching efficiency was 93%, whereas the remaining metal ions (Figure 2.23a and Figure 2.23b) showed significantly lower quenching efficiencies (range: 4-38%). These fluorescence titration results reveal that the Al-MIL-53-N_3 compound is highly selective for the sensing of Fe(III) ion over other metal ions in the aqueous medium.

TH-2604_156122006

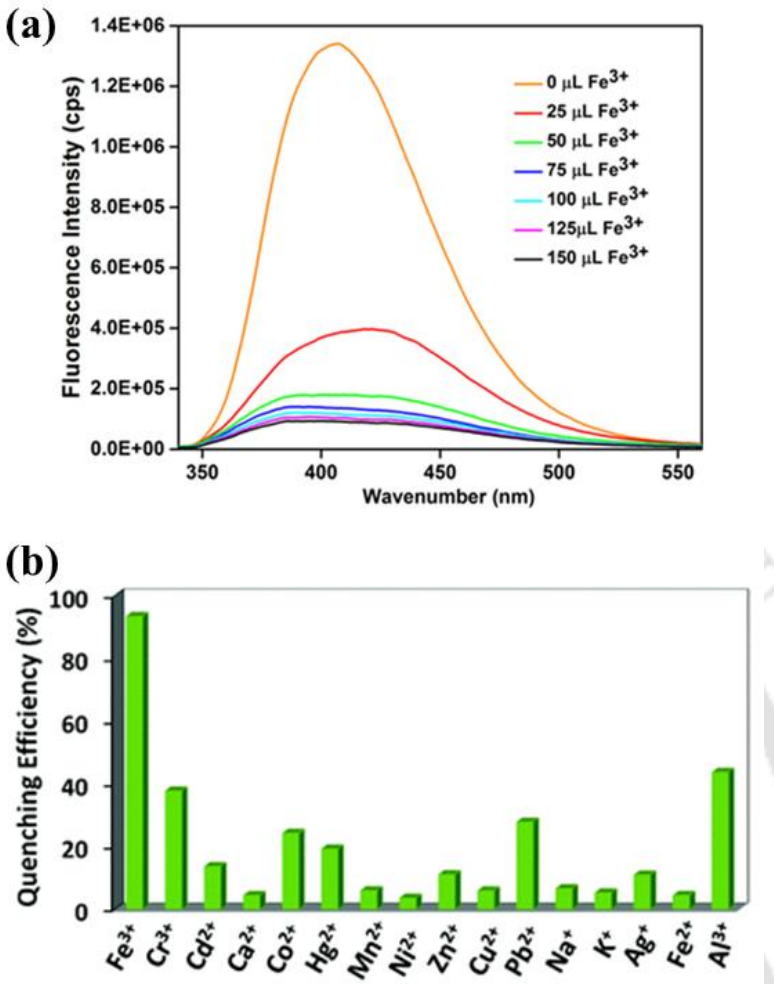

Figure 2.23 (a) Quenching of the fluorescence intensity of **1′** by incremental addition of 2 mM Fe(III) solution to a 3 mL stable suspension of **1′** in water. (b) Fluorescence quenching efficiencies upon the addition of 150 μL of different metal ions (2 mM) to a 3 mL suspension of **1′**.

To explore the selectivity of the probe for Fe(III) in the presence of other metal ions, we have performed fluorescence experiments in which we have added aqueous solutions of different metal ions independently to the well-dispersed aqueous suspension of **1′** in a quartz cuvette. Subsequently, an aqueous solution of Fe(III) ion was added to the same cuvette and the fluorescence spectra were collected (Figure 2.24). There were no noticeable changes in the fluorescence quenching efficiency of Fe(III) ion in the presence of different metal ions. These observations imply that the Al-MIL-53-N_3 probe can recognize Fe(III) ion selectively even when other metal ions are present in the same medium.

TH-2604_156122006

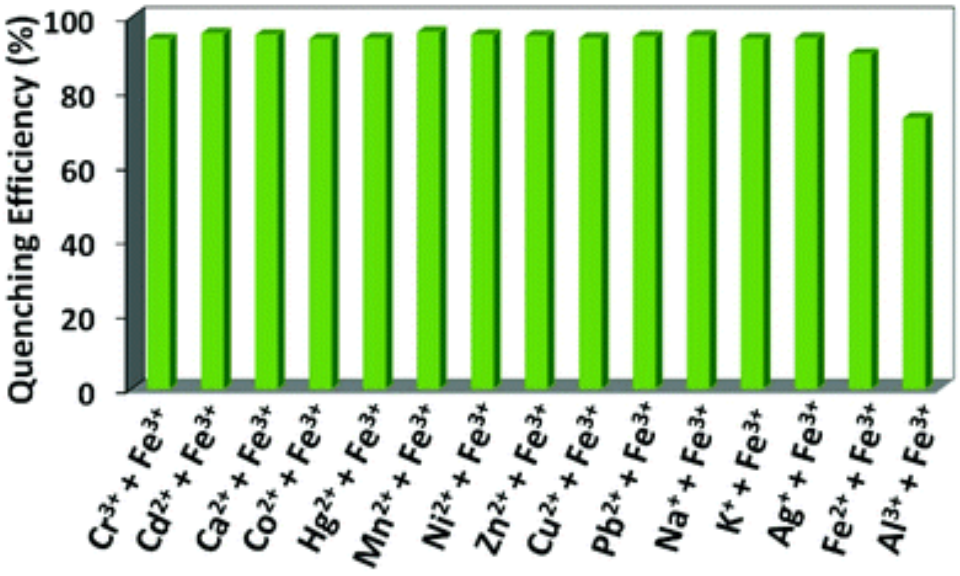

Figure 2.24 Fluorescence quenching efficiencies of Fe(III) ion towards **1′** in presence of other interfering metal ions.

The Stern-Volmer (S-V) equation was employed for calculating the quenching constant (K_{sv}) for Fe(III) sensing.[26] The K_{sv} value was found to be 6.13×10^{-3} M^{-1} which is comparable with those of the existing MOF probes for Fe(III) ion (Table 2.4). The S-V plots for all the metal ions are shown in Figure 2.25. These plots are almost linear for all the metal ions, except Fe(III). In case of Fe(III) ion, the S-V plot shows linearity in the lower concentration range and non-linearity in the higher concentration range. The S-V plot of this kind points out the presence of both dynamic and static quenching mechanisms for Fe(III) sensing process. To distinguish between the two quenching mechanisms, time-resolved fluorescence decay measurements were conducted. The results of these experiments are shown in Figure 2.26 and Table 2.5. In the absence and presence of 150 µL of 2 mM Fe(III) solution, the average excited-state lifetime values of **1′** were determined as 7.62 and 3.38 ns, respectively. Hence, the fluorescence quenching behavior in this system follows dynamic mechanism.

TH-2604_156122006

Table 2.4 A comparison of the Stern-Volmer constant (K_{sv}), detection limit and medium used for the sensing of Fe^{3+} ion for MOFs reported till date.

Sl. No.	MOF	K_{sv} ($\times 10^4$ M^{-1})	Detection Limit	Medium Used	Ref.
1.	Al-MIL-53-N_3	61.32	0.03 µM	water	this work
2.	Al-MIL-53	-	0.90 µM	PBS buffer	61
3.	$[Zr_6O_4(OH)_4(2,7\text{-}CDC)_6]\cdot 19H_2O\cdot 2DMF$	0.55	0.91 µM	water	26
4.	$[La(TPT)(DMSO)_2]\cdot H_2O$	1.36	-	ethanol	62
5.	$[H(H_2O)_8][DyZn_4(imdc)_4(im)_4]$	2.88	-	DMSO	63
6.	EuL_3	0.41	100.0 µM	ethanol	64
7.	$[Eu_2(MFDA)_2(HCOO)_2(H_2O)_6]\cdot H_2O$	-	0.33 µM	DMF	65
8.	$[Cd(H_2L_a)_{0.5}(H_2L_b)_{0.5}(H_2O)]$	-	10.0 µM	water	66
9.	$[(CH_3)_2NH_2]\cdot[Tb(bptc)]\cdot x$solvent	-	72.76 ppm	ethanol	67

TH-2604_156122006

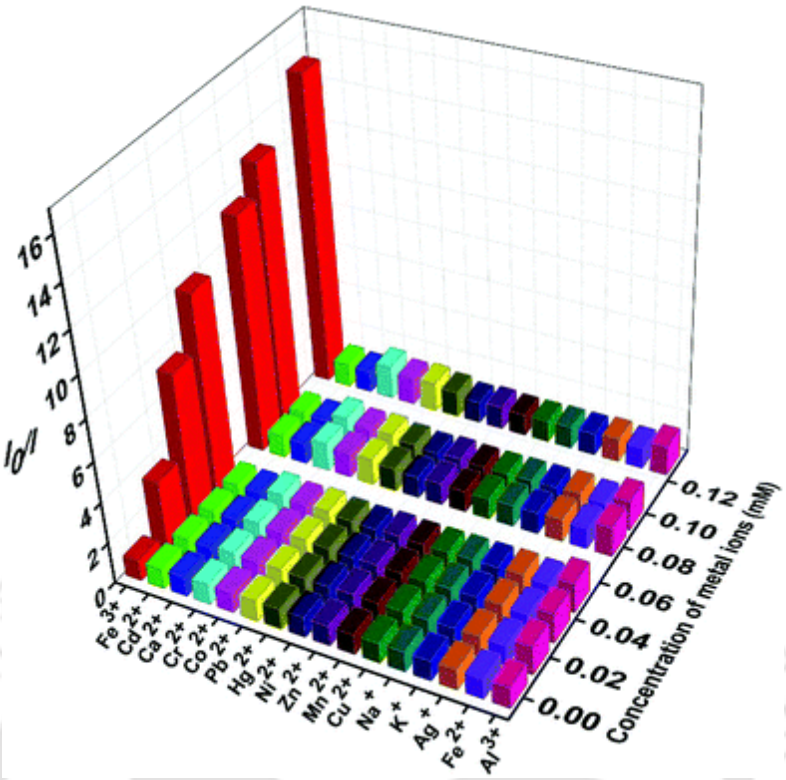

Figure 2.25 3D Stern-Volmer plots obtained for various metal ions.

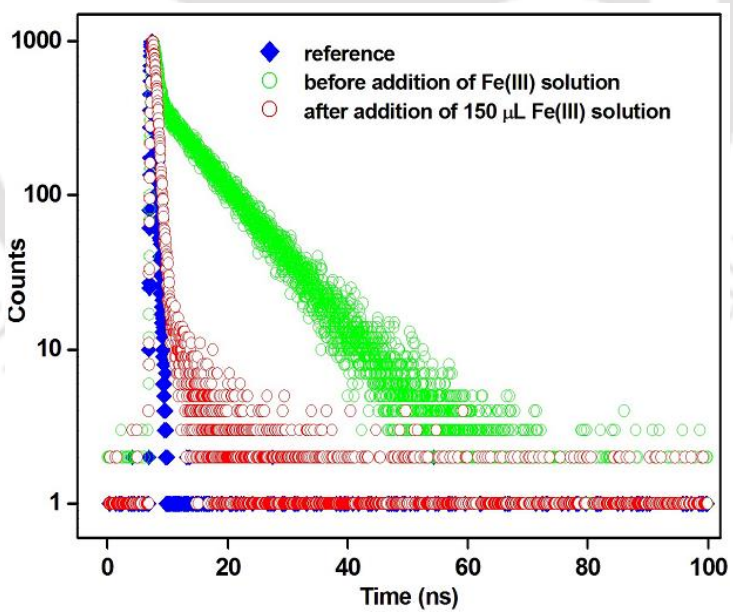

Figure 2.26 Lifetime decay profile of **1′** before and after addition of 150 μL of 2 mM Fe^{3+} solution.

The LOD for Fe(III) ion was determined by the procedure reported earlier by us.[26] The estimated LOD for Fe(III) ion corresponds to 0.03 μM, which is lower than many of the

TH-2604_156122006

previously reported MOF type sensors for Fe(III) ion including the Al-MIL-53 compound (Table 2.4).

The recyclability of **1′** was investigated up to three cycles of sensing experiments. The compound was filtered off after each sensing experiment (150 μL of 2 mM Fe(III) solution), washed with water repeatedly and then employed in the next sensing experiment (150 μL of 2 mM Fe(III) solution). The Al-MIL-53-N_3 material could recover 81% and 59% of its original fluorescence intensity after the second and third sensing experiments, respectively (Figure 2.27). Hence, the fluorescent probe exhibited poor recyclability of its quenching efficiency towards Fe(III) ion. However, the XRPD experiments (Figure 2.28) revealed that that the crystallinity of **1′** remained unaffected after the Fe(III) sensing experiment. The results from the recyclability experiments are similar with the un-functionalized Al-MIL-53 material.[8] The poor recyclability of the probe can be attributed to the partial replacement of the framework Al(III) ions by the Fe(III) ions during the sensing process (*cf.* next section).

Table 2.4 Average excited state lifetime (<τ>) values of **1′** before and after addition of 150 μL of 2 mM Fe^{3+} solution (λ_{ex} = 308 nm).

Volume of Fe^{3+} solution added (μL)	B_1	B_2	a_1	a_2	τ_1 (ns)	τ_2 (ns)	<τ>* (ns)	χ^2
0	0.067	0.014	0.183	0.817	0.443	9.222	7.62	0.997
150	0.098	0.001	0.919	0.806	0.437	3.699	3.38	0.960

TH-2604_156122006

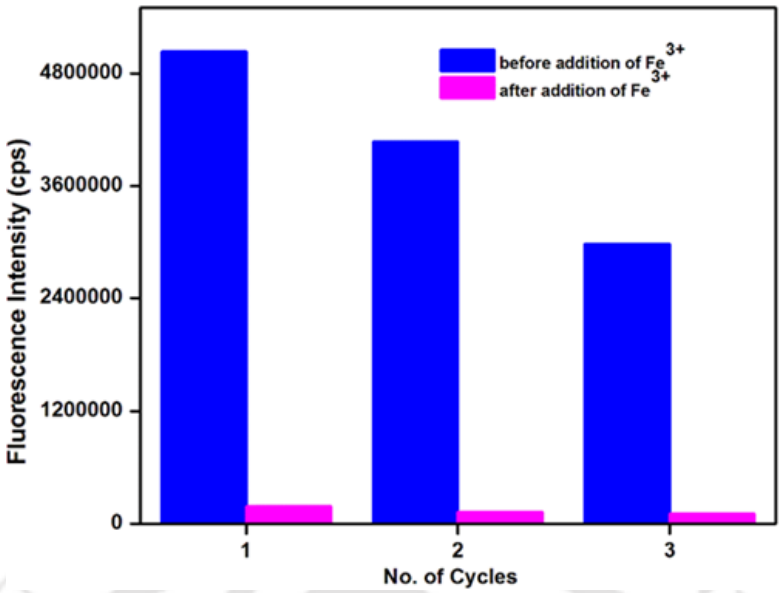

Figure 2.27 Reproducibility of the fluorescence quenching efficiency of the aqueous suspension of **1′** towards 2 mM Fe^{3+} solution.

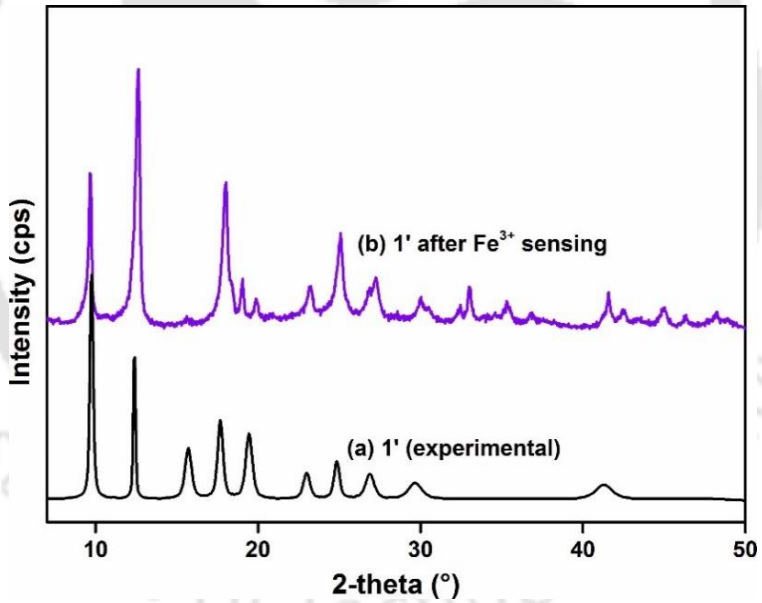

Figure 2.28 XRPD patterns of **1′** (a) before and (b) after sensing of Fe^{3+} ion in water medium.

2.3.12 Mechanism for Fe(III) Sensing

According to the literature, mainly two possible mechanisms can govern the Fe(III) detection process. They are: (i) ion-exchange reaction between the framework metal ions with Fe(III) and (ii) interactions[27] of the framework linkers with the Fe(III) ions. The complete ion-exchange reaction can lead to destruction of the framework.[19] On the other

TH-2604_156122006

side, the partial ion-exchange process can still retain the framework structure.[8] Since the –N_3 groups anchored with the linkers can not have strong interactions with the Fe(III) ions, the second mechanism is less likely to influence the detection process. As shown in Figure 2.24, the XRPD patterns of **1′** before and after the Fe(III) sensing experiment are very similar. Thus, the possibility of the structural collapse due to complete ion-exchange can be excluded. To explore the probability of partial ion-exchange mechanism, we have conducted EDX experiments. The EDX spectrum (Figure 2.29) of **1′** obtained after treatment with 2 mM Fe(III) solution confirms that ~1.7% Al(III) ions are replaced by Fe(III) under the experimental sensing conditions. Therefore, the EDX results support the partial ion-exchange mechanism for Fe(III) sensing. The same mechanism has been also proposed recently for the Fe(III) sensing by the pristine Al-MIL-53 compound.[8] We recorded the UV-vis spectra of all the metal ions in water and observed that there is considerable overlap between the absorption spectrum of Fe(III) ions and the emission spectrum of **1′** (Figure 2.30). The spectral overlap is negligible for the interfering metal ions. These results suggest that resonance energy transfer occurs from electron-rich **1′** to electron-deficient Fe(III) ions.[52] Hence, both partial ion-exchange and energy transfer mechanisms can be attributed to the fluorescence quenching of **1′** during Fe(III) sensing.

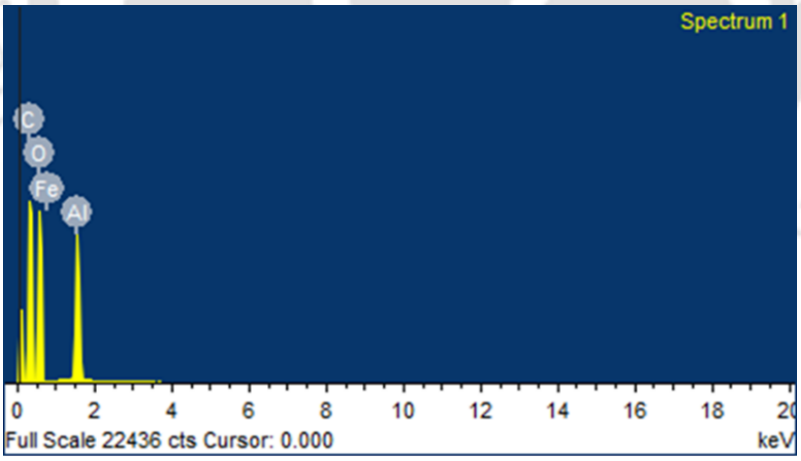

Element	Weight%	Atomic%
C K	41.35	50.69
O K	46.53	42.82
Al K	11.70	6.38
Fe K	0.42	0.11
Total	100.00	100.00

Figure 2.29 EDX spectrum of **1′** after treatment with 2 mM Fe^{3+} aqueous solution.

TH-2604_156122006

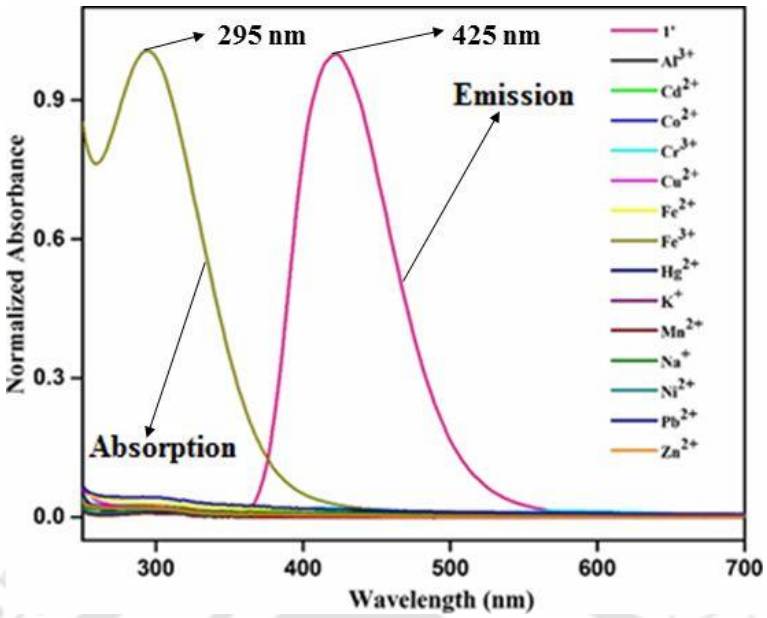

Figure 2.30 Spectral overlap between the absorption spectra of different metal ions and the emission spectra of **1′** in water.

2.4 Conclusions

A highly stable Al(III) MOF compound called Al-MIL-53-N_3 has been prepared under solvothermal conditions. The compound has been characterized comprehensively. It is the first example of an azide-functionalized MOF compound which acts as a dual-functional sensor for H_2S as well as Fe(III) ion in the aqueous medium. From the thermogravimetric (TG) analysis, it has been observed that the compound is thermally stable up to 300 °C. The activated compound **1′** exhibits high CO_2 adsorption capacity (7.2 wt%) at 25 °C and 1 bar. From the fluorescence sensing experiments, it has been found that **1′** is highly selective towards H_2S (*turn-on* mechanism) and Fe(III) ion (*turn-off* mechanism) in aqueous medium even in the presence of potentially intrusive species. The fluorescence microscopic images unveil that the J774A.1 macrophage cells incorporating the probe exhibits bright blue florescence after treatment with Na_2S. Moreover, the compound has been found suitable for detecting H_2S in human blood plasma and determining sulfide concentration in real water samples. The LOD values for H_2S and Fe(III) ion in the aqueous medium are 90.47 nM and 0.03 µM, respectively. These values lie in the range of concentration of H_2S and Fe(III) ions in biological systems. Furthermore, the LOD values for H_2S and Fe(III) ion are lower than the literature values for other MOFs. The reduction of azide to amine functionality can be accounted for the fluorescence increment behavior

TH-2604_156122006

of **1′** in presence of H_2S. On the other hand, the partial replacement of the Al(III) ions of the framework by Fe(III) is responsible for the fluorescent *turn-off* properties in the existence of Fe(III) ion. The unprecedented sensitivity, high selectivity as well as quick response of the Al-MIL-53-N_3 probe will make it a potential bifunctional probe for the practical recognition of Fe(III) ion as well as sensing of in vitro and in vivo H_2S (via cellular imaging).

2.5 References

1. R.-Z. Wu, X. Yang, L.-W. Zhang and P.-P. Zhou, *Dalton Trans.*, 2017, **46**, 9859-9867.
2. A. Dhakshinamoorthy, M. Alvaro and H. Garcia, *Appl. Catal., A*, 2010, **378** 19–25.
3. B. Li, H.-M. Wen, W. Zhou and B. Chen, *J. Phys. Chem. Lett.* , 2014, **5**, 3468−3479.
4. J.-R. Li, R. J. Kuppler and H.-C. Zhou, *Chem. Soc. Rev.* , 2009, **38**, 1477–1504.
5. C. Orellana-Tavra, E. F. Baxter, T. Tian, T. D. Bennett, N. K. H. Slater, A. K. Cheetham and D. Fairen-Jimenez, *Chem. Commun.* , 2015, **51**, 13878-13881.
6. S. Nandi, E. Sharma, V. Trivedi and S. Biswas, *Inorg. Chem.*, 2018, **57**, 15149-15157.
7. K. Müller-Buschbaum, F. Beuerle and C. Feldmann, *Micropor. Mesopor. Mat.*, 2015, **216**, 171-199.
8. C. Yang, H. Ren and X. Yan, *Anal. Chem.*, 2013, **85**, 7441-7446.
9. S. Nandi, H. Reinsch, S. Banesh, N. Stock, V. Trivedi and S. Biswas, *Dalton Trans.*, 2017, **46**, 12856-12864.
10. C. Liu and B. Yan, *Sens. Actuators, B*, 2016, **235**, 541–546.
11. F. M. Hinterholzinger, B. Ruhle, S. Wuttke, K. Karaghiosoff and T. Bein, *Sci. Rep.*, 2013, **3**, 2562-2568.
12. X.-Y. Xu and B. Yan, *Dalton Trans.*, 2016, **45**, 7078-7084.
13. J. Li, C. Yin and F. Huo, *RSC Adv.*, 2015, **5**, 2191–2206.
14. B. Doujaiji and J. A. Al-Tawfiq, *Ann Saudi Med.*, 2010, **30**, 76-80.
15. K. Eto, T. Asada, K. Arima, T. Makifuchi and H. Kimura, *Biochem. Biophys. Res. Commun.*, 2002, **293**, 1485–1488.

TH-2604_156122006

16. M. Seyama, Y. Iwasaki, S. Ogawa, I. Sugimoto, A. Tate and O. Niwa, *Anal. Chem.*, 2005, **77**, 4228-4234.
17. I. Andreadou, E. K. Iliodromitis, T. Rassaf, R. Schulz, A. Papapetropoulos and P. Ferdinandy, *Br. J. Pharmacol.*, 2015, **172**, 1587-1606.
18. X.-H. Zhou, L. Li, H.-H. Li, A. Li, T. Yanga and W. Huang, *Dalton Trans.*, 2013, **42**, 12403-12409.
19. S. Dang, E. Ma, Z. Sun and H. Zhang, *J. Mater. Chem.*, 2012, **22**, 16920–16926.
20. A. Rose, Z. Zhu, C. F. Madigan, T. M. Swager and V. Bulovic, *Nature*, 2005, **434**, 876-879.
21. A. Buragohain and S. Biswas, *CrystEngComm*, 2016, **18**, 4374–4381.
22. R. Dalapati, S. N. Balaji, V. Trivedi, L. Khamari and S. Biswas, *Sens. Actuators, B*, 2017, **245**, 1039–1049.
23. A. Legrand, A. Pastushenko, V. Lysenko, A. Geloen, E. A. Quadrelli, J. Canivet and D. Farrusseng, *ChemNanoMat*, 2016, **2**, 866 –872.
24. X. Zhang, J. Zhang, Q. Hu, Y. Cui, Y. Yang and G. Qian, *Appl. Surf. Sci.*, 2015, **355**, 814–819.
25. S. S. Nagarkar, T. Saha, A. V. Desai, P. Talukdar and S. K. Ghosh, *Sci. Rep.*, 2014, **4**, 7053-7058.
26. A. Das and S. Biswas, *Sens. Actuators, B*, 2017, **250**, 121–131.
27. P. Li, Y. Zhao, L. Yao, H. Nie and M. Zhang, *Sens. Actuators, B*, 2014, **191**, 332–336.
28. M. Trigo-López, J. L. Barrio-Manso, F. Serna, F. C. García and J. M. García, *Macromol. Chem. Phys.*, 2013, **214**, 2223-2231.
29. R. Deshmukh and V. Trivedi, *PLoS One*, 2014, **9**, e103706-e103718.
30. T. Loiseau, C. Serre, C. Huguenard, G. Fink, F. Taulelle, M. Henry, T. Bataille and G. Férey, *Chem. Eur. J.*, 2004, **10**, 1373-1382.
31. S. Biswas, T. Ahnfeldt and N. Stock, *Inorg. Chem.*, 2011, **50**, 9518–9526.
32. C. Banwell and E. McCash, *Fundamentals of Molecular Spectroscopy*, McGraw Hill Education, New York, 1994.
33. S. Couck, J. F. M. Denayer, G. V. Baron, T. Rémy, J. Gascon and F. Kapteijn, *J. Am. Chem. Soc.*, 2009, **131**, 6326–6327.
34. C.-X. Yang, H.-B. Ren and X.-P. Yan, *Anal. Chem.*, 2013, **85**, 7441−7446.

TH-2604_156122006

35. S. Bourrelly, P. L. Llewellyn, C. Serre, F. Millange, T. Loiseau and G. Férey, *J. Am. Chem. Soc.*, 2005, **127**, 13519-13521.
36. C. Serre, F. Millange, C. Thouvenot, M. Noguès, G. Marsolier, D. Louër and G. Fe'rey, *J. Am. Chem. Soc.*, 2002, **124**, 13519-13526.
37. T. K. Trung, P. Trens, N. Tanchoux, S. Bourrelly, P. L. Llewellyn, S. Loera-Serna, C. Serre, T. Loiseau, F. Fajula and G. Fe´rey, *J. Am. Chem. Soc.*, 2008, **130**, 16926–16932.
38. S. Biswas, T. Remy, S. Couck, D. Denysenko, G. Rampelberg, J. F. M. Denayer, D. Volkmer, C. Detavernier and P. V. D. Voort, *Phys. Chem. Chem. Phys.*, 2013, **15**, 3552-3561.
39. S. Biswas, S. Couck, D. Denysenko, A. Bhunia, J. F. M. Denayer, D. Volkmer, C. Janiak and P. V. D. Voort, *Microporous Mesoporous Mater.*, 2013, **181**, 175-181.
40. W. Xuan, C. Sheng, Y. Cao, W. He and W. Wang, *Angew. Chem. Int. Ed.*, 2012, **51**, 2282-2284.
41. Z. Wu, Z. Li, L. Yang, J. Han and S. Han, *Chem. Commun.*, 2012, **48**, 10120-10122.
42. Y.-N. Wu, M. Zhou, S. Li, Z. Li, J. Li, B. Wu, G. Li, F. Li and X. Guan, *Small*, 2014, **10**, 2927–2936
43. H. Li, X. Feng, Y. Guo, D. Chen, R. Li, X. Ren, X. Jiang, Y. Dong and B. Wang, *Sci. Rep.*, **4**, 4366-4370.
44. Y. Ma, H. Su, X. Kuang, X. Li, T. Zhang and B. Tang, *Anal. Chem.*, 2014, **86**, 11459−11463.
45. S. S. Nagarkar, A. V. Desai and S. K. Ghosh, *Chem. Eur. J.*, 2015, **21**, 9994-9997.
46. X. Xin, J. Wang, C. Gong, H. Xu, R. Wang, S. Ji, H. Dong, Q. Meng, L. Zhang, F. Dai and D. Sun, *Sci. Rep.*, 2016, **6**, 21951-21959.
47. S. Nandi, H. Reinsch, S. Banesh, N. Stock, V. Trivedi and S. Biswas, *Dalton Trans.*, 2017, **46**, 12856-12864.
48. R. Dalapati, S. N. Balaji, V. Trivedi, L. Khamari and S. Biswas, *Sens. Actuators, B*, 2017, **245**, 1039–1049.
49. S. S. Nagarkar, T. Saha, A. V. Desai, P. Talukdar and S. K. Ghosh, *Sci. Rep.*, 2014, **4**, 7053-7058.
50. S. S. Nagarkar, A. V. Desai and S. K. Ghosh, *Chem. Eur. J.* , 2015, **21**, 9994–9997.

TH-2604_156122006

51. X. Zhang, J. Zhang, Q. Hu, Y. Cui, Y. Yang and G. Qian, *Appl. Surf. Sci.*, 2015, **355**, 814-819.
52. H. Li, X. Feng, Y. Guo, D. Chen, R. Li, X. Ren, X. Jiang, Y. Dong and B. Wang, *Sci. Rep.*, 2014, **4**, 4366-4370.
53. Y. Ma, H. Su, X. Kuang, X. Li, T. Zhang and B. Tang, *Anal. Chem.*, 2014, **86**, 11459-11463.
54. A. Legrand, A. Pastushenko, V. Lysenko, A. Geloen, E. A. Quadrelli, J. Canivet and D. Farrusseng, *ChemNanoMat*, 2016, **2**, 866 – 872.
55. X. Zhang, Q. Hu, T. Xia, J. Zhang, Y. Yang, Y. Cui, B. Chen and G. Qian, *ACS Appl. Mater. Interfaces*, 2016, **8**, 32259-32265.
56. X. Zheng, R. Fan, Y. Song, A. Wang, K. Xing, X. Du, P. Wang and Y. Yang, *J. Mater. Chem. C*, 2017, **5**, 9943-9951.
57. J. Zhang and W. Guo, *Chem. Commun.*, 2014, **50**, 4214-4217.
58. W. He and Z. Liu, *RSC Adv.*, 2016, **6**, 59073–59080.
59. Y. Ma, W. Luo, P. J. Quinn, Z. Liu and R. C. Hider, *J. Med. Chem.*, 2004, **47**, 6349-6362.
60. X. Ren and L. Lu, *Chin. Chem. Lett.*, 2015, **26**, 1439–1445.
61. C.-X. Yang, H.-B. Ren and X.-P. Yan, *Anal. Chem.* , 2013, **85**, 7441−7446.
62. C. Zhang, Y. Yan, Q. Pan, L. Sun, H. He, Y. Liu, Z. Liang and J. Li, *Dalton Trans.*, 2015, **44**, 13340-13346.
63. Y.-F. Li, D. Wang, Z. Liao, Y. Kang, W.-H. Ding, X.-J. Zheng and L.-P. Jin, *J. Mater. Chem. C*, 2016, **4**, 4211-4217.
64. M. Zheng, H. Tan, Z. Xie, L. Zhang, X. Jing and Z. Sun, *ACS Appl. Mater. Interfaces*, 2013, **5**, 1078-1083.
65. X.-H. Zhou, L. Li, H.-H. Li, A. Li, T. Yang and W. Huang, *Dalton Trans.*, 2013, **42**, 12403-12409.
66. Y. Wu, G.-P. Yang, Y. Zhang, N. Shi, J. Han and Y.-Y. Wang, *RSC Adv.*, 2015, **5**, 90772-90777.
67. X.-L. Zhao, D. Tian, Q. Gao, H.-W. Sun, J. Xu and X.-H. Bu, *Dalton Trans.*, 2016, **45**, 1040-1046.

TH-2604_156122006

TH-2604_156122006

Ph.D. Thesis
Chapter 3

A Dual Functional MOF-Based Fluorescent Sensor for Intracellular Phosphate and Extracellular 4-Nitrobenzaldehyde

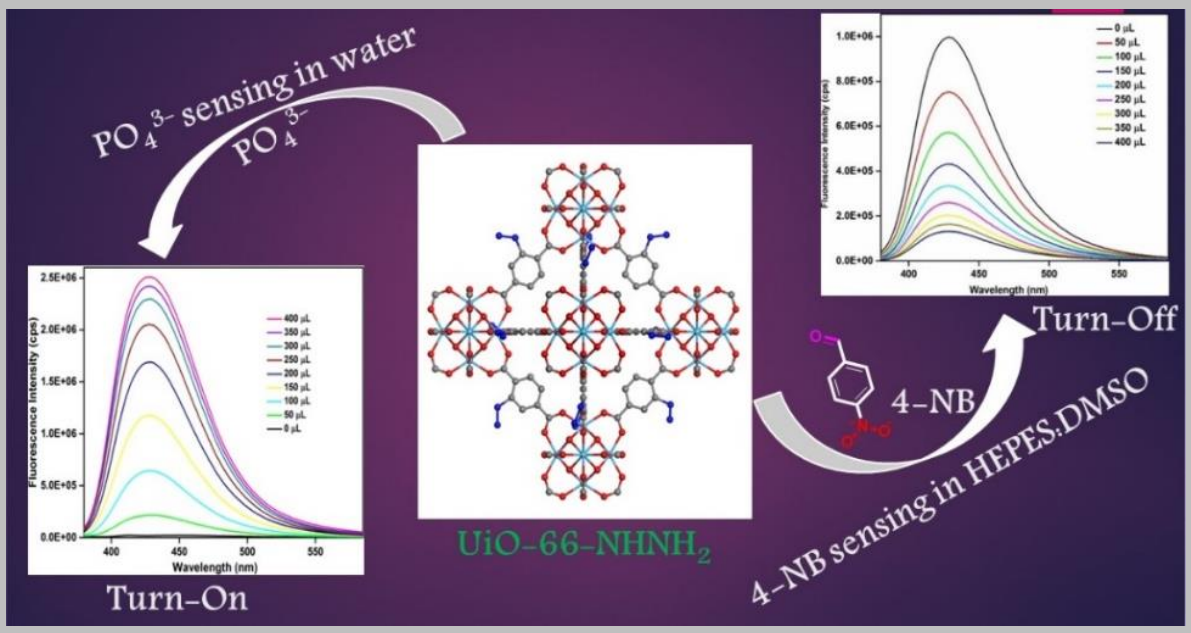

Chapter 3

3.1 Introduction

Phosphate (PO_4^{3-}), being an inorganic anion, is a basic fragment of nucleotides and plays very vital roles in signal transduction and energy storage. The other important roles of this anion in the biological systems include bone mineralization, muscle function, membrane robustness, cellular signal, etc. The maximum permissible level of PO_4^{3-} ion varies from 0.0143 to 0.143 mM for waste water and it is 0.32 µM for river water.[1] Excess amounts of PO_4^{3-} ion in food or water are often responsible for several digestive problems.[2-4] Because of its detrimental as well as favorable roles, the development of a practical method for the aqueous-phase detection of PO_4^{3-} ion in an extremely selective and sensitive way will be beneficial for environmental protection as well as for human health.

On the other hand, chloramphenicol, which is extensively used as a first-line therapy for the treatment of typhoid fever patients and most commonly in eye-drops (mainly in developing countries), gets decomposed in presence of UV-A radiation of sunlight to produce various decomposition products such as 4-nitrobenzaldehyde (4-NB), 4-nitrobenzoic acid and 4-nitrosobenzoic acid.[5] The toxicities of all the three photoproducts towards bone-marrow cells were studied, which concluded that 4-NB, 4-nitrobenzoic acid and 4-nitrosobenzoic acid were 20, 6 and 6 times more toxic than chloramphenicol, respectively.[6] Moreover, the use of this drug leads to increased amount of methemoglobin (Met-Hb) in blood, which is the cause of oxidative stress. Therefore, the *in-vitro* sensing of 4-NB in a cell or in the fluid secreted from eye being exposed to sunlight after application of the eye drop is highly required, since it might be a prior indication of fatal aplastic anemia disease.[7]

Due to the unique structures and fascinating properties such as tunable and extraordinary porosity, high physicochemical and mechanical stability and outstanding catalytic activity, metal-organic frameworks (MOFs) have received extensive research interests in recent years.[8-10] Besides gas storage, chemical catalysis,[11, 12] chemical separation,[13, 14] drug delivery,[15, 16] and enzymatic catalysis,[17-20] MOFs have also been considered as one of the leading fluorescent sensor materials. The fluorescent MOFs have been used for the detection of variety of organic and inorganic molecules, radicals, ions, etc.[21-23] The choice of proper functional groups in the framework linkers is very crucial for the exhibition of sensing properties, since specific functional groups can act as binding sites for particular analytes, allowing their detection through fluorescence spectroscopy.

TH-2604_156122006

MOFs having high physicochemical stability (air, water, acid, base, thermal etc.) are highly needed for their practical applications. The Zr(IV)-based MOF namely UiO-66 (UiO = University of Oslo) has received much attention in past few years due to its high thermal and chemical stability as well as significant microporosity.[24-28] The 3D cubic framework of this MOF is constructed from $[Zr_6O_4(OH)_4]^{12+}$ building units, which are interconnected by the carboxylates groups of 1,4-benzenedicarboxylate (BDC) linkers.[29] In compound **2**, the BDC linker molecules are replaced by the 2-hydrazinyl-1,4-benzenedicarboxylate (BDC-N_2H_3) linkers. The guest-free form of **2** (termed as **2′**) can sense PO_4^{3-} ion in water and HEPES buffer (10 mM, pH = 7.4). It can also detect 4-NB in HEPES (10 mM, pH = 7.4)/DMSO (v/v, 9:1) medium. The detection processes for both analytes occur with high selectivity, which is preserved in the presence of intrusive analytes (Scheme 2.1). Herein, we report the highly selective and sensitive fluorescence sensing properties of **2′** for PO_4^{3-} ion and 4-NB via *turn-on* and *turn-off* mechanisms, respectively.

In addition to their high physicochemical stability, the Zr-based MOF was chosen for the sensing of PO_4^{3-} ions due to the high binding affinity of Zr(IV) ions with PO_4^{3-} ions. There is already a report in the literature on the PO_4^{3-} sensing by a Zr-based MOF.[30] Moreover, the Zr(IV) ions having d^0 electronic configuration are electronically inert. Hence, there is good electronic communication between the Zr(IV) ions and BDC-N_2H_3 linkers.[31, 32] As a result, **2′** showed high fluorescence intensity.

TH-2604_156122006

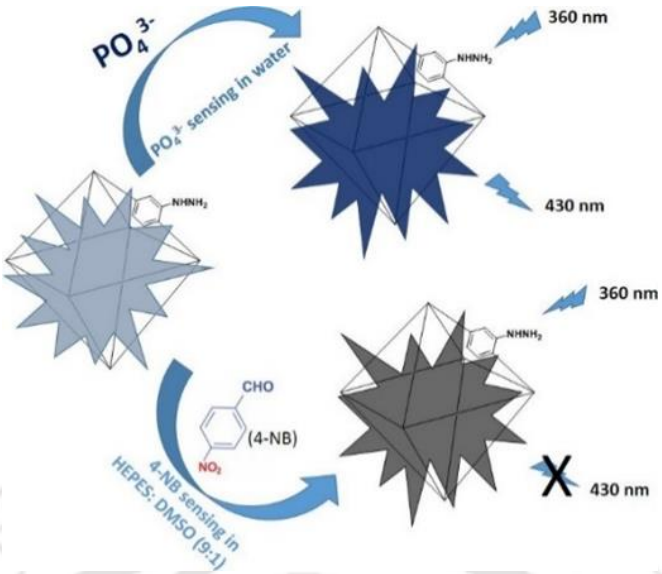

Scheme 3.1 Schematic representation displaying the sensing properties of **2′** towards PO_4^{3-} ion in aqueous medium and 4-NB in HEPES/DMSO (v/v, 9:1) medium through fluorescence *turn-on* and *turn-off* mechanisms, respectively.

3.2 Experimental Section

3.2.1 Materials and General Methods

The 2-hydrazinyl-1,4-benzenedicarboxylic acid ($H_2BDC\text{-}N_2H_3$) linker was synthesized by following the previously reported procedure[33] for 2-hydrazinyl-4-(methoxycarbonyl) benzoic acid. All the chemicals used in this work were commercially available and they were used without any further purification. For fluorescence sensing experiments, Milli-Q water was used as a medium. Fourier transform infrared spectroscopy was performed in the region 400-4000 cm^{-1} with the Perkin Elmer Spectrum Two FT-IR spectrometer. The following indications were used to indicate the corresponding absorption bands: very strong (vs), strong (s), medium (m), weak (w), shoulder (sh) and broad (br). TGA were carried out using a SDT Q600 thermogravimetric analyzer in the temperature range 25-700 °C under air atmosphere at a heating rate of 10 °C min^{-1}. A Bruker D2 Phaser X-ray diffractometer (30 kV, 10 mA) using Cu-Kα (λ = 1.5406 Å) radiation was used to perform the XRPD patterns. An Edinburgh Instrument Life-Spec II equipment was used to measure the fluorescence lifetimes (TRPL) by employing time-correlated single-photon counting (TCSPC) procedure. The solution ^{1}H and ^{13}C NMR spectra were recorded on a Bruker AM 600 spectrometer. Nitrogen sorption isotherms were recorded on a Quantachrome

TH-2604_156122006

Autosorb iQMP gas sorption analyzer. Fluorescence emission studies were performed using a HORIBA JOBIN YVON Fluoromax-4 spectrofluorometer. The compound was heated at 120 °C for 24 h before the sorption experiments.

3.2.2 Synthesis of MOF and Activation

3.2.2.1 Synthesis of $[Zr_6O_4(OH)_4(BDC\text{-}N_2H_3)_6]\cdot 3.5H_2O\cdot 3DMF$ (Zr-UiO-66-N_2H_3, 2)

A mixture of $ZrOCl_2\cdot 8H_2O$ (65 mg, 0.20 mmol), $H_2BDC\text{-}N_2H_3$ linker (40 mg, 0.20 mmol) and benzoic acid (746 mg, 6.0 mmol) in 3 mL of *N*,*N*-dimethylformamide (DMF) was sealed in a glass tube and heated using a block heater at 120 °C for 24 h. The light yellow precipitate was collected by vacuum filtration and washed with acetone (2 × 3 mL). The material was dried at 60 °C for 4 h in a conventional oven. The yield was 45 mg (0.02 mmol, 60%) based on the Zr salt. FT-IR (KBr, cm^{-1}): 3420 (br), 2916 (w), 2853 (w), 1658 (s), 1627 (vs), 1422 (s), 1418 (vs), 1381(m), 1188 (m), 1100(w), 1028 (m), 900(m), 880 (sh), 845 (s), 782 (vs), 711 (sh), 663 (vs), 558 (w), 495 (s).

3.2.2.2 Activation of 2

To get the activated form, 50 mg of the as-synthesized compound was stirred for 24 h in 30 mL of methanol in a round-bottom flask at room temperature, during which fresh methanol was added discarding the initially added methanol at a time interval of 12 h. After that the compound was filtered and the solid powder was dried at 80 °C in a conventional oven for 1 h. Afterward, the compound was heated at 120 °C under vacuum for 24 h to obtain material **2′**.

3.2.3 Preparation of the Suspensions of 2′ for Fluorescence Sensing Experiments

To get the stable suspensions for the luminescence detection experiments, 2 mg of **2′** was taken in three separate 5 mL glass vials. Then, 3 mL of water, HEPES (10 mM, pH = 7.4) (the first two for PO_4^{3-} sensing) or HEPES (10 mM, pH = 7.4)/DMSO (v/v = 9:1) mixture (for 4-NB sensing) was separately added to these vials. These mixtures were allowed to sonicate for 1 h and subsequently kept for 24 h under ambient conditions.

TH-2604_156122006

3.2.4. Fluorescence Sensing Experiments

In order to perform the sensing experiment for PO_4^{3-} ion, 100 µL of the suspension of **2′** from the stock suspension was placed in a quartz cuvette and 2900 µL of water or HEPES buffer was added to it in order to make a suspension having a total volume of 3 mL. Then, a solution of PO_4^{3-} ion was added to it up to 400 µL with an incremental volume of 50 µL and the emission spectra were recorded after every 10 min until the fluorescence intensity reached saturation point. For the sensing of 4-NB, 100 µL of the suspension of **2′** from the stock suspension was taken in a quartz cuvette and 2900 µL of HEPES/DMSO (v/v = 9:1) mixture was added to it in order to make a suspension having a total volume of 3 mL. Then, a solution of 4-NB in DMSO was added to it up to 400 µL with an incremental volume of 50 µL and the fluorescence spectra were recorded until the saturation point for the fluorescence intensity was attained. For all these cases, the suspension of **2′** was excited at 360 nm and the fluorescence spectra were measured in the range of 385-585 nm. The fold increment for the PO_4^{3-} sensing via *turn-on* mechanism was calculated using the formula: fold increment = $(I/I_0 - 1)$. Quenching efficiency (η) for the 4-NB sensing was calculated using the familiar equation: $\eta = (1-I/I_0) \times 100$ %, where I_0 initial fluorescence intensity of the suspension of **2′** and I is the fluorescence intensity after addition of the analyte.

3.2.5 Cell Culture and Intracellular PO_4^{3-} Sensing

The macrophage J774A.1, cervical cancer HeLa and gliblastoma U87MG cells were cultured in DMEM:F12 media containing 10% FBS and 1% antibiotic cocktail as described earlier.[34-36] The cells were loaded with probe **2′** (0.5 mg/mL) for 6 h in complete medium. The cells were observed in the bright field and the blue channel (λ_{ex}= 390 nm, λ_{em}= 430 nm) using Cytell cell imaging system (GE Healthcare) and images were captured from randomly selected fields.

3.2.6 PO_4^{3-} Sensing in Real Samples

We have analyzed PO_4^{3-} ion in six different types of real samples: tap and lake water (collected locally), urine 1 and 2 (collected from two different human volunteers), blood serum 1 and serum 2 (collected from two different human volunteers). Human urine samples were kept at 4 °C for overnight and then the supernatant liquid was collected

TH-2604_156122006

which was used for the sensing experiment. Human serum samples were centrifuged at 5000 rpm for 5 min and then filtered with Amicon®Ultra-4 Centrifugal Filter Units (30 kDa). The filtrate was collected which was diluted 100 times with HEPES buffer (10 mM, pH = 7.4). The resulting liquid was used for the sensing experiment. These samples were distributed in twenty four glass vials so that four vials contain samples of one type. Afterwards, a known amount of Na_3PO_4 was spiked into every vial so that the final concentration of PO_4^{3-} ion in four different glass vials having samples of one kind become 0, 10, 20 and 30 μM. Then, each PO_4^{3-} spiked sample (100 μL) was added to the aqueous suspension (2900 μL) of **2′**. We have recorded the fluorescence spectrum after 100 min of addition.

3.3 Results and Discussion

3.3.1 Preparation and Activation Procedure

Before getting the optimized synthesis conditions for **2**, several possible reactions were carried out with $H_2BDC\text{-}N_2H_3$ linker using three Zr(IV) salts ($ZrCl_4$, $ZrOCl_2{\cdot}8H_2O$) in presence of two different amide solvents (DMF and DMA) and four different modulators (acetic acid, formic acid, benzoic acid and trifluoroacetic acid)[37] at different temperatures. Highly crystalline compound **2** was obtained when a mixture of $ZrOCl_2{\cdot}8H_2O$, $H_2BDC\text{-}N_2H_3$ linker and benzoic acid was placed in DMF in a sealed glass tube and heated at 120 °C for 24 h using a block heater.

In order to remove the guest molecules trapped inside the pores of **2**, an activation procedure was performed which involves a solvent-exchange step followed by a heating step under high vacuum. In the solvent-exchange step, 100 mg of **2** was suspended in 30 mL of methanol inside a 50 mL round-bottom flask and stirred for 24 h at room temperature. Then, it was filtered and dried at 60 °C in a conventional oven. Further, it was activated at 120 °C under vacuum for 24 h.

3.3.2 Infrared Spectroscopy

In the FT-IR spectra (Figure 3.1) of the as-synthesized **2** and activated **2′**, the strong absorption bands at around 1570 and 1400 cm^{-1} can be attributed to the asymmetric and symmetric carboxylate stretching vibrations of the coordinated $BDC\text{-}N_2H_3$ linker

TH-2604_156122006

molecules, respectively.[38] In the IR spectrum of the as-synthesized sample, the strong absorption band at 1658 cm^{-1} can be attributed to the carbonyl stretching vibration of the occluded DMF molecules in the framework structure.[39] This absorption band is completely absent in the FT-IR spectrum of **2′**, which confirms that the thermally activated compound is devoid of any guest DMF molecule inside the pores.

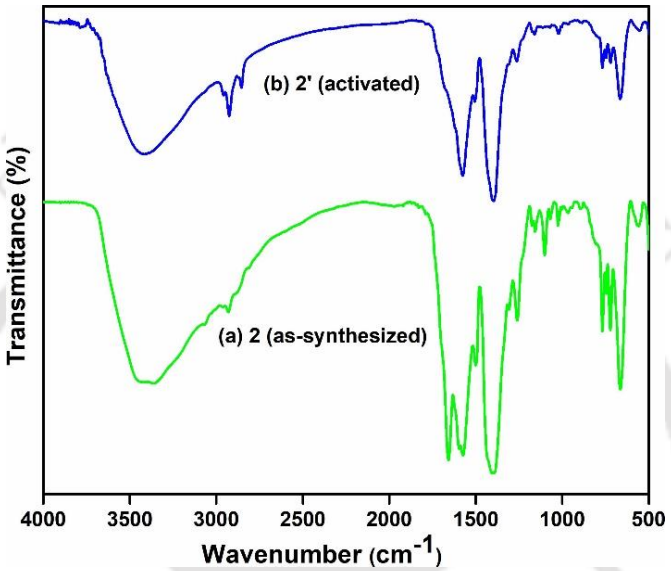

Figure 3.1 FT-IR spectra of (a) as-synthesized **2** and (b) activated **2′**.

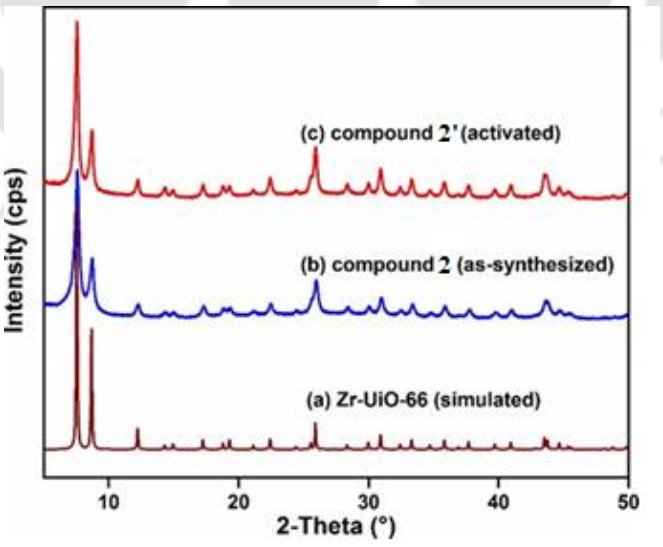

Figure 3.2 XRPD patterns of (a) simulated Zr-UiO-66, (b) as-synthesized **2** and (c) activated **2′**.

TH-2604_156122006

3.3.3 XRPD Analysis and Structure Description

The experimental XRPD patterns (Figure 3.2) of **2** and **2′** match nicely with the simulated XPRD pattern of the previously reported UiO-66 compound.[40,41] By indexing the XRPD pattern of **2**, its unit cell parameters were deduced. The observed lattice parameters (Table 3.1) are very close with the reported, un-functionalized Zr-UiO-66 compound. In addition, a Pawley fit (Figure 3.3) was carried out, which displayed very good similarity between the experimental and calculated XRPD patterns of **2**. All these results suggest that the presented compound has the same framework topology as the UiO-66 material.[40]

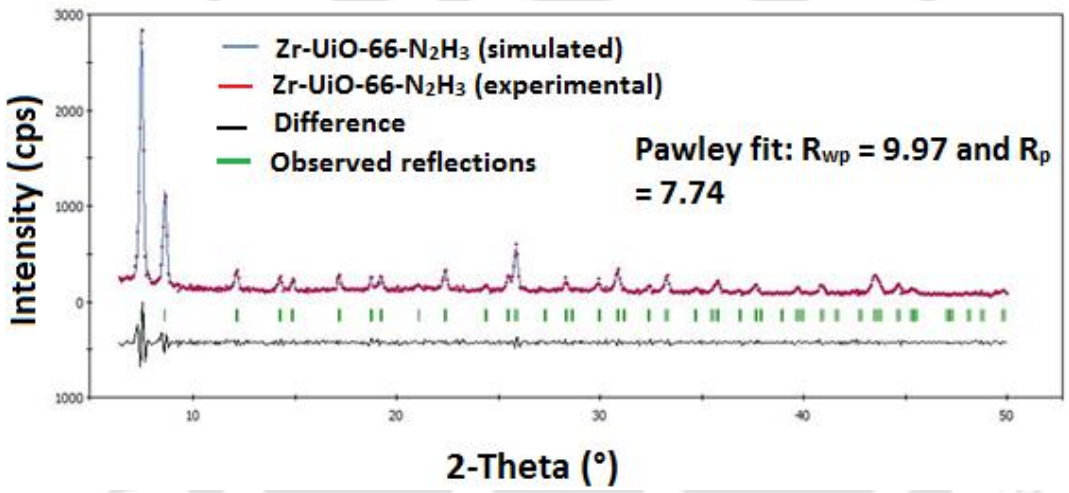

Figure 3.3 Pawley fit for the XRPD pattern of as-synthesized **2**. Blue lines and red dots denote calculated and observed patterns, respectively. The peak positions and difference plot are displayed at the bottom (R_{wp} = 9.97, R_p = 7.74).

TH-2604_156122006

Table 3.1 Unit cell parameters of as-synthesized Zr-UiO-66-N_2H_3 obtained by indexing its XRPD pattern. The obtained values were compared with those of the previously reported un-functionalized Zr-UiO-66 MOF.

Compound Name	Zr-UiO-66-N_2H_3 MOF (this work)	Zr-UiO-66 MOF (reported)[41]
Crystal System	Cubic	cubic
a = b = c (Å)	20.723(4)	20.7004(2)
V (Å^3)	8898.8(26)	8870.3(2)

The noticeable similarity between the XRPD patterns of the as-synthesized and thermally activated samples of **2** indicates that the compound retained its structural robustness after the thermal activation process.

As confirmed by the XRPD experiments (Figure 3.2), the hydrazine-functionalized Zr(IV)-based UiO-66 material (**2**) shows the same framework topology as the un-functionalized UiO-66 material. Lillerud and co-workers have previously described the framework structure of UiO-66 material.[42] The UiO-66 framework contains hexanuclear $[Zr_6O_4(OH)_4]^{12+}$ bricks as the secondary building units which are interlinked by the carboxylates of twelve 1,4-benzenedicarboxylate (BDC) linkers. In the presented work, the BDC-N_2H_3 plays the same role as BDC linker played in previously reported[42, 43] UiO-66 framework structure. This 3D framework contains octahedral as well as tetrahedral cages. Each central octahedral cage is connected by eight corner tetrahedral cages via narrow triangular windows. Each zirconium atom resides in square anti-prismatic coordination environment of the framework. The organic connecter and the inorganic building units together make the framework three-dimensional via the interconnection with each other.

3.3.4 Thermal Stability

For investigating the thermal stability of **2** and **2′**, TG analyses were performed under argon atmosphere in the temperature range of 25-700 °C. According to the TG analyses, **2** is thermally stable up to 400 °C under air atmosphere.

TH-2604_156122006

In the TG curve (Figure 3.4) of **2**, the first loss of 2.6 wt% in the temperature range of 25-120 °C can be attributed to the elimination of 3.5 water molecules per formula unit (cald.: 2.5 wt%). The second weight loss of 12.2 wt% in the temperature range of 120-400 °C can be assigned to the removal of 3 occluded DMF molecules per formula unit (cald:. 11.8 wt%). After 400 °C, the decomposition of the compound starts to occur owing to the loss of organic linkers from the framework structure of **2**. In the TG trace of **2′**, the one weight loss in the low temperature range can be assigned to the removal of adsorbed water molecules from moisture. It is worthy to note that thermal stability of our compound **2′** is lower than the existing, parent and functionalized Zr-based UiO-66 MOF materials.[44-46]

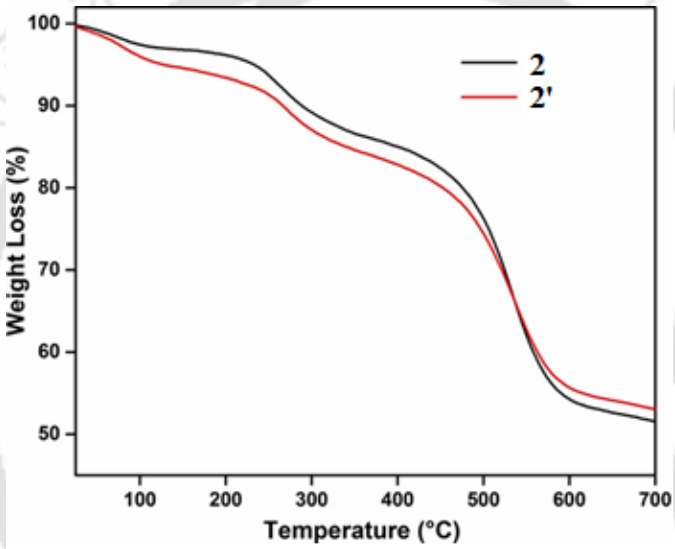

Figure 3.4 TG curves of as-synthesized **2** (black) and thermally activated **2′** (red) recorded in an argon atmosphere in the temperature range of 25-700 °C with a heating rate of 10 °C min^{-1}.

3.3.5 Chemical stability

The chemical stability of **2′** was investigated by stirring the samples in water, acetic acid and 1(M) HCl solutions at room temperature for 12 h. Afterwards, the samples were collected by filtration and the crystallinity of the filtered materials were checked by XRPD analysis. As displayed in (Figure 3.5), the compound retained its crystallinity (and thus structural robustness) after treatment with water, acetic acid and 1(M) HCl solutions. Hence, **2′** exhibited remarkable chemical stability which is comparable with that of the previously reported parent and other functionalized UiO-66 materials.[47]

TH-2604_156122006

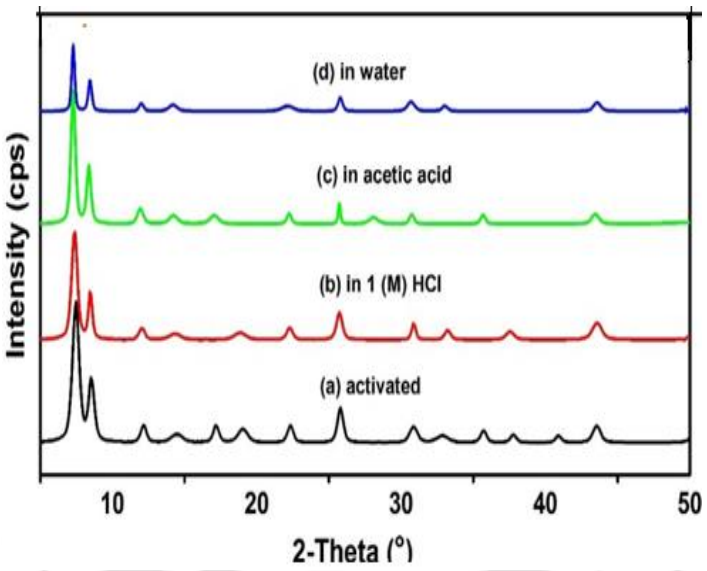

Figure 3.5 XRPD patterns of compound **2′** in different forms: (a) activated, (b) after treatment with 1(M) HCl, (c) after treatment with acetic acid and (d) after treatment with water.

3.3.6 N_2 Sorption Analysis

The N_2 sorption experiments were carried out for determination of specific surface area and micropore volume of **2′**. From Figure 3.6a, it is obvious that the N_2 adsorption isotherm follows type-I behavior, which is characteristic for microporous materials. The BET surface area and micropore volume of **2′** were estimated to be 818 $m^2\ g^{-1}$ and 0.47 $cm^3\ g^{-1}$ (at $p/p_0 = 0.5$), respectively. This value of BET surface area is comparable with the known, functionalized UiO-66 MOF materials.[48-54]

We have also performed N_2 sorption measurement (Figure 3.6b) with the compound recovered after the phosphate sensing experiment. As anticipated, the BET surface area and micropore volume (at $p/p_0 = 0.5$) of the phosphate-treated material were lower than the untreated material and they corresponded to 442 $m^2\ g^{-1}$ and 0.25 $cm^3\ g^{-1}$, respectively.

TH-2604_156122006

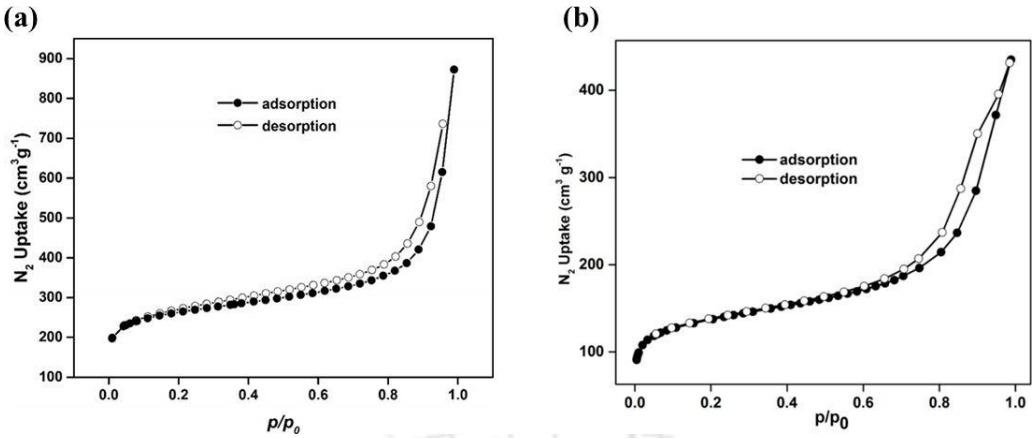

Figure 3.6 (a) N_2 adsorption (solid circles) and desorption (empty circles) isotherms of **2′** measured at –196 °C. (b) N_2 adsorption (solid circles) and desorption (empty circles) isotherms of **2′** recovered after the phosphate sensing experiment. The isotherms were measured at -196 °C.

3.3.7 Photoluminescence Properties of 2′

We have studied the solid-state fluorescence properties of both free $H_2BDC\text{-}N_2H_3$ linker and **2′**. The free $H_2BDC\text{-}N_2H_3$ linker displayed weak fluorescence intensity (λ_{max} = 447 nm) and **2′** exhibited strong luminescence intensity (λ_{max} = 478 nm) in the solid state (Figure 3.7a). The fluorescence emission band of the free linker arises due to the π-π* electronic transition of the aromatic ring.[55] The enhanced luminescence intensity of **2′** as compared to the free linker can be assigned to the linker-to-metal charge transfer (LMCT).[56, 57] The blue shift in the λ_{max} value of **2′** as compared to the free linker might be also assigned to the LMCT transition.[58, 59]

We have also investigated the luminescence properties of both free $H_2BDC\text{-}N_2H_3$ linker and **2′** in the aqueous medium. The free linker showed strong luminescence intensity (λ_{max} = 443 nm) and **2′** exhibited weak luminescence intensity (λ_{max} = 458 nm) in the aqueous medium (Figure 3.7b). This difference in the luminescence intensity can be ascribed to the interaction between the Zr-O nodes and water molecules. When water molecules enter inside the pores of **2′**, they can form hydrogen bonding with the Zr-O nodes of **2′** and thus perturb the electron transfer from the linker to metal (i.e., LMCT transition).[60] This perturbation reduces the luminescence intensity of **2′** in the aqueous medium.

TH-2604_156122006

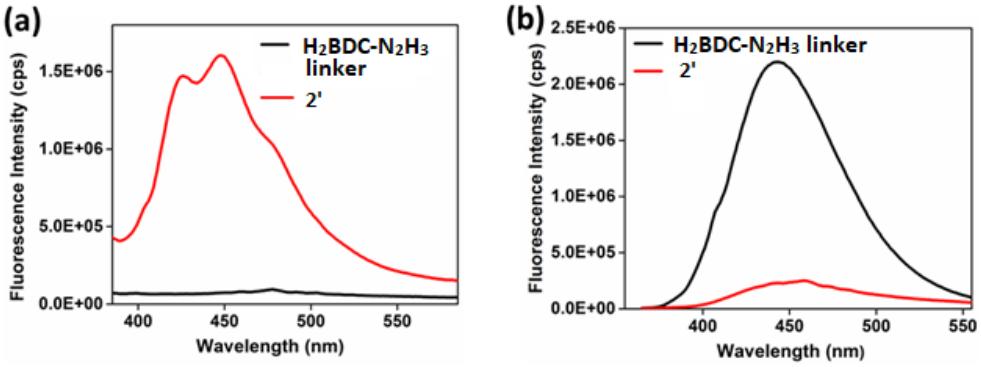

Figure 3.7 (a) Solid-state fluorescence spectra of free $H_2BDC\text{-}N_2H_3$ linker and **2′**. (b) Fluorescence spectra of free $H_2BDC\text{-}N_2H_3$ linker and **2′** in the aqueous medium.

3.3.8 Sensing Behavior toward PO_4^{3-} Ions

In order to determine the potential of $UiO\text{-}66\text{-}N_2H_3$ as a fluorogenic sensor for PO_4^{3-} detection in aqueous or HEPES buffer medium, fluorescence titration experiments were performed with the suspension of **2′**. The fluorescence emission (λ_{ex} = 360 nm) spectra of the suspension of **2′** were recorded in the range of 385-585 nm upon gradual addition (50 µL for each addition) of 2 mM PO_4^{3-} solution. The fluorescence emission intensities were regulated at 430 nm. As displayed in Figure 3.8, the saturation of the fluorescence intensity was observed after the addition of 400 µL of 2 mM PO_4^{3-} solution to the aqueous suspension of **2′**. Further addition of PO_4^{3-} solution did not result in any considerable increment in the fluorescence intensity.

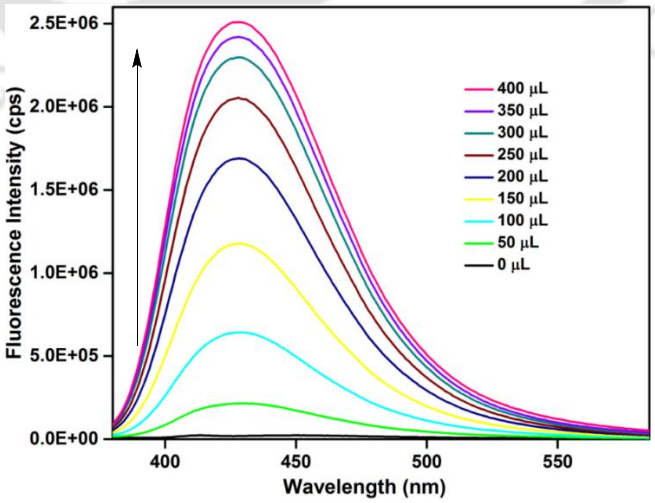

Figure 3.8 Enhancement of the fluorescence intensity of **2′** (0.87 mM) upon gradual addition of 400 µL of 2 mM aqueous solution of PO_4^{3-} ion in water (λ_{ex} = 360 nm, λ_{em} = 430 nm).

TH-2604_156122006

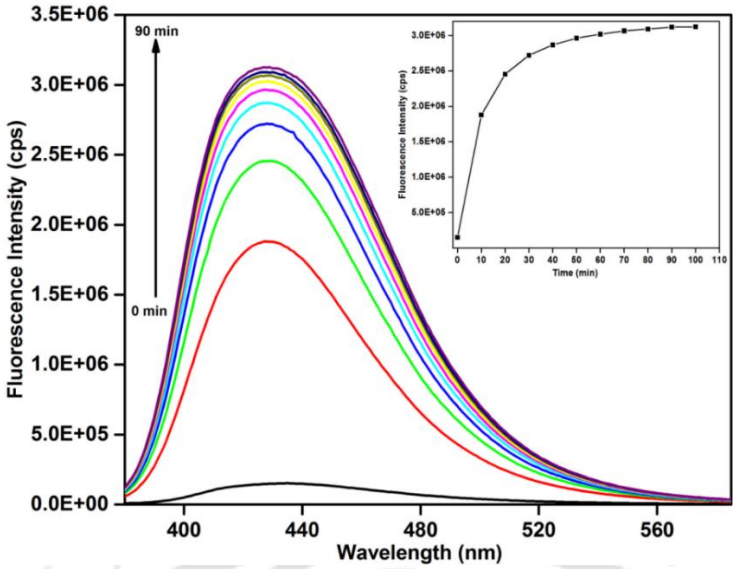

Figure 3.9 Enhancement of the fluorescence intensity of **2′** (0.87 mM) with time upon addition of 400 µL of the 2 mM aqueous solution of PO_4^{3-} ions (λ_{ex} = 360 nm, λ_{em} = 430 nm) in water.

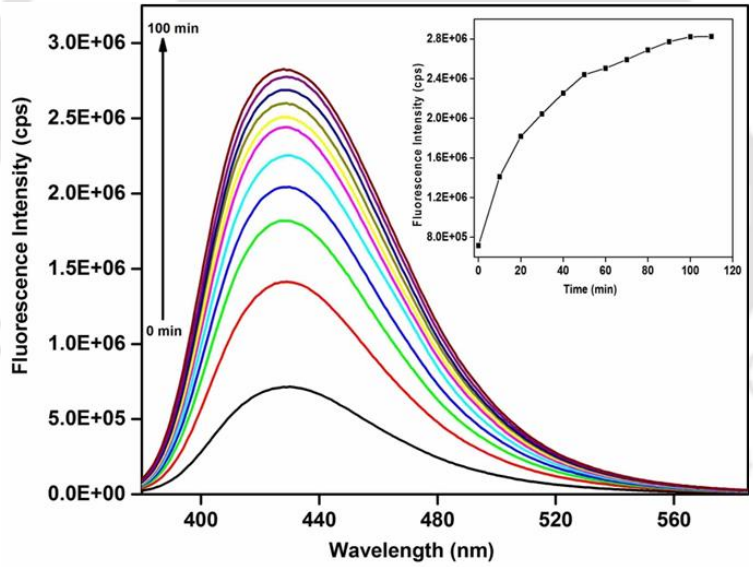

Figure 3.10 Enhancement of the fluorescence intensity of **2′** (suspended in 10 mM HEPES buffer, pH = 7.4) with time upon the addition of 400 µL of 2 mM Na_3PO_4 solution in 10 mM HEPES buffer.

The detection performance of **2′** towards PO_4^{3-} ions was evaluated by performing time-dependent sensing experiments. Upon the addition of 400 µL of 2 mM PO_4^{3-} solution, the fluorescence emission spectra of **2′** (in both aqueous and HEPES buffer media) were measured at a regular time interval of 10 min until the saturation in the fluorescent

TH-2604_156122006

emission intensity was attained. The addition of PO_4^{3-} solution to the suspension of **2′** lead to gradual transformation of the compound into *turn-on* state from its initial *turn-off* state. The saturation in the fluorescence emission intensity of **2′** occurred after 90 and 100 min in aqueous (Figure 3.9) and HEPES (Figure 3.10) buffer media, respectively. Therefore, the compound is a potential fluorescent *turn-on* probe for the detection of PO_4^{3-} ions under both aqueous and physiological conditions.

The high selectivity of a sensor towards PO_4^{3-} ion over other potentially competing anions is very crucial for practical applications. Hence, we have measured the fluorescence *turn-on* response of **2′** (in both water and 10 mM HEPES buffer) towards various potentially interfering inorganic anions and organic molecules containing PO_4^{3-} ion such as NaCl, NaBr, NaF, NaH_2PO_4, Na_2HPO_4, $Na_3P_2O_7$, NaI, $NaNO_2$, $NaNO_3$, NaOAc, Na_2S, Na_2SO_4, NaHS, NaCN, $NaHCO_3$, $NaClO_4$, NaSCN, adenosine diphosphate (ADP) and adenosine triphosphate (ATP). It can be seen from Figure 3.11 and Figure 3.12 that the addition of inorganic PO_4^{3-} solution to the suspension of **2′** causes a dramatic increment in the fluorescence emission intensity. In presence of all the other possibly competing anions, there was almost negligible enhancement in the fluorescence emission intensity as compared to PO_4^{3-} anion. These results suggest that the fluorescent *turn-on* probe is highly selective towards PO_4^{3-} ions over other potentially interfering anions.

For practical applications in complicated biological systems,[4, 61] the high selectivity of a fluorescent sensor material towards the target analyte in the presence of other potentially interfering analytes is highly required. For accomplishment of this purpose, we have carried out competitive fluorescence titration experiments in which PO_4^{3-} solution was added to the suspension of **2′** (in aqueous or HEPES buffer media), which also contained the potentially competing anions. From Figure 3.13 and Figure 3.14 it becomes obvious that the significant fluorescence *turn-on* response of the compound towards PO_4^{3-} ion is retained even in the presence of other potentially competing anions under both aqueous and physiological conditions. Therefore, the remarkable selectivity of **2′** towards PO_4^{3-} ions is retained even when other potentially interfering anions are present in the solution.

TH-2604_156122006

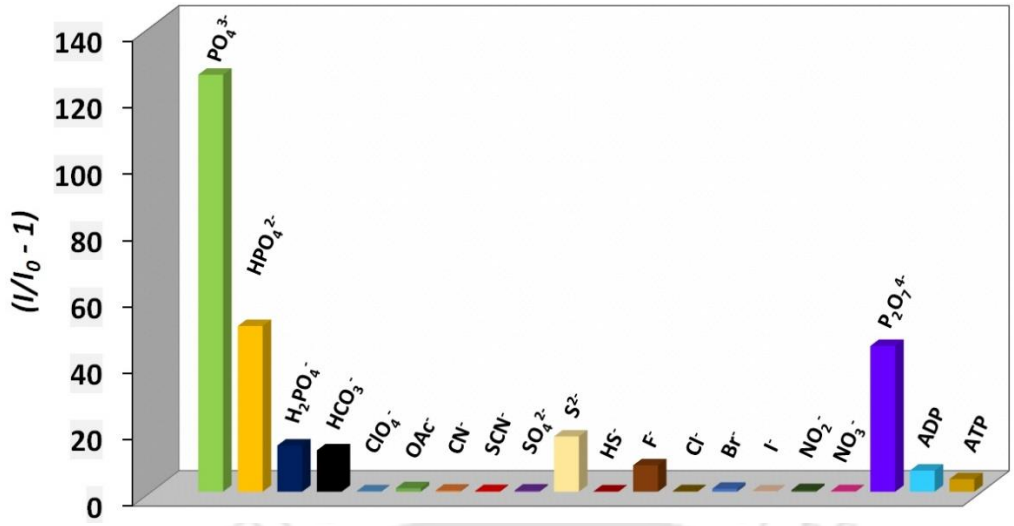

Figure 3.11 Change in the fluorescence intensity of the aqueous suspension of **2′** (0.87 mM) upon the addition of 400 µL of 2 mM aqueous solutions of various anions (λ_{ex} = 360 nm, λ_{em} = 430 nm) in water.

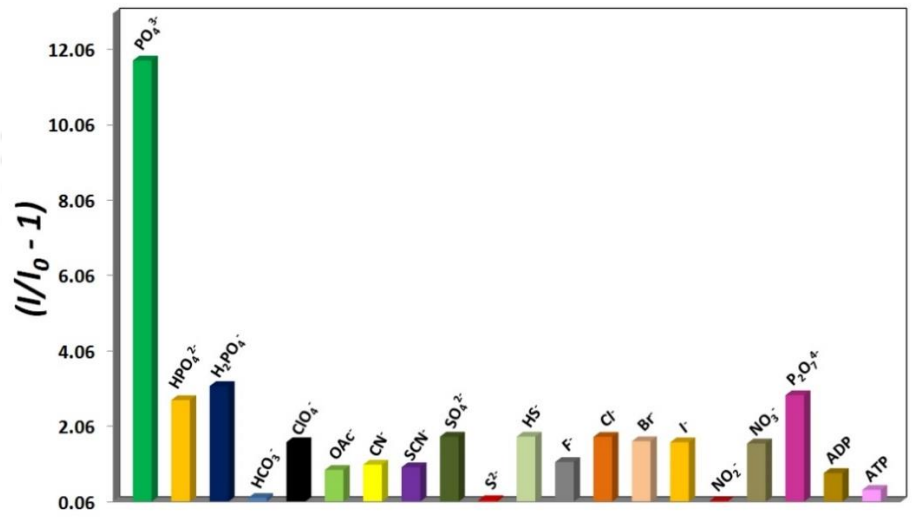

Figure 3.12 Change in the fluoresecnce intensity of the buffer suspension of **2′** (in 10 mM HEPES buffer, pH = 7.4) upon the addition of 400 µL of 2 mM aqueous solutions of different anions in 10 mM HEPES buffer, pH = 7.4.

TH-2604_156122006

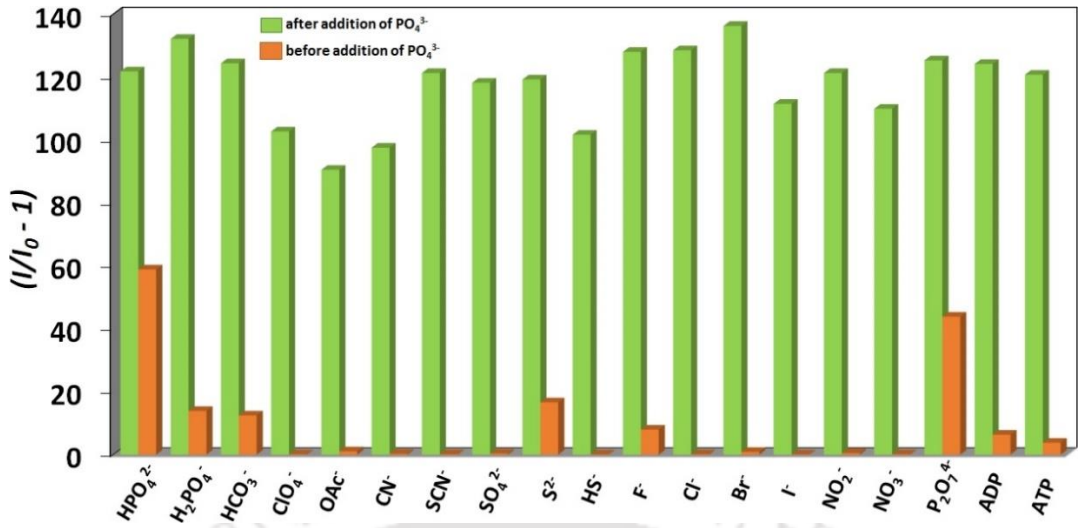

Figure 3.13 Change in the fluorescence intensity of the aqueous suspension of **2′** (0.87 mM) upon the addition of 400 µL of 2 mM aqueous solution of PO_4^{3-} ion in presence of 400 µL of 2 mM aqueous solutions of other potentially competing anions (λ_{ex} = 360 nm, λ_{em} = 430 nm) in water.

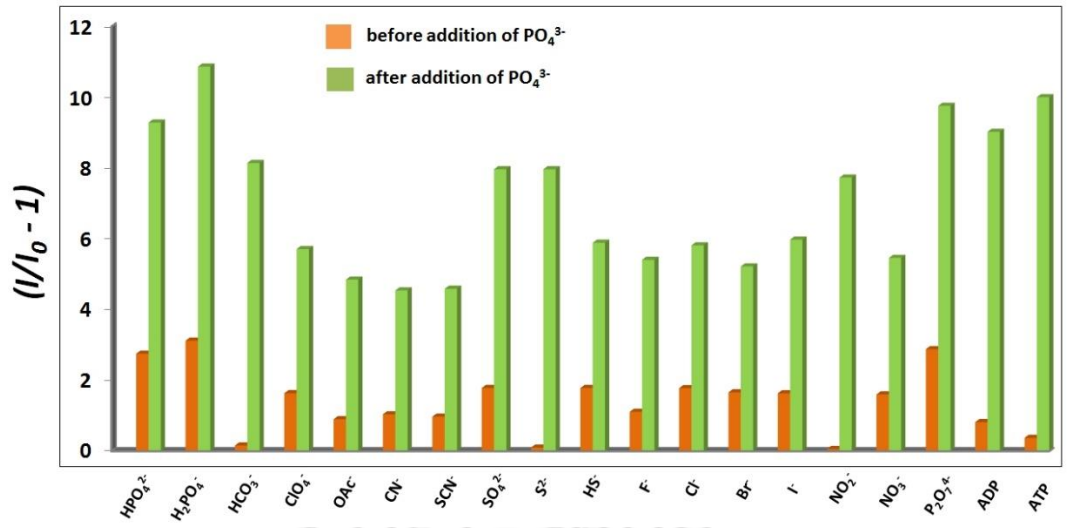

Figure 3.14 Change in the fluorescence intensity of the suspension of **2′** (in 10 mM HEPES buffer, pH = 7.4) upon the addition of aqueous solution of PO_4^{3-} ion in presence of other potentially competing anions in 10 mM HEPES buffer, pH = 7.4.

TH-2604_156122006

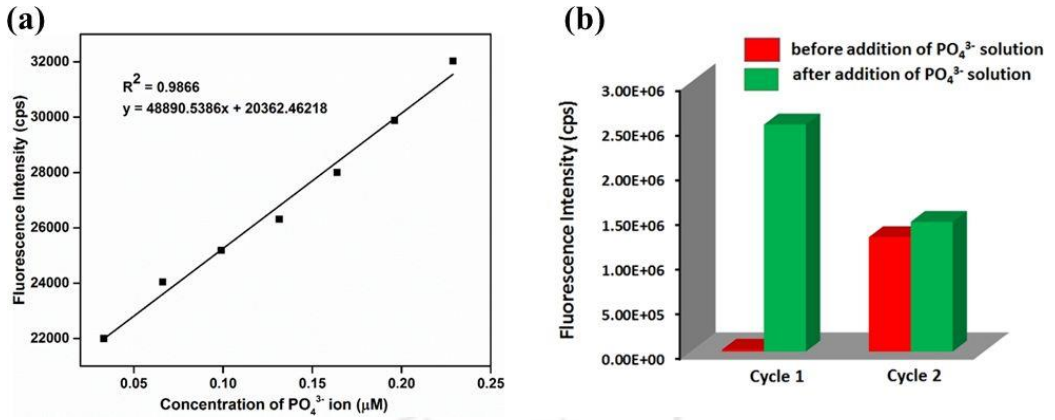

Figure 3.15 (a) Change in the fluorescence intensity of **2′** as a function of concentration of PO_4^{3-} ion in water. (b) Recyclability test in water for the fluorescence *turn-on* response of the aqueous suspension of **2′** towards 2 mM aqueous solution of PO_4^{3-}.

The limit of detection (LOD) of the aqueous suspension of **2′** towards PO_4^{3-} ion was determined by regulating the fluorescence emission intensity upon gradual addition of very low concentration of PO_4^{3-} solution to the suspension of **2′** in aqueous medium. The plot of the fluorescence emission intensity of the aqueous suspension of **2′** against the concentration of PO_4^{3-} solution resulted in a linear curve (Figure 3.15a). The LOD value was determined according to the formula: LOD = $3\sigma/m$, where σ represents the standard deviation of the initial intensity of **2′** without analyte and *m* corresponds to the slope of the above-stated linear curve.[62] The LOD value of **2′** for PO_4^{3-} sensing was estimated to be 0.196 μM in aqueous medium. This LOD value is lower than that of the UiO-66-NH_2 compound, which displayed a LOD of 1.25 μM.[30]

The recyclability of the detection ability of **2′** towards PO_4^{3-} ion was investigated up to two cycles. After the first cycle of fluorescence sensing experiment, the dispersed MOF material was collected by centrifugation, washed with copious amounts of water and finally dried in a conventional oven at 60 °C for 3 h. The material recovered in this way was employed in the second cycle. The compound showed already high fluorescence intensity before the addition of PO_4^{3-} solution in the second cycle and a very less increment in fluorescence intensity after the addition of PO_4^{3-} in the same cycle. Thus, **2′** showed dramatic decrease in the fluorescence *turn-on* response towards PO_4^{3-} detection in the second cycle (Figure 3.15b). Therefore, the material displayed poor recyclability of its detection capability towards PO_4^{3-} ion in the aqueous medium.

TH-2604_156122006

3.3.9 Mechanism for PO_4^{3-} Sensing

Several instrumental techniques such as FT-IR spectroscopy, N_2 sorption experiment and XRPD analysis were employed to investigate the probable mechanism of PO_4^{3-} detection by the UiO-66-N_2H_3 material. After incubation with an aqueous solution of PO_4^{3-} ion, the compound showed broad absorption bands between 900 and 1190 cm^{-1} in the IR spectrum (Figure 3.16) due to P–O stretching vibrations,[63] which confirmed the coordination of PO_4^{3-} ion with the framework of **2′**. This might indicate the complexation between the PO_4^{3-} ions and Zr–O clusters because the P–O bonds would limit their stretching vibrations, resulting in decrease their vibrational frequencies.[30] The symmetric stretching vibrations of the carboxylate groups in phosphate-incubated **2′** exhibited a blue shift (from 1385 cm^{-1} to 1392 cm^{-1}) as compared to untreated **2′**. This might provide further evidence that PO_4^{3-} ions have a coordination effect with the Zr–O clusters and weaken the interactions between the BDC-N_2H_3 linkers and Zr-O clusters, thus making the carboxylate groups more free and their vibrations stronger.[64] Moreover, the phosphate-treated **2′** showed a BET surface area of 442 m^2 g^{-1} (Figure 3.6b), which is significantly lower as compared to the untreated sample (828 m^2 g^{-1}) (Figure 3.6a). Furthermore, **2′** was treated with phosphate in different molar ratio with respect to zirconium and XRPD measurements were carried with these phosphate-treated samples. With increasing the PO_4^{3-}:Zr molar ratio, the framework of **2′** gradually collapsed (Figure 3.17) and consequently the organic linker became free. These observations indicate that the fluorescence *turn-on* response of **2′** upon addition of PO_4^{3-} solution can be attributed to the competitive coordination effect. Upon the gradual addition of PO_4^{3-} solution, the interactions between the attached carboxylate groups and the Zr–O clusters become relatively weaker as compared to the un-treated compound. The linker-to-metal charge transfer (LMCT) transition from the linker released in this way into the solution might enhance the fluorescence emission intensity (Figure 3.7b).

TH-2604_156122006

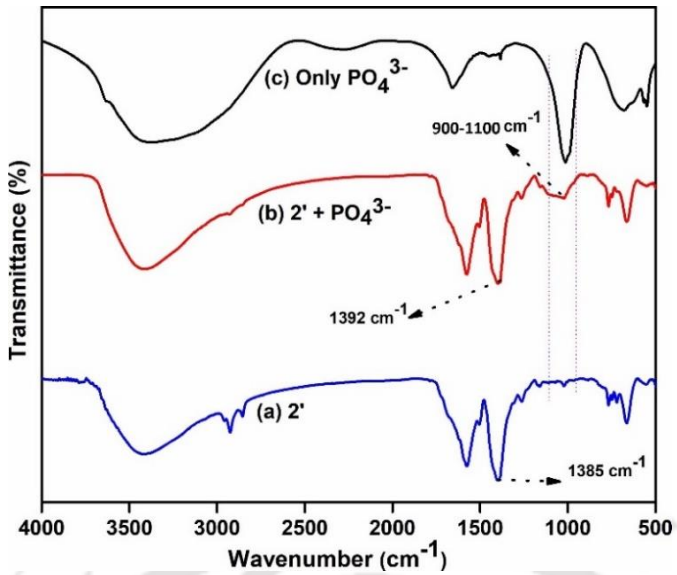

Figure 3.16 FT-IR spectra of (a) activated **2′**, (b) **2′** after treatment with Na_3PO_4 (Zr/P = 0.6) in water, and (c) only Na_3PO_4.

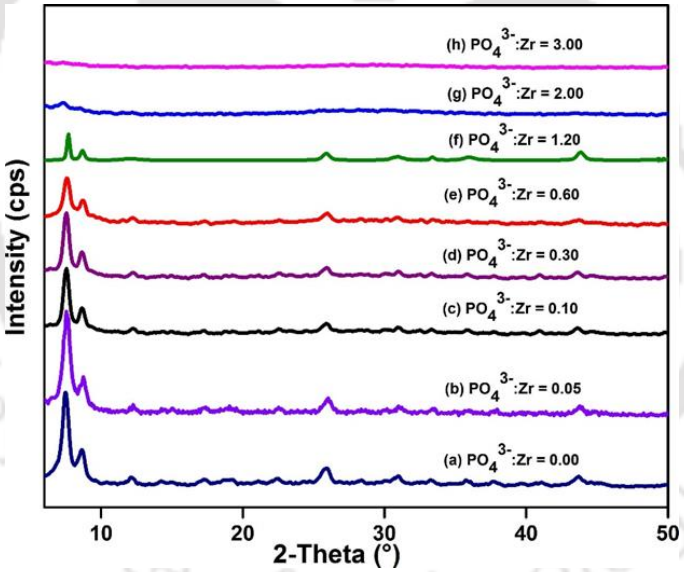

Figure 3.17 XRPD patterns of compound **2′** after treatment with different molar ratio of phosphate with respect to zirconium: **2′** after treatment with (a) PO_4^{3-}:Zr = 0.00, (b) PO_4^{3-}:Zr = 0.05, (c) PO_4^{3-}:Zr = 0.10, (d) PO_4^{3-}:Zr = 0.30, (e) PO_4^{3-}:Zr = 0.60, (f) PO_4^{3-}:Zr = 1.20, (g) PO_4^{3-}:Zr = 2.00 and (h) PO_4^{3-}:Zr = 3.00. In all cases **2′** were treated with Na_3PO_4 in water for 90 min.

3.3.10 Effect of pH for PO_4^{3-} Sensing in HEPES Buffer

We have carried out both concentration and time-dependent PO_4^{3-} sensing experiments at four different pH (pH = 3.4, 5.4, 7.4 and 9.4) values in 10 mM HEPES buffer. The

TH-2604_156122006

results (Figure 3.18) from the concentration-dependent fluorescence sensing experiments showed that the fold increments (I/I_0) in fluorescence intensity for **2′** after treatment with 400 µL of 2 mM PO_4^{3-} solution were 6.7, 26.0, 12.7 and 0.9 at pH of 3.4, 5.4, 7.4 and 9.4, respectively. Thus, the fold increment was the maximum at pH = 5.4 whereas the fold increment was the minimum at highly basic pH (pH = 9.4). The fold increment increased on increasing the solution pH from 3.4 to 5.4 but it decreased at higher pH values (pH = 7.4 and 9.4). At pH = 3.4, the degree of protonation of the PO_4^{3-} ion is higher compared to that at pH = 5.4. Hence, less amount of PO_4^{3-} ion is available for binding with Zr(IV) ion at pH = 3.4 than at pH = 5.4. As a result, **2′** showed lower fold increment at pH = 3.4 compared to that at pH = 5.4. At basic pH, partial decomposition of the framework of **2′** occurs. Moreover, in basic medium, the –NH proton of the hydrazinyl group can be deprotonated.[65] As a result, **2′** showed high fluorescence intensity at basic pH, even before the addition of PO_4^{3-} solution. Therefore, the fold increment in fluorescence intensity decreased with increment in pH from 7.4 to 9.4.

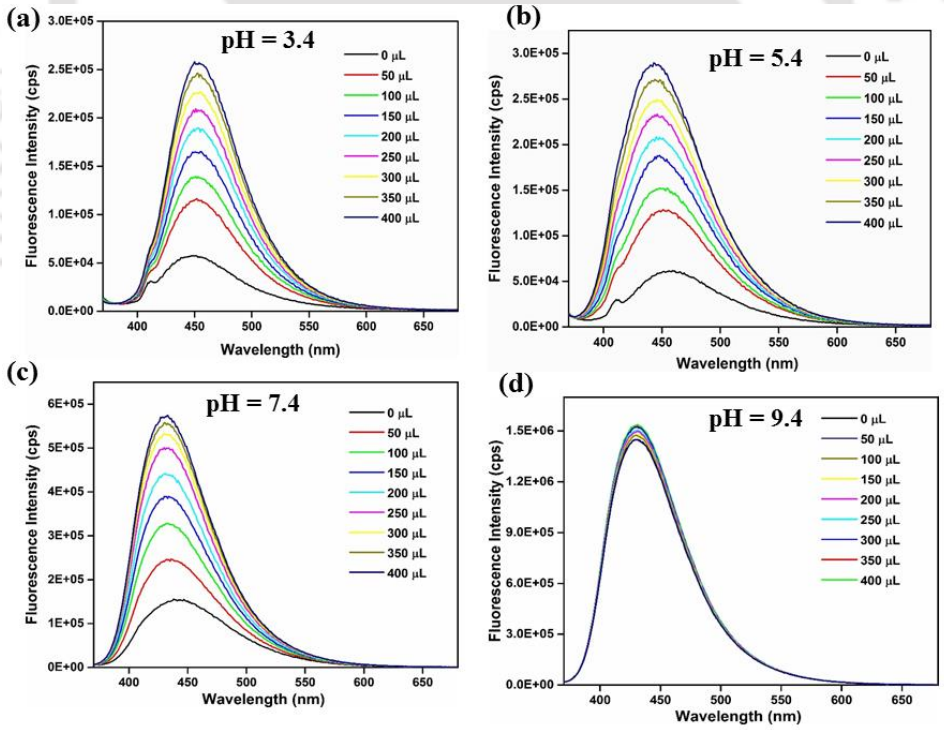

Figure 3.18 Enhancement of the fluorescence intensity of **2′** at different pH (pH = (a) 3.4, (b) 5.4, (c) 7.4 and (d) 9.4) upon gradual addition of 400 µL of 2 mM aqueous solution of PO_4^{3-} ion. **2′** were suspended in 10 mM HEPES buffer at pH = (a) 3.4, (b) 5.4, (c) 7.4 and (d) 9.4) (λ_{ex} = 360 nm, λ_{em} = 430 nm).

TH-2604_156122006

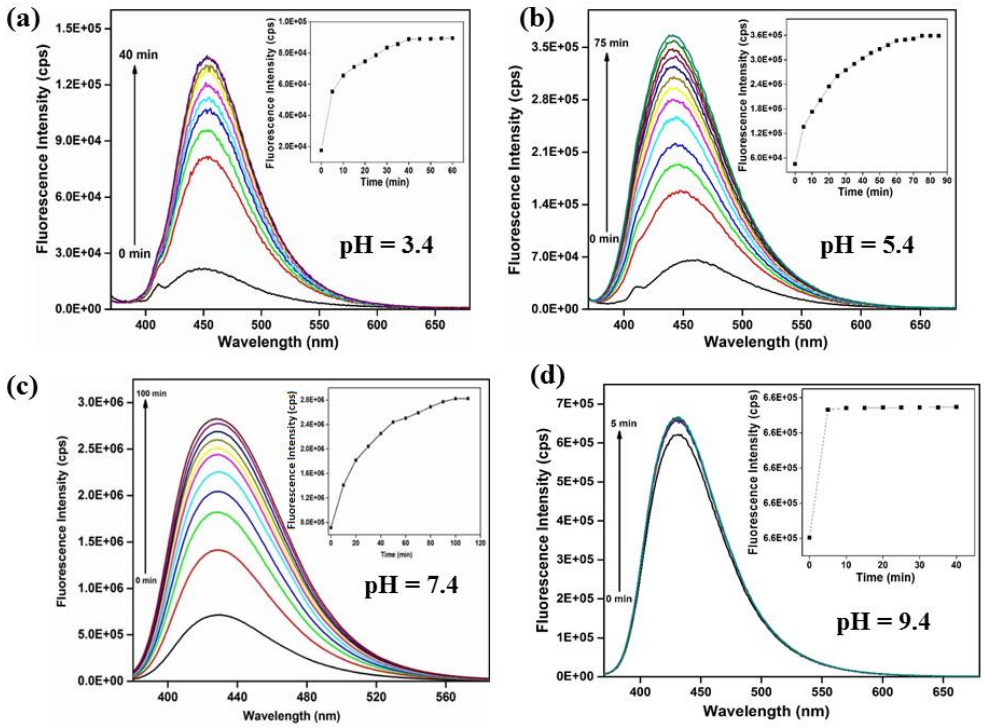

Figure 3.19 Enhancement of the fluorescence intensity of **2′** at different pH (pH = (a) 3.4, (b) 5.4, (c) 7.4 and (d) 9.4) with time upon gradual addition of 400 µL of 2 mM aqueous solution of PO_4^{3-} ion. Compound **2′** was suspended in 10 mM HEPES buffer at pH = (a) 3.4, (b) 5.4, (c) 7.4 and (d) 9.4) (λ_{ex} = 360 nm, λ_{em} = 430 nm).

The saturation times (i.e., time to reach saturation point in fluorescence intensity after the addition of 400 µL of 2 mM PO_4^{3-} solution) were 45, 75, 100 and 5 min at pH of 3.4, 5.4, 7.4 and 9.4, respectively (Figure 3.19). With increasing pH, the saturation time increased up to pH = 7.4. At pH = 9.4, **2′** was already in highly fluorescent state, even before the addition of PO_4^{3-} solution. Therefore, the fluorescence intensity of **2′** did not increase significantly with time after the addition of PO_4^{3-} solution at pH = 9.4.

3.3.11 PO_4^{3-} Sensing in Real Samples

As compound **2′** is highly sensitive towards PO_4^{3-} ion in aqueous as well as in HEPES medium, we have decided to perform the sensing experiments with real biological and environmental samples. For this purpose, we have chosen a total of six samples of three different types (water, human urine and human blood serum). We have spiked each of these samples with known concentrations of PO_4^{3-} solution. Then, we have treated the MOF probe with these spiked samples and recorded the fluorescence spectra after 90 min.

TH-2604_156122006

After the spiked-and-recovery experiments, the amount of PO_4^{3-} ion found and as well as the recovery percentages are summarized in Table 3.2. In case of all the samples, excellent recovery percentages and low RSD values make probe **2′** a smart candidate for quantifying the PO_4^{3-} concentration present in different real and complicated biological as well as environmental samples.

Table 3.2 Detection performance of **2′** for PO_4^{3-} ion in real water, human urine and human blood serum samples.

Sample Name	Na_3PO_4 Spiked (μM)	Na_3PO_4 Found[a] (μM)	Recovery (%)
Tap Water	0	5.30 ± 0.75	NA
	10	8.72 ± 0.91	87.20
	20	19.62 ± 1.93	98.10
	30	29.66 ± 1.18	98.87
Lake Water	0	5.74 ± 0.69	NA
	10	9.18 ± 3.92	91.80
	20	20.08 ± 0.15	100.40
	30	29.23 ± 0.61	97.43
Human Urine 1	0	58.21 ± 1.44	NA
	10	9.78 ± 3.27	97.80
	20	19.56 ± 1.53	97.80
	30	29.52 ± 0.92	98.40
Human Urine 2	0	63.73 ± 0.59	NA
	10	9.80 ± 1.73	98.00
	20	19.68 ± 1.42	98.40
	30	29.57 ± 1.21	98.57
Human Blood Serum 1	0	34.58 ± 0.12	NA
	10	9.73 ± 0.62	97.30
	20	19.30 ± 0.72	96.50
	30	28.42 ± 0.45	94.73
Human Blood Serum 2	0	35.98 ± 1.63	NA
	10	9.55 ± 1.98	95.5
	20	19.57 ± 1.33	97.85
	30	28.36 ± 1.13	94.53

3.3.12 Intracellular PO_4^{3-} Sensing

Before performing the live cell imaging experiment for PO_4^{3-} ion, we checked the particle size of **2′** by FE-SEM experiment. Figure 3.20 reveals that **2′** has an average

TH-2604_156122006

particle size of less than 100 nm. Thus, its particles can easily penetrate through the cell membrane.

The intrinsic phosphate species (inorganic phosphate and other phosphorylated derivatives) varies among different cell types and may correlate strongly with metabolism and energy status.[66, 67] To check the potential of **2′** to perform intracellular phosphate detection, fluorescence imaging experiments were performed in macrophage J774A.1, cervical cancer HeLa and glioblastoma U87MG cells. The unlabeled cells were healthy and they did not exhibit any blue fluorescence (Figure 3.20 a, g and m). Macrophage J774A.1 cells loaded with probe (Figure 3.20 d, J774 panel) were healthy and exhibited blue fluorescence (Figure 3.20 e, J774 panel). The superposition of phase and fluorescence indicates that the signal is coming from the cells (Figure 3.20 f, J774 panel, Superimposed). HeLa cancer cells loaded with probe showed distorted cellular morphology but this could be due to uptake of suspension of probe (Figure 3.20 g and j, HeLa panel). These cells exhibited intense bright blue fluorescence (Figure 3.20 h and k, HeLa panel, Fluorescence). The superposition of phase and fluorescence indicates that the signal is arising from the cells (Figure 3.20 i and k, HeLa panel, Superimposed). The probe loaded glioblastoma U87MG cells displayed good fluorescence signal (Figure 3.20 n and q, HeLa panel, Fluorescence), and the superposition of phase and fluorescence indicates that the signal is stemming from the cells (Figure 3.20 o and r, U87MG panel, Superimposed). The comparison of fluorescence in all three cells indicates that the fluorescence signal is more in HeLa and U87MG cells compared to the J774A.1 cells. This difference in fluorescence could be due to the inherent difference in their intracellular total phosphate level[68-70] or because of the differential level of stress inside the dissimilar cells owing to probe loading. Overall, probe **2′** has potential to detect the intracellular phosphate and it also has the potential to show difference in intracellular phosphate level.

TH-2604_156122006

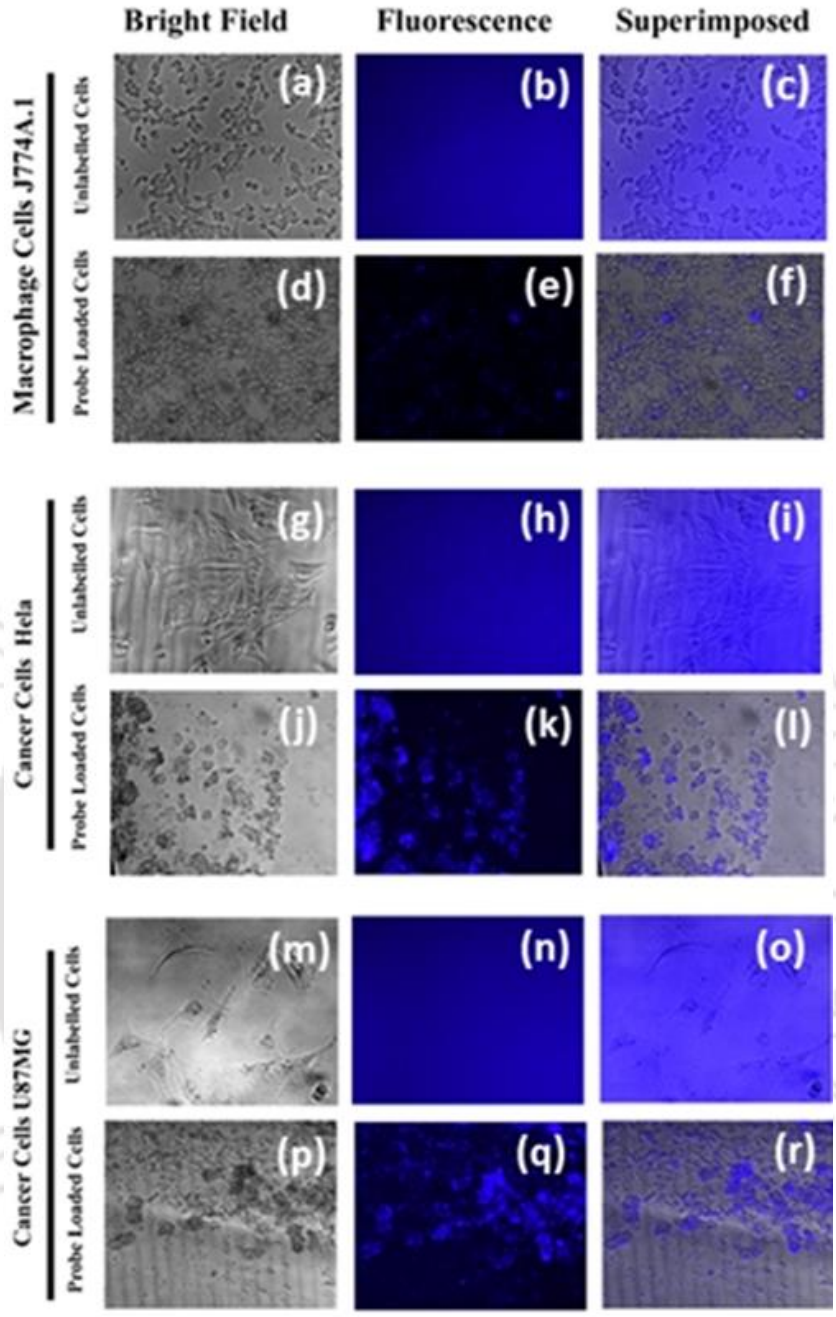

Figure 3.20 Three different type of cells, macrophage J774A.1 (J774 panel), cervical cancer HeLa (HeLa panel) and glioblastoma U87MG (U87MG panel) were either as such (a, b, g, h, m, n) or loaded with probe **2′** (d, j, p). Probe loaded cells are giving bright blue fluorescence (e, k, q) and superposition of bright field (c, i, o) and fluorescence (f, l, r) indicates that the signal is coming from the cells associated with probe (λ_{ex}= 390 nm, λ_{em}= 430 nm).

TH-2604_156122006

3.3.13 Sensing Behaviour Towards 4-NB

The fluorescence emission spectra of **2′** (Figure 3.21) were recorded in water as well as various organic solvents such as acetonitrile, methanol, ethanol, toluene, DMF and dimethylsulphoxide (DMSO).[71] Among the different solvents tested, **2′** showed the highest fluorescence emission intensity in DMSO. The compound also exhibited good fluorescence intensity in DMSO/HEPES (10 mM, pH = 7.4) buffer (v/v = 9:1) (Figure 3.21). Furthermore, the compound showed outstanding selectivity towards 4-NB over other aldehydes in DMSO/HEPES buffer (v/v = 9:1) medium. Therefore, this solvent mixture was chosen as the medium for preparing the suspension of **2′** in order to perform the sensing experiments for 4-NB.

In order to determine the potential of Zr-UiO-66-N_2H_3 as a fluorogenic sensor for 4-NB detection, fluorescence titration experiments were performed with the suspension of **2′** in DMSO/HEPES (9:1, v/v) mixure, even in the presence of potentially competitive aldehydes. The fluorescence emission (λ_{ex} = 360 nm) spectra of the suspension of **2′** were recorded in the range of 385-585 nm upon gradual addition (50 µL for each addition) of 50 mM 4-NB solution. The fluorescence emission intensities were regulated at 430 nm. As displayed in Figure 3.22, the saturation of the fluorescence intensity was observed after the addition of 400 µL of 50 mM 4-NB solution. Further addition of 4-NB solution did not result in any considerable decrease in the fluorescence intensity.

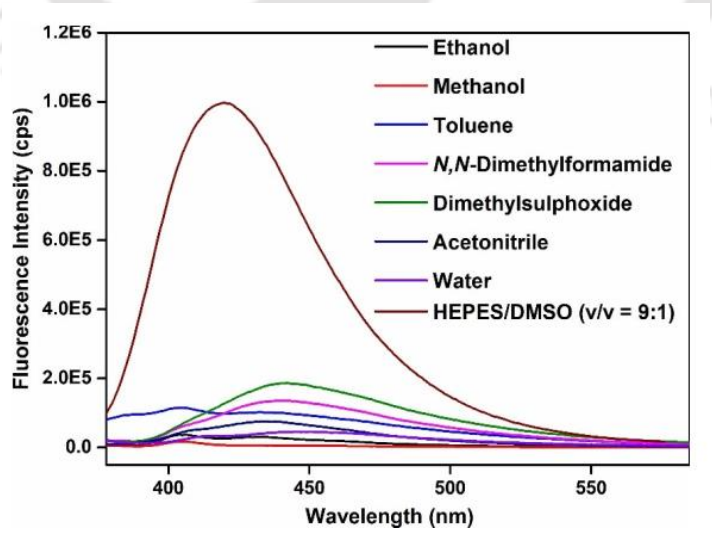

Figure 3.21 Fluorescence emission spectra of **2′** suspended in different solvents.

TH-2604_156122006

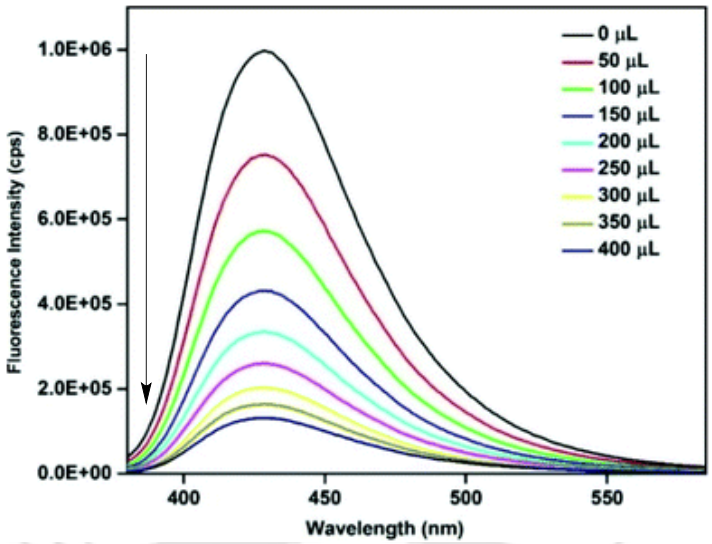

Figure 3.22 Quenching of the fluorescence intensity of **2′** (0.87 mM) by incremental addition of 400 µL of 50 mM 4-NB solution to a 3 mL stable suspension of **2′** in HEPES/DMSO (9:1, v/v) (λ_{ex} = 360 nm, λ_{em} = 430 nm).

For real-world applications of the sensor material, the high selectivity for 4-NB over other potentially competing aldehydes is highly required. Therefore, the fluorescence *turn-off* responses of **2′** towards various other aldehydes were recorded including formaldehyde, benzaldehyde, acetaldehyde, 4-chlorobenzaldehyde, valeraldehyde, butyraldehyde, crotonaldehyde, anisaldehyde, propionaldehyde, 2-nitrobenzaldehyde (2-NB) and 3-nitrobenzaldehyde (3-NB). As shown in Figure 3.23a, the addition of 4-NB solution to the suspension of **2′** in DMSO/HEPES mixture resulted in dramatic decrease (quenching efficiency = 92%) in the fluorescence emission intensity. The fluorescence queching efficiencies of all other potentially competing aldehydes were relatively less as compared to that of 4-NB (Figure 3.23b). Hence, it can be concluded that **2′** is highly selective towards 4-NB over other potentially intrusive aldehydes in DMSO/HEPES mixture.

TH-2604_156122006

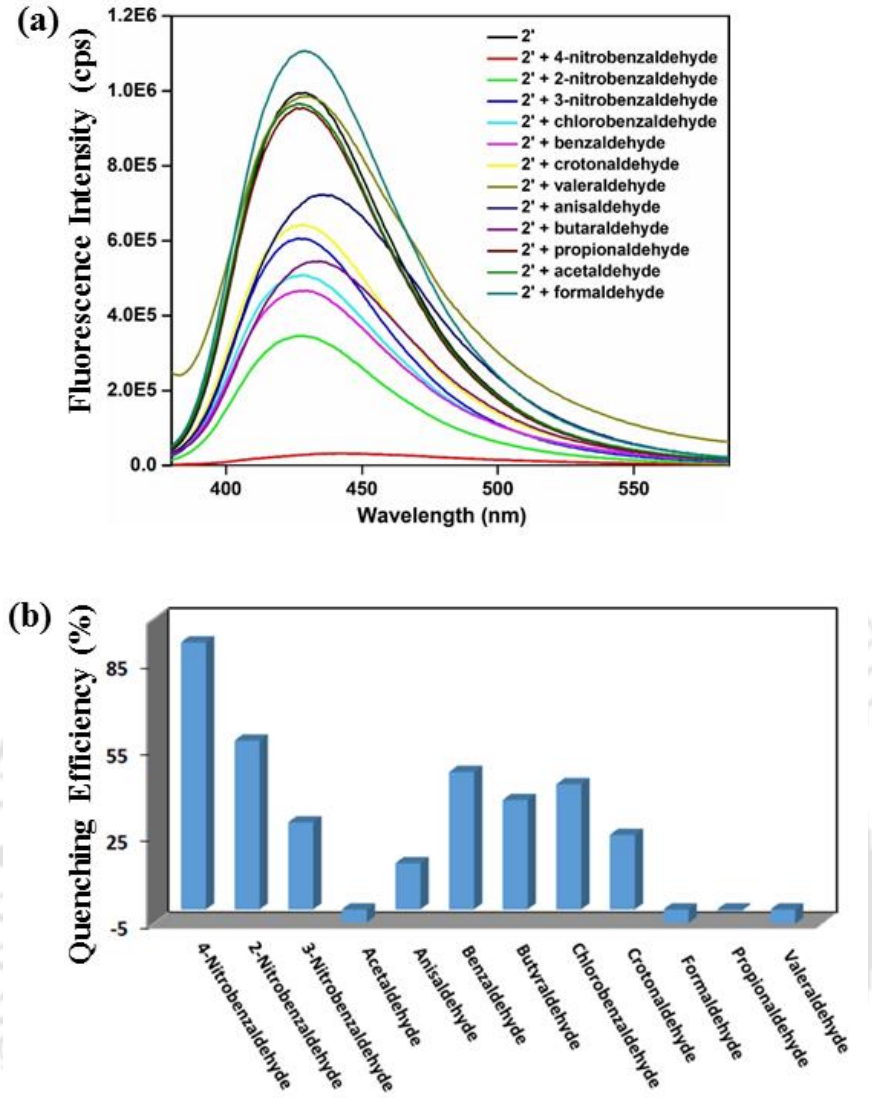

Figure 3.23 (a) Fluorescence emission spectra representing the selectivity of **2′** towards 4-NB over other competing aldehydes in HEPES/DMSO (v/v = 9:1) mixture. 400 μL of 50 mM aldehyde solutions were added and (b) Fluorescence quenching efficiencies of different aldehydes towards **2′** (0.87 mM) in DMSO/HEPES (9:1, v/v) mixture. The fluorescence spectra were collected after the addition of 400 μL of 50 mM aldehyde solutions (λ_{ex} = 360 nm, λ_{em} = 430 nm).

A fluorescent probe must show high selectivity towards the target analyte in the presence of other possibly competing analytes, which is highly required for the practical applications of a fluorescent sensor material in complex biological media.[72, 73] In order to fulfil this purpose, we have carried out competitive fluorescence titration experiments in which 4-NB solution was added to the suspension of **2′**, which also contained the possibly competing aldehydes. It is obvious from Figure 3.24a and Figure 3.24b that the outstanding

TH-2604_156122006

fluorescence quenching efficiency of the compound towards 4-NB was retained even in the presence of other possibly interfering aldehydes in DMSO/HEPES mixture. Hence, the compound showed remarkable selectivity towards 4-NB, even in the existence of other potentially interfering aldehydes.

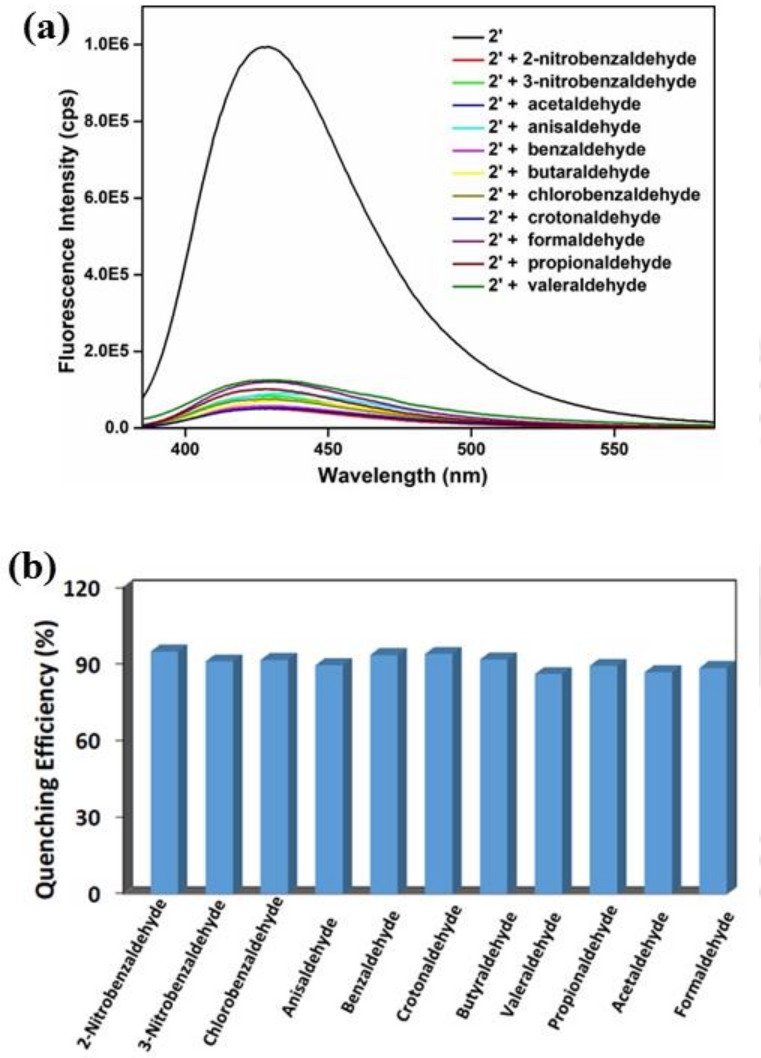

Figure 3.24 (a) Fluorescence emission spectra representing the selectivity of 4-NB towards **2′** in the presence of other competing aldehydes in HEPES/DMSO (v/v = 9:1) mixture. 400 µL of 50 mM aldehyde solutions were added. (b) Fluorescence quenching efficiencies of 400 µL of 50 mM solution of 4-NB towards **2′** (0.87 mM) (DMSO/HEPES (9:1, v/v)) in presence of 400 µL of 50 mM solution of other potentially competing aldehydes (λ_{ex} = 360 nm, λ_{em} = 430 nm).

TH-2604_156122006

The limit of detection (LOD) of **2′** for 4-NB was evaluated by regulating the fluorescence emission intensity of the compound upon gradual addition of very low concentrations of 4-NB solution in DMSO/HEPES (9:1, v/v) mixture. The LOD value was estimated by using the formula: LOD = 3σ/*m*, where σ is the standard deviation of the initial intensity of **2′** without analyte and *m* denotes the slope of the above-stated linear curve.[62] The LOD value of **2′** for 4-NB was found to be 4.7 μM.

For checking the recyclability of the detection capability of **2′** towards 4-NB, fluorescence sensing experiments were carried out up to four cycles. The compound was collected by centrifugation after the each cycle of fluorescence sensing measurement. Then, it was washed with sufficient amount of acetone and finally dried in a conventional oven at 70 °C for 30 min. After the first cycle, the fluorescence emission intensity of **2′** decreased significantly. However, there was no considerable decrease in the fluorescence emission intensity after the subsequent cycles. Therefore, the fluorescence quenching efficiency of the compound decreased considerably in the second cycle, although it remained almost unaltered in the later cycles (Figure 3.25a). Therefore, **2′** exhibited partial recyclability of its detection performance towards 4-NB.

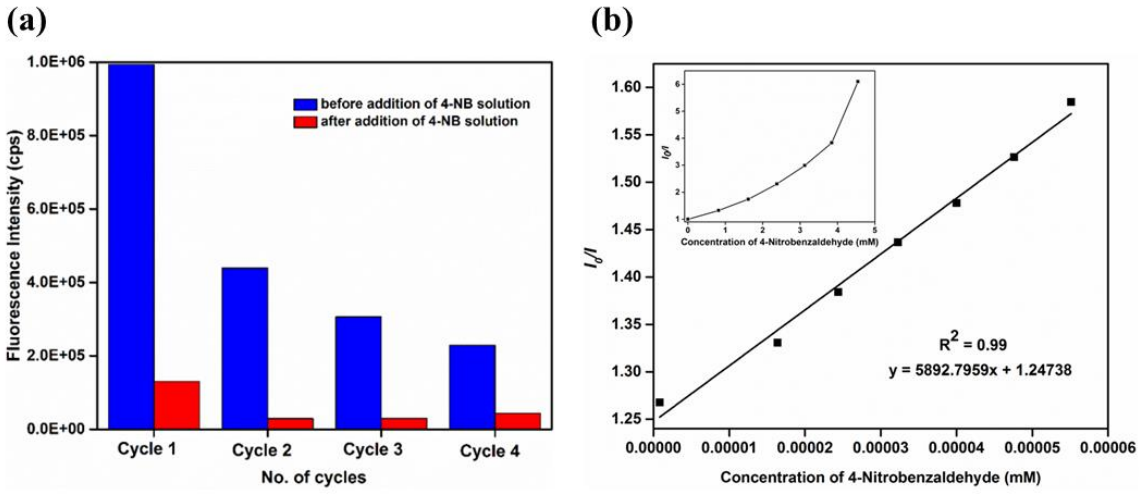

Figure 3.25 (a) Recyclability of the quenching efficiency of **2′** towards 4-NB in HEPES/DMSO (v/v = 9:1) mixture and (b) Stern-Volmer plot for the fluorescence quenching of **2′** upon the addition of 4-NB solution. Inset: non-linearity of the plot at higher concentrations of 4-NB solution.

TH-2604_156122006

For determination of the nature of the quenching (static versus dynamic) process, we have analyzed the fluorescence quenching data by the Stern-Volmer (S-V) equation, which is shown below: towards 4-NB.

$$(I_0/I) = K_{sv}[A] + 1$$

where I_0 and I denote the fluorescence intensities of **2′** in the absence and presence of the analyte respectively, [A] corresponds to the molar concentration of the analyte, and K_{sv} represents the quenching constant.[71] In Figure 3.25b, the S-V plot for quenching the fluorescence intensity of **2′** by 4-NB is displayed. The value of K_{sv} for 4-NB, which was determined from this plot, was found to be 0.59 $\times 10^4$ M^{-1}. The S-V plot is linear in nature in the lower concentration range of 4-NB, although it shows non-linearity in the higher concentration range. These results suggest that either static or dynamic quenching process is occurring in this system.[62, 71, 74, 75]

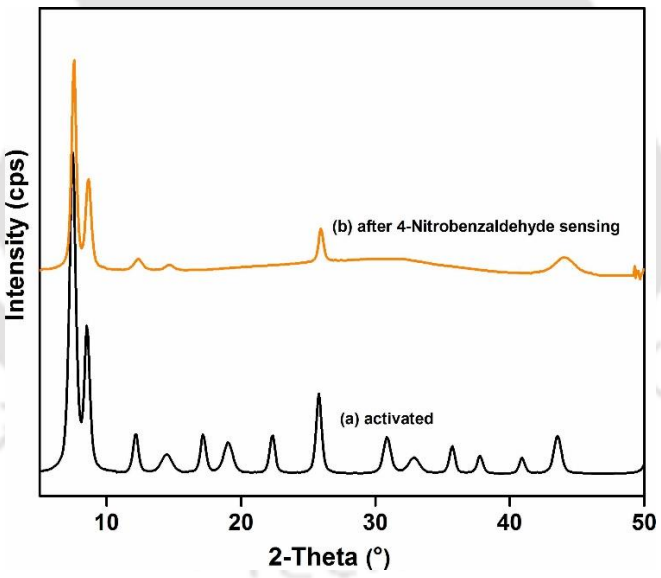

Figure 3.26 XRPD patterns of compound **2′** in different forms: (a) activated and (g) after 4-NB sensing experiment.

3.3.14 Mechanism for the Sensing of 4-NB

It is very well known that amine compounds form imines upon condensation with aldehyde compounds. All the aldehydes are supposed to form imine bond with the –$NHNH_2$ moiety attached with the BDC-$NHNH_2$ linker. Among all the selected aldehydes,

TH-2604_156122006

the electron withdrawing effect of 4-NB upon imine formation will be higher as compared to the others due to the long conjugation of the imine group with the electron withdrawing nitro group at the para position. As a result, the nitro group of 4-NB reduces the electron density from the imine group much more than the other aldehydes. Hence, the electron density in the BDC-$NHNH_2$ linker is reduced in a larger extent for 4-NB as compared to the other aldehydes. Therefore, the highest fluorescence quenching effect is observed for 4-NB among all the chosen aldehydes.[76, 77]

In order to prove the proposed sensing mechanism, the XRPD pattern of 4-NB treated sample was recorded (Figure 3.26). It showed that the structure collapse mechanism is ruled out for sensing of 4-NB. Afterwards, we have performed FT-IR spectroscopy, mass spectrometry and time-resolved photoluminescence lifetime experiment also. In the mass spectrum of the **2′** (without treatment of 4-NB), (Figure 3.27) there is a peak at (+ESI) m/z = 195.0497, whereas 4-NB treated **2′** (Figure 3.28) showed a peak at (+ESI) m/z = 328.0631, which corresponds to (E)-2-(2-(4-nitrobenzylidene)hydrazinyl) terephthalic acid. This observation confirms that there is an imine product formed by the condensation reaction between hydrazine functionalized BDC linker and 4-NB. In the FT-IR spectrum of untreated **2′** there is no peak at around 1630 cm^{-1} whereas there is a new peak at 1637 cm^{-1} in the IR spectrum of **2′** treated with 4-NB (Figure 3.29). This peak corresponds to the imine bond formed between the hydrazine group of BDC-N_2H_3 linker and the aldehyde group of 4-NB. Hence, from FT-IR spectroscopy and mass spectrometry, it can be confirmed that the reaction of **2′** with 4-NB forms the imine compound.

TH-2604_156122006

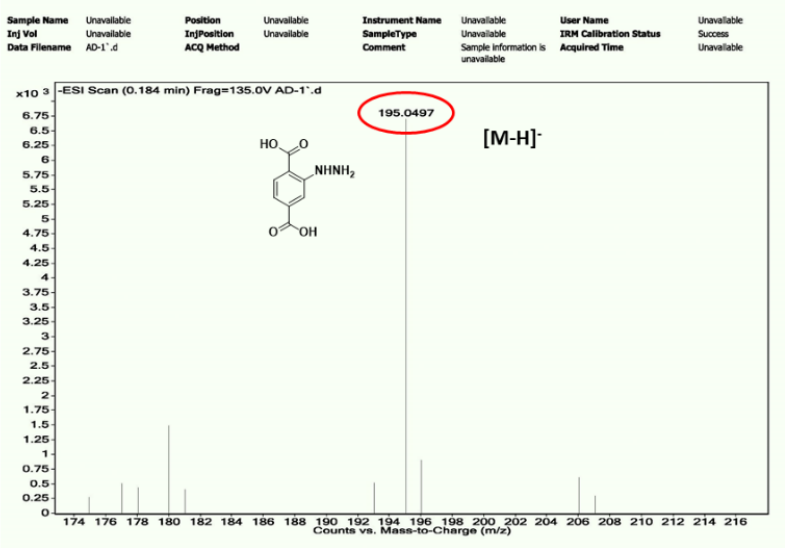

Figure 3.27 ESI-MS spectrum of the un-treated **2′** (digested in MeOH/HF). The spectrum shows m/z (negative ion mode) peak at 195.0497, which corresponds to $(M\text{-}H)^-$ ion (M = mass of $H_2BDC\text{-}N_2H_3$ linker).

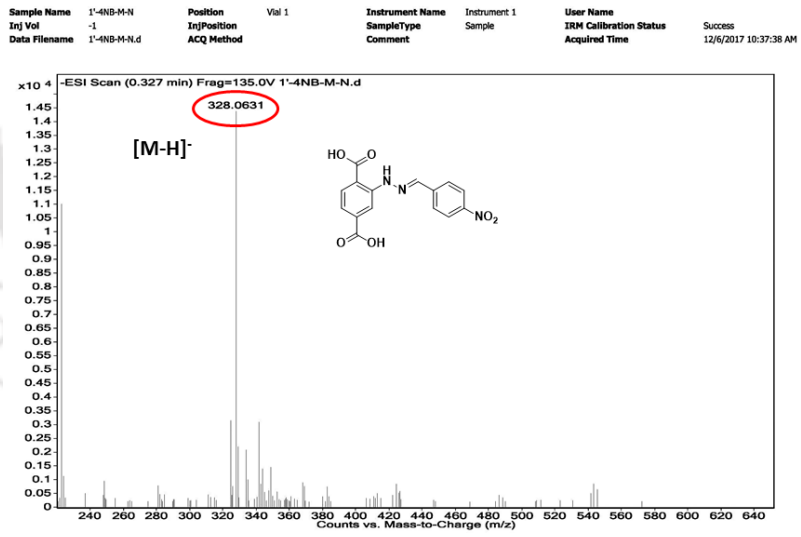

Figure 3.28 ESI-MS spectrum of the 4-NB treated **2′** (digested in MeOH/HF). The spectrum shows m/z (negative ion mode) peak at 328.0631, which corresponds to $(M\text{-}H)^-$ ion of (*E*)-2-(2-(4-nitrobenzylidene)hydrazinyl)terephthalic acid linker.

TH-2604_156122006

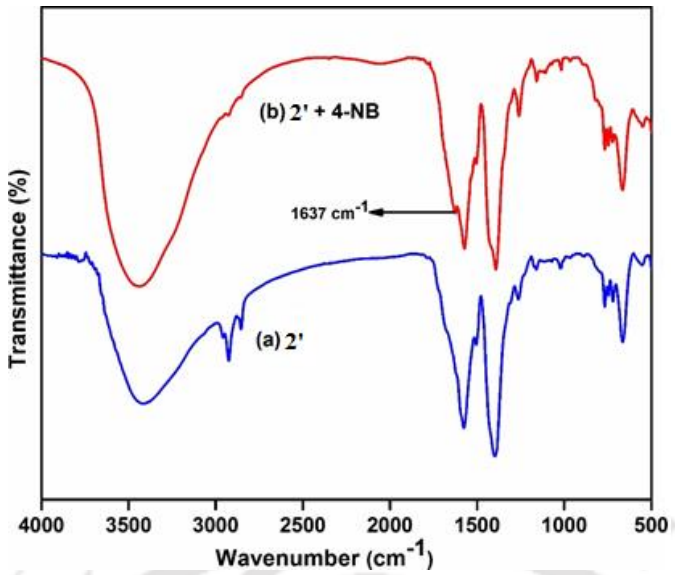

Figure 3.29 FT-IR spectra of **2′** (a) before and (b) after 4-NB sensing.

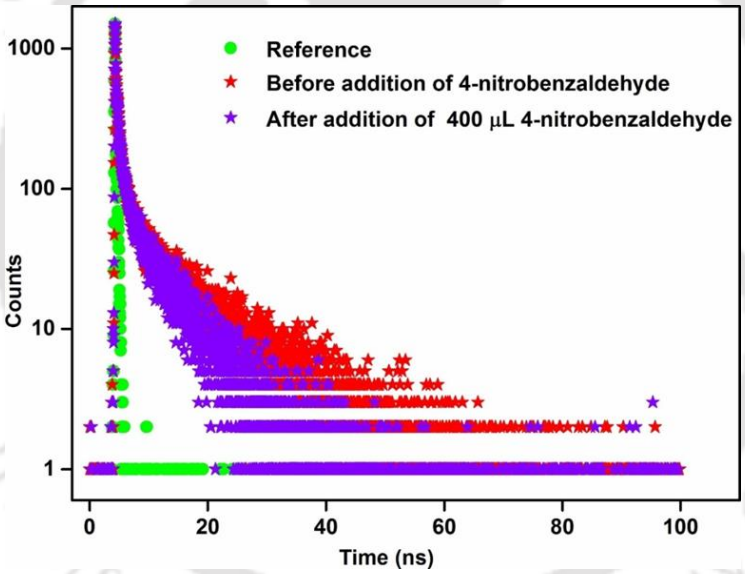

Figure 3.30 Lifetime decay profile of **2′** before and after the addition of 400 μL of 50 mM 4-NB solution.

The two quenching mechanisms (static and dynamic) can be differentiated by studying time-resolved fluorescence experiments of luminescence decay of the fluorophore compound at different concentrations of the quencher. If the fluorescence lifetime of the sensor material decreases, the quenching process is considered as dynamic because additional relaxation of the excited-state lifetime in this process results from the collision with the quencher. If the fluorescence lifetime of the sensor material does not change after

TH-2604_156122006

increasing addition of the quencher, it is regarded as a static quenching process.[75, 78, 79] Figure 3.30 represents the lifetime decay profile of **2′** before and after the addition of 400 µL of 50 mM 4-NB solution. As displayed in (Table 3.3), the average excited-state lifetime ($\langle\tau\rangle^*$) of **2′** are 2.70 and 1.52 ns before and after the addition of 400 µL of 50 mM 4-NB solution, respectively. Hence, it can be concluded that the fluorescence quenching mechanism in this system is mainly static in nature.

Table 3.3 Average excited-state lifetime ($<\tau>^*$) values of **2′** before and after the addition of 400 µL of 50 mM 4-NB solution (λ_{ex} = 360 nm, λ_{em} = 430 nm).

Volume of 4-NB Solution Added (µL)	B_1	B_2	a_1	a_2	τ_1 (ns)	τ_2 (ns)	$<\tau>^*$ (ns)
0	0.3575	0.0070	0.744	0.256	0.516	9.068	2.704
400	0.4874	0.0101	0.787	0.213	0.427	5.557	1.519

* $<\tau> = a_1\tau_1 + a_2\tau_2$

3.4 Conclusions

We have successfully synthesized and characterized a hydrazine-functionalized Zr(IV) MOF material **2**, which has the UiO-66 framework topology. The compound was synthesized by heating a mixture of $ZrOCl_2 \cdot 8H_2O$, $H_2BDC\text{-}N_2H_3$ linker and benzoic acid ($ZrOCl_2 \cdot 8H_2O$/$BDC\text{-}N_2H_3$/benzoic acid molar ratio = 1:1:30) in DMF at 120 °C for 24 h. The activated compound (**2′**) showed moderate thermal stability up to 200 °C. It retained its crystallinity and hence structural robustness when exposed to water, acetic acid and 1(M) HCl solutions. As verified by the N_2 sorption experiments, the specific BET surface area of **2′** is 828 $m^2\ g^{-1}$. We have employed **2′** as a fluorescent *turn-on* probe for the selective detection of phosphate (both *in vivo* and *in vitro*) and also as a fluorescent *turn-off* probe for the selective sensing of 4-NB in DMSO/HEPES (9:1, v/v) medium. Even in the presence of interfering intrusive species, the probe retains its high selectivity. The probe also features high sensitivity. Its detection limits for PO_4^{3-} ion and 4-NB are 0.196 and 4.7 µM, respectively. Probe **2′** is able to detect phosphate in living cells. It can also respond towards the difference in intracellular phosphate level. The MOF probe can be

TH-2604_156122006

used efficiently for determining PO_4^{3-} ion in real samples such as tap water, lake water, human urine and human blood serum. Furthermore, it can be utilized for the *in vitro* detection of 4-NB in the fluid secreted from eye upon exposure to sunlight after applying chloramphenicol eye-drop.

3.5 References

1. W.-L. Cheng, J.-W. Sue, W.-C. Chen, J.-L. Chang and J.-M. Zen, *Anal. Chem.*, 2010, **82**, 1157–1161.
2. K.-Y. A. Lin, S.-Y. Chen and A. P. Jochems, *Mater. Chem. Phys.*, 2015, **160** 168-176.
3. C. Warwick, A. Guerreiro and A. Soares, *Biosens. Bioelectron.*, 2013, **41** 1–11.
4. C. Dai, C.-X. Yang and X.-P. Yan, *Anal. Chem.*, 2015, **87**, 11455−11459.
5. B. Henegouwen and G. M. J., *J. Photochem. Photobiol*, 1991, **10**, 183-210.
6. H. Bauer and S. M. Rosenthal, *J. Am. Chem. Soc.*, 1944, **66**, 611-614.
7. H. Lowry, N. J. Rosebrough, A. L. Farr and R. J. Randall, *J. Biol. Chem.*, 1951, **193**, 265-275.
8. O. M. Yaghi, M. O'Keeffe, N. W. Ockwig, H. K. Chae, M. Eddaoudi and J. Kim, *Nature*, 2003, **423**, 705-714.
9. S. Kitagawa, R. Kitaura and S. Noro, *Angew. Chem. Int. Ed*, 2004, **43**, 2334–2375.
10. G. Férey, *Chem. Soc. Rev.*, 2008, **37**, 191–214.
11. J. Lee, O. K. Farha, J. Roberts, K. A. Scheidt, S. T. Nguyen and J. T. Hupp, *Chem. Soc. Rev.*, 2009, **38**, 1450–1459.
12. L. Ma, C. Abney and W. Lin, *Chem. Soc. Rev.*, 2009, **38**, 1248−1256.
13. D. Banerjee, A. J. Cairns, J. Liu, R. K. Motkuri, S. K. Nune, C. A. Fernandez, R. Krishna, D. M. Strachan and P. K. Thallapally, *Acc. Chem. Res.* , 2015, **48**, 211−219.
14. J. Liu, Y. Wei, P. Li, Y. Zhao and R. Zou, *J. Phys. Chem. C*, 2017, **121**, 13249−13255.
15. C. Orellana-Tavra, R. J. Marshall, E. F. Baxter, I. A. La´zaro, A. Tao, A. K. Cheetham, R. S. Forgan and D. Fairen-Jimenez, *J. Mater. Chem. B*, 2016, **4**, 7697-7707.

TH-2604_156122006

16. S. Rojas, F. J. Carmona, C. R. Maldonado, P. Horcajada, T. Hidalgo, C. Serre, J. A. R. Navarro and E. Barea, *Inorg. Chem.* , 2016, **55**, 2650−2663.
17. E. Gkaniatsou, C. Sicard, R. Ricoux, J.-P. Mahy, N. Steunou and C. Serre, *Mater. Horiz.*, 2017, **4**, 55-63.
18. M. B. Majewski, A. J. Howarth, P. Li, M. R. Wasielewski, J. T. Hupp and O. K. Farha, *CrystEngComm*, 2017, **19**, 4082–4091.
19. D. Feng, T.-F. Liu, J. Su, M. Bosch, Z. Wei, W. Wan, D. Yuan, Y.-P. Chen, X. Wang, K. Wang, X. Lian, Z.-Y. Gu, J. Park, X. Zou and H.-C. Zhou, *Nat. Commun.*, 2015, **6**, 5979-5987.
20. R. Dalapati, B. Sakthivel, M. K. Ghosalya, A. Dhakshinamoorthy and S. Biswas, *CrystEngComm*, 2017, **19**, 5915–5925.
21. S. Sen, N. N. Nair, T. Yamada, H. Kitagawa and P. K. Bharadwaj, *J. Am. Chem. Soc.*, 2012, **134**, 19432−19437.
22. S. Nandi, H. Reinsch, S. Banesh, N. Stock, V. Trivedi and S. Biswas, *Dalton Trans.*, 2017, **46**, 12856–12864.
23. S. S. Nagarkar, T. Saha, A. V. Desai, P. Talukdar and S. K. Ghosh, *Sci. Rep.*, 2014, **4**, 7053-7058.
24. M. Kandiah, M. H. Nilsen, S. Usseglio, S. Jakobsen, U. Olsbye, M. Tilset, C. Larabi, E. A. Quadrelli, F. Bonino and K. P. Lillerud, *Chem. Mater.*, 2010, **22**, 6632–6640.
25. X. Liu, N. K. Demir, Z. Wu and K. Li, *J. Am. Chem. Soc.*, 2015, **137**, 6999−7002.
26. B. V. D. Voorde, I. Stassen, B. Bueken, F. Vermoortele, D. D. Vos, R. Ameloot, J.-C. Tan and T. D. Bennett, *J. Mater. Chem. A*, 2015, **3**, 1737–1742.
27. M. L. Pinto, S. Dias and J. O. Pires, *ACS Appl. Mater. Interfaces*, 2013, **5**, 2360−2363.
28. Z. Wang, H. Ren, S. Zhang, F. Zhang and J. Jin, *J. Mater. Chem. A*, 2017, **5**, 10968–10977.
29. D. J. Tranchemontagne, J. L. Mendoza-Corte´s, M. O'Keeffe and O. M. Yaghi, *Chem.Soc.Rev.*, 2009, **38**, 1257–1283
30. J. Yang, Y. Dai, X. Zhu, Z. Wang, Y. Li, Q. Zhuang, J. Shi and J. Gu, *J. Mater. Chem. A*, 2015, **3**, 7445–7452.
31. G.-Y. Wang, C. Song, D.-M. Kong, W.-J. Ruan, Z. Chang and Y. Li, *J. Mater. Chem. A*, 2014, **2**, 2213–2220.

TH-2604_156122006

32. B. Gole, A. K. Bar and P. S. Mukherjee, *Chem. Commun.*, 2011, **47**, 12137-12139.
33. S. Okorochenkov, K. Burglova, I. Popa and J. Hlavac, *Org. Lett.*, 2015, **17**, 180−183.
34. S. J. Deka, A. Roy, V. Ramakrishnan, D. Manna and V. Trivedi, *Chem. Biol. Drug Des.*, 2017, **89**, 953–963.
35. R. Deshmukh and V. Trivedi, *PLoS One*, 2014, **9**, e103706.
36. B. Muthuraj, S. Layek, S. N. Balaji, V. Trivedi and P. K. Iyer, *ACS Chem. Neurosci.*, 2015, **6**, 1880-1891.
37. N. Stock and S. Biswas, *Chem. Rev.*, 2012, **112**, 933–969.
38. A. Buragohain and S. Biswas, *CrystEngComm*, 2016, **18**, 4374–4381.
39. R. Dalapati, S. N. Balaji, V. Trivedi, L. Khamari and S. Biswas, *Sens. Actuators, B*, 2017, **245** 1039–1049.
40. A. Schaate, P. Roy, A. Godt, J. Lippke, F. Waltz, M. Wiebcke and P. Behrens, *Chem. Eur. J.*, 2011, **17**, 6643 – 6651.
41. J. H. Cavka, S. Jakobsen, U. Olsbye, N. Guillou, C. Lamberti, S. Bordiga and K. P. Lillerud, *J. Am. Chem. Soc.*, 2008, **130**, 13850–13851
42. L. Valenzano, B. Civalleri, S. Chavan, S. Bordiga, M. H. Nilsen, S. Jakobsen, K. P. Lillerud and C. Lamberti, *Chem. Mater.*, 2011, **23**, 1700–1718.
43. M. R. Destefano, T. Islamoglu, S. J. Garibay, J. T. Hupp and O. K. Farha, *Chem. Mater.*, 2017, **29**, 1357−1361.
44. D. Cunha, C. Gaudin, I. Colinet, P. Horcajada, G. Maurin and C. Serre, *J. Mater. Chem. B*, 2013, **1**, 1101–1108.
45. Y. Luan, Y. Qi, Z. Jin, X. Peng, H. Gaoa and G. Wang, *RSC Adv.*, 2015, **5**, 19273-19278
46. X. Du, Y. Luan, F. Yang, D. Ramella and X. Shu, *New J. Chem.*, 2017, **41**, 4400-4405.
47. A. J. Howarth, Y. Liu, P. Li, Z. Li, T. C. Wang, J. T. Hupp and O. K. Farha, *Nat. Rev. Mater.*, 2016, **1**, 1-15.
48. M. J. Katz, Z. J. Brown, Y. J. Colo´n, P. W. Siu, K. A. Scheidt, R. Q. Snurr, J. T. Hupp and O. K. Farha, *Chem. Commun.*, 2013, **49**, 9449-9451.
49. S. J. Garibay and S. M. Cohen, *Chem. Commun.*, 2010, **46**, 7700–7702.
50. M. Kim, S. J. Garibay and S. M. Cohen, *Inorg. Chem.*, 2011, **50**, 729–731.

TH-2604_156122006

51. Y. Dong, H. Zhang, F. Lei, M. Liang, X. Qian, P. Shen, H. Xu, Z. Chen, J. Gao and J. Yao, *J. Solid State Chem.*, 2017, **245**, 160–163.
52. I. Ahmed, N. A. Khan and S. H. Jhung, *Chem. Eng. J.*, 2017, **321** 40–47.
53. R. Dalapati, B. Sakthivel, A. Dhakshinamoorthy, A. Buragohain, A. Bhunia, C. Janiak and S. Biswas, *CrystEngComm*, 2016, **18**, 7855–7864.
54. F. Ragon, B. Campo, Q. Yang, C. Martineau, A. D. Wiersum, A. Lago, V. Guillerm, C. Hemsley, J. F. Eubank, M. Vishnuvarthan, F. Taulelle, P. Horcajada, A. Vimont, P. L. Llewellyn, M. Daturi, S. Devautour-Vinot, G. Maurin, C. Serre, T. Devic and G. Clet, *J. Mater. Chem. A*, 2015, **3**, 3294–3309.
55. L. Shen, R. Liang, M. Luo, F. Jing and L. Wu, *Phys. Chem. Chem. Phys.*, 2015, **17**, 117-121.
56. G.-Y. Wang, C. Song, D.-M. Kong, W.-J. Ruan, Z. Chang and Y. Li, *J. Mater. Chem. A* 2014, **2**
57. X.-C. Yi, M.-X. Huang, Y. Qi and E.-Q. Gao, *Dalton Trans.*, 2014, **43**, 3691–3697.
58. S. Wang, J. Wang, W. Cheng, X. Yang, Z. Zhang, Y. Xu, H. Liu, Y. Wu and M. Fang, *Dalton Trans.*, 2015, **44**, 8049–8061.
59. K. S. Asha, K. Bhattacharyya and S. Mandal, *J. Mater. Chem. C*, 2014, **2**, 10073–10081.
60. Z.-Z. Lu, R. Zhang, Y.-Z. Li, Z.-J. Guo and H.-G. Zheng, *J. Am. Chem. Soc.*, 2011, **133**, 4172–4174.
61. P. A. Jr, Y. Liu, M. A. Palacios, T. Minami, Z. Wang and R. Nishiyabu, *Chem. Eur. J.*, 2013, **19**, 8497 – 8506.
62. A. Das and S. Biswas, *Sens. Actuators, B*, 2017, **250** 121–131.
63. C. Luengo, M. Brigante, J. Antelo and M. Avena, *J. Colloid Interface Sci.*, 2006, **300**, 511–518.
64. X. Zhu, J. Gu, Y. Wang, B. Li, Y. Li, W. Zhao and J. Shi, *Chem. Commun.*, 2014, **50**, 8779-8782
65. R. Dalapati, S. Nandi, H. Reinsch, B. K. Bhunia, B. B. Mandal, N. Stock and S. Biswas, *CrystEngComm*, 2018, **20**, 4194-4201.
66. B. L. Foster, K. A. Tompkins, R. B. Rutherford, H. Zhang, E. Y. Chu, H. Fong and M. J. Somerman, *Birth Defects Res. Part C*, 2008, **84**, 281-314.
67. A. H. Malik, S. Hussain, A. S. Tanwar, S. Layek, V. Trivedi and P. K. Iyer, *Analyst*, 2015, **140**, 4388-4392.

TH-2604_156122006

68. M. Nakajima, M. Nagahashi, O. M. Rashid, K. Takabe and T. Wakai, *Tumor Biol.*, 2017, **39**, 1-9.
69. A. Maiti, K. Takabe and N. C.Hait, *Cell. Signalling*, 2017, **32**, 85-92.
70. L. E. Guo, J. F. Zhang, X. Y. Liu, L. M. Zhang, H. L. Zhang, J. H. Chen, X. G. Xie, Y. Zhou, K. Luo and J. Yoon, *Anal. Chem.*, 2015, **87**, 1196−1201.
71. A. Buragohain, M. Yousufuddin, M. Sarma and S. Biswas, *Cryst. Growth Des.* , 2016, **16**, 842−851.
72. F. V. Mansano, R. M. A. Kazaoka, G. E. Ronsein, F. M. Prado, T. C. Genaro-Mattos, M. Uemi, P. D. Mascio and S. Miyamoto, *Anal. Chem.*, 2010, **82**, 6775–6781.
73. M. Li, L. Shi, T. Xie, C. Jing, G. Xiu and Y.-T. Long, *ACS Sens.*, 2017, **2**, 263−267.
74. M. SK and S. Biswas, *CrystEngComm*, 2016, **18**, 3104–3113.
75. X. Sun, Y. Wang and Y. Lei, *Chem. Soc. Rev.*, 2015, **44**, 8019-8061
76. M. Ganguly, J. Pal, C. Mondal, A. Pal and T. Pal, *Dalton Trans.*, 2015, **44**, 4370–4379.
77. K. Ngamdee, S. Martwiset, T. Tuntulani and W. Ngeonte, *Sens. Actuators, B*, 2012, **173**, 682-691.
78. A. Ueno, I. Suzuki and T. Osa, *J. Am. Chem. Soc.*, 1989, **11**, 6391-6397
79. A.-Q. Gong and X.-S. Zhu, *J. Pharm. Anal.*, 2013, **3**, 415–420.

TH-2604_156122006

Highly Active Urea-Functionalized Zr(IV)-UiO-67 Metal–Organic Framework as Hydrogen Bonding Heterogeneous Catalyst for Friedel–Crafts Alkylation

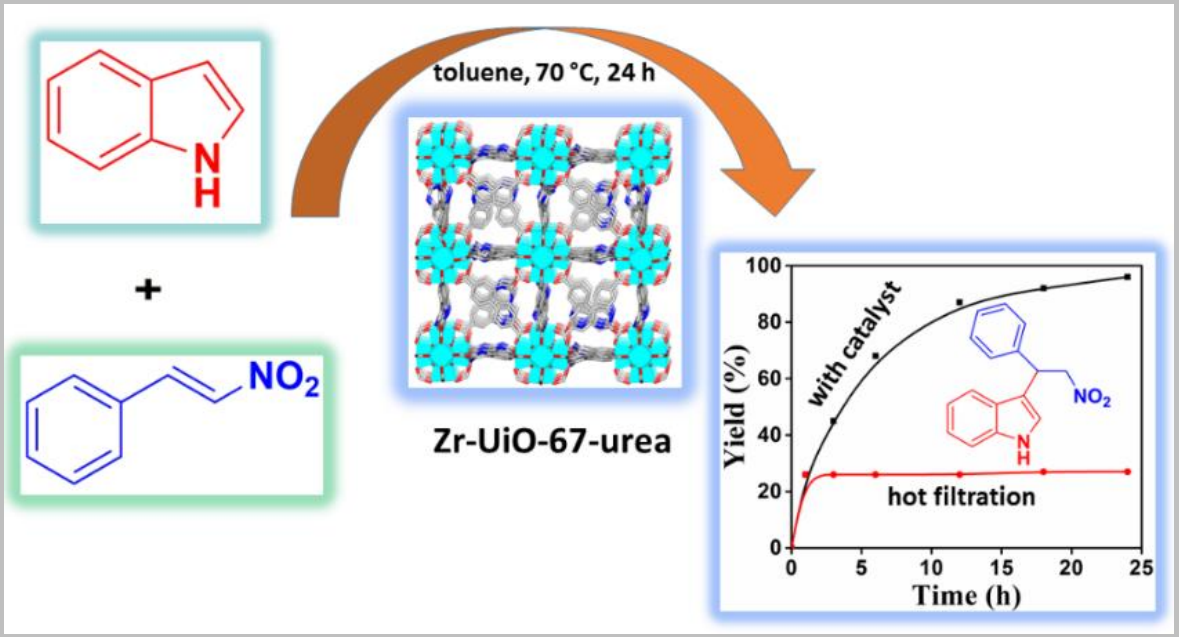

Chapter 4

4.1 Introduction

The Friedel-Crafts alkylation reaction of indoles with β-nitrostyrene is one of the fundamental organic reactions often catalyzed by the presence of Lewis acids leading to C-C bond formation.[1-4] Among these substrates, nitroalkenes are one of the preferred Michael acceptors widely used in this reaction due to the strong electron-withdrawing nature of nitro group[5] and have been extensively used in organic synthesis.[6] Furthermore, Friedel-Crafts alkylation reactions between arenes and nitroalkenes have been reported with a wide range of homogeneous Lewis acid catalysts.[7-11] Although this reaction can afford asymmetric product, there are limited examples of these types of reactions catalyzed by Lewis acids with high enantiomeric values due to the significant restrictions on the substrates.[12-15]

Hydrogen-bond-donating (HBD) catalysis has been shown to be an effective approach as an alternative to Lewis acid activation.[16-18] This type of catalysis typically uses urea or thiourea as the core moieties capable of forming two-point hydrogen bonding with their acidic N−H bonds. For example, a wide range of reactions have been reported with very high yield and selectivity by employing HBD catalysis including Strecker reactions,[19] Diels−Alder reactions,[20] Claisen rearrangements,[21] Mannich reactions[22] and Friedel−Crafts reactions.[23] Although HBD catalysts have been frequently employed in many reactions as commented earlier, the competency of H-bond donors present in HBD catalysts significantly lead to dimerization and oligomerization through hydrogen bonding of catalyst molecules to each other.[24, 25] As a result, HBD catalysts undergo self-quenching to produce unproductive interactions, thus strongly affecting the catalyst solubility and reactivity. One of the effective strategies to overcome these issues in HBD catalysis is to incorporate in MOFs with defined environments and accessibility (Scheme 1). With this aim, the present work reports the synthesis of UiO-67 MOF using urea-functionalized 4,4′-biphenyldicarboxylic acid as the linker and $ZrCl_4$ as a source of central metal ion with accessible N-H bonds to form hydrogen bonding to activate the substrate in the Friedel-Crafts reaction between indole and β-nitrostyrene.

The growing interests in metal-organic frameworks (MOFs) have originated from their structural varieties, possibility of incorporation of various functional groups (which can act as recognition sites for different molecules and ions) without hampering the framework topology and likely applications in the field of gas storage and separation, magnetism, drug

TH-2604_156122006

delivery, optoelectronics, heterogeneous catalysis and sensing of small organic molecules, metal ions, toxic anions, toxic molecules, nitroaromatic explosives, gasotransmitters, etc.[27-37] In particular, Zr(IV) MOFs have some special features like huge surface area, high thermal and chemical stability and low toxicity.[38-49] These features of Zr(IV)-based MOFs are highly preferred for applications in heterogeneous catalysis.

In this chapter, a new Zr(IV) MOF material (**3**) is presented, which has an analogous structure as UiO-67[50] and consists of an urea-functionalized biphenyl-4,4′-dicarboxylic (H_2**L**) linker. The incorporation of the urea functionality in the organic linker helps the activated MOF material (**3′**) through HBD catalysis to accomplish Friedel-Crafts alkylation of indole with β-nitrostyrene to achieve industrially relevant pharmaceutical analogues (Scheme 4.1).[26, 51-58] In addition, the catalyst stability has been also surveyed by performing reusability and hot filtration experiments. The substrate scope and the effect of metal salt as well as linker in the catalysis have been also presented here separately. Catalyst **3′** has been demonstrated to result in extremely high yield (97%) for the Friedel-Crafts alkylation reaction of indoles with β-nitrostyrene.

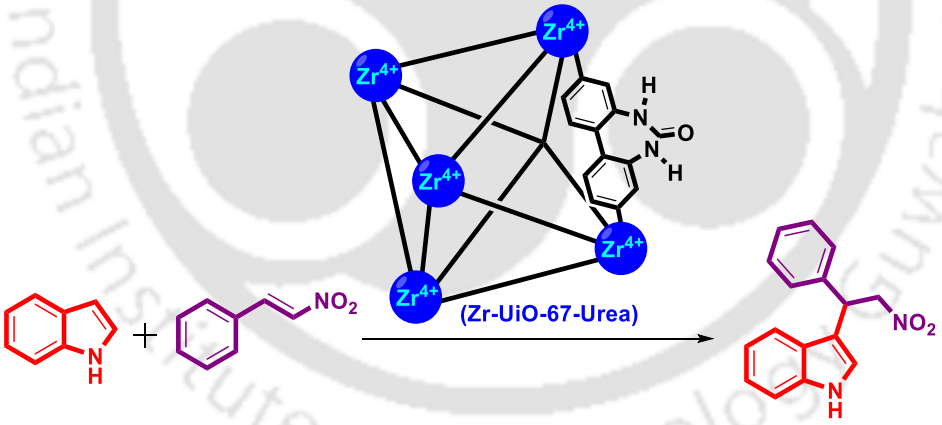

Scheme 4.1 Schematic representation displaying the catalytic activities of **3′** towards Friedel-Crafts alkylation between indole and β-nitrostyrene.

4.2 Experimental Section

4.2.1 Materials and Methods

The urea-functionalized biphenyl-4,4′-dicarboxylic linker (H_2**L**) was synthesized by following the reported procedure.[56] All the other chemicals and starting materials including the indole derivatives and β-nitrostyrene used in the present study were

TH-2604_156122006

purchased from the commercial sources and they were used as received. The recording of the Fourier transform infrared spectra in the region 400-4000 cm^{-1} was conducted at room temperature with the Perkin Elmer Spectrum Two FT-IR spectrometer. The absorption bands were labelled with the following notations: very strong (vs), strong (s), medium (m), weak (w), shoulder (sh) and broad (br). The thermogravimetric (TG) curves were recorded with the SDT Q600 thermogravimetric analyzer with a heating rate of 10 °C/min under a stream of air. The measurement of XRPD patterns was carried out with the Bruker D2 Phaser X-ray diffractometer (30 kV, 10 mA) by means of Cu-*K*α (λ = 1.5406 Å) radiation. The recording of the nitrogen sorption isotherms at -196 °C was performed by utilizing the Quantachrome Autosorb iQMP instrument. Before performing the nitrogen sorption measurement, the MOF sample was degassed under dynamic vacuum at 70 °C for 16 h.

4.2.2 Synthesis of MOF and Activation of 3

4.2.2.1 Synthesis of $[Zr_6O_4(OH)_4(L)_6]\cdot 1.0H_2O\cdot 0.4DMF$ (3)

$ZrCl_4$ (40 mg, 0.134 mmol), H_2**L** linker (40 mg, 0.134 m mol) and trifluoroacetic acid (310 µL, 4.02 mmol) were added into a glass tube having 3 mL of *N*,*N*-dimethylformamide (DMF). After sealing the tube with a cap, it was heated at 150 °C by utilizing an aluminum block heater for 24 h. After the completion of heating, the sealed glass tube was cooled down to ambient temperature and the yellow precipitate was collected over a membrane filter paper by vacuum filtration. The powder sample was then washed with acetone (2 × 3 mL) and air-dried. Additional drying of the material was carried out inside an oven at 80 °C for 8 h. The yield was 45 mg (0.02 mmol, 63%) based on the Zr salt. Elemental analysis calcd for **3**: C 43.75, H 2.28, N 6.93%. Found: C 43.50, H 2.04, N 6.61%. FT-IR (KBr pellet, cm^{-1}): 3436 (br), 2924 (w), 2851 (w), 1689 (s), 1658 (w), 1620 (s), 1551 (vs), 1415 (vs), 1418 (vs), 1376 (m), 1264 (s), 1224 (s), 1114 (m), 1034 (w), 906 (w), 779 (vs), 665 (vs).

4.2.2.2 Activation of 3

Material **3** (100 mg) was first placed into a 50 mL round bottom flask and 20 mL methanol was added to it. The mixture was allowed to stir for 24 h at room temperature. Subsequently, collection of the powder sample by vacuum filtration and drying in air resulted in the methanol-exchanged form of the material. Heating of this powder material

TH-2604_156122006

under vacuum at 70 °C for 16 h resulted in the thermally activated form of the material, which was named as **3′**. Elemental analysis calcd for **3′**: C 43.99, H 2.13, N 6.74%. Found: C 43.71, H 1.90, and N 6.90%.

4.2.3 Catalytic Studies

In a typical reaction, a Schlenk tube (10 mL) was charged with 10 mg of **3′**, 0.1 mmol of indole, 0.105 mmol of β-nitrostyrene and 0.1 mL of solvent. Then, this mixture was homogeneously mixed and placed in a preheated oil bath which was maintained at 70 °C for the required reaction time mentioned in Table 1. The progress of the reaction was monitored by Agilent 7820A gas chromatograph system by sampling aliquots at different time intervals. The purity and selectivity of the products were also checked by gas chromatography. The determination of yield was carried out by gas chromatography by means of the internal standard method. The GC-MS technique was employed for the characterization of the obtained products. For the recyclability experiments, the same catalytic reaction procedure was repeated except that the catalyst was filtered after the reaction, washed thrice with fresh toluene and dried at 80 °C in an oven for 5 h. The dried catalyst was utilized in the consecutive cycles with the fresh reactants.

4.3 Results and Discussion

4.3.1 Synthesis and Activation Procedure

Solvothermal reactions were performed in all the probable combinations by using three zirconium salts ($ZrCl_4$, $ZrOCl_2{\cdot}8H_2O$, $Zr(SO_4)_2{\cdot}4H_2O$), three solvents (DMF, *N*,*N*-diethylformamide and *N*,*N*-dimethylacetamide) and four modulators[59] (acetic acid, formic acid, benzoic acid and trifluoroacetic acid). The reaction temperature and time were also varied, keeping the molar ratio of $ZrCl_4$ to H_2**L** linker fixed at 1:1. A yellow powder of **3** with optimum crystallinity was obtained when $ZrCl_4$, DMF and trifluoroacetic acid were utilized as metal salt, solvent and modulator, respectively. The optimized reaction temperature and time was 150 °C and 24 h, respectively. The activation of the as-synthesized product involved solvent-exchange with methanol and subsequent heating under vacuum. The activated compound was named as **3′**.

TH-2604_156122006

4.3.2 Infrared Spectroscopy

In the FT-IR spectra (Figure 4.1) of as-synthesized and activated **3**, the strong peaks at 1415 and 1565 cm^{-1} belong to the symmetric and antisymmetric stretching vibrations of the coordinated carboxylate groups from the H_2**L** linker molecules, respectively. The peak at 1660 cm^{-1} in the FT-IR spectrum of as-synthesized material correspond to the carbonyl stretching vibration of the guest DMF molecules.[28] The peak attributable to the DMF molecules is absent in the activated material, which indicates that the complete activation of the material has been achieved.[28] The peak at 1719 cm^{-1} is present in H_2**L** ligand, **3** and **3′** due to the presence of carbonyl group of urea moiety (Figure 4.1).

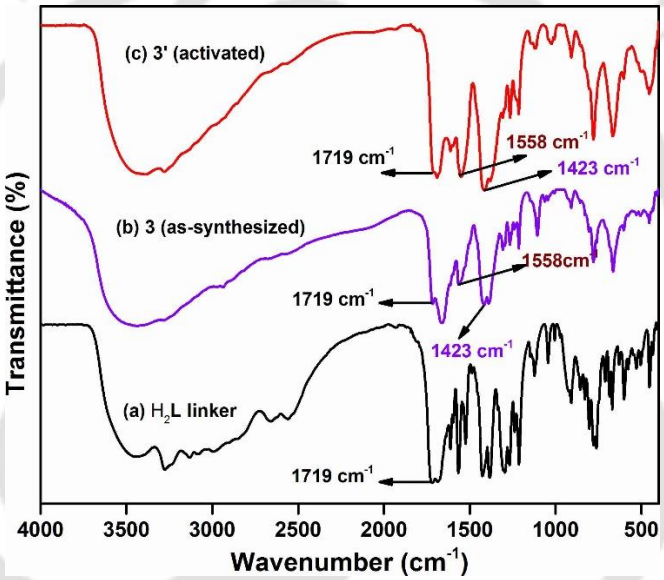

Figure 4.1 FT-IR spectra of (a) H_2**L** linker, (b) as-synthesized **3** and (c) activated **3′**.

4.3.3 XRPD Analysis and Structure Description

As shown in Figure 4.2, there is a nice agreement between the XRPD pattern of as-synthesized **3** and the calculated XPRD pattern of the parent Zr-UiO-67 material.[50] We have performed indexing of the experimental XRPD pattern of compound **3** to deduce the unit cell parameters. The results of indexing are displayed in Table 4.1, Supporting Information. The unit cell parameters obtained from indexing are in well agreement with the reported un-functionalized and functionalized Zr-UiO-67 MOFs.[60, 61] We have also conducted a Pawley fit (Figure 4.3) of the observed XRPD pattern of compound **3**. The results obtained from Pawley fit showed quite good similarity with the simulated XRPD

TH-2604_156122006

pattern of UiO-67 MOF. Hence, it can be inferred that compound **3** has UiO-67 framework topology. The comparison between the XRPD patterns of the activated and as-synthesized materials (Figure 4.2) also reveals noticeable similarity in terms of peak positions, indicating the high stability of the framework after the removal of guest molecules from the microporous cages.

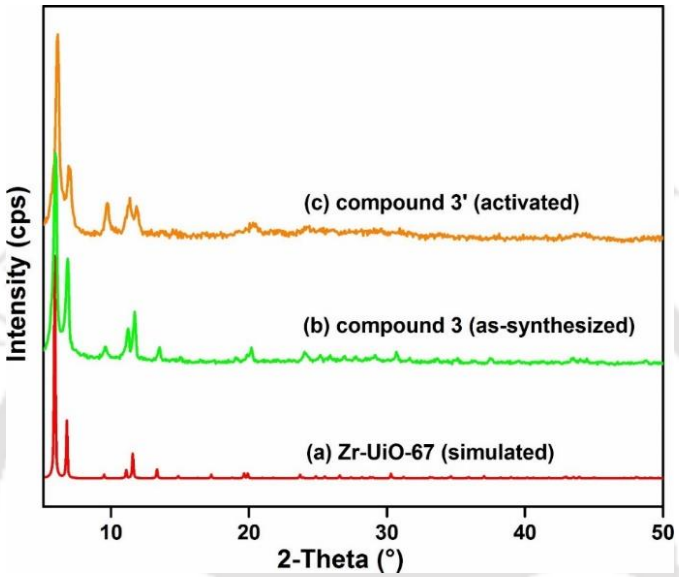

Figure 4.2 XRPD patterns of (a) simulated Zr-UiO-67 and (b) as-synthesized (experimental) **3** and (c) activated **3**.

Table 4.1 Unit cell parameters of as-synthesized Zr-UiO-67-urea obtained by indexing its XRPD pattern. The obtained values were compared with those of the previously reported un-functionalized and functionalized Zr-UiO-67 MOFs.

Compound	Zr-UiO-67-urea (this work)	Zr-UiO-67[61]	Zr-UiO-67-Me_2[60]	Zr-UiO-67-BN[60]
Crystal System	cubic	cubic	cubic	cubic
a = b = c (Å)	26.841(3)	26.783(3)	26.869(3)	26.816(2)
V ($Å^3$)	19336.4(33)	19212(4)	19397.9(6)	19284.8(4)

TH-2604_156122006

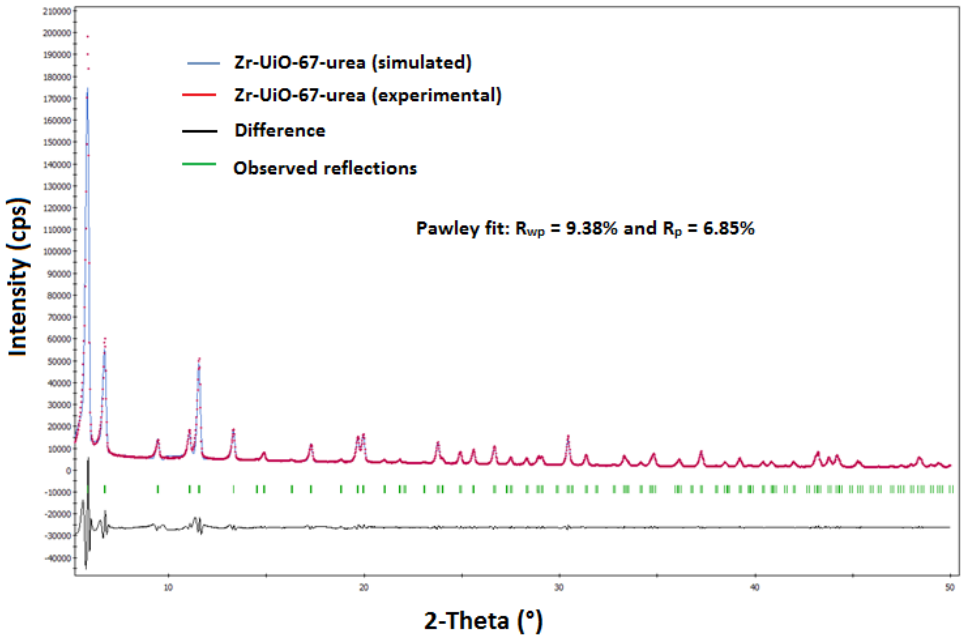

Figure 4.3 Pawley fit for the XRPD pattern of as-synthesized **3**. Blue lines and red dots denote calculated and observed patterns, respectively. The peak positions and difference plot are displayed at the bottom (R_p = 6.85, R_{wp} = 9.38).

As confirmed by the XRPD experiment (Figure 4.2), compound **3** has shown similar XRPD pattern with the un-functionalized Zr-UiO-67 compound. Hence, it can be inferred that the framework topology of **3** is similar as the pristine Zr-UiO-67 compound.[50] The comprehensive description of the crystal structure of Zr-UiO-67 compound has been already reported in the literature.[50] The framework structure of Zr-UiO-67 contains hexanuclear $[Zr_6O_4(OH)_4]^{12+}$ secondary building units (SBUs). The SBUs are interconnected by the carboxylates of twelve 4,4′-biphenyldicarboxylate (BPDC) linkers resulting in the construction of a 3D cubic framework. Within this cubic framework, there exists both tetrahedral (smaller) and octahedral (larger) cages. Every central octahedral cage is surrounded by eight tetrahedral cages at the corners. The connection between the tetrahedral and octahedral cages occurs via narrow triangular windows, which have a free diameter of ~ 8 Å. In the structure of Zr-UiO-67, each Zr atom is eight-coordinated and features square anti-prismatic geometry. The structure of **3** consists of the urea-functionalized biphenyl-4,4′-dicarboxylate (**L**) linkers instead of un-functionalized BPDC linkers, which are present in Zr-UiO-67 compound. Figure 4.4 reveals the structures of the tetrahedral and octahedral cages present within the framework of **3**.

TH-2604_156122006

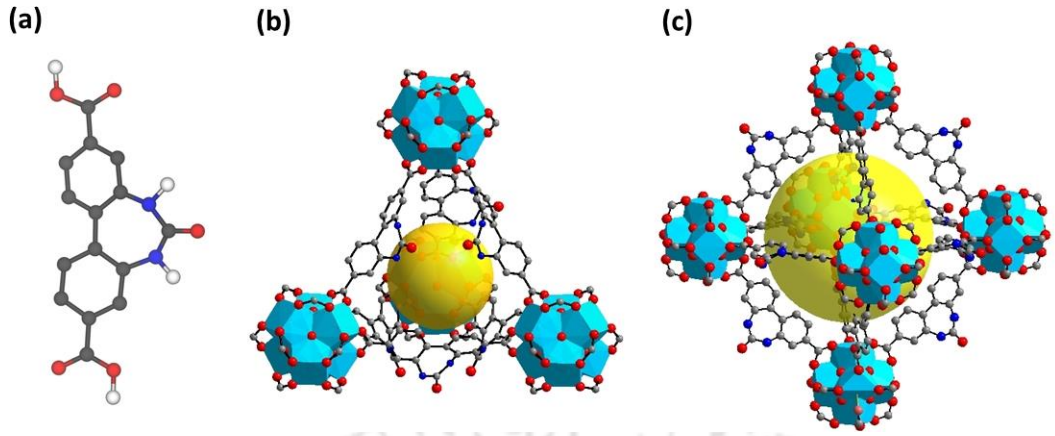

Figure 4.4 Ball-and-stick representation of the (a) H_2**L** linker, (b) tetrahedral and (c) octahedral cages present within the framework structure of **3**. Color codes: Zr, cyan polyhedra; C, grey; O, red; N, blue; H, white. The cavities are represented by yellow spheres. The structure of **3** was modelled and drawn by using the Materials Studio (version 5.0, Accelrys Inc., San Diego, 2009) software package.

4.3.4 Thermal Stability

The thermogravimetric (TG) analyses, which were performed under air atmosphere, disclose that the compound is stable up to 290 °C. Three distinct weight loss steps were observed in the TG profile of as-synthesized **3** (Figure 4.5). The first and second weight losses are 4.5 and 8.3 wt% in the temperature range of 25-150 and 150-290 °C, respectively. Such losses in weight could be attributed to the elimination of one water (cald.: 4.5 wt%) and 0.4 DMF (cald.: 8.4 wt%) molecule per formula unit, respectively. The weight loss step starting at 290 °C was observed due to the removal of coordinated linker molecules from the structural framework of **3**. The physisorbed water molecules gave rise to the first weight loss step of 2.8 wt% from 25 to 130 °C in the TG trace **3′**. In the TG trace of **3′**, a second weight loss of 7.8 wt% was found in the temperature range of 130-300 °C. After 300 °C the organic linker molecules start to leave the framework of **3′**. A comparison of the thermal stability of **3** with pristine and functionalized Zr-UiO-67 compounds revealed considerable similarity.[62, 63]

TH-2604_156122006

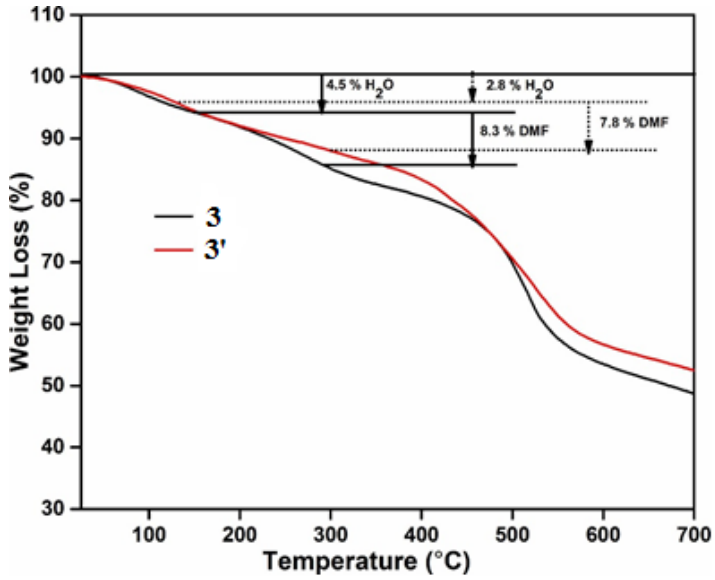

Figure 4.5 TG curves of as-synthesized **3** (black) and thermally activated **3′** (red) recorded in an air atmosphere in the temperature range of 25-700 °C with a heating rate of 10 °C min^{-1}.

4.3.5 Chemical Stability

The chemical stability of **3′** was examined via XRPD analysis (Figure 4.6). Initially, the samples of **3′** were separately immersed in water, glacial acetic acid and 1M HCl at room temperature for 4 h. After 4 h, the solid materials were collected via vacuum filtration and XRPD data of the dry powdered samples were recorded. The XRPD studies revealed no significant change in the crystallinity of **3′** in water and acetic acid, whereas **3′** slightly lost its crystallinity after immersion in 1M HCl for 4 h. It should be noted that the chemical stability of **3′** is in good agreement with the chemical stability of the existing functionalized and pristine Zr-based UiO-67 MOF compounds.[64]

TH-2604_156122006

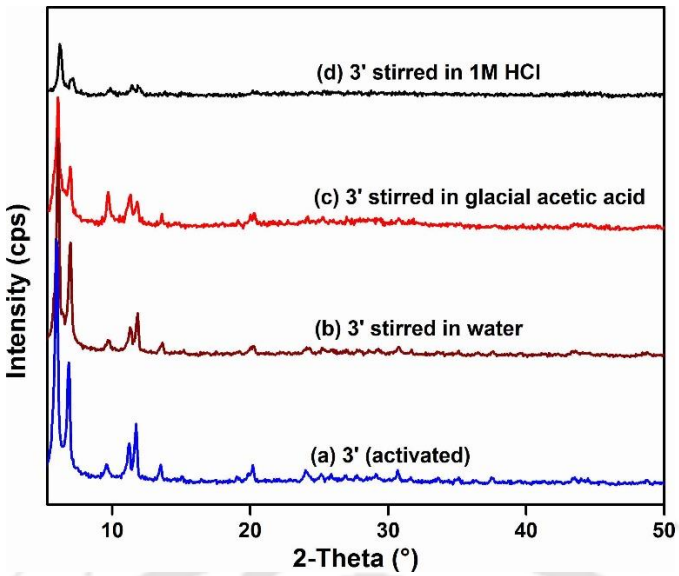

Figure 4.6 XRPD patterns of **3′** in different conditions: (a) activated, (b) after stirring in water, (c) after stirring in glacial acetic acid and (d) after stirring in 1M HCl.

4.3.6 Surface Area Analysis

The permanent porosity of **3′** was demonstrated by conducting the nitrogen sorption experiments at -196 °C. The resulting sorption isotherms (Figure 4.7) showed type-I behavior, indicating microporosity. From the adsorption isotherm, the BET surface area and micropore volume were calculated. The respective values are 1300 $m^2 g^{-1}$ and 0.75 $cm^3 g^{-1}$ at p/p_0 = 0.5. A noticeable similarity can be also observed when the BET surface area of **3′** is compared with the parent, functionalized Zr-UiO-67 materials.[63, 65]

TH-2604_156122006

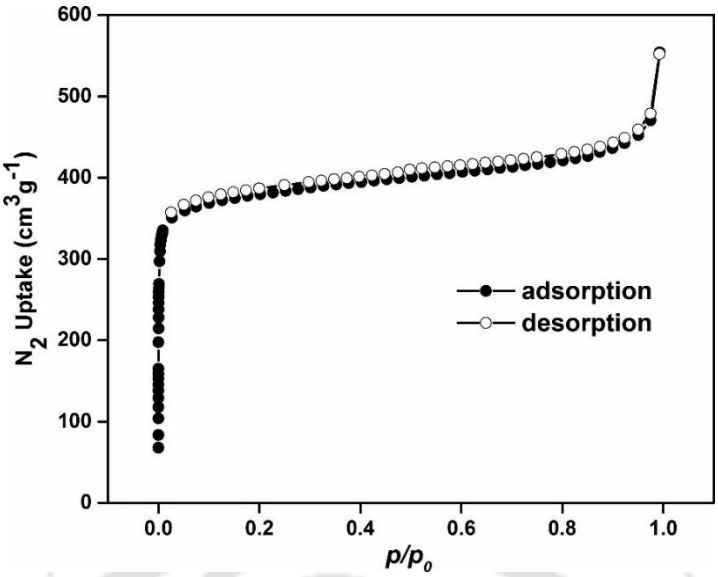

Figure 4.7 N_2 adsorption (solid circle) and desorption (empty circle) isotherms of **3′** measured at –196 °C.

4.3.7 Catalytic Studies

The Friedel-Crafts reaction between indole and β-nitrostyrene has received considerable attention due to its importance in the synthesis of tryptamine derivatives.[66] On the other hand, the Friedel-Crafts reaction between β-nitrostyrene and indole is relatively slow due to the lower nucleophilicity of indole. One of the possible ways to overcome this issue is to develop heterogeneous catalysts to activate electrophilic β-nitrostyrene towards nucleophilic addition of indole through hydrogen bonding. This reaction has been previously exploited using a series of MOF catalysts which include squaramide functionalized UiO-67 MOF,[67] NU-601,[26] Cr-MIL-101-UR3,[58] Cu-UBTA,[54] Cu(dbda),[68] [Zn_4O(4,4′-ureylene-benzenedicarboxylate) $(DMF)_2$]·3DMF[52] and $Cu_3(BTC)_2$[69].

Initially, the catalytic activity of **3′** was studied in the Friedel-Crafts reaction between β-nitrostyrene and indole as model substrates and the reaction was optimized by the variation of catalyst loading, reaction temperature and reaction medium. The catalytic reaction between β-nitrostyrene and indole was conducted in the presence of **3′** at different catalyst loadings such as 3 (1.2 mol%), 6 (2.3 mol%) and 10 mg (3.8 mol%) in toluene at 70 °C. The time-conversion plots for these catalyst loadings are provided in Figure 4.8. The results indicate that the initial reaction rate and the final yield of the product are higher with 3.8 mol% catalyst than the other two loadings. Therefore, the optimization of this

TH-2604_156122006

reaction with respect to temperature and solvent was performed using 3.8 mol% catalyst loading. The observed catalytic data are summarized in Table 4.2. The reaction between indole and β-nitrostyrene afforded 53% yield at room temperature in toluene. The same reaction has shown 60% yield at 50 °C in toluene as solvent. Additionally, the increment in the reaction temperature from 50 to 70 °C resulted in significant enhancement in the activity of **3′** to achieve 97% yield of the desired product under identical experimental conditions. In contrast, a blank control experiment in the absence of catalyst between indole and β-nitrostyrene provided 11% yield at 70 °C in toluene as a solvent. These catalytic results clearly indicate that **3′** plays the active role to promote this reaction. On the other hand, the Friedel-Crafts reaction between indole and β-nitrostyrene using **3′** as a catalyst exhibited 87% and 81% yields in acetonitrile and dichloroethane as solvents, respectively at 70 °C. Similarly, the reaction of indole and β-nitrostyrene using **3′** as a catalyst gave 52% yield in dichloromethane at room temperature after 24 h. All these catalytic data conclude that the use of toluene as a solvent and the reaction temperature of 70 °C are the optimum reaction conditions to achieve 97% yield of the desired product and hence further reactions were performed under these reaction conditions. Figure 4.9 shows the time-conversion plot for the Friedel-Crafts reaction between indole and β-nitrostyrene using **3′** as a solid catalyst. It can be realized from this figure that **3′** is highly effective in catalyzing the Friedel-Crafts reaction between indole and β-nitrostyrene to achieve 97% yield after 24 h. In order to verify the heterogeneity of the reaction under these experimental conditions, hot filtration test was conducted by removing the catalyst through filtration at the reaction temperature after 1 h. Subsequently, the reaction in the absence of solid catalyst was continued for another 23 h under identical reaction conditions. The progress of the reaction in the absence of catalyst was examined by sampling at different time intervals. The comparison of the kinetic curves between the reactions with and without catalyst suggests that the reaction rate is completely stopped upon removal of **3′** from the reaction mixture. These reaction kinetic data indicate that **3′** is highly essential to promote the reaction towards completion.

TH-2604_156122006

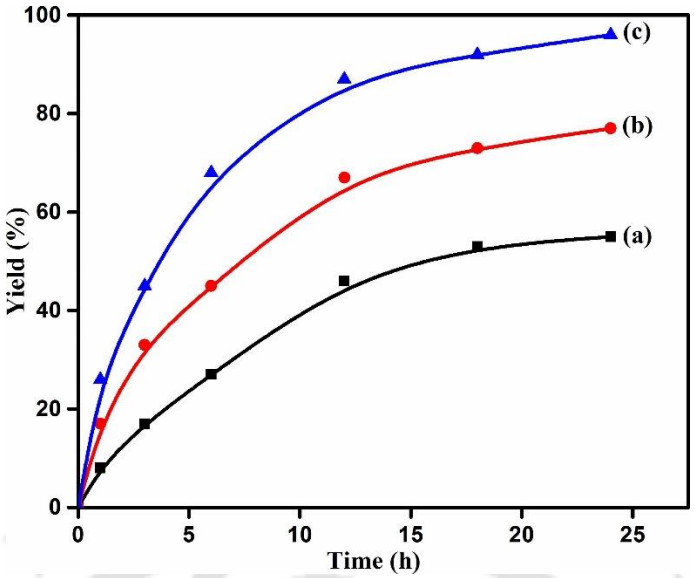

Figure 4.8 Effect of catalyst loading on the Friedel-Crafts alkylation reaction between indole and β-nitrostyrene with (a) 3 mg (1.2 mol%), (b) 6 mg (2.3 mol%) and (c) 10 mg (3.8 mol%) of **3′**. Catalyst mol% was calculated with respect to β-nitrostyrene.

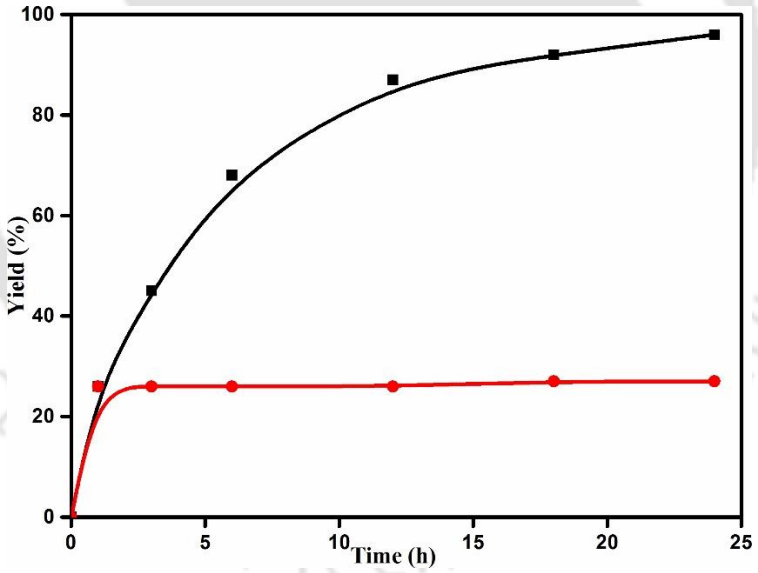

Figure 4.9 Time conversion plot in the presence of **3′** (■) and hot filtration test (●) upon filtration of catalyst after 1 h from the reaction mixture and the reaction mixture maintained under identical conditions for remaining time in the absence of catalyst.

TH-2604_156122006

Table 4.2 Optimization of reaction conditions for the Friedel-Crafts alkylation reaction between indole and β-nitrostyrene using **3′** as a solid heterogeneous catalyst.[a]

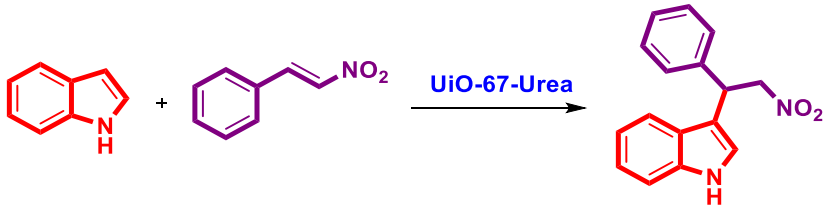

Entry	Solvent	Temp. (°C)	Yield (%)[b]
1	toluene	25	53
2	toluene	50	60
3	toluene	70	97
4[c]	toluene	70	11
5	acetonitrile	70	87
6	dichloroethane	70	81
7	dichloromethane	25	52
8[d]	toluene	70	69
9[e]	toluene	70	43

[a] Reaction conditions: indole (0.1 mmol), β-nitrostyrene (0.105 mmol), solvent (0.1 mL), catalyst (10 mg, 3.8 mol%), 70 °C, 24 h.

[b] Yield was determined by GC.

[c] Blank experiment (in the absence of catalyst).

[d] 7 mg of H_2**L** linker was used.

[e] 5.5 mg of $ZrCl_4$ was used.

Having demonstrated the activity of **3′** in promoting the reaction between β-nitrostyrene and indole in a heterogeneous manner under the optimized conditions, we were also interested to compare the activity of **3′** with a series of analogous catalysts. The results are shown in Figure 4.10 The activity of UiO-67-$(NH_2)_2$ was identical with that of **3′**. This

TH-2604_156122006

may be ascribed to the presence of N-H bonds which can activate β-nitrostyrene. Furthermore, the use of urea-functionalized linker (BPDC-Urea) afforded 69% yield, which is lower than the activity of the above catalysts. This lower activity of the linker compared to **3′** may be due to the self-quenching of the N-H bonds between each molecule through dimerization.[24] In contrast, the activity of UiO-67 was much lower than the activities of **3′**, UiO-67-$(NH_2)_2$ and BPDC-Urea. This activity difference may be due to the lack of hydrogen bonding groups in UiO-67. However, the activity of UiO-67 arises due to the Lewis acidity around central metal ions which is in accordance with earlier precedents.[70, 71] Finally, $ZrCl_4$ as a homogeneous catalyst showed 43% yield under identical conditions and it is the lowest activity in these series of catalysts. Although the activities of $ZrCl_4$ and BPDC-Urea linker are comparatively lower than **3′**, the observed catalytic data using **3′** as a catalyst serve to illustrate the synergism between these two components located in the framework structure and the operation of hydrogen bonding catalysis in promoting this reaction in an efficient manner.

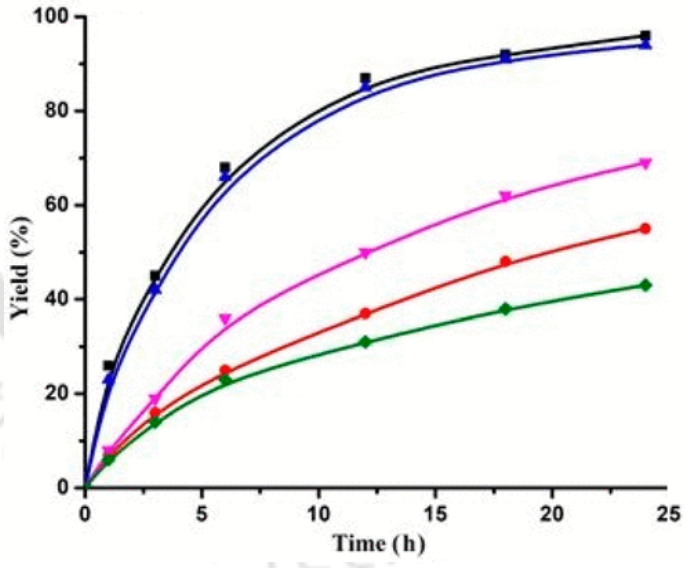

Figure 4.10 Time conversion plots for the Friedel-Crafts alkylation reaction between indole and β-nitrostyrene using (■) UiO-67-urea, (▲) UiO-67-$(NH_2)_2$, (▼) BPDC-urea ligand, (●) UiO-67 and (♦) $ZrCl_4$.

Figure 4.11 shows the catalytic data of reusability experiments for the Friedel-Crafts reaction between indole and β-nitrostyrene using **3′** as a catalyst. This figure demonstrates that the catalytic activity of **3′** is retained up to four cycles. Although, there is a slight

TH-2604_156122006

decrease in the catalytic performance of **3′**, the catalytic data in the third cycle reveal that 90% of the initial activity is still retained. This slight decrease in the product yield can be ascribed to the loss of catalyst during the recovery process in every catalytic cycle. In addition, a control experiment was performed to ensure that the recovered catalyst is free from the reactants or products. This hypothesis was confirmed by treating the three times reused **1′** with toluene at 70 °C for 3 h. This solution was analyzed by GC-MS and no evidence for the existence of either reactant or product was observed. This experimental result indirectly supports that the slight reduction in the catalytic performance of **3′** is not due to the catalyst deactivation under the present experimental conditions and furthermore the decrease in yield during the reusability experiment can be related to the loss of catalyst during the recovery process. This hypothesis was further supported by comparing the XRPD pattern between the fresh and four cycles used **3′**. Figure 4.12 shows that the crystalline nature of the four times used catalyst is certainly retained and no significant change in the XRPD pattern is noticed as compared to the fresh solid material. Moreover, from the FT-IR spectrum (Figure 4.13), it is obvious that the peak for carbonyl stretching of urea moiety is present in **3′** used up to the 4^{th} catalytic cycle at 1715 cm^{-1}. The IR spectrum also shows that the asymmetric and symmetric carboxylate stretching peaks are present in **3′** used up to 4^{th} catalytic cycle at similar positions as that of **1′** before catalysis. The stability of the catalyst was further supported by FE-SEM images (Figures 4.14a and 4.14b), which revealed that the morphology of **3′** was similar before and after the catalytic study. Furthermore, the EDX elemental analysis and EDX elemental mapping of compound **3′** before and after catalysis were performed to confirm the presence of different elements in compound **3′**. Figures 4.15a and 4.15b revealed that different elements present in compound **3′** before catalysis remain intact after catalysis also.

TH-2604_156122006

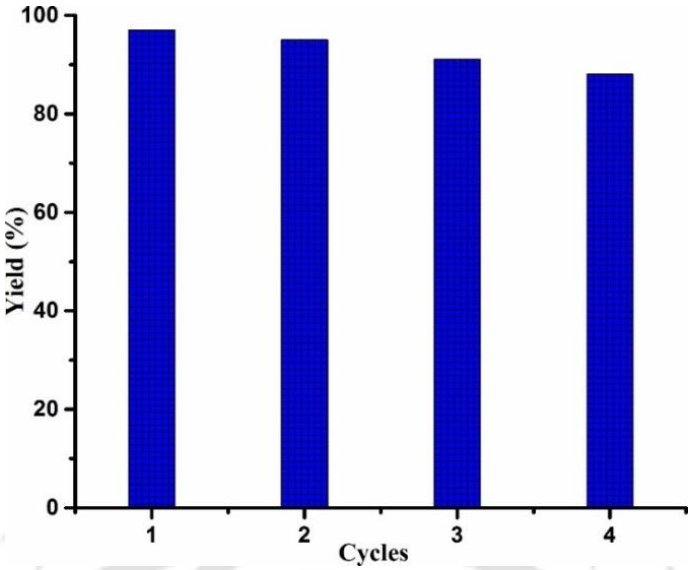

Figure 4.11 Reusability experiment for the Friedel-Crafts reaction of indole with β-nitrostyrene using **3′** as a solid heterogeneous catalyst.

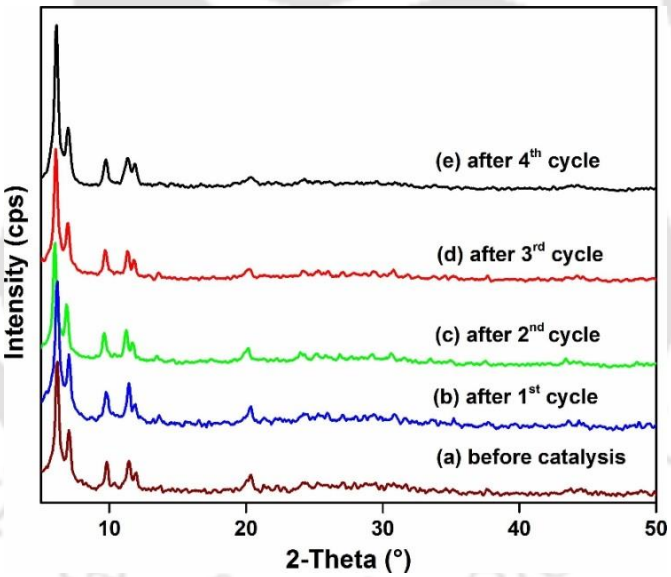

Figure 4.12 XRPD patterns of **3′** (a) before catalysis, (b) after 1st cycle, (c) after 2nd cycle, (d) after 3rd cycle and (e) after 4th cycle.

TH-2604_156122006

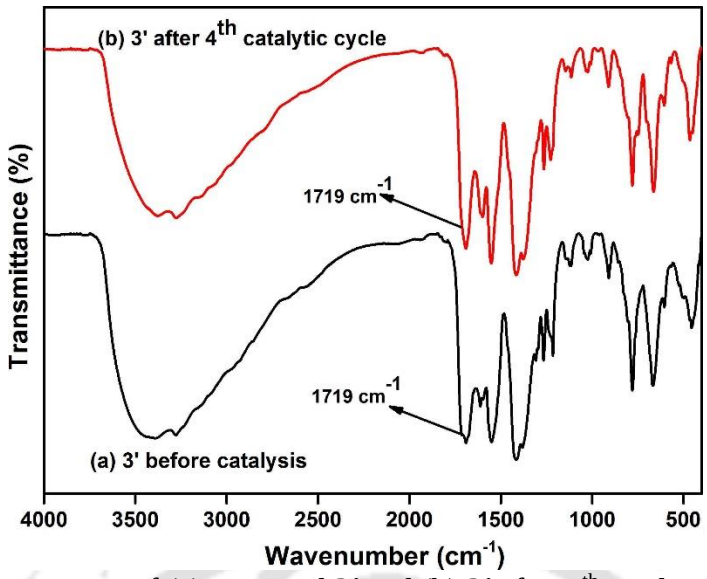

Figure 4.13 FT-IR spectra of (a) activated **3′** and (b) **3′** after 4th catalytic cycle.

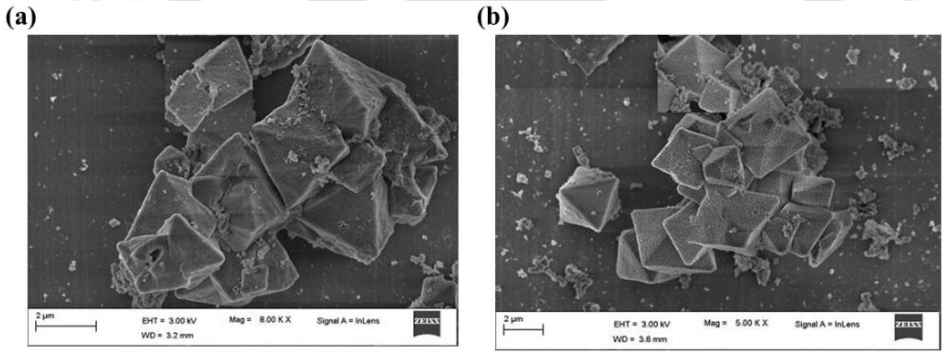

Figure 4.14 FE-SEM images of **1′** (a) before catalysis and (b) after catalysis.

TH-2604_156122006

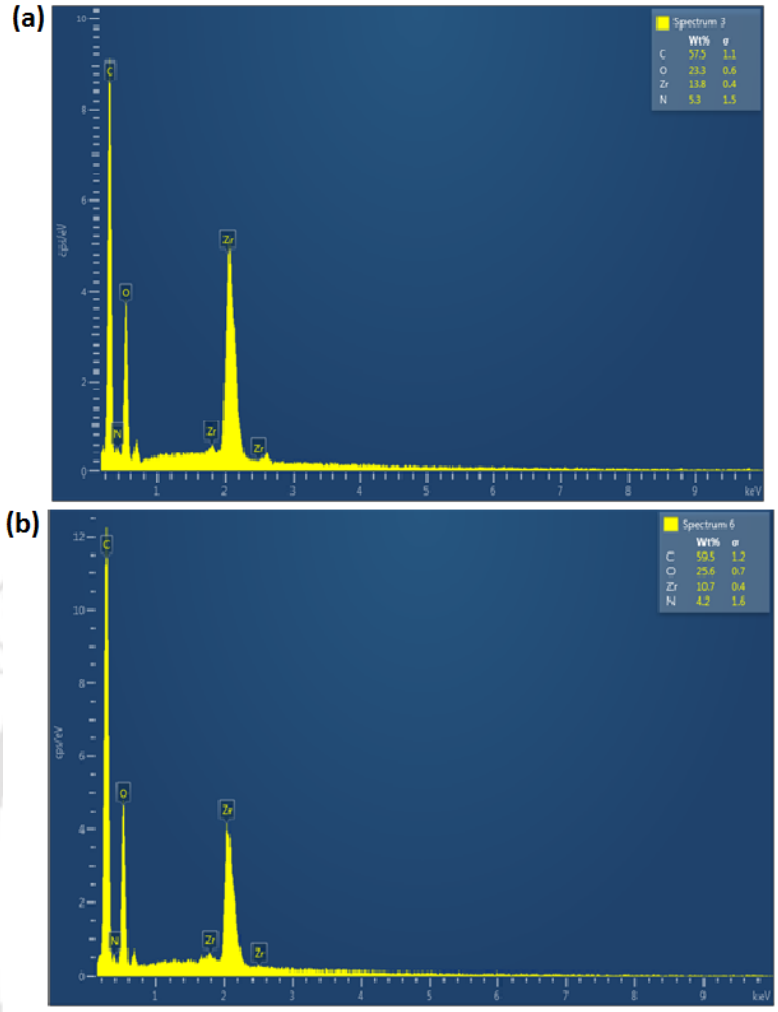

Figure 4.15 EDX spectra of **3′** (a) before and (b) after catalysis.

After optimizing the conditions for the Friedel-Crafts reaction between indole and β-nitrostyrene using **3′** as a heterogeneous catalyst, the scope of **3′** was further examined with substituted indoles under the identical reaction conditions. The observed catalytic data are provided in Table 4.3. The Friedel-Crafts reaction between *N*-methylindole and β-nitrostyrene produced 86% yield. Similarly, the reaction between 2-methylindole and β-nitrostyrene was efficiently promoted by **3′** to achieve 96% of the desired adduct. Furthermore, the reaction of 5-methylindole and β-nitrostyrene in the presence of **3′** exhibited 96% yield. Similarly, an encouraging yield of 94% was also observed for the reaction between 5-methoxyindole and β-nitrostyrene under identical reaction conditions. In contrast, the reaction of 5-chloro and 5-bromo indoles with β-nitrostyrene in the presence of **3′** resulted in the formation of desired products with 61 and 55% of yields, respectively. On the other hand, a poor yield of only 6% was observed for the reaction

TH-2604_156122006

between 5-nitroindole and β-nitrostyrene under the identical experimental conditions. This low yield may be explained from the fact that the presence of nitro substituent largely reduces the nucleophilicity at the C3 carbon of indole moiety whereas the presence of methyl and methoxy substituents at the indole moiety afforded the highest yield as discussed above. In addition, the moderate yield observed for the halogen substituted indoles may be explained from the electronic factor as well as the steric nature of these substrates to reach the active site in the MOF. Interestingly, the reaction of pyrrole with β-nitrostyrene also afforded the expected product in 97% yield under the optimized reaction conditions. Finally, the Friedel-Crafts reaction between *N,N*-dimethylaniline and β-nitrostyrene provided the expected product in 22% yield. The results of these catalytic investigations undoubtedly demonstrate that the MOF catalyst **3′** plays the key role in carrying out the reactions proficiently under the optimized reaction conditions. In any case, the data presented in Table 4.2 and Figures 4.17-4.35 (Appendix I) clearly point out that the solid catalyst **3′** can be conveniently used to perform Friedel-Crafts alkylation reaction at 70 °C within short reaction time.

Table 4.3 Friedel-Crafts alkylation reaction of indoles with β-nitrostyrene using **3′** as a solid heterogeneous catalyst.[a]

Entry	Indoles	β-Nitrostyrene	Product	Yield (%)[b]
1	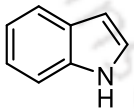	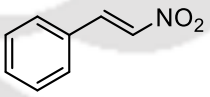	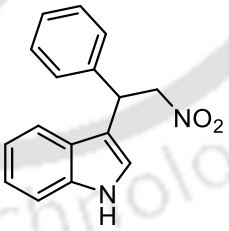	97
2	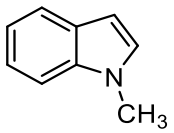	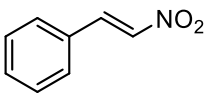	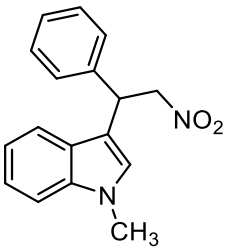	86

TH-2604_156122006

3	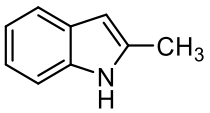	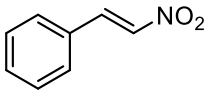	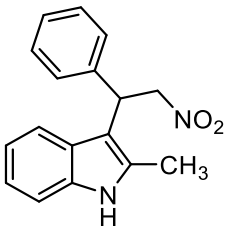	96
4	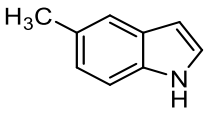	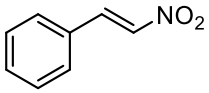	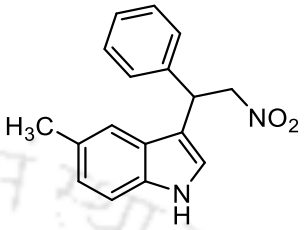	96
5	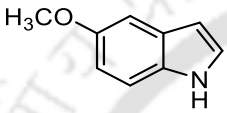	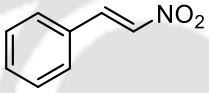	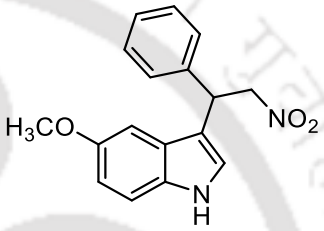	94
6	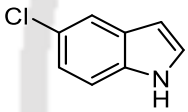	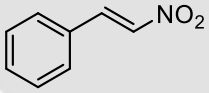	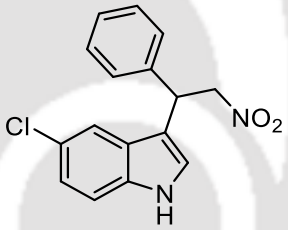	61
7	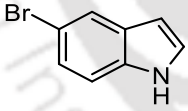	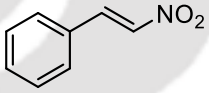	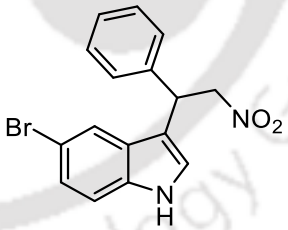	55
8	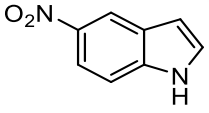	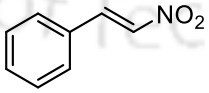	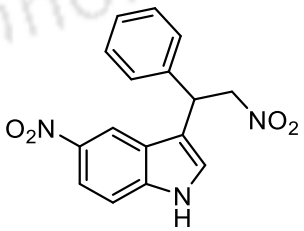	6

TH-2604_156122006

9		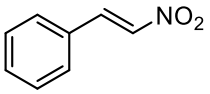	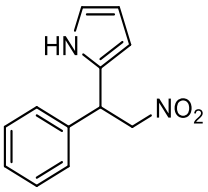	97
10	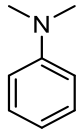	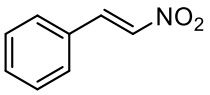	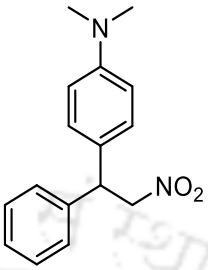	22
11	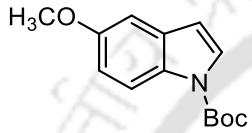	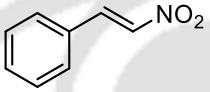	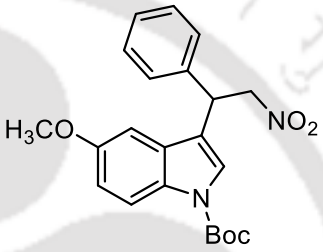	-

[a] Reaction conditions: indoles (0.1 mmol), β-nitrostyrene (0.105 mmol), toluene (0.1 mL), **3′** (10 mg), 70 °C, 24 h.

[b] Yield was determined by GC.

The operation of size-selective catalysis using **3′** as catalyst was examined for the reaction between N-Boc protected indole derivative and β-nitrostyrene as substrates under the present experimental conditions. The catalytic data in Table 4.3 indicate that this reaction does to lead to any product formation. This may be ascribed to the diffusion limitation of N-Boc protected indole derivative to reach the active site in **3′**. This experiment clearly suggests that the catalytic reaction occurs within the pores of **3′**, demonstrating the size-selective catalysis. The pore-size distribution plot of **3′** is displayed in Figure 4.16. The plot shows that the micropores of **3′** are centered at around 15.4 Å.

The catalytic performance of **3′** has been assessed by comparing the yield, reaction time, temperature and catalyst stability in terms of multiple reuses with earlier reports on MOF catalysts in the literature. The comparison data are presented in Table 4.4. These data clearly indicate that the activity of **3′** is comparable or superior to some existing MOF catalysts as the present catalyst requires short reaction time and can be reused for more

TH-2604_156122006

cycles. Furthermore, the reported catalysts require 50-60 °C as the reaction temperature for this catalytic reaction, whereas the present catalyst requires 70 °C which is not too high from the reported catalysts. Some of the salient features of this catalytic system include wide substrate scope of **3′** as compared to the earlier catalysts and easy synthesis procedure of **3′** without tedious functionalization of the linker.

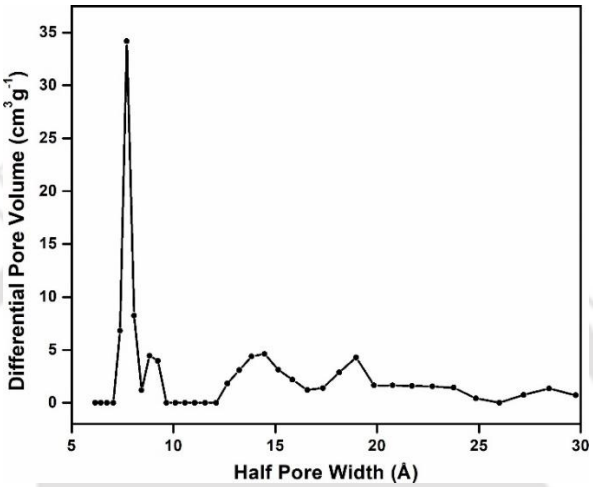

Figure 4.16 Density functional theory pore-size distribution of compound **3′** as determined from its N_2 adsorption isotherms at -196 °C.

Table 4.4 Comparison of catalytic performance of **3′** with MOF catalysts of earlier reports.

Entry	Catalyst	Time (h)	Temp. (°C)	Yield (%)	No. of Uses	Ref.
1	NU-601	36	60	98	5	26
2	Cr-MIL-101-UR**3**	30	60	96	4	58
3	UiO-67-Squar/bpdc	24	50	95	4	67
4	Cu-UBTA	48	60	85	3	54
5	Cu(dbda)	24	50	99	5	72
6	[Zn_4O(4,4′-ureylene-benzenedicarboxylate)$(DMF)_2$]·3DMF	24	60	90	3	52
7	[$Zr_6O_4(OH)_4$(**L**)$_6$]·1.0H_2O·0.4DMF (**3′**)	24	70	97	4	present work

TH-2604_156122006

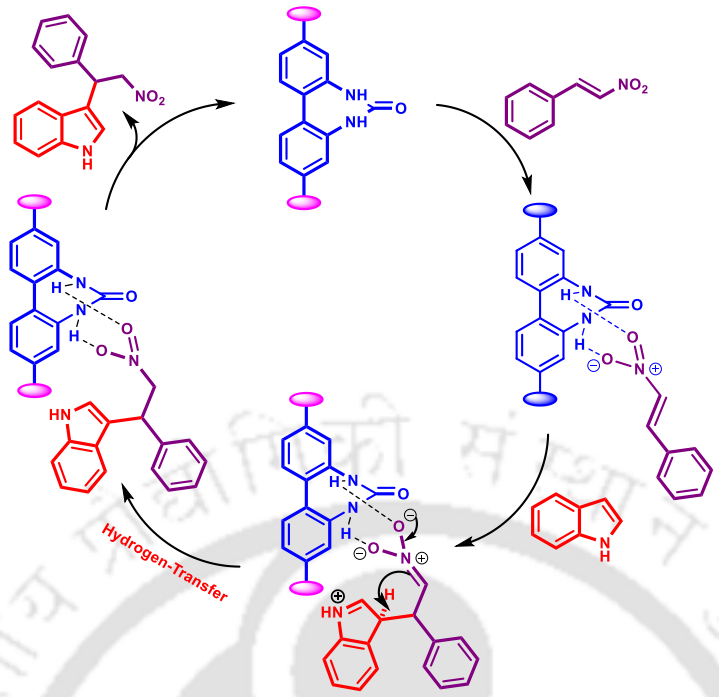

Scheme 4.2 Possible mechanism for the Friedel-Crafts alkylation of indole with β-nitrostyrene catalyzed by **3′**.

Scheme 4.2 provides the possible mechanism for the Friedel-Crafts alkylation of indole with β-nitrostyrene using **3′** as a solid catalyst. As stated earlier, the urea-functionalized linker in **3′** interacts with β-nitrostyrene through hydrogen bonding. The formation of this type of hydrogen bonding with substrates have been proposed in many studies involving HBD catalysis.[20, 23, 26, 73, 74] Hence, the activities of **3′**, UiO-67-$(NH_2)_2$ and BPDC-Urea were much higher than UiO-67 and $ZrCl_4$ under identical reaction conditions. Furthermore, this interaction creates electron deficiency in the C=C double bond of β-nitrostyrene. Later, indole attacks β-nitrostyrene through the C3 carbon atom to provide the expected product.

4.4 Conclusions

In summary, a new Zr(IV)-based urea-functionalized UiO-67 MOF has been synthesized and characterized thoroughly by appropriate techniques to understand its structural features. The material showed high chemical and thermal stability as well as considerable specific BET surface area. The solid material **1′** was successfully employed in the Friedel-Crafts alkylation reaction between β-nitrostyrene and indole. In this reaction, an excellent

TH-2604_156122006

yield of 97% for the desired product was achieved in toluene at 70 °C for 24 h. The active role of urea moiety in the linker was established by performing a series of experiments with UiO-67-$(NH_2)_2$, urea-functionalized linker, UiO-67 and $ZrCl_4$. The activity of the catalyst possessing urea moiety was higher or comparable to the other tested catalysts. These control experiments clearly suggest the active participation of HBD catalysis through the presence of N-H bonds in the linker. The solid MOF catalyst was utilized up to four cycles with an insignificant reduction in its catalytic performance. However, the control experiments and XRPD analysis confirmed that this loss in catalytic activity is not due to the deactivation of the MOF catalyst. Moreover, the reaction is found to be heterogeneous in nature. This catalyst also exhibits a wide substrate scope in providing a series of products with moderate to high yields.

4.5 References

1. G. A. Olah, R. Khrisnamurti and G. K. S. Prakash, *Pergamon: New York*, 1991, **3**, 293-339.
2. A. Z. Halimehjani, M. V. Farvardin, H. P. Zanussi, M. A. Ranjbari and M. Fattahi, *J. Mol. Catal. A: Chem.*, 2014, **381**, 21-25.
3. S.-L. You, Q. Cai and M. Zeng, *Chem. Soc. Rev.*, 2009, **38**, 2190-2201.
4. Z.-H. Shi, H. Sheng, K.-F. Yang, J.-X. Jiang, G.-Q. Lai, Y. Lu and L.-W. Xu, *Eur. J. Org. Chem.*, 2010, **2011**, 66–70.
5. R. Kastl and H. Wennemers, *Angew. Chem. Int. Ed.*, 2013, **52**, 7228 –7232.
6. O. M. Berner, L. Tedeschi and D. Enders, *Eur. J. Org. Chem.*, 2002, 1877-1894.
7. H. Firouzabadi, N. Iranpoor and F. Nowrouzi, *Chem. Commun.*, 2005, **6**, 789-791.
8. G. Bartoli, M. Bosco, S. Giuli, A. Giuliani, L. Lucarelli, E. Marcantoni, L. Sambri and E. Torregiani, *J. Org. Chem.*, 2005, **70**, 1941-1944.
9. I. Komoto and S. Kobayashi, *J. Org. Chem.*, 2004, **69**, 680–688.
10. P. E. Harrington and M. A. Kerr, *Synlett*, 1996, **1996**, 1047-1048.
11. M. Bandini, P. Melchiorre, A. Melloni and A. U.-Ronchi, *Synthesis*, 2002, 1110-1114.
12. M. Bandini, A. Melloni and A. U.-Ronchi, *Angew. Chem. Int. Ed.*, 2004, **43**, 550 –556.

TH-2604_156122006

13. M. Bandini, M. Fagioli, M. Garavelli, A. Melloni, V. Trigari and A. U.-Ronchi, *J. Org. Chem.*, 2004, **69**, 7511-7518.
14. K. B. Jensen, J. Thorhauge, R. G. Hazell and K. A. Jørgensen, *Angew. Chem. Int. Ed. Engl.*, 2001, **40**, 160-163.
15. J. Zhou and Y. Tang, *J. Am. Chem. Soc.*, 2002, **124**, 9030–9031.
16. P. R. Schreiner, *Chem. Soc. Rev.*, 2003, **32**, 289-296
17. M. S. Taylor and E. N. Jacobsen, *Angew. Chem. Int. Ed.*, 2006, **45**, 1520–1543.
18. A. G. Doyle and E. N. Jacobsen, *Chem. Rev.*, 2007, **107**, 5713-5743.
19. M. S. Sigman and E. N. Jacobsen, *J. Am. Chem. Soc.*, 1998, **120**, 4901–4902.
20. P. R. Schreiner and A. Wittkopp, *Org. Lett.*, 2002, **4**, 217–220.
21. M. C. Etter and S. M. Reutzel, *J. Am. Chem. Soc.*, 1991, **113**, 2586–2598.
22. A. G. Wenzel and E. N. Jacobsen, *J. Am. Chem. Soc.*, 2002, **124**, 12964–12965.
23. G. Dessole, R. P. Herrera and A. Ricci, *Synlett*, 2004, **13**, 2374-2378
24. S. V. Deshapande, C. C. Meredith and R. A. Pasterna, *Acta Cryst.*, 1968, **B24**, 1396
25. S. Stankovic and G. D. Andreetti, *Acta Cryst.*, 1978, **B34**, 3787-3790.
26. J. M. Roberts, B. M. Fini, A. A. Sarjeant, O. K. Farha, J. T. Hupp and K. A. Scheidt, *J. Am. Chem. Soc.*, 2012, **134**, 3334-3337.
27. A. Das and S. Biswas, *Sens. Actuators, B*, 2017, **250**, 121-131.
28. A. Das, S. Banesh, V. Trivedi and S. Biswas, *Dalton Trans.*, 2018, **47**, 2690-2700.
29. R. Ricco, L. Malfatti, M. Takahashi, A. J. Hillad and P. Falcaro, *J. Mater. Chem. A*, 2013, **1**, 13033–13045.
30. V. Stavila, A. A. Talin and M. D. Allendorf, *Chem. Soc. Rev.*, 2014, **43**, 5994-6010.
31. R. Dalapati, B. Sakthivel, M. K. Ghosalya, A. Dhakshinamoorthy and S. Biswas, *CrystEngComm*, 2017, **19**, 5915-5925.
32. L. Wang, M. Zheng and Z. Xie, *J. Mater. Chem. B*, 2018, **6**, 707-717
33. S. S. Nagarkar, A. V. Desai and S. K. Ghosh, *Chem. Commun.*, 2014, **50**, 8915-8918.
34. A. Karmakar, N. Kumar, P. Samanta, A. V. Desai and S. K. Ghosh, *Chem. - Eur. J*, 2016, **22**, 864 –868.
35. S. Sharma and S. K. Ghosh, *ACS Omega*, 2018, **3**, 254−258.
36. B. Gole, A. K. Bar, A. Mallick, R. Banerjee and P. S. Mukherjee, *Chem. Commun.*, 2013, **49**, 7439-7441.

TH-2604_156122006

37. B. Gole, A. K. Bar and P. S. Mukherjee, *Chem. Commun.*, 2011, **47**, 12137-12139.
38. T. C. Wang, W. Bury, D. A. Gómez-Gualdrón, N. A. Vermeulen, J. E. Mondloch, P. Deria, K. Zhang, P. Z. Moghadam, A. A. Sarjeant, R. Q. Snurr, J. F. Stoddart, J. T. Hupp and O. K. Farha, *J. Am. Chem. Soc.*, 2015, **137**, 3585-3591.
39. T. C. Wang, I. Hod, C. O. Audu, N. A. Vermeulen, S. B. T. Nguyen, O. K. Farha and J. T. Hupp, *ACS Appl. Mater. Interfaces*, 2017, **9**, 12584-12591.
40. L. Stewart, W. Lu, Z.-W. Wei, D. Ila, C. Padilla and H.-C. Zhou, *Dalton Trans.*, 2017, **46**, 14270-14276.
41. O. V. Gutov, W. Bury, D. A. Gomez-Gualdron, V. Krungleviciute, D. Fairen-Jimenez, J. E. Mondloch, A. A. Sarjeant, S. S. Al-Juaid, R. Q. Snurr, J. T. Hupp, T. Yildirim and O. K. Farha, *Chem. - Eur. J.*, 2014, **20**, 12389-12393.
42. D. Feng, W. C. Chung, Z. Wei, Z. Y. Gu, H. L. Jiang, Y. P. Chen, D. J. Darensbourg and H. C. Zhou, *J. Am. Chem. Soc.*, 2013, **135**, 17105-17110.
43. M. SK, S. Nandi, R. K. Singh, V. Trivedi and S. Biswas, *Inorg. Chem.*, 2018, **57**, 10128-10136.
44. R. Dalapati, S. Nandi, H. Reinsch, B. K. Bhunia, B. B. Mandal, N. Stock and S. Biswas, *CrystEngComm*, 2018, **20**, 4194 - 4201.
45. S. Nandi, S. Banesh, V. Trivedi and S. Biswas, *Analyst*, 2018, **143**, 1482-1491.
46. Y.-L. Wong, K.-K. Yee, Y.-L. Hou, J. Li, Z. Wang, M. Zeller, A. D. Hunter and Z. Xu, *Inorg. Chem.*, 2018, **57**, 6198−6201.
47. M. Kandiah, M. H. Nilsen, S. Usseglio, S. Jakobsen, U. Olsbye, M. Tilset, C. Larabi, E. A. Quadrelli, F. Bonino and K. P. Lillerud, *Chem. Mater.*, 2010, **22**, 6632−6640.
48. O. K. Farha, I. Eryazici, N. C. Jeong, B. G. Hauser, C. E. Wilmer, A. A. Sarjeant, R. Q. Snurr, S. B. T. Nguyen, A. O. Yazaydın and J. T. Hupp, *J. Am. Chem. Soc.*, 2012, **134**, 15016−15021.
49. S. S. Nagarkar, T. Saha, A. V. Desai, P. Talukdar and S. K. Ghosh, *Sci. Rep.*, 2014, **4**, 7053–7058.
50. J. H. Cavka, S. Jakobsen, U. Olsbye, N. Guillou, C. Lamberti, S. Bordiga and K. P. Lillerud, *J. Am. Chem. Soc.*, 2008, **130**, 13850-13851.
51. I. G. Sonsona, E. Marqués-López, M. Häring, D. D. Díaz and R. P. Herrera, *Catalysts*, 2018, **8**, 305-320.
52. P. C. Rao and S. Mandal, *ChemCatChem*, 2017, **9**, 1172-1176.

TH-2604_156122006

53. E. K. Raja, S. O. N. Lill and D. A. Klumpp, *Chem. Commun.*, 2012, **48**, 8141-8143.
54. X.-J. Wang, J. Li, Q.-Y. Li, P.-Z. Li, H. Lu, Q. Lao, R. Ni, Y. Shi and Y. Zhao, *CrystEngComm*, 2015, **17**, 4632-4636.
55. C. Zhu, Q. Mao, D. Li, C. Li, Y. Zhou, X. Wu, Y. Luo and Y. Li, *Catal. Commun.*, 2018, **104**, 123–127.
56. S. Glomb, D. Woschko, G. Makhloufi and C. Janiak, *ACS Appl. Mater. Interfaces*, 2017, **9**, 37419-37434.
57. E. A. Hall, L. R. Redfern, M. H. Wang and K. A. Scheidt, *ACS Catal.*, 2016, **6**, 3248−3252.
58. X.-W. Dong, T. Liu, Y.-Z. Hu, X.-Y. Liu and C.-M. Che, *Chem. Commun.*, 2013, **49**, 7681-7683.
59. N. Stock and S. Biswas, *Chem. Rev.*, 2012, **112**, 933–969.
60. S. Øien-Ødegaard, B. Bouchevreau, K. Hylland, L. Wu, R. Blom, C. Grande, U. Olsbye, M. Tilset and K. P. Lillerud, *Inorg. Chem.*, 2016, **55**, 1986−1991.
61. N. Ko, J. Hong, S. Sung, K. E. Cordova, H. J. Park, J. K. Yang and J. Kim, *Dalton Trans.*, 2015, **44**, 2047-2051.
62. A. Schaate, P. Roy, A. Godt, J. Lippke, F. Waltz, M. Wiebcke and P. Behrens, *Chem. Eur. J.* , 2011, **17**, 6643-6651.
63. Z. Xu, G. Zhao, L. Ullah, M. Wang, A. Wang, Y. Zhang and S. Zhang, *RSC Adv.*, 2018, **8**, 10009-10016.
64. S. Ø. Ødegaard, B. Bouchevreau, K. Hylland, L. Wu, R. Blom, C. Grande, U. Olsbye, M. Tilset and K. P. Lillerud, *Inorg. Chem.*, 2016, **55**, 1986−1991.
65. H. Fei and S. M. Cohen, *Chem. Commun.*, 2014, **50**, 4810-4812.
66. S. Lancianesi, A. Palmieri and M. Petrini, *Chem. Rev.*, 2014, **114**, 7108–7149.
67. C. M. McGuirk, M. J. Katz, C. L. Stern, A. A. Sarjeant, J. T. Hupp, O. K. Farha and C. A. Mirkin, *J. Am. Chem. Soc.*, 2015, **137**, 919–925.
68. X. Zhang, Z. Zhang, J. Boissonnault and S. M. Cohen, *Chem. Commun.*, 2016, **52**, 8585-8588.
69. N. Anbu and A. Dhakshinamoorthy, *J. Colloid Interface Sci.*, 2017, **494**, 282–289.
70. M. Rimoldi, A. J. Howarth, M. R. D. Stefano, L. Lin, S. Goswami, P. Li, J. T. Hupp and O. K. Farha, *ACS Catal.*, 2017, **7**, 997–1014.
71. C. Caratelli, J. Hajek, F. G. Cirujano, M. Waroquier, F. X. L. Xamena and V. V. Speybroeck, *J. Catal.*, 2017, **352**, 401-414.

TH-2604_156122006

72. X.-J. Wang, J. Li, Q.-Y. Li, P.-Z. Li, H. Lu, Q. Lao, R. Ni, Y. Shia and Y. Zhao, *CrystEngComm*, 2015, **14**, 4632-4636.

73. D. P. Curran and L. H. Kuo, *J. Org. Chem.*, 1994, **59**, 3259–3261.

74. E. Fan, S. A. V. Arman, S. Kincaid and A. D. Hamilton, *J. Am. Chem. Soc.*, 1993, **115**, 369–370.

TH-2604_156122006

TH-2604_156122006

Ph.D. Thesis
Chapter 5

A Thiophene-2-Carboxamide Functionalized Zr(IV) Organic Framework as a Prolific and Recyclable Heterogeneous Catalyst for Regioselective Ring Opening of Epoxides

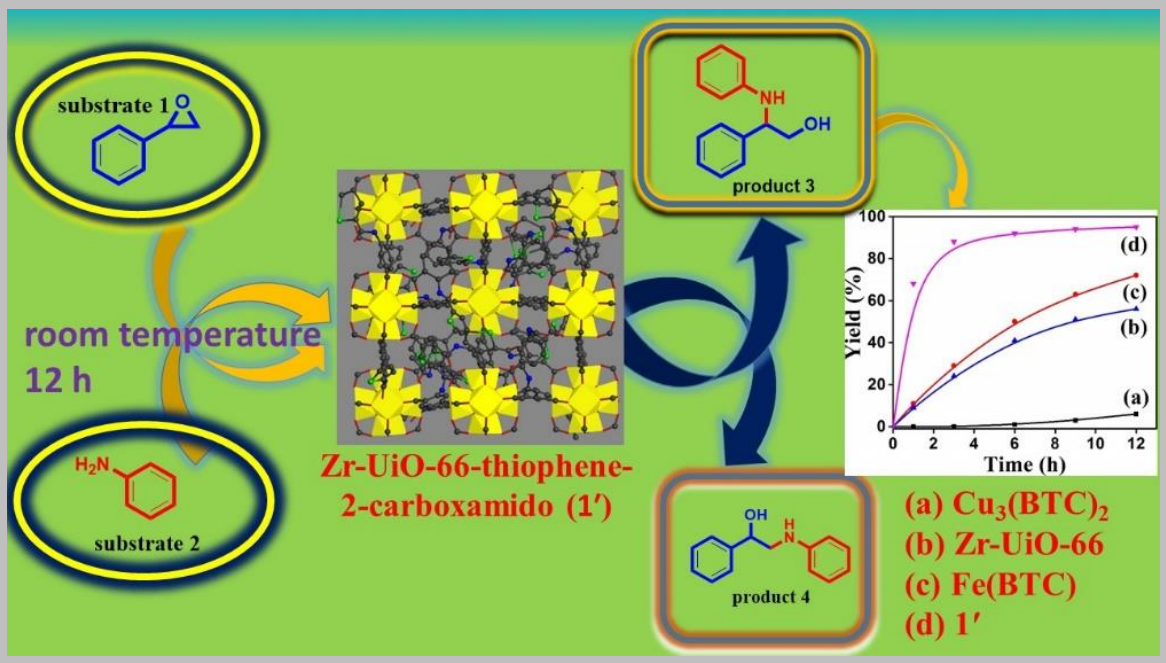

Chapter 5

5.1 Introduction

Epoxides are considered to be privileged molecules in organic chemistry because of their versatile nucleophilic opening character producing 1,2-difunctionalized structures and also because such cleavages often occur with *trans* stereochemistry.[1-4] In the field of asymmetric catalysis, β-amino alcohols are significant as chiral ligands and chiral auxiliaries mostly originating from nature.[5-9] Amino alcohols are often derivatized to increase their chelating abilities or steric influences.[10, 11] In the field of synthetic organic chemistry, biological chemistry and medicinal industry, β-amino alcohols have occupied a dominant position because they are used as building units for therapeutic agents, insecticidal agents, b-blockers, antimalarial agents and numerous biologically active natural products.[12-17] Cyclic amino alcohols like quinines are a class of naturally occurring, biologically active products that are required in the treatment of malaria.[18] Renin and HIV-1 protein inhibitors constitute pharmacologically active amino alcohols and one such example is saquinavir.[18] Often, β-adrenergic blockers, which is a class of β-amino alcohols, are used to regulate cardiovascular diseases like hypertension, cardiac arrhythmias and angina pectoris.[18-21] Ring opening of oxiranes by nucleophilic attack of various amines is the easiest way for preparation of β-amino alcohols.[7, 22] However, this approach is not acceptable due to its disadvantages such as sluggish rate of reaction because of sensitivity of epoxides and fall in regioselectivity. Many reports are there involving the preparation of β-amino alcohols utilizing epoxides as electrophiles.[17, 23-29] Researchers have designed several materials such as various homogeneous catalysts,[30, 31] alumina,[1] alkali metals,[32] metal amides[33] and silica gel in order to increase the electrophilicity of epoxides. Unfortunately, most of these methods have several drawbacks such as moisture sensitive character of catalysts, low efficiency of catalysts, long reaction time, less regioselectivity, high reaction temperature and pressure, poor yield and recyclability, etc.[1, 4, 22, 34-36]

Three dimensional (3D) MOFs (MOF: metal-organic framework) being stable, very crystalline solid porous compounds have attracted very much scientific interest for gas adsorption and separation,[37-39] heterogeneous catalysis of numerous organic reactions,[40-43] sensing,[44-47] photonic application,[46] drug delivery,[48] proton conductivity,[49] etc. Moreover, porous MOFs have shown considerable heterogeneous catalytic activities in many organic reactions because of insoluble character, exceptionally large surface area,[40] tunable pore

TH-2604_156122006

size,[50] adjustable internal surface properties and easy separation of catalyst after reaction.[51] In this regard, Zr-MOFs possessing exceptional thermal as well as high chemical stabilities are considered as remarkable candidates for various heterogeneous catalysis reactions.[34, 52-57] Synthetically, new MOFs with desirable structures and specific properties can be designed and synthesized by tuning the side functional groups of linker molecules. In case of epoxide ring opening reaction by means of amine, those catalysts will be preferred, which enhance the electrophilic character of epoxides or increase the nucleophilic character of amines.

Keeping in mind all the factors mentioned above, we have designed a new Zr(IV) based UiO-66 compound having thiophene-2-carboxamide side functional moiety attached with linker molecule. We have explored the heterogeneous catalytic activity of this compound in the ring opening reaction of epoxide by amine. The Zr-UiO-66 compound with thiophene-2-carboxamido functionality was synthesized solvothermally and systematically characterized. The compound showed thermal stability and chemical stability towards water and acids (acetic acid and 1M HCl). Compound **4′** can be considered as a porous material due to its large BET surface area (781 m^2/g). The catalytic performances of **4′** are outstanding in terms of remarkable yield, purity and regioselectivity (Scheme 5.1) of products, size selectivity of substrates and reusability of catalyst.

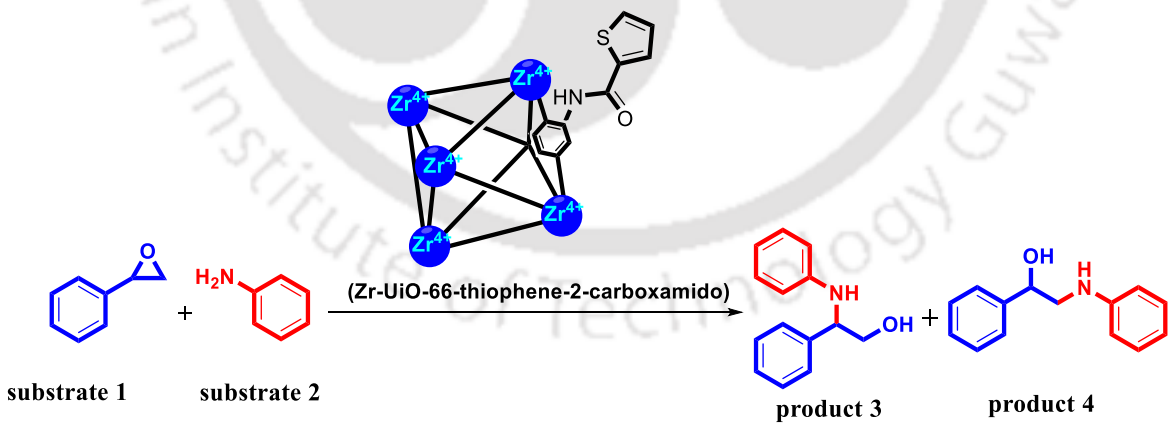

Scheme 5.1 Schematic representation displaying the catalytic activities of **4′** towards Friedel-Crafts alkylation between indole and β-nitrostyrene.

TH-2604_156122006

5.2 Experimental Section

5.2.1 Synthesis of $[Zr_6O_4(OH)_4(BDC\text{-}C_5H_4NOS)_6]\cdot 4.5H_2O\cdot 3.5DMF$ or (Zr-UiO-66-thiophene-2-carboxamido, 4)

$ZrCl_4$ (32 mg, 0.14 mmol) and 2-(thiophene-2-carboxamido)benzene-1,4-dicarboxylic acid linker ($H_2BDC\text{-}C_5H_4NOS$; 40 mg, 0.14 mmol) were taken in a glass tube in 1:1 molar ratio. *N*,*N*-dimethylformamide (DMF; 2 mL) and formic acid (572 µL, 4.55 mmol) were poured into the glass tube holding the reaction mixture. Afterwards, the glass tube was placed onto a block heater which was maintained at 120 °C for 1 day. After 1 day, a white colored precipitation was collected by vacuum filtration, followed by washing with acetone. For drying purpose, the powder sample was kept inside an oven at 80 °C for 4 h. The yield calculated considering zirconium salt was 58 mg (0.02 mmol, 92%). Elem. anal. calcd for $C_{88.5}H_{85.5}N_{9.5}O_{46}S_6Zr_6$ (2757.90 g mol^{-1}): C, 38.54; H, 3.12; N, 4.82%. Found: C, 38.41; H, 2.63; N, 4.73%. FT-IR (KBr, cm^{-1}): 3436 (br), 1646 (s), 1582 (s), 1509 (w), 1423 (vs), 1380 (vs), 1306 (s), 1258 (s), 1170 (w), 1110 (w), 1070 (w), 858 (w), 767 (vs), 738 (w), 662 (vs), 596 (w), 542 (w), 481 (s).

5.2.2 Activation of 4

Activation of compound **4** was carried out in two stages. In the first stage, 100 mg of compound **4** was dispersed in methanol (25 mL) and stirring was conducted at room temperature for 1 day. Later, the solvent was removed by filtration and drying of the precipitate was executed inside an oven at 70 °C for 4 h. Finally, the solid powder was placed in a sealed activation tube, which was degassed for 1 day at 130 °C to achieve the activated sample called **4′**.

5.2.3 Reaction Procedure for Catalysis

In a typical reaction, substrate **1** (0.6 mmol) and substrate **2** (0.5 mmol) were added to a reaction vessel containing 15 mg of catalyst. Then, this mixture was mixed thoroughly and kept for 12 h at ambient conditions. The progress of the ring opening of epoxide reaction with respect to time was monitored by GC through sampling of aliquots at various time intervals. GC was utilized to access the yield of the final product by means of internal standard method. Identification of the products was carried out by using GC-MS and ^1H

TH-2604_156122006

NMR techniques (Figures 5.21-5.58, Appendix II). At the end of reaction, dilution of the mixture, washing the catalyst with dichloromethane (2 × 5 mL) and its drying (at 80 °C for 45 min) were carried out consecutively. The recovered catalyst was used in the next cycle with new substrates. Each cycle followed the same procedure for catalyst recycling.

5.3 Results and Discussion

5.3.1 Preparation

Different possible reactions were carried out using $ZrCl_4$ and $H_2BDC\text{-}C_5H_4NOS$ linker in DMF at different temperatures using four modulators (benzoic acid, acetic acid, trifluoroacetic acid and formic acid).[58, 59] A highly crystalline sample of **4** was achieved when a mixture of $ZrCl_4$, $H_2BDC\text{-}C_5H_4NOS$ linker, formic acid and DMF in required molar ratio was subjected to a solvothermal reaction at 120 °C for 1 day.

5.3.2 FT-IR Study

The IR spectra of **4** and **4′** were recorded to confirm the presence of linker molecule in the compounds. As described in Figure 5.1, the very strong peak at 1586 cm^{-1} is for asymmetric stretching vibration and the strong peak at 1423 cm^{-1} is due to the presence of symmetric stretching vibration of carboxylate linker molecules. Therefore, these results assure the existence of the linker molecules within the frameworks of **4** and **4′**.[60, 61] In the spectrum of free linker molecule, the peak at 1654 cm^{-1} is attributed to the carbonyl group from amide moiety.[62] This peak was shifted to 1647 cm^{-1} for both **4** and **4′**, indicating the incorporation of amide linkage within the framework of MOF.

TH-2604_156122006

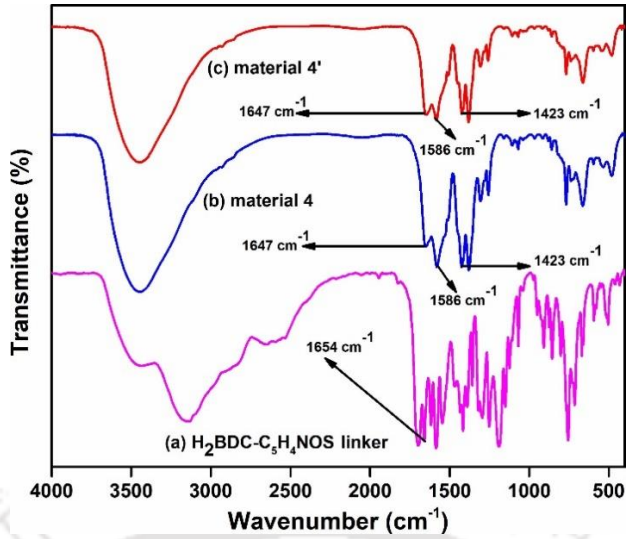

Figure 5.1 FT-IR spectra of (a) $H_2BDC\text{-}C_5H_4NOS$ linker, (b) material **4** (as-synthesized) and (c) material **4′** (activated).

5.3.3 XRPD Analysis

Figure 1 shows the XRPD patterns of **4** and **4′**. From the XRPD patterns, it is obvious that both compounds have shown peak intensity as well as the same peak positions as the theoretical peak pattern of analogous UiO-66 compound.[63, 64] Therefore, it is concluded that **4** has UiO-66 framework topology. From Figure 5.2, it is also concluded that **4** is robust enough towards the activation conditions and the activated compound also has the UiO-66 framework.[63-65]

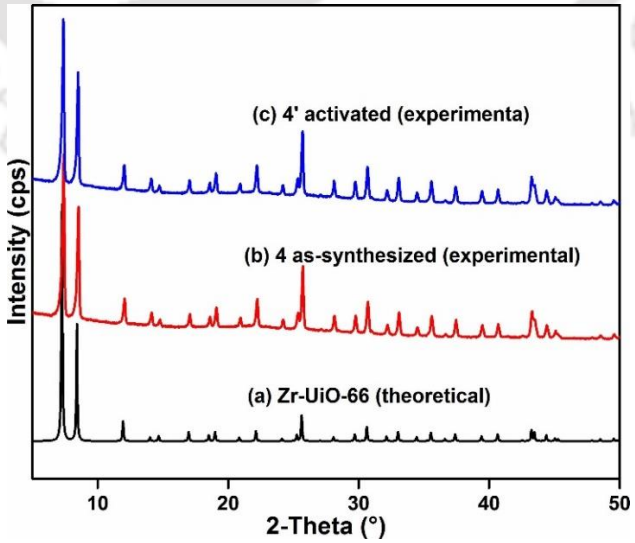

Figure 5.2 XRPD patterns of (a) Zr(IV) based UiO-66 (theoretical), (b) **4** (experimental) and (c) **4′** (experimental).

TH-2604_156122006

5.3.4 Structure Description

The UiO-66 MOF with Zr(IV) ion was discovered by Lillerud's group in 2008.[64] As demonstrated by Lillerud's group, Zr-UiO-66 framework is composed of $[Zr_6O_4(OH)_4]^{12+}$ clusters in which every Zr(IV) ion is octa-coordinated (square antiprismatic geometry). 1,4-Benzenedicarboxylate (BDC) linker molecules interconnect one SBU with other one in the framework. A 3D cubic framework is obtained by interconnecting Zr_6 clusters with BDC linkers (12 linkers per cluster). The 3D framework possesses larger octahedral and smaller tetrahedral cages. Narrow triangular windows connect the two types of cages. For the present MOF, thiophene-2-carboxamide functionalized BDC plays similar role as un-functionalized BDC plays in the formation for UiO-66 framework.[64, 65] Figure 5.3 shows the pore size distribution plot for **4′**. This plot confirms that the microspores of **4′** are centered at 7.6 Å.

For structural analysis, the XRPD pattern of **4** was indexed. The derived lattice parameters are compared in Table 5.1 with the reported un-functionalized Zr-UiO-66 MOF in Table 5.1.[59, 63] The similarities in lattice parameters indicate that the structure of **4** is cubic and possesses UiO-66 framework topology.[59, 63] The structural similarity of **4** with Zr-UiO-66 was further confirmed by Pawley refinement Figure 5.4 with the XRPD pattern of **4**.

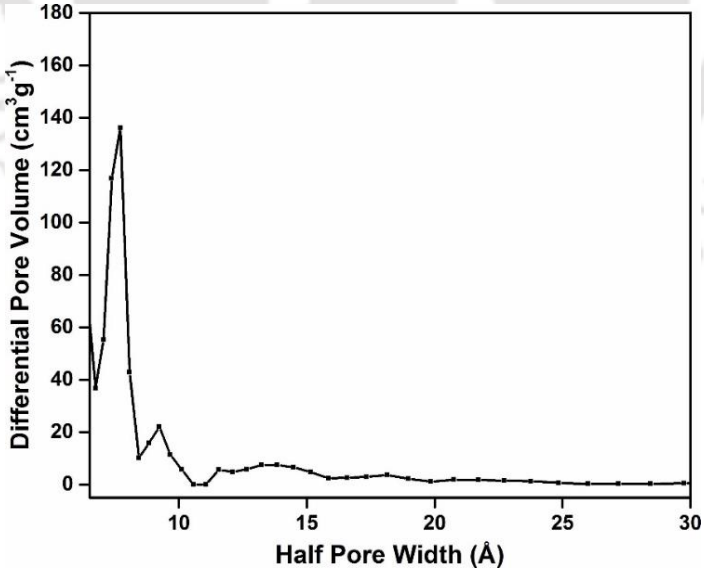

Figure 5.3 Density functional theory pore-size distribution of compound **4′** as determined from its N_2 adsorption isotherms at -196 °C.

TH-2604_156122006

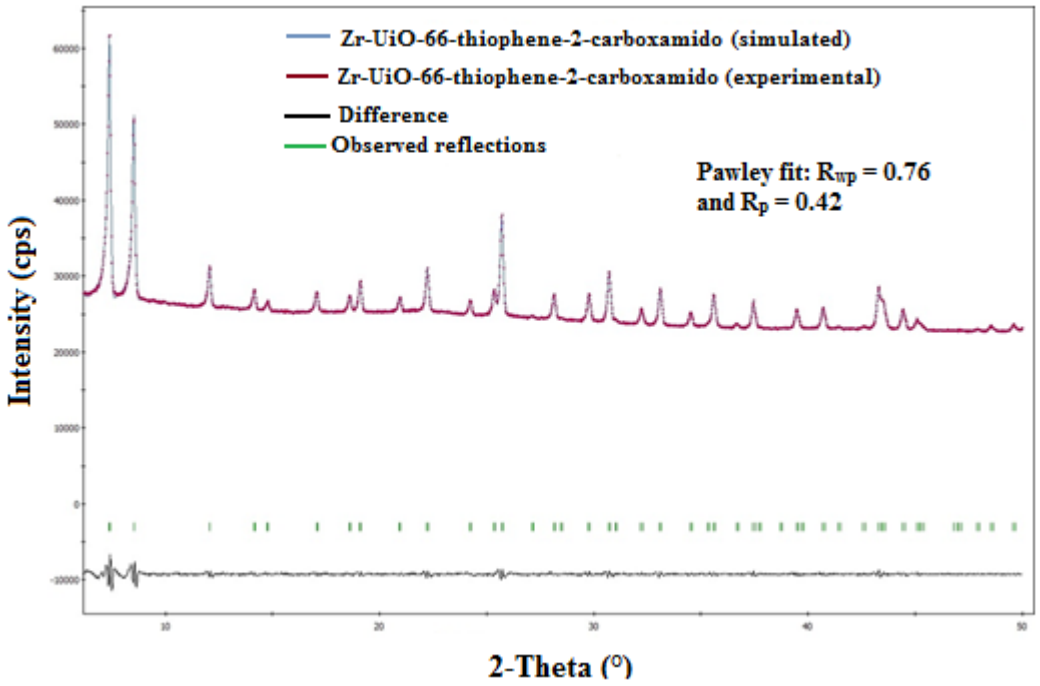

Figure 5.4 Pawley refinement for the XRPD pattern of as-synthesized **4**. Red dots and blue lines denote observed and simulated patterns, respectively. The peak markers (green bars) and difference plot (black line) are displayed at the bottom (R_p = 0.42%, R_{wp} = 0.76%).

Table 5.1 Unit cell parameters of as-synthesized Zr-UiO-66-thiophene-2-carboxamido MOF obtained by indexing its XRPD pattern. The obtained values were compared with those of the previously reported un-functionalized Zr-UiO-66 MOF.

Compound	Zr-UiO-66-thiophene-2-carboxamido (this work)	Zr-UiO-66 (reported)[1]
Crystal System	cubic	cubic
a = b = c (Å)	20.7814 (10)	20.7004(2)
V (Å^3)	8975.0 (7)	8870.3(2)

TH-2604_156122006

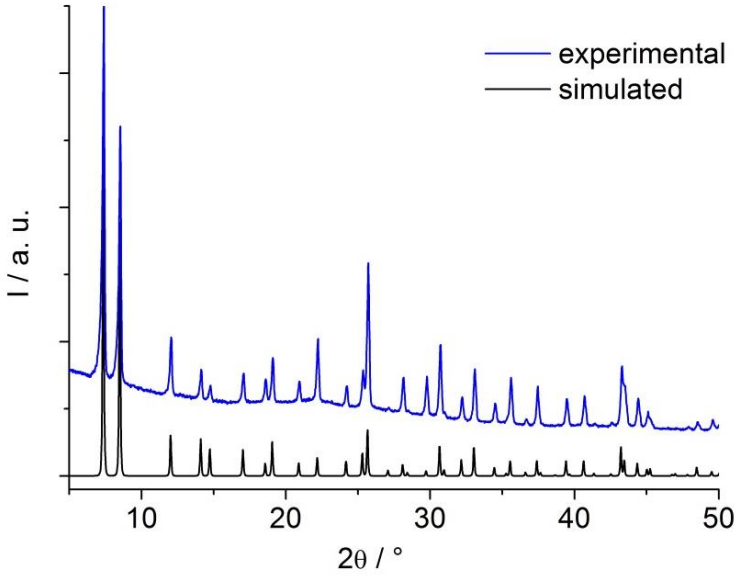

Figure 5.5 Comparison of the simulated XRPD pattern obtained from the structural model of **4** in triclinic symmetry (black line) with the experimental XRPD pattern (blue line) of as-synthesized **4**.

As indicated by indexing and Pawley refinement, the structure of **4** exhibits a cubic symmetry like the parent framework of UiO-66. This also means that the attached functional groups are fully distributed over different possible positions. Due to the this inherent configurational and conformational disorder, the localization of the attached moieties by Rietveld method is impossible. However, the structure of such variants of UiO-66 can be well modelled in a lower symmetry as described, for example, for UiO-66-CO_2H.[66] In such cases, the resulting model represents the pseudo-rhombohedral setting of the cubic unit cell with identical cell edges and all angles fixed to 60°. However, due to the attached functional groups, the actual symmetry of such a model is only triclinic *P*1. Thus, we modelled the structure of **4** starting with the reported model for UiO-66-CO_2H in triclinic symmetry, using the Material Studio software suite.[67] Starting with the literature values for the unit cell parameters ($a = b = c$ = 14.7106 Å, $\alpha = \beta = \gamma$ = 60°) of UiO-66-CO_2H, we deduced the values for **4** by Pawley refinement to be $a = b = c$ = 14.7174 Å with angles fixed to 60°. After imposing these cell parameters, the functional -CO_2H groups were replaced by thiophene-2-carboxamide moieties. Eventually, protons were added to the linker molecules and the model was fully relaxed by force-field calculations using the Universal fore field UFF.[68] The calculated XRPD pattern for this resulting final model is in close agreement with the experimental data as shown in Figure 5.5.

TH-2604_156122006

5.3.5 Thermal Stability

The thermal stability was determined by performing thermogravimetric (TG) experiments under argon atmosphere. From Figure 5.6, it is inferred that both **4** and **4′** are stable up to 340 °C. The existing UiO-66 type MOFs have shown similar thermal stability as that of **4**.[69, 70]

From Figure 5.6, it is noticed that there are distinct weight loss stages for **4**. In the temperature range of 25-150 °C, there was the first weight loss of 2.9 wt% (cald.: 2.9 wt%) due to the loss of 4.5 water molecules. The second weight loss was found to be 9.2 wt% (cald.: 9.3 wt%) due to the loss of 3.5 DMF molecules. The linker molecules start to be eliminated from the framework of **4** beyond 340 °C. Therefore, it is confirmed that **1** is stable up to 340 °C. The desolvated sample (**4′**) adsorbs moisture when it is stored under air atmosphere. As a result, it shows a weight loss of 2.7 wt% in the region of 25-150 °C for the removal of adsorbed water molecules.

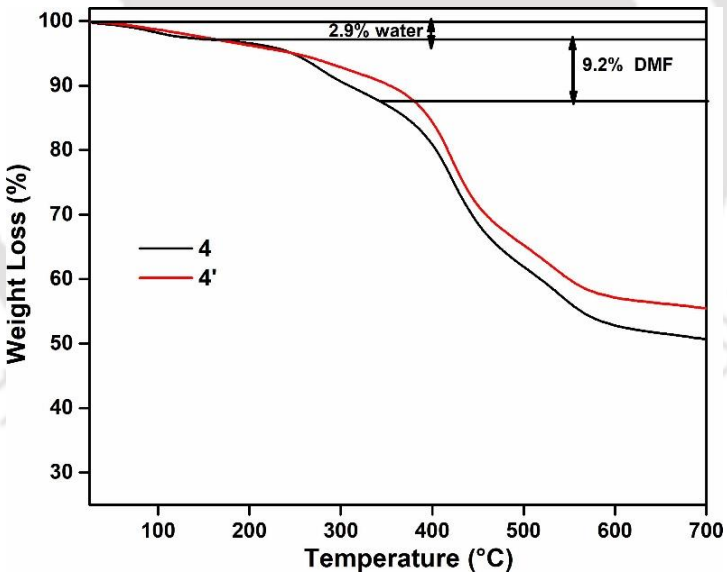

Figure 5.6 TG curves of as-synthesized **4** (black) and thermally activated **4′** (red) recorded in an argon atmosphere in the temperature range of 25-700 °C with a heating rate of 10 °C min^{-1}.

TH-2604_156122006

5.3.6 Chemical Stability

Chemical stability is one of the important factors, which is crucial for the practical application of a MOF. The chemical stability of **4′** was ascertained by treating with water, 1M HCl, glacial acetic acid and 0.1M NaOH solutions for 14 h. Subsequently, the solid residues were obtained by filtration and they were placed in an oven maintained at 100 °C for 6 h. XRPD patterns were collected with the dry solids. Although the structural integrity of **4′** was lost upon treatment with 0.1 M NaOH solution, it remained stable in water, 1 M HCl and glacial acetic acid, as evidenced by XRPD patterns (Figure 5.7). These results point out that the chemical stability of **4′** is quite satisfactory and comparable with the previously reported UiO-66 MOFs.[59, 70]

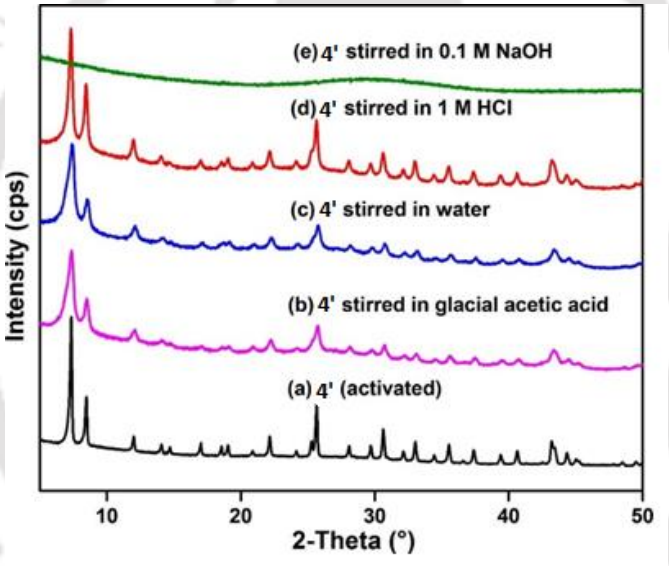

Figure 5.7 XRPD patterns of **4′** under different conditions: (a) **4′** (activated), (b) **4′** after stirring in glacial acetic acid, (c) **4′** after stirring in water, (d) **4′** after stirring in 1M HCl and (d) **4′** after stirring in 0.1M NaOH.

5.3.7 N_2 Sorption Study

The activated compound **4′** was used to carry out N_2 physisorption analysis. The obtained type-I type N_2 sorption isotherms are shown in Figure 5.8. From this physisorption analysis, the surface area and micropore volume of the material were derived as 781 m^2/g and 0.44 cm^3/g at a p/p_0 value of 0.5, respectively. The shape of N_2 sorption curves and the value of pore volume revealed that **4′** is a microporous material. Compound

TH-2604_156122006

4′ is comparable with reported parent and functionalized UiO-66 MOF with regard to surface area and micropore volume.[59, 70, 71]

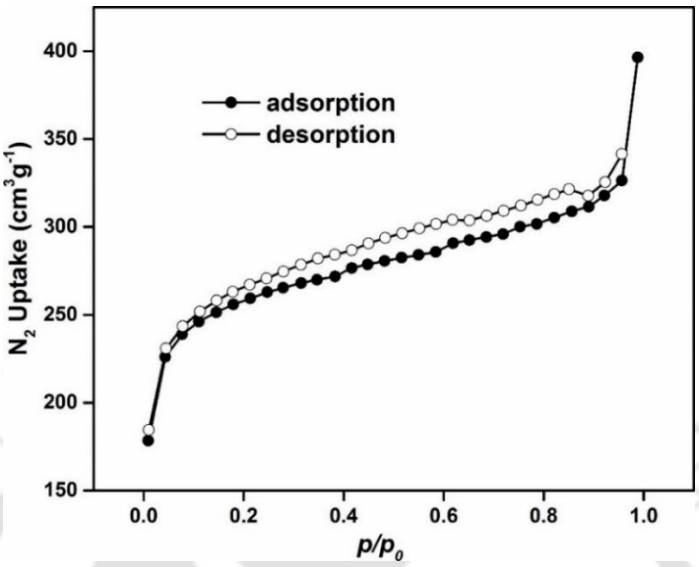

Figure 5.8 N_2 adsorption (solid circle) and desorption (empty circle) isotherms of **4′** measured at –196 °C.

5.3.8 Catalytic Activity

The catalytic performance of **4′** was investigated in the aminolysis of epoxide. Styrene oxide (substrate **1**) and aniline (substrate **2**) were chosen as representative substrates. This reaction afforded two regioisomers and they are shown in Scheme 5.1 as products **3** and **4**. The achieved results are provided in Table 5.2. The analysis of the observed products was executed by GC-MS and ^{1}H NMR methods. The ring opening reaction between **1** and **2** using **4′** as a catalyst in various solvents like ACN (acetonitrile), THF (tetrahydrofuran), DCM (dichloromethane), benzene and toluene exhibited moderate yields between 23-67% after stirring for 12 h at ambient temperature (Table 5.2, entries 1-5). In contrast, the reaction of **1** and **2** with **4′** as solid catalyst afforded 95% yield under solvent-free conditions at ambient temperature after 12 h (Table 5.2, entry 6). In contrast, only 2% conversion was obtained under identical conditions when a control experiment was conducted in absence of catalyst (Table 5.2, entry 7). In all these cases, the use of **4′** as solid catalyst showed the formation of **3** as the major product. These experiments clearly suggest that the reaction is promoted solely by **4′** as catalyst in affording **3** as the major product. Then, the next logical move was to investigate the influence of catalyst loading

TH-2604_156122006

of this reaction under identical conditions. Figure 5.9 provides time yield profile for the ring opening reaction of substrate **1** by substrate **2** to obtain the desired product **3** and by observing enhancement in the initial reaction rate as a function of catalyst loading. This observation is due to the availability of high population of active sites with higher catalyst loading.

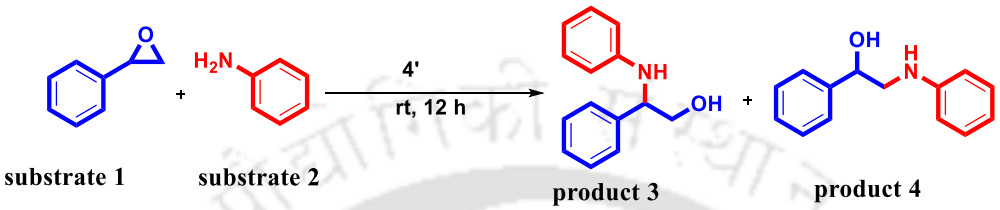

Scheme 5.2 Reaction scheme for the ring opening of substrate **1** by substrate **2** using **4′** as a heterogeneous catalyst.

Table 5.2 Optimization of reaction parameters for the ring opening of substrate **1** by substrate **2** employing **4′** as a heterogeneous catalyst.[a]

Entry	Solvent	Yield[b] (%)	Selectivity	
			3	**4**
1	ACN	44	96	4
2	THF	23	87	13
3	DCM	54	93	7
4	benzene	51	94	6
5	toluene	67	95	5
6	-	95	96	4
7	-	2[c]	100	-

[a] Reaction conditions: substrate **1** (0.6 mmol), substrate **2** (0.5 mmol), solvent (1 mL), catalyst **4′** (15 mg), rt, 12 h.

[b] Determined by GC using internal standard method.

[c] In absence of catalyst **4′**.

TH-2604_156122006

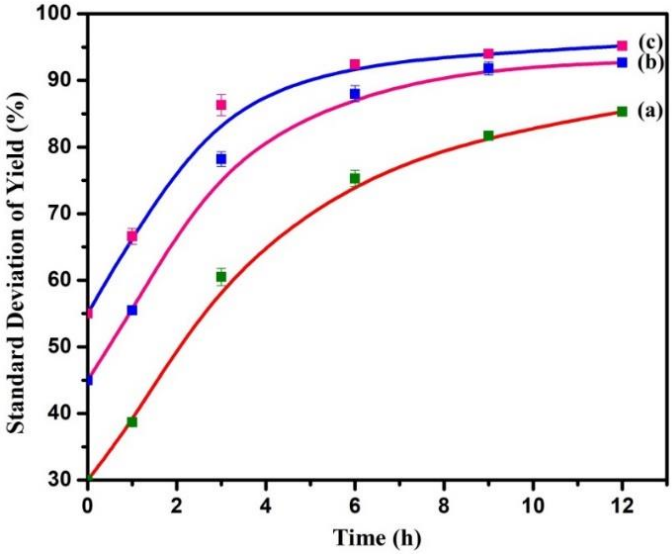

Figure 5.9 Effect of catalyst loading for the aminolysis of **1** by **2** in the presence (a) 5 mg (b) 10 mg and (c) 15 mg of **4′**. Standard deviation analysis was performed by measuring four individual experiments for each catalyst loading.

Figure 5.10 presents the time-conversion profile for the conversion of **1** to **3** and **4** by **2** using **4′** as solid catalyst and a control experiment without **4′** in toluene at room temperature. These catalytic results suggest that the presence of catalyst is required for this reaction even in the presence of solvents. Further, to validate whether the present catalytic method is inherently heterogeneous in nature, the catalyst was taken out from reaction mixture after 1 h when conversion of **1** was about 18%. Then, the reaction in the absence of **4′** was continued under identical experimental conditions for the remaining time (Figure 5.10). The observed results suggest that the rate of reaction became completely constant after elimination of catalyst from the reaction vessel. Further, the filtrate of the reaction was investigated by ICP-AES, which verified the absence of zirconium (below the detection limit). These results convincingly demonstrate that the reaction is heterogeneous in nature. Moreover, the catalyst was conveniently retrieved from the reaction mixture by filtration and reused for five cycles without any decay its catalytic performance (Figure 5.11). The five-time reused catalyst showed identical crystalline pattern (Figure 5.12) with that of the fresh solid through XRPD analysis, thus verifying the structural integrity of **4′** under reaction conditions. Moreover, the crystalline nature of **4′** was verified by FE-SEM analysis (Figures 5.13a and 5.13b) and unaltered morphology of **4′** after catalysis was observed compared to its fresh sample. In addition, EDX elemental analysis revealed no

TH-2604_156122006

changes in elemental composition of **4′** before and after catalysis as shown in Figures 5.14a and 5.14b.

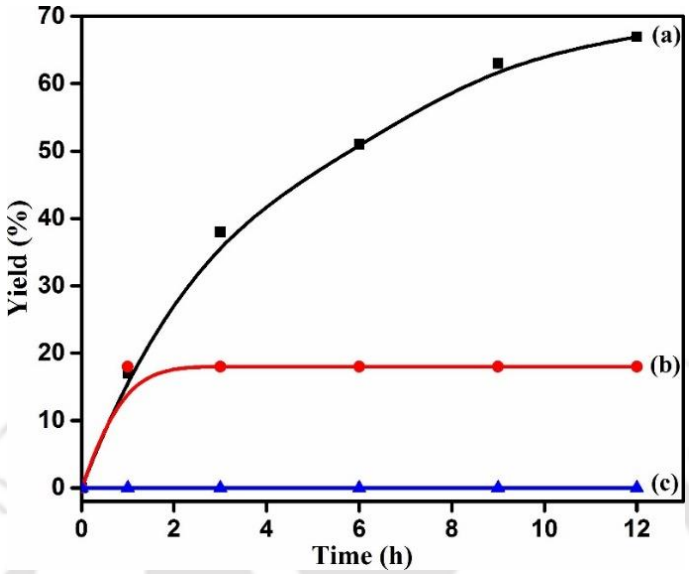

Figure 5.10 Time-conversion plot for ring opening of substrate **1** by substrate **2** using **4′** as a heterogeneous solid catalyst: (a) with catalyst, (b) catalyst filtered after 1 h and (c) without catalyst. Reaction conditions: substrate **1** (0.6 mmol), substrate **2** (0.5 mmol), toluene (1 mL), **4′** (15 mg), rt, 12 h.

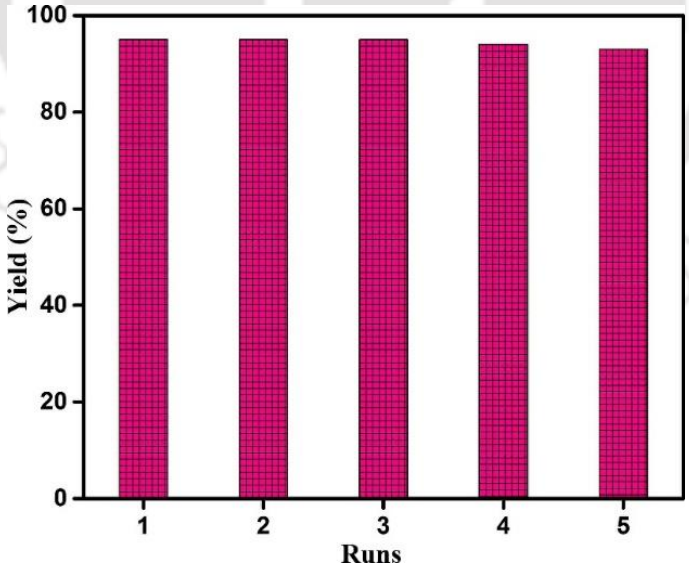

Figure 5.11 Reusability plot for ring opening of substrate **1** by substrate **2** using **4′** as a solid catalyst.

TH-2604_156122006

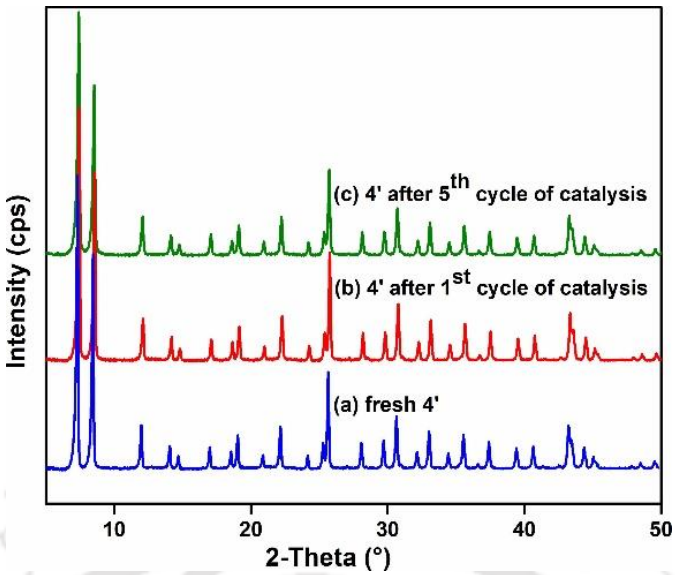

Figure 5.12 Comparison of the XRPD pattern of a fresh sample of **4′** (a) with that of the same sample recovered after the first (b) and fifth (c) cycle of catalysis.

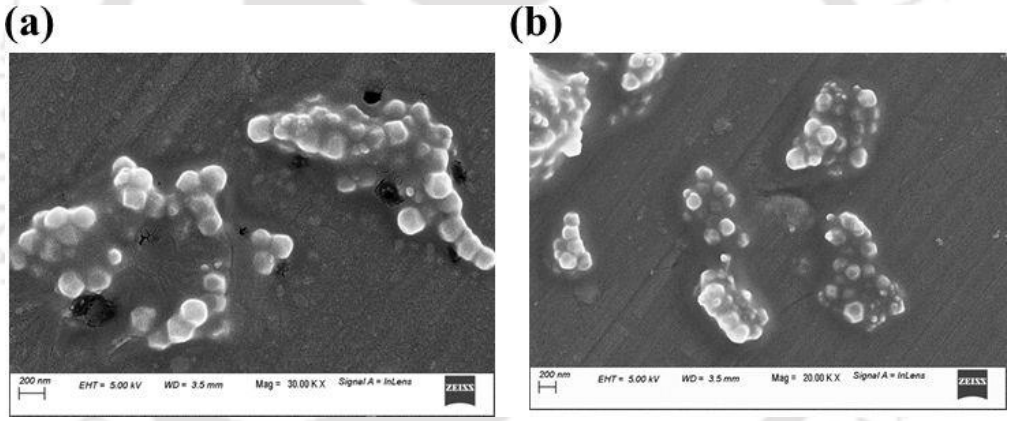

Figure 5.13 FE-SEM images of **4′** (a) before and (b) after catalysis.

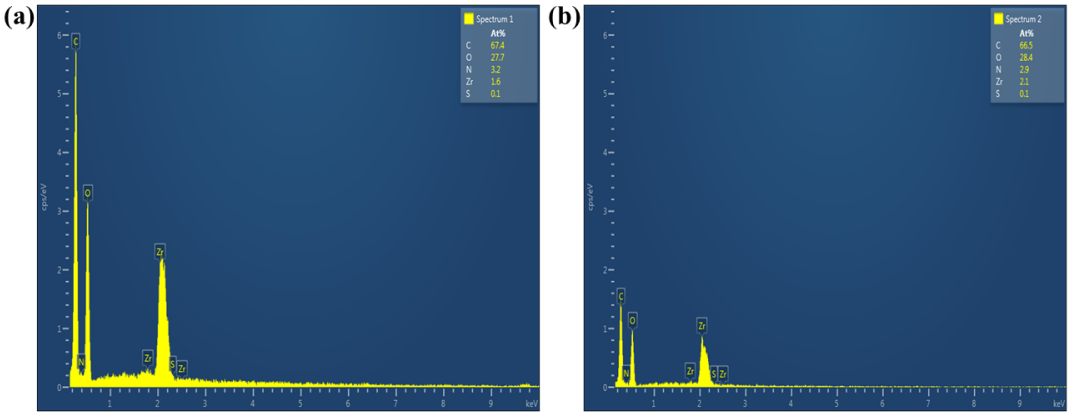

Figure 5.14 EDX analysis of **4′** (a) before and (b) after catalysis.

TH-2604_156122006

The nature of active sites was also examined in **4′** by comparing its activity with the corresponding metal salt and linker. The achieved results are displayed in Figure 5.15. The activity of **4′** is significantly higher compared to $ZrCl_4$ (metal component) and 2-(thiophene-2-carboxamido)benzene-1,4-dicarboxylic acid (linker). This may be attributed to the presence of dual active sites in **4′** through metal node (Lewis acidic site) and 2-(thiophene-2-carboxamido) functionalized linker (pseudo Lewis acidic site) for the ring opening of **1**. This hypothesis was established by conducting a masking experiment with pyridine. The activities of $ZrCl_4$, linker and **4′** were completely quenched by the introduction of pyridine to the reaction mixture. These results unambiguously prove that pyridine behaves as a Lewis base by coordinating strongly to the metal ion like σ bond, thus inhibiting the interactions of substrate **1** with the metal centers.[72] Furthermore, the activities of **4′** and linker were quenched by pyridine due to the formation of hydrogen bonding between -NH group of linker and N atom of pyridine.[73]

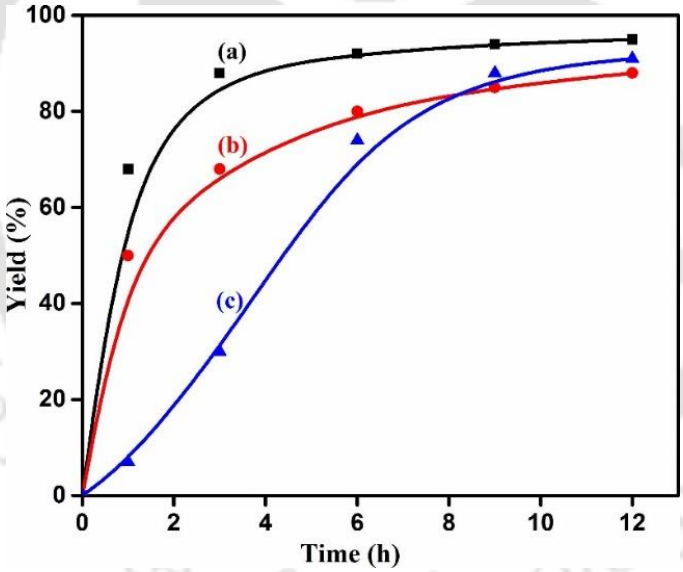

Figure 5.15 Time-conversion plot for the ring opening of substrate **1** by substrate **2** using **4′** (a) and its corresponding homogeneous counterparts: metal salt ($ZrCl_4$) (b) and linker [H_2BDC-(thiophene-2-carboxamido)] (c).

The activity of **4′** was also screened with a series of MOFs possessing Lewis acidic sites like Fe(BTC), $Cu_3(BTC)_2$ and Zr-UiO-66 and the observed results are shown in Figure 5.16. These data prove that **1′** has better catalytic performance compared to other tested MOFs under identical conditions. This superior performance of **4′** can be due to the high

TH-2604_156122006

population of active sites compared to other catalysts. Interestingly, the enhanced catalytic performance of **4′** than Zr-UiO-66 is due to the operation of dual active sites in **4′**.

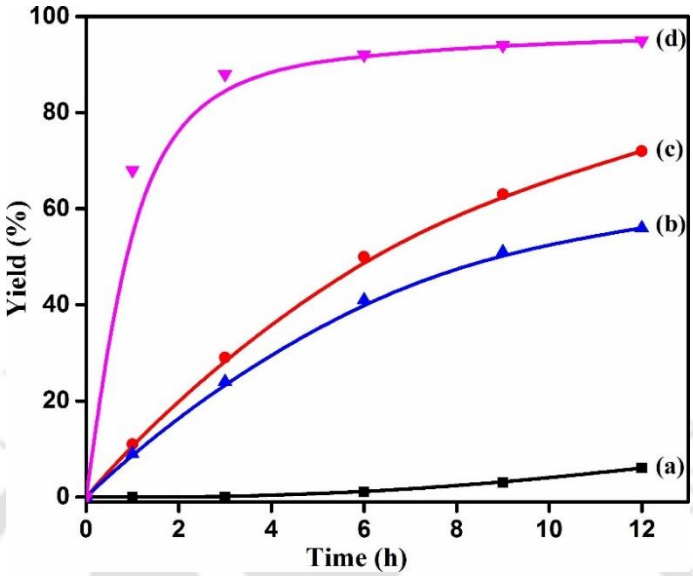

Figure 5.16 Time-conversion plot for ring opening of substrate **1** by substrate **2** using different MOFs as solid heterogeneous catalysts: (a) $Cu_3(BTC)_2$, (b) Zr-UiO-66, (c) Fe(BTC) and (d) **4′**.

Besides comparing the activity of **4′** with other related MOFs, the catalytic performance of **4′** was also compared with some of the conventional catalysts like MIL-53(Al), neutral Al_2O_3, SiO_2 and K10 montmorillonite clay employed for the ring opening of epoxides by amines under similar conditions. The observed catalytic data are given in Figure 5.17. K10 montmorillonite clay provided slightly higher activity than **4′** but this activity difference is due to the difference in the structure and active sites. Furthermore, the reactants reach the active sites without having any diffusion limitation in clay while the use of **4′** impedes diffusion of reactants. On other hand, the activity of **4′** was comparable to SiO_2 while the activity of Al_2O_3 and MIL-53(Al) was significantly lower compared to **4′**. Hence, it is very difficult to compare the activity of **4′** with other conventional catalysts, since the activity of solid depends on many factors like structure of catalyst, active sites, diffusion limitation and others. The activity of **4′** may be higher or lower compared to conventional catalysts, but the objective of this work is not to rank the present catalyst in the series rather to demonstrate the ability of **4′** to promote ring opening of epoxides by amines.

TH-2604_156122006

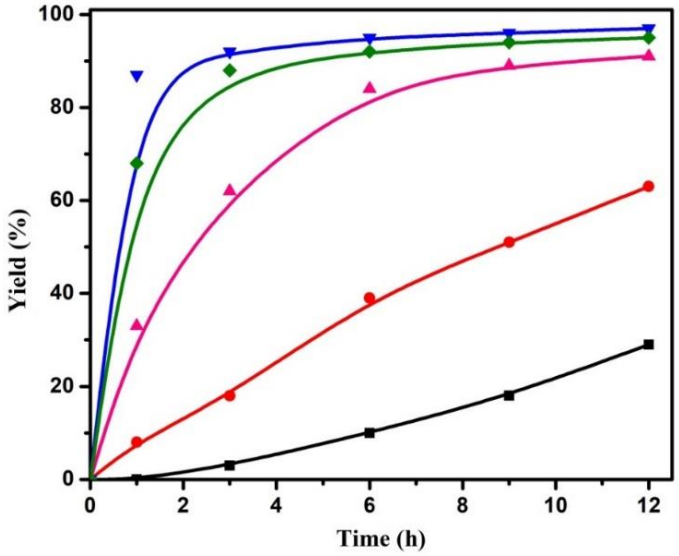

Figure 5.17 Time conversion plots for the aminolysis of substrate **1** by substrate **2** using different solid heterogeneous catalysts: (■) MIL-53(Al), (●) neutral Al_2O_3, (▲) SiO_2, (♦) **4′** and (▼) K10 montmorillonite clay.

In order to enlarge the scope of our catalyst, aminolysis of epoxides was performed with various amine substrates catalysed by **4′** using optimized reaction parameters. The obtained catalytic results are presented in Table 5.3. The reaction of **1** with **2** in the presence of **4′** afforded 95% yield with β-amino alcohol as the major regioisomer (Table 5.3, entry 1). Similarly, 4- and 2-methylanilines were reacted effectively with **1** to provide respective products in 95% yields under identical conditions (Table 5.3, entries 2 and 3). Further, the aminolysis reaction of **1** by 4- and 2-methoxyanilines showed 94 and 95% yields respectively showing identical isomer as aniline (Table 5.3, entries 4 and 5). In addition, the reaction of **1** with 4-chloro and 4-bromoanilines exhibited the corresponding β-amino alcohols in 95 and 94% yields, respectively, under optimized reaction conditions (Table 5.3, entries 6 and 7). On the other side, the aminolysis of **1** by 4-nitroaniline showed 31% yield at room temperature after 12 h whereas the yield enhanced to 89% at 60 °C after 24 h (Table 5.3, entry 8). This decreased rate with 4-nitroaniline may be due to the poor nucleophilic character of the amino group caused by the existence of electron withdrawing nitro group. A similar behaviour was also witnessed for the aminolysis reaction between **1** and 4-aminobenzoic acid (Table 5.3, entry 9). In addition, the reaction between 3-cyanoanilne and **1** with **4′** as a solid catalyst exhibited 82% yield at ambient temperature and 93% yield at 60 °C after 12 h (Table 5.3, entry 10).

TH-2604_156122006

Furthermore, the reaction of **1** and aminocyclohexane using **4′** as a solid catalyst afforded secondary alcohol as the major product at room temperature, however, the yield increased to 92% at 60 °C after 12 h (Table 5.3, entry 11). This inverse selectivity may be due to the steric hindrance of cyclohexane ring, which prefers to attack the methylene carbon in **1**. Interestingly, aminolysis reaction of **1** and *n*-butylamine exhibited equal ratio of regioisomers either at room temperature or at 60 °C (Table 5.3, entry 12).

Table 5.3 Ring opening of substrate **1** by various aryl and alkyl amine substrates using **4′** as a solid heterogeneous catalyst.[a]

Entry	Amine	Regioisomer		Yield[b]	Selectivity[c]	
		Isomer **I**	Isomer **II**	(%)	**I**	**II**
1	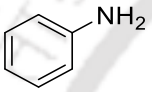	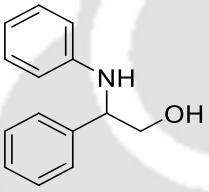	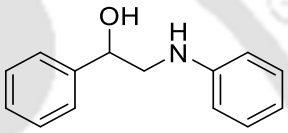	95	96	4
2	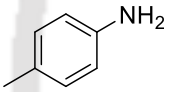	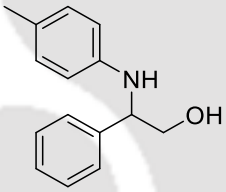	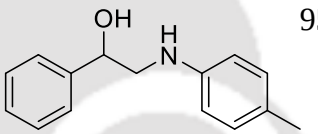	95	95	5
3	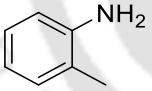	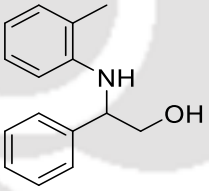	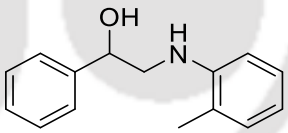	95	96	4
4	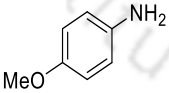	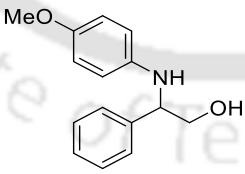	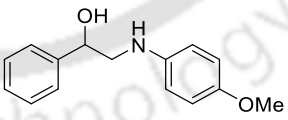	94	95	5
5	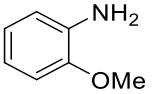	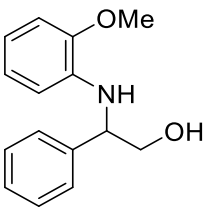	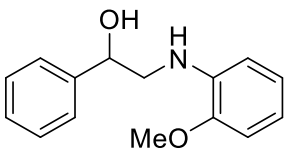	95	96	4

TH-2604_156122006

6	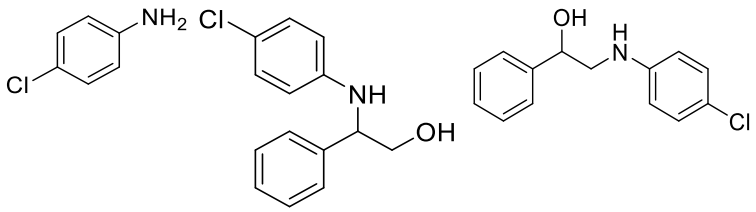	95	97	3
7	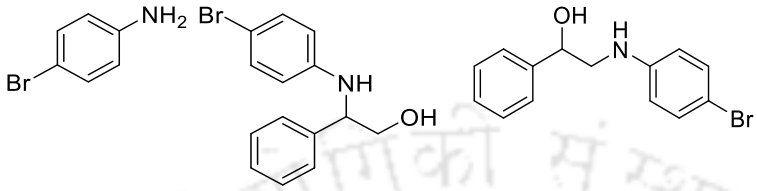	94	98	2
8	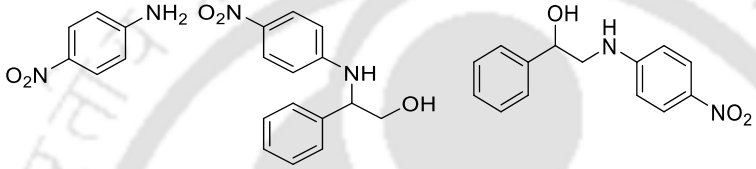	31	97	3
		89[d]	96	4
9	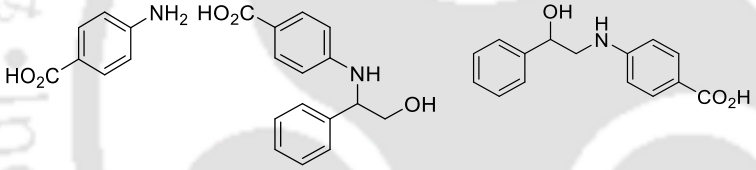	44	100	-
		53[d]	100	-
10	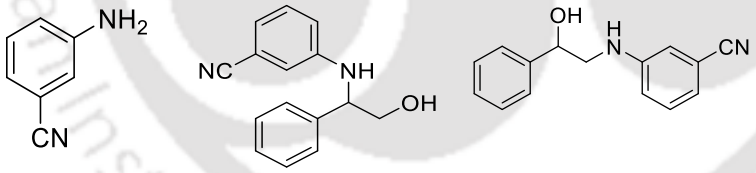	82	97	3
		93[e]	98	2
11	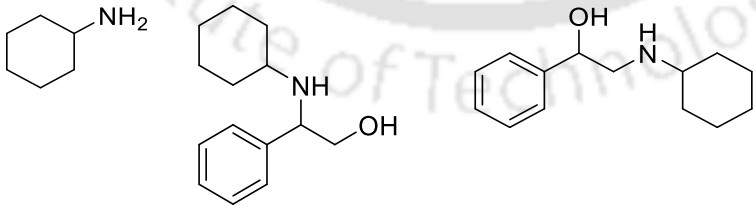	66	17	83
		92[e]	29	71
12	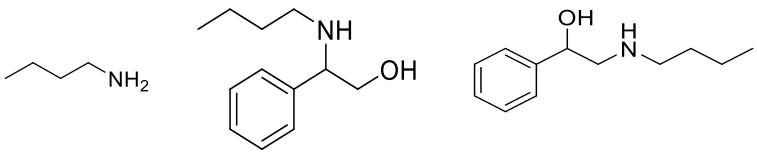	74	47	53
		89[e]	51	49

[a] Reaction conditions: substrate **1** (0.6 mmol), amine (0.5 mmol), **4′** (15 mg), rt, 12 h.

[b] Determined by GC using internal standard method.

TH-2604_156122006

[c] Determined by GC and GC-MS.

[d] At 60 °C for 24 h.

[e] At 60 °C for 12 h.

Furthermore, ring opening of other epoxide substrates with **2** using **4′** as catalyst was also tested under identical conditions. The obtained results are presented in Table 5.4. The reaction of cyclohexene oxide with **2** in the existence of **4′** afforded a single product in 97% yield at ambient temperature (Table 5.4, entry 1). Further, the aminolysis of epichlorohydrin with **2** using **4′** as a solid catalyst showed secondary alcohol as the only product (Table 5.4, entry 2). This may be explained due to the steric nature of chlorine atom. Finally, mixtures of regioisomers with equal selectivity were obtained for the reaction between isobutylene oxide and substrate **2** with **4′** as a catalyst at room temperature or at 60 °C (Table 5.4, entry 3).

Table 5.4 Ring opening of other epoxide substrates by substrate **2** using **4′** as a heterogeneous solid catalyst.[a]

Entry	Epoxide	Regioisomer		Yield[b] (%)	Selectivity[c]	
		Isomer **I**	Isomer **II**		**I**	**II**
1	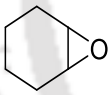	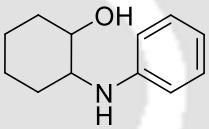	-	97	-	-
2	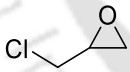	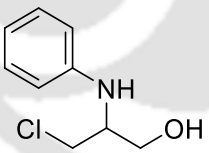	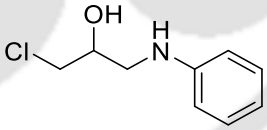	93	-	100
3		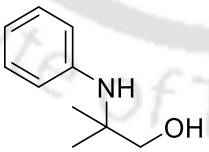	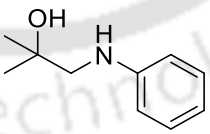	79	46	54
				88[d]	48	52

[a] Reaction conditions: epoxide (0.6 mmol), substrate **2** (0.5 mmol), catalyst **4′** (15 mg), rt, 12 h.

[b] Determined by GC using internal standard method.

[c] Determined by GC and GC-MS.

[d] At 60 °C.

TH-2604_156122006

A suitable reaction mechanism is proposed for the aminolysis of substrate **1** by substrate **2** with **4′** as a solid catalyst in Scheme 5.2a and 5.2b. As discussed earlier, there are two types of active sites in **1′** namely the metal sites (Zr^{4+}) and the linker. Hence, the mechanism is proposed by involving both active sites. Scheme 5.2a shows the interaction of substrate **1** with **4′** through oxygen by decreasing the electron density in the carbon attached to phenyl thus favoring for nucleophilic attack. This carbon site was attacked by **2** to give the expected product **3**. This mechanism is in agreement with earlier literature reports involving metal sites as active sites.[74-77]

On other hand, Scheme 5.2b provides the possible mechanism through the linker installed in **4′**. The interaction of substrate **1** with catalyst **4′** occurs through the weak coordination of oxygen atom of substrate **1** with the N-H and thiophene moieties in **4′**. This interaction decreases the electron density at secondary carbon in substrate **1**, thus favouring the nucleophilic attack by substrate **2** to provide an intermediate as shown in Scheme 5.2b. This further rearranges to provide the expected product in major proportion. Furthermore, the formation of other product is also possible through the attack of nucleophile (substrate **2**) at methylene carbon under identical reaction conditions.

One of the proposed intermediates in Scheme 5.2b is the interaction of substrate **1** through the oxygen with **4′** of N-H bond. In order to prove this interaction, ^{1}H-NMR spectra were recorded for the linker, substrate **1** and the physical mixture of linker with substrate **1**. The observed results are shown in Figure 5.18. The N-H proton in the linker is seen at 12.08 ppm while upon adding substrate **1**, this peak was shifted to downfield to 12.14 ppm after 10 min and further to 12.30 and 12.29 ppm after 1 and 8 h, respectively. These results are in close agreement with earlier report.[78] Furthermore, additional control experiment was performed to prove the proposed mechanism with deuterated methanol (CD_3OD) as a nucleophile for the ring opening of substrate **1** under similar experimental conditions. The analysis of the reaction mixture by GC-MS clearly indicates the formation of a product with m/z value of 156 (Figure 5.19) whereas the m/z value is 152 for CH_3OH (Figure 5.20). These experiments confirm that the hydrogen transfer occurs from the protonated intermediate to the final product originates from the nucleophile as shown in Scheme 5.2b.

TH-2604_156122006

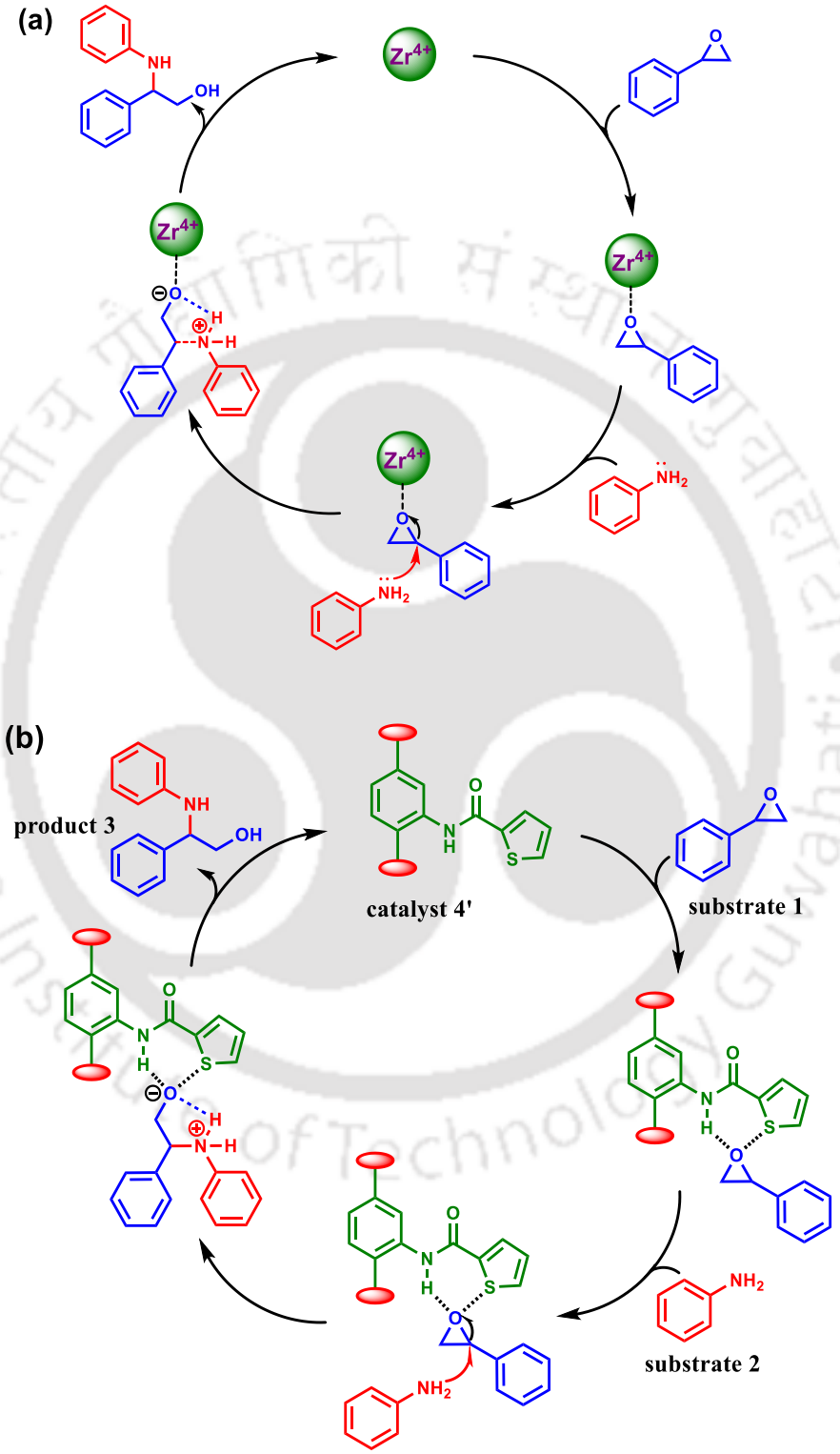

Scheme 5.2 Possible mechanism for the ring opening of substrate **1** by substrate **2** through (a) metal sites (Zr^{4+}) and (b) thiophene-2-carboxamido linker in **4′**.

TH-2604_156122006

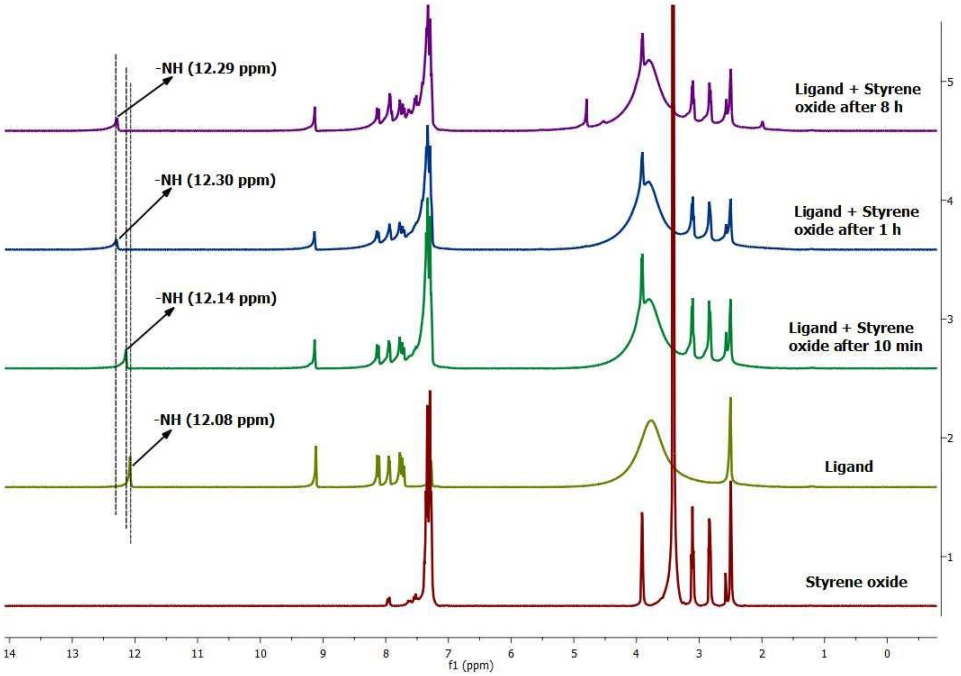

Figure 5.18 Stacked ^{1}H-NMR spectra of substrate **1**, linker and the physical mixture of linker and substrate **1** at different time intervals in DMSO-d_6.

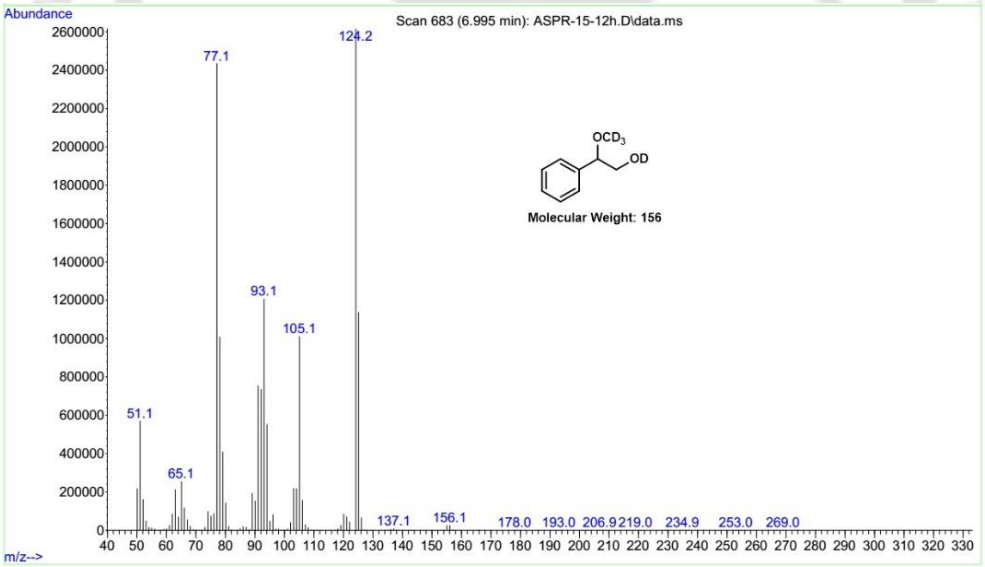

Figure 5.19 GC-MS trace of 2-(methoxy-d_3)-2-phenylethan-1-ol-d.

TH-2604_156122006

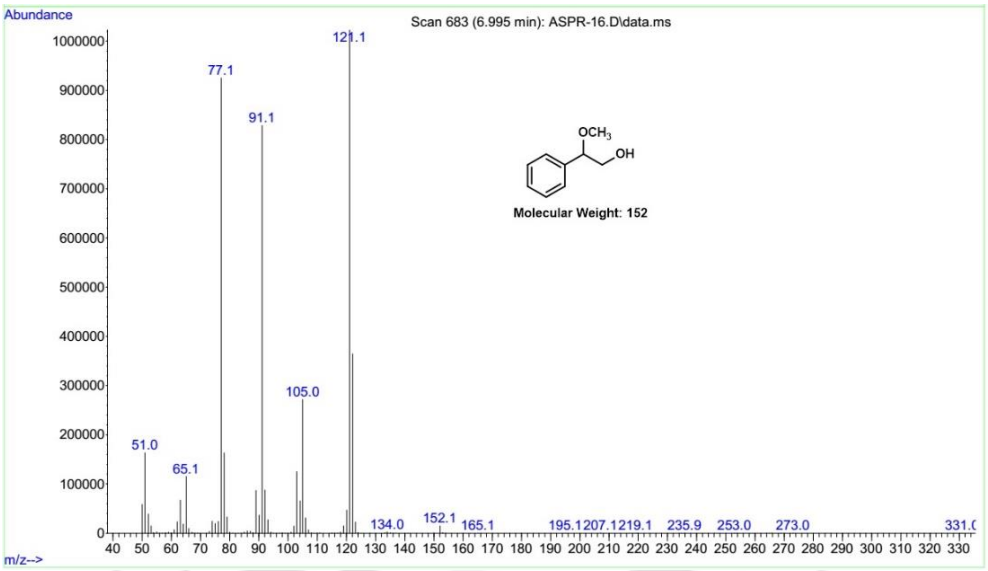

Figure 5.20 GC-MS trace of 2-methoxy-2-phenylethan-1-ol.

5.4 Conclusions

We have demonstrated the synthesis and characterization of the new 2-(thiophene-2-carboxamido)benzene-1,4-dicarboxylic acid linker and successfully utilized it for the synthesis of Zr(IV) based UiO-66 MOF. The MOF was synthesized using traditional solvothermal method and characterized using XRPD, FT-IR, TG and BET analysis. The specific BET surface area of **4′** derived from nitrogen physisorption experiment was 781 $m^2 g^{-1}$. The material showed high chemical stability (in acetic acid, 1M HCl and water) as well as thermal stability (up to 340 °C). Material **4′** was employed as a heterogeneous solid catalyst for ring opening of epoxide by amine. Catalyst **4′** showed higher yields of the ring-opened products and broad substrate scope for both epoxide and amine. The catalyst displayed better activity than existing Lewis acidic MOF catalysts like $Cu_3(BTC)_2$, Fe(BTC) and Zr-UiO-66. The exclusive role of **4′** in the catalysis reaction was verified by executing control experiments with free linker, zirconium salt and without catalyst **4′**. The reusability of the catalyst was illustrated up to five cycles. A plausible mechanism for the catalytic reaction has been also provided.

5.5 References

1. G. H. Posner and D. Z. Rogers, *J. Am. Chem. Soc.*, 1977, **99**, 8208–8214.
2. J. Lieosccher, S. Jin, A. Otto and K. Woydowski, *J. Heterocycl. Chem.*, 2000, **37**, 509-518.

TH-2604_156122006

3. I. Vilotijevic and T. F. Jamison, *Angew. Chem., Int. Ed. Engl.*, 2009, **48**, 5250–5281.
4. S. Bonollo, D. Lanari and L. Vaccaro, *Eur. J. Org. Chem.*, 2011, **2011**, 2587-2598.
5. K. Kopka, S. Wagner, B. Riemann, M. P. Law, C. Puke, S. K. Luthra, V. W. Pike, T. Wichter, W. Schmitz, O. Schober and M. Schäfers, *Bioorg. Med. Chem.*, 2003, **11**, 3513–3527.
6. D. J. Ager, I. Prakash and D. R. Schaad, *Chem. Rev.*, 1996, **96**, 835–876.
7. N. Azizi, B. Mirmashhori and M. R. Saidi, *Catal. Commun.*, 2007, **8**, 2198-2203.
8. J.-D. Zhang, X.-X. Yang, Q. Jia, J.-W. Zhao, L.-L. Gao, W.-C. Gao, H.-H. Chang, W.-L. Wei and J.-H. Xu, *Catal. Sci. Technol.*, 2019, **9**, 70-74.
9. A. V. Malkov, M. A. Kabeshov, M. Bella, O. Kysilka, D. A. Malyshev, K. Pluháčková and P. Kočovský, *Org. Lett.*, 2007, **9**, 5473-5476.
10. J. M. Andrés, R. Barrio, M. A. Martínez, R. Pedrosa and A. Pérez-Encabo, *J. Org. Chem.*, 1996, **61**, 4210-4213.
11. M. E. Jung and S. W. Yi, *Tetrahedron Lett.*, 2012, **53**, 4216–4220.
12. S. C. Bergmeier, *Tetrahedron*, 2000, **56**, 2561-2576.
13. K. Tanaka, M. Kinoshita, J. Kayahara, Y. Uebayashi, K. Nakaji, M. Morawiak and Z. Urbanczyk-Lipkowska, *RSC Adv.*, 2018, **8**, 28139–28146.
14. W. Chen, Z.-H. Zhou and H.-B. Chen, *Org. Biomol. Chem.*, 2017, **15**, 1530-1536.
15. A. K. Kinage, P. P. Upare, A. B. Shivarkar and S. P. Gupte, *Green Sustainable Chem.*, 2011, **1**, 76-84
16. T.-X. Métro, J. Appenzeller, D. G. Pardo and J. Cossy, *Org. Lett.*, 2006, **8**, 3509-3512.
17. V. T. Kamble and N. S. Joshi, *Green Chem. Lett. Rev.*, 2010, **3**, 275-281.
18. D. S. Bhagavathula, G. Boddeti and R. Venu, *Res. Rev.: J. Chem.*, 2017, **6**, 27-46.
19. J. P. Michael, *Nat. Prod. Rep.*, 2001, **18**, 520–542.
20. J. D. Cree, H. Geukens, J. Leempoels and H. Verhaegen, *Drug Dev. Res.*, 1986, **8**, 109–117.
21. R. Kamboj, A. Bhadani and S. Singh, *Ind. Eng. Chem. Res.*, 2011, **50**, 8379–8383.
22. D. Julião, A. D. S. Barbosa, A. F. Peixoto, C. Freire, B. D. Castro, S. S. Balula and L. Cunha-Silva, *CrystEngComm*, 2017, **19**, 4219–4226.
23. H. Varshney, A. Ahmad and A. Rauf, *Food Nutr. Sci.*, 2013, **4**, 21-24

TH-2604_156122006

24. S. Bansal, Y. Kumar, P. Pippal, D. K. Das, P. Pramanik and P. P. Singh, *New J. Chem.*, 2017, **41**, 2668-2671.
25. N. Azizi and M. R. Saidi, *Org. Lett.*, 2005, **7**, 3649-3651.
26. M. Lee, J. R. Lamb, M. J. Sanford, A. M. LaPointe and G. W. Coates, *Chem. Commun.*, 2018, **54**, 12998-13001.
27. J. Wu and H.-G. Xia, *Green Chem.*, 2005, **7**, 708–710.
28. T. Baskaran, A. Joshi, G. Kamalakar and A. Sakthivel, *Appl. Catal., A*, 2016, **524**, 50-55.
29. T. Nobuta, G. Xiao, D. Ghislieri, K. Gilmore and P. H. Seeberger, *Chem. Commun.*, 2015, **51**, 15133-15136.
30. S. Tobisch, *Chem.–Eur. J.*, 2015, **21**, 6765-6779.
31. B. Y. a. V. M. N. Aramesh, *Inorg. Chem. Commun.*, 2013, **28**, 37–40.
32. M. Chini, P. Crotti and F. Macchia, *Tetrahedron Lett.*, 1990, **31**, 4661-4664.
33. A. Papini, A. Ricci, M. Taddei, G. Seconi and P. Dembech, *J. Chem. Soc., Perkin Trans. 1*, 1984, **0**, 2261-2265.
34. P. Rani and R. Srivastava, *RSC Adv.*, 2015, **5**, 28270–28280.
35. J. A. Deyrup and C. L. Moyer, *J. Org. Chem.*, 1969, **34**, 175-179.
36. J. Otera, Y. Niibo, N. Tatsumi and H. Nozaki, *J. Org. Chem.*, 1988, **53**, 275-278.
37. H.-C. Zhou, J. R. Long and O. M. Yaghi, *Chem. Rev.*, 2012, **112**, 673-674.
38. D. Bradshaw, A. Garai and J. Huo, *Chem. Soc. Rev.*, 2012, **41**, 2344-2381.
39. A. Karmakar, A. V. Desai and S. K. Ghosh, *Coord. Chem. Rev.*, 2016, **307**, 313-341.
40. A. H. Chughtai, N. Ahmad, H. A. Younus, A. Laypkov and F. Verpoort, *Chem. Soc. Rev.*, 2015, **44**, 6804-6849.
41. T. K. Pal, D. De, S. Senthilkumar, S. Neogi and P. K. Bharadwaj, *Inorg. Chem.*, 2016, **55**, 7835-7842.
42. A. K. Gupta, D. De, K. Tomar and P. K. Bharadwaj, *Dalton Trans.*, 2018, **47**, 1624-1634
43. B. Gole, U. Sanyal, R. Banerjee and P. S. Mukherjee, *Inorg. Chem.*, 2016, **55**, 2345-2354.
44. S. Sharma and S. K. Ghosh, *ACS Omega*, 2018, **3**, 254-258.
45. A. Das and S. Biswas, *Sens. Actuators, B.*, 2017, **250**, 121-131.

TH-2604_156122006

46. W. P. Lustig, S. Mukherjee, N. D. Rudd, A. V. Desai, J. Li and S. K. Ghosh, *Chem. Soc. Rev.*, 2017, **46**, 3242-3285
47. A. Karmakar, N. Kumar, P. Samanta, A. V. Desai and S. K. Ghosh, *Chem. Eur. J*, 2016, **22**, 864-868.
48. L. Wang, M. Zheng and Z. Xie, *J. Mater. Chem. B*, 2018, **6**, 707-717
49. Y. Gao, R. Broersen, W. Hageman, N. Yan, M. C. Mittelmeijer-Hazeleger, G. Rothenberg and S. Tanase, *J. Mater. Chem. A*, 2015, **3**, 22347-22352.
50. J. Liu, L. Chen, H. Cui, J. Zhang, L. Zhang and C.-Y. Su, *Chem. Soc. Rev.*, 2014, **43**, 6011-6061.
51. L. Zhu, X.-Q. Liu, H.-L. Jiang and L.-B. Sun, *Chem. Rev.*, 2017, **117**, 8129−8176.
52. L. Shen, R. Liang, M. Luo, F. Jing and L. Wu, *Phys. Chem. Chem. Phys.*, 2015, **17**, 117–121.
53. L. T. M. Hoang, L. H. Ngo, H. L. Nguyen, H. T. H. Nguyen, C. K. Nguyen, B. T. Nguyen, Q. T. Ton, H. K. D. Nguyen, K. E. Cordova and T. Truong, *Chem. Commun.*, 2015, **51**, 17132–17135.
54. T. L. H. Doan, T. Q. Dao, H. N. Tran, P. H. Tran and T. N. Le, *Dalton Trans.*, 2016, **45**, 7875–7880.
55. F. G. Cirujano, A. Corma and F. X. L. I. Xamena, *Catal. Today*, 2015, **257**, 213-220.
56. Y. Y. H.-F. Yao, F.-G. Xi and E.-Q. Gao, *J. Mol. Catal. A: Chem.*, 2014, **390**, 198-205.
57. T. L. H. Doan, T. Q. Dao, H. N. Tran, P. H. Tran and T. N. Le, *Dalton Trans.*, 2016, **45**, 7875-7880
58. N. Stock and S. Biswas, *Chem. Rev.*, 2012, **112**, 933−969.
59. A. Das, S. Das, V. Trivedi and S. Biswas, *Dalton Trans.*, 2019, **48**, 1332-1343.
60. A. Das, S. Banesh, V. Trivedi and S. Biswas, *DaltonTrans.*, 2018, **47**, 2690-2700.
61. A. Das, N. Anbu, M. SK, A. Dhakshinamoorthy and S. Biswas, *Inorg. Chem.*, 2019, **58**, 5163-5172.
62. S. Mallakpour and A. Zadehnazari, *J. Adv. Res.*, 2014, **5**, 311-318.
63. J. H. Cavka, S. Jakobsen, U. Olsbye, N. Guillou, C. Lamberti, S. Bordiga and K. P. Lillerud, *J. Am. Chem. Soc.*, 2008, **130**, 13850-13851.
64. L. Valenzano, B. Civalleri, S. Chavan, S. Bordiga, M. H. Nilsen, S. Jakobsen, K. P. Lillerud and C. Lamberti, *Chem. Mater.*, 2011, **23**, 1700–1718.

TH-2604_156122006

65. A. Schaate, P. Roy, A. Godt, J. Lippke, F. Waltz, M. Wiebcke and P. Behrens, *Chem.–Eur. J.*, 2011, **17**, 6643–6651.
66. F. Ragon, B. Campo, Q. Yang, C. Martineau, A. D. Wiersum, A. Lago, V. Guillerm, C. Hemsley, J. F. Eubank, M. Vishnuvarthan, F. Taulelle, P. Horcajada, A. Vimont, P. L. Llewellyn, M. Daturi, S. Devautour-Vinot, G. Maurin, C. Serre, T. Devic and G. Clet, *J. Mater. Chem. A*, 2015, **3**, 3294-3309.
67. *Accelrys Materials Studio Version 5.0*, San Diego, CA, USA, 2009.
68. A. K. Rappe, C. J. Casewit, K. S. Colwell, W. A. GoddardIII and W. M. Skiff, *J. Am. Chem. Soc.*, 1992, **114**, 10024–10035.
69. A. J. Howarth, Y. Liu, P. Li, Z. Li, T. C. Wang, J. T. Hupp and O. K. Farha, *Nature Rev. Mater.*, 2016, **1**, 1–15.
70. S. Nandi, S. Banesh, V. Trivedi and S. Biswas, *Analyst*, 2018, **143**, 1482-1491.
71. L. Zhou, X. Zhang and Y. Chen, *Mater. Lett.*, 2017, **197**, 167-170.
72. S. Pal, *Pyridine: A Useful Ligand in Transition Metal Complexes*, IntechOpen, 2018.
73. H.-J. Yen, J.-H. Lin, Y. O. Su and G.-S. Liou, *Electrochim. Acta*, 2018, **261**, 307-313.
74. P. B. Shivani and A. K. Chakraborti, *J. Org. Chem.*, 2007, **72**, 3713-3722.
75. K. Tabatabaeian, M. Mamaghani, N. O. Mahmoodi and A. Khorshidi, *Tetrahedron Lett.*, 2008, **49**, 1450-1454.
76. A. Dhakshinamoorthy, M. Alvaro and H. Garcia, *Chem. Eur. J.*, 2010, **16**, 8530-8536.
77. A. T. Placzek, J. L. Donelson, R. Trivedi, R. A. Gibbs and S. K. De, *Tetrahedron Lett.*, 2005, **46**, 9029-9034.
78. R. Luo, W. Zhang, X. Zhou and H. Ji, *Chin. J. Chem.*, 2017, **35**, 659-664.

TH-2604_156122006

TH-2604_156122006

Conclusions

In Chapter 1, the evolution from pure coordination compounds to the pioneering chemistry of MOFs is discussed. The design and synthesis of functionalized, highly stable MOFs can be carried out *via* proper linker design. MOFs can be successfully utilized towards chemical sensing *via* the fluorescence method. They can be also used as heterogeneous solid catalysts for organic transformation reactions. This study focuses on the design and synthesis of functionalized MOFs based on the carboxylic acid linkers and high-valent metal ions. Using the concept of isoreticular chemistry, the linkers are functionalized with the proper choice of functional groups to utilize the MOFs for desired fluorometric sensing and catalytic applications. Various synthesis methods of MOFs are discussed here. The role of solvents, temperature and modulator have a significant impact on the crystallinity, particle size, porosity and stability of MOFs. Hence, the development of some highly stable MOFs will have significant implications in modern science, since they can make the chemical reactions faster and enable the detection of toxic chemicals existing in the environment.

In Chapter 2, the Al-MIL-53-N_3 (**1**) metal-organic framework (MOF) was synthesized under solvothermal reaction conditions using $Al(NO_3)_3 \cdot 9H_2O$ and $H_2BDC\text{-}N_3$ linker. The activated **1** (called **1′**) showed a speedy *turn-on* fluorescence response to H_2S and *turn-off* response to Fe(III) ions in an aqueous medium. For both the sensing, the probe showed excellent sensitivity and selectivity even in the presence of other potentially intrusive analytes. The detection limits (90.47 nM for H_2S and 0.03 μM for Fe(III) ions in water) of **1′** are lower than those of the formerly reported MOF type of fluorescent sensors. Compound **1′** responds to intracellular H_2S by exhibiting strong blue fluorescence. Besides, **1′** can detect H_2S in human blood plasma (HBP) and sulfide ions in real water samples. In the presence of H_2S, the azide moiety is converted to amine and gives turn-on fluorescence. On the other hand, the partial replacement of framework Al(III) ions by Fe(III) and energy transfer from the MOF to Fe(III) mechanism can be assigned for the selective detection behavior to Fe(III) ions. Hence, **1′** is a very suitable candidate for the on-site detection of Fe(III) ions and intracellular as well as extracellular H_2S in an aqueous medium.

In Chapter 3, a hydrazinyl functionalized Zr(IV)-based UiO-66 MOF called Zr-UiO-66-N_2H_3 (**2**) was synthesized and thoroughly characterized using various analytical techniques.

Conclusions

The guest-free material **2′** can detect phosphate (PO_4^{3-}) anions in HEPES buffer (10 mM, pH = 7.4) and aqueous medium *via turn-on* fluorescence. It can also detect 4-nitrobenzaldehyde (4-NB) in a HEPES : DMSO (9 : 1, v/v) medium *via turn-off* fluorescence. The selectivity for both analytes is retained in the presence of other potentially competitive analytes. The detection limit for PO_4^{3-} ions is 0.196 μM, which is far below the PO_4^{3-} level present in the aqueous environment, and the detection limit for sensing of 4-NB is = 4.7 μM. Compound **2′** can detect intracellular phosphate. It also has the capacity to exhibit differences in the intracellular phosphate level. Furthermore, the probe is capable of sensing PO_4^{3-} ions in real samples such as tap water, lake water, human urine, and human blood serum. The release of free linker from the framework upon the interaction between Zr and PO_4^{3-} is responsible for sensing of PO_4^{3-} ions and formation of imine bond between hydrazinyl and aldehyde is responsible for 4-NB sensing.

In Chapter 4, a new Zr(IV)-UiO-67-urea MOF (**3**) was synthesized with urea-functionalized biphenyl-4,4′-dicarboxylic acid (BPDC-urea) as the linker using solvothermal technique and thoroughly characterized using several analytical tools. The activated form of **3** (called **3′**) exhibited great BET surface area in spite of having a large functional moiety (urea) in the linker side. Material **3′** is highly stable, both thermally and chemically. It was successfully employed as a heterogeneous catalyst for the Friedel–Crafts alkylation of indole with β-nitrostyrene, and 97% yield was achieved in toluene at 70 °C. Furthermore, the catalyst was used for four cycles, with no significant loss in its activity. In addition, the operation of the free BPDC-urea linker was nearly 2-fold higher than that of $ZrCl_4$, suggesting the crucial role played by the urea moiety than the metal node. Also, catalyst **3′** exhibited a broad substrate scope, allowing the preparation of a series of compounds with moderate to high yields under the optimized reaction conditions. The mechanism for the catalysis has been discussed elaborately.

In Chapter 5, a functionalized new Zr-UiO-66-thiophene-2-carboxamide MOF (**4**) was synthesized by solvothermal procedure and characterized by employing various analytical tools. Material **4** displayed high thermal (up to 340 °C) and chemical stability (in water, 1 M HCl, and acetic acid). Material **4′** was able to heterogeneously catalyze the ring-opening reaction of epoxides with amines (styrene oxide and aniline were used as model substrates).

Conclusions

Catalyst **4′** exhibited significant yields as well as broad substrate scope in the ring-opening of epoxides by means of amines. Control experiments were performed with a free linker, Zr(IV) salt and without catalyst **4′**, confirming the exclusive role of **4′** in the catalytic reaction. The reusability characteristics of catalyst **4′** was established up to five consecutive catalytic cycles. The mechanism of the catalysis reaction involving **4′** as a heterogeneous catalyst was studied elaborately.

भारतीय प्रौद्योगिकी संस्थान गुवाहाटी • Indian Institute of Technology Guwahati •

Appendix I

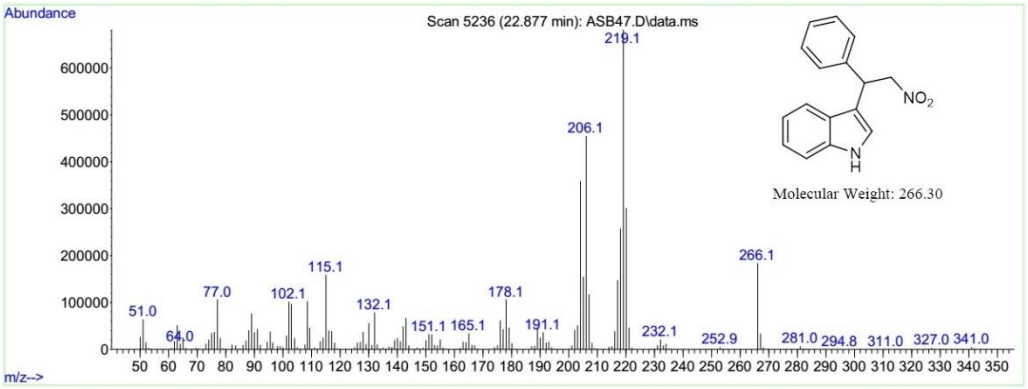

Figure 4.17 GC-MS trace of 3-(2-nitro-1-phenylethyl)-1*H*-indole.

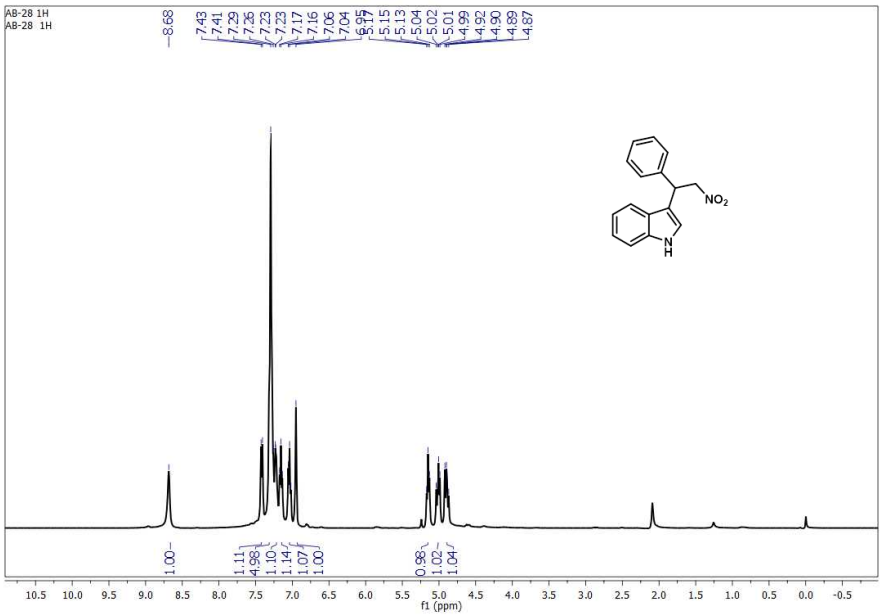

Figure 4.18 ^{1}H-NMR spectrum of 3-(2-nitro-1-phenylethyl)-1*H*-indole.

^{1}H NMR (400 MHz, $CDCl_3$): δ = 8.68 (s, 1H), 7.42 (d, *J* = 7.8 Hz, 1H), 7.28 (d, *J* = 13.5 Hz, 5H), 7.23 (d, *J* = 1.9 Hz, 1H), 7.15 (t, *J* = 7.5 Hz, 1H), 7.04 (t, *J* = 7.4 Hz, 1H), 6.95 (s, 1H), 5.15 (t, *J* = 7.8 Hz, 1H), 5.01 (dd, *J* = 12.3, 7.7 Hz, 1H), 4.89 (dd, *J* = 11.6, 9.2 Hz, 1H).

TH-2604_156122006

Appendix I

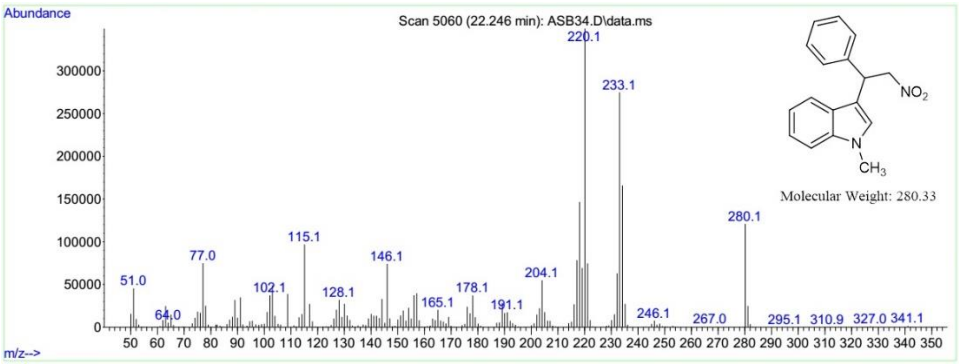

Figure 4.19 GC-MS trace of 1-methyl-3-(2-nitro-1-phenylethyl)-1*H*-indole.

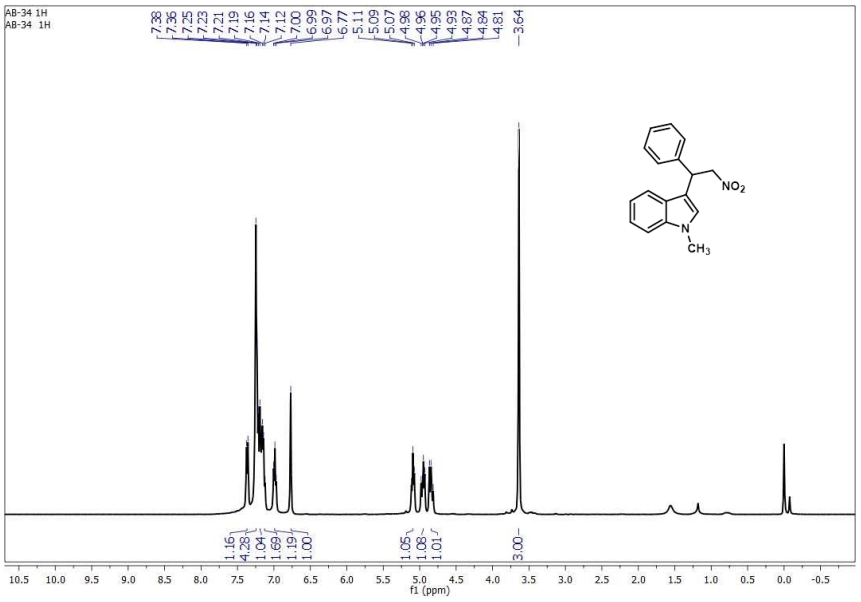

Figure 4.20 ^{1}H-NMR spectrum of 1-methyl-3-(2-nitro-1-phenylethyl)-1*H*-indole.

^{1}H NMR (400 MHz, $CDCl_3$): δ = 7.37 (d, *J* = 7.8 Hz, 1H), 7.28 – 7.21 (m, 4H), 7.19 (s, 1H), 7.17 – 7.09 (m, 2H), 6.99 (t, *J* = 7.2 Hz, 1H), 6.77 (s, 1H), 5.09 (t, *J* = 7.8 Hz, 1H), 4.95 (dd, *J* = 12.1, 7.6 Hz, 1H), 4.89 – 4.80 (m, 1H), 3.64 (s, 3H).

TH-2604_156122006

Appendix I

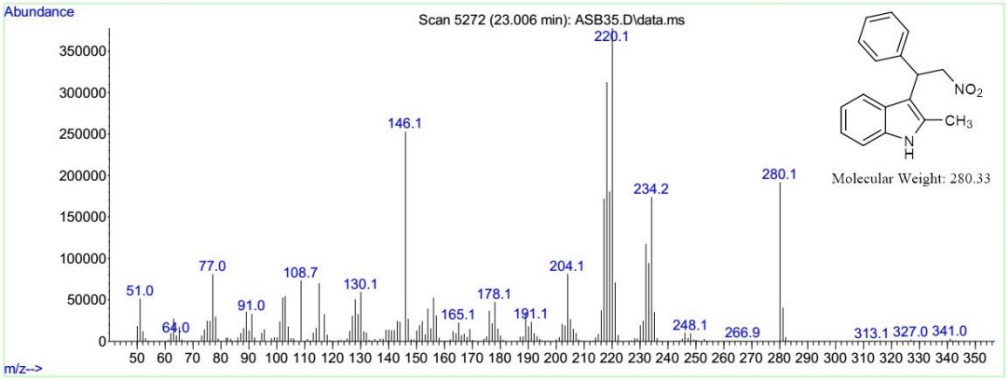

Figure 4.21 GC-MS trace of 2-methyl-3-(2-nitro-1-phenylethyl)-1*H*-indole.

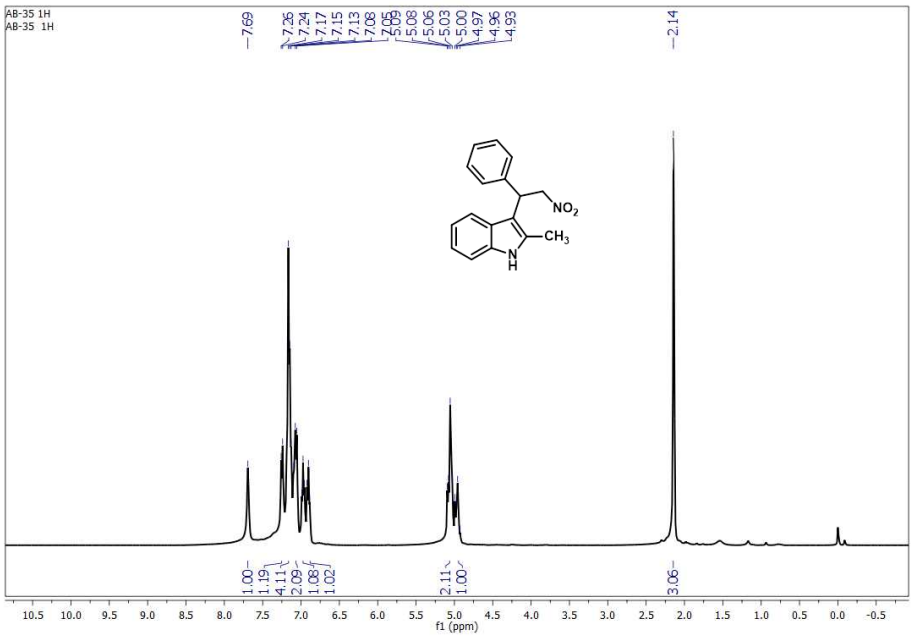

Figure 4.22 ^{1}H-NMR spectrum of 2-methyl-3-(2-nitro-1-phenylethyl)-1*H*-indole.

^{1}H NMR (400 MHz, $CDCl_3$): δ = 7.69 (s, 1H), 7.25 (d, *J* = 7.5 Hz, 1H), 7.21 – 7.11 (m, 4H), 7.11 – 7.02 (m, 2H), 6.97 (t, *J* = 7.3 Hz, 1H), 6.90 (t, *J* = 6.9 Hz, 1H), 5.06 (dd, *J* = 17.3, 8.4 Hz, 2H), 4.96 (dd, *J* = 17.1, 10.7 Hz, 1H), 2.14 (s, 3H).

TH-2604_156122006

Appendix I

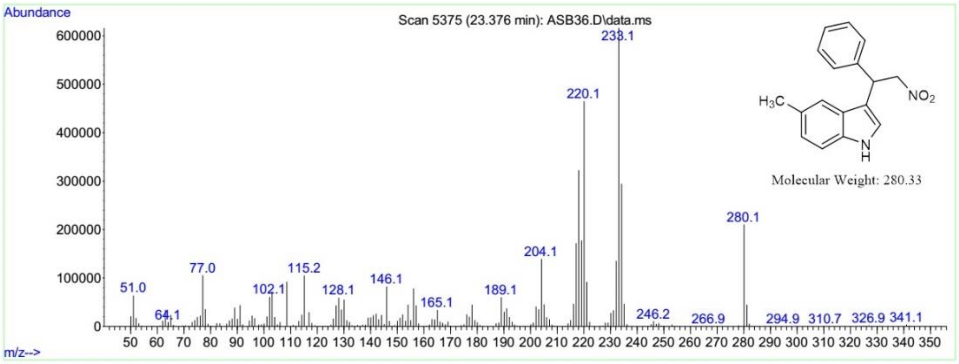

Figure 4.23 GC-MS trace of 5-methyl-3-(2-nitro-1-phenylethyl)-1*H*-indole.

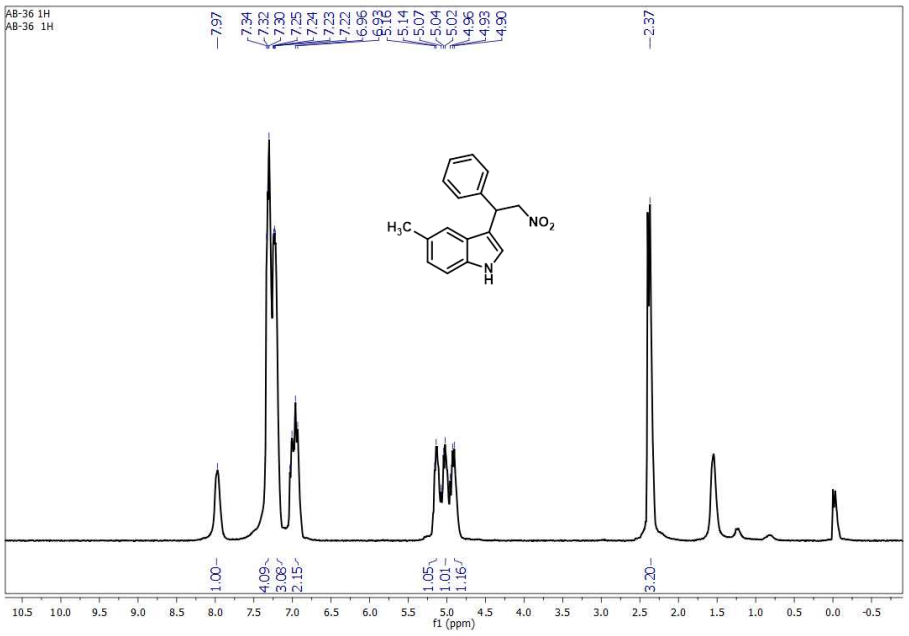

Figure 4.24 ^{1}H-NMR spectrum of 5-methyl-3-(2-nitro-1-phenylethyl)-1*H*-indole.

^{1}H NMR (400 MHz, $CDCl_3$): δ = 7.97 (s, 1H), 7.36 – 7.27 (m, 4H), 7.25 – 7.15 (m, 3H), 6.98 (dd, *J* = 29.2, 11.0 Hz, 2H), 5.15 (d, *J* = 8.0 Hz, 1H), 5.03 (d, *J* = 7.4 Hz, 1H), 4.97 – 4.83 (m, 1H), 2.37 (s, 3H).

TH-2604_156122006

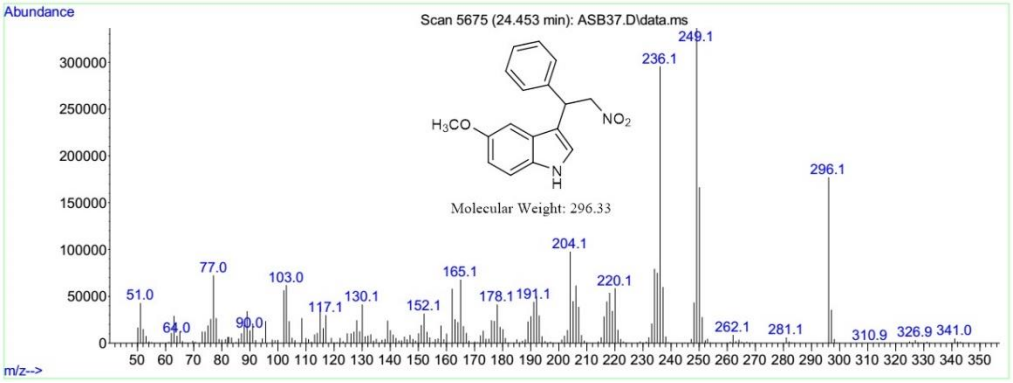

Figure 4.25 GC-MS trace of 5-methoxy-3-(2-nitro-1-phenylethyl)-1*H*-indole.

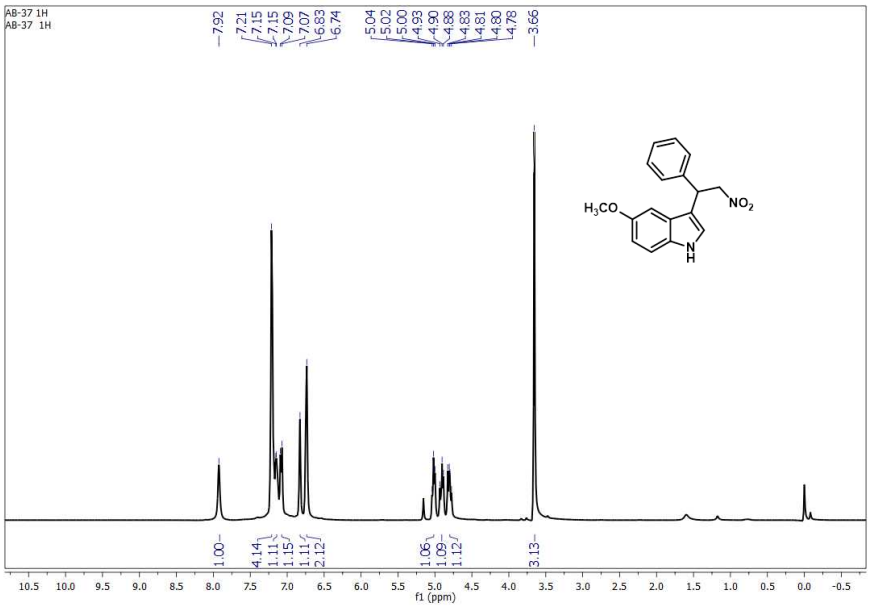

Figure 4.26 ^{1}H-NMR spectrum of 5-methoxy-3-(2-nitro-1-phenylethyl)-1*H*-indole.

^{1}H NMR (400 MHz, $CDCl_3$): δ = 7.92 (s, 1H), 7.21 (s, 4H), 7.15 (d, *J* = 3.2 Hz, 1H), 7.08 (d, *J* = 9.2 Hz, 1H), 6.83 (s, 1H), 6.74 (s, 2H), 5.02 (t, *J* = 7.7 Hz, 1H), 4.95 – 4.87 (m, 1H), 4.80 (dd, *J* = 12.0, 8.6 Hz, 1H), 3.66 (s, 3H).

TH-2604_156122006

Appendix I

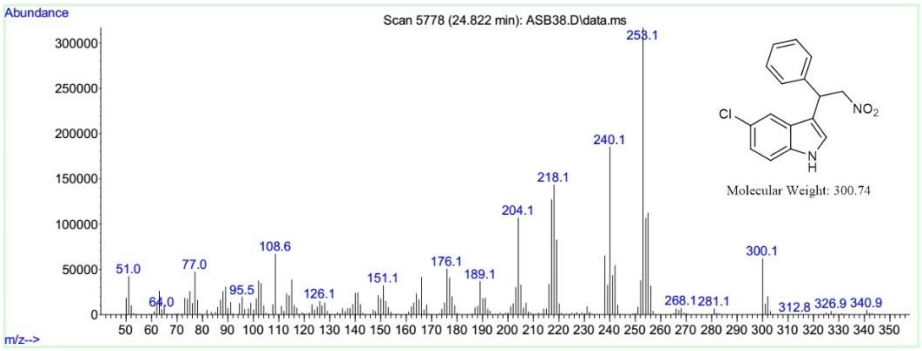

Figure 4.27 GC-MS trace of 5-chloro-3-(2-nitro-1-phenylethyl)-1*H*-indole.

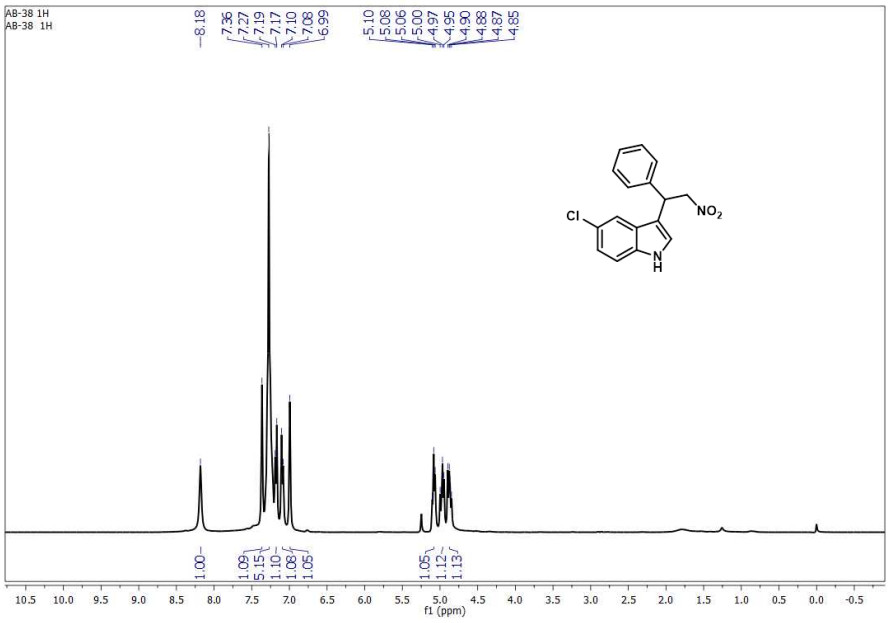

Figure 4.28 ^{1}H-NMR spectrum of 5-chloro-3-(2-nitro-1-phenylethyl)-1*H*-indole.

^{1}H NMR (400 MHz, $CDCl_3$): δ = 8.18 (s, 1H), 7.36 (s, 1H), 7.27 (s, 5H), 7.18 (d, *J* = 8.4 Hz, 1H), 7.09 (d, *J* = 8.3 Hz, 1H), 6.99 (s, 1H), 5.08 (t, *J* = 7.6 Hz, 1H), 5.02 – 4.91 (m, 1H), 4.87 (dd, *J* = 11.6, 8.2 Hz, 1H).

TH-2604_156122006

Appendix I

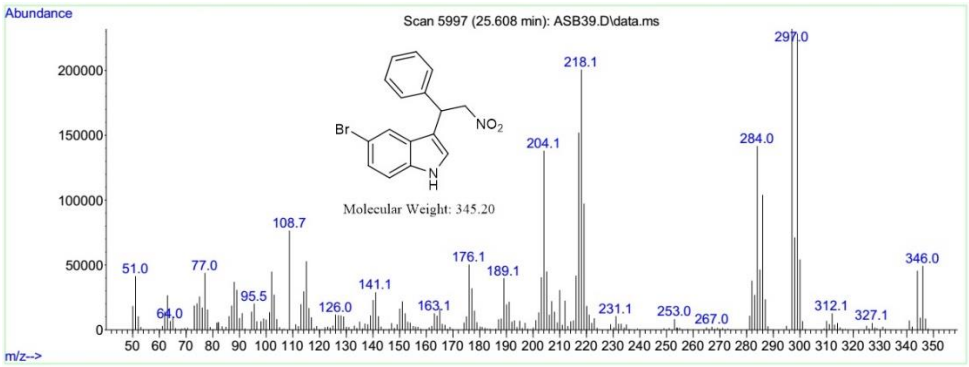

Figure 4.29 GC-MS trace of 5-bromo-3-(2-nitro-1-phenylethyl)-1*H*-indole.

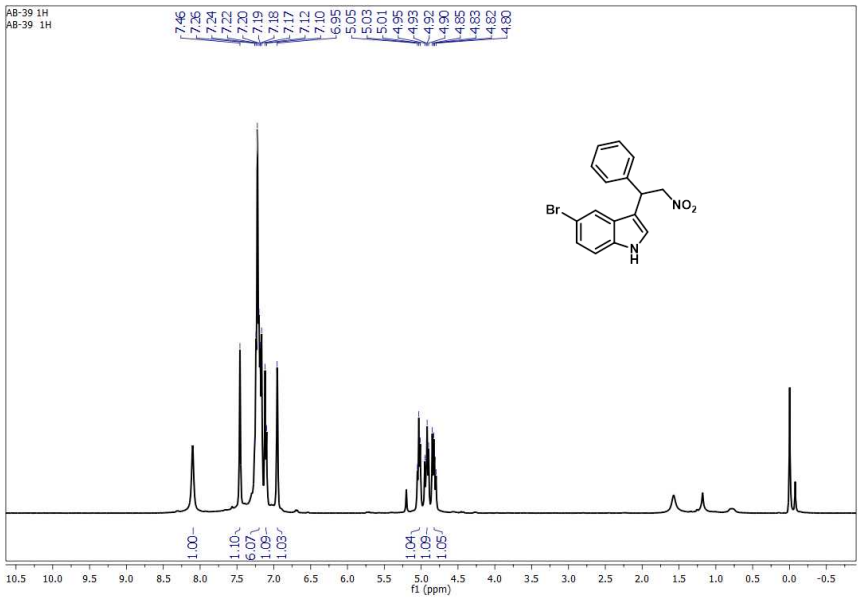

Figure 4.30 ^{1}H-NMR spectrum of 5-bromo-3-(2-nitro-1-phenylethyl)-1*H*-indole.

^{1}H NMR (400 MHz, $CDCl_3$): δ = 8.10 (s, 1H), 7.46 (s, 1H), 7.20 (dt, *J* = 8.3, 7.2 Hz, 6H), 7.11 (d, *J* = 8.6 Hz, 1H), 6.95 (s, 1H), 5.03 (t, *J* = 7.8 Hz, 1H), 4.92 (dd, *J* = 12.3, 8.1 Hz, 1H), 4.82 (dd, *J* = 12.4, 8.0 Hz, 1H).

TH-2604_156122006

Appendix I

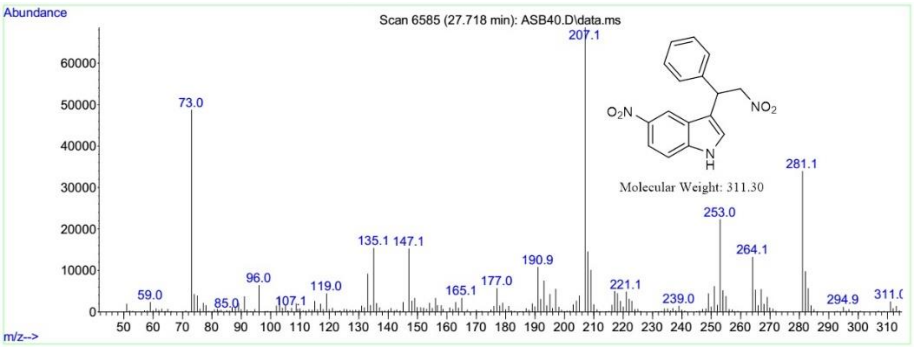

Figure 4.31 GC-MS trace of 5-nitro-3-(2-nitro-1-phenylethyl)-1*H*-indole.

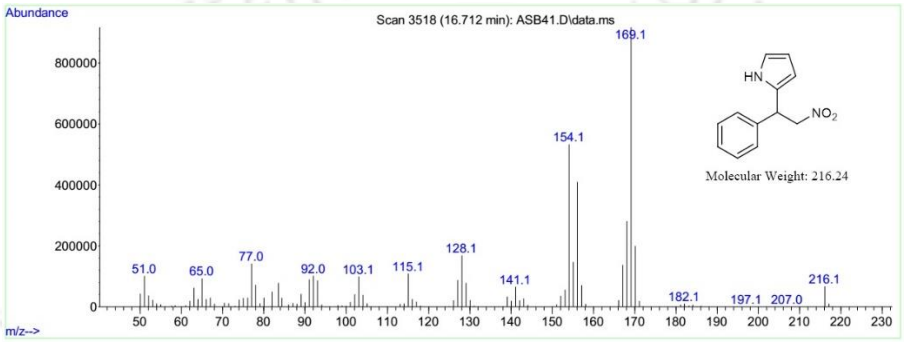

Figure 4.32 GC-MS trace of 2-(2-nitro-1-phenylethyl)-1*H*-pyrrole.

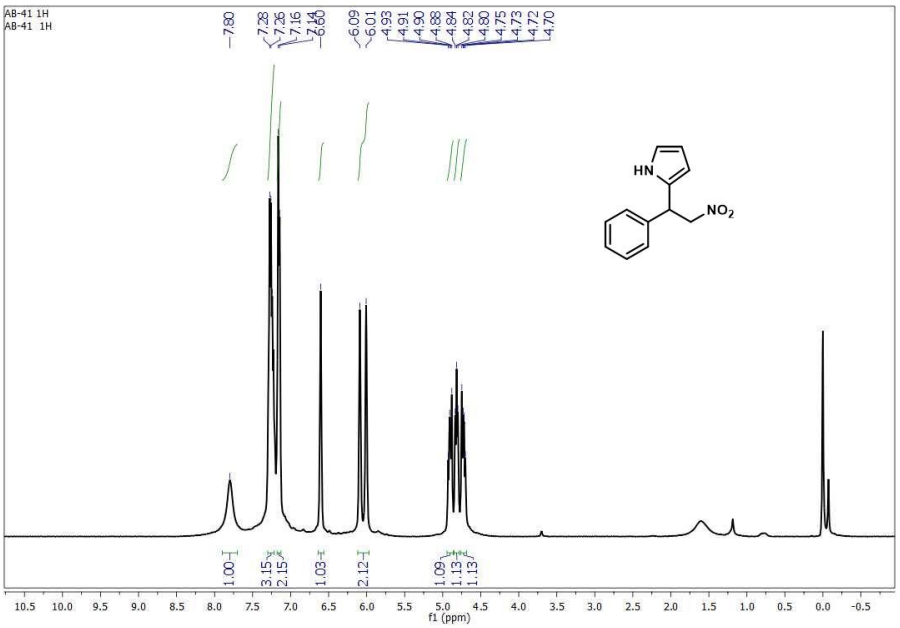

Figure 4.33 ^{1}H-NMR spectrum of 2-(2-nitro-1-phenylethyl)-1*H*-pyrrole.

TH-2604_156122006

^{1}H NMR (400 MHz, $CDCl_3$): δ = 7.80 (s, 1H), 7.25 (dd, *J* = 12.7, 6.3 Hz, 3H), 7.15 (d, *J* = 6.9 Hz, 2H), 6.60 (s, 1H), 6.05 (d, *J* = 33.2 Hz, 2H), 4.90 (dd, *J* = 11.5, 7.2 Hz, 1H), 4.85 – 4.78 (m, 1H), 4.72 (dd, *J* = 10.8, 7.6 Hz, 1H).

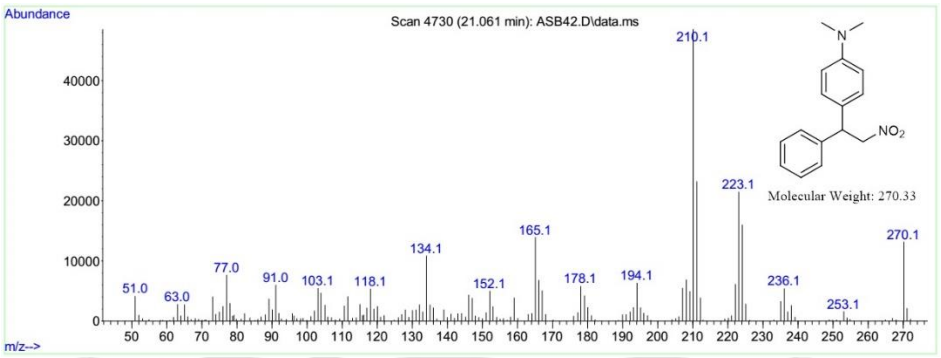

Figure 4.34 GC-MS trace of *N*,*N*-dimethyl-4-(2-nitro-1-phenylethyl)aniline.

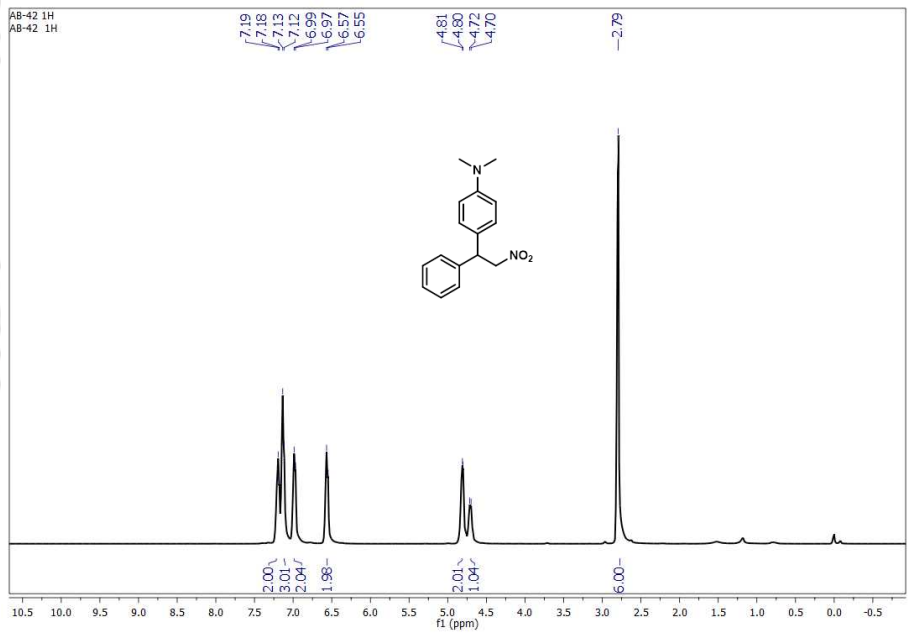

Figure 4.35 ^{1}H-NMR spectrum of *N*,*N*-dimethyl-4-(2-nitro-1-phenylethyl)aniline.

^{1}H NMR (400 MHz, $CDCl_3$): δ = 7.19 (d, *J* = 6.2 Hz, 2H), 7.13 (d, *J* = 6.5 Hz, 3H), 6.98 (d, *J* = 7.3 Hz, 2H), 6.56 (d, *J* = 7.9 Hz, 2H), 4.81 (d, *J* = 3.2 Hz, 2H), 4.71 (d, *J* = 7.0 Hz, 1H), 2.79 (s, 6H).

TH-2604_156122006

Appendix I

TH-2604_156122006

Appendix II

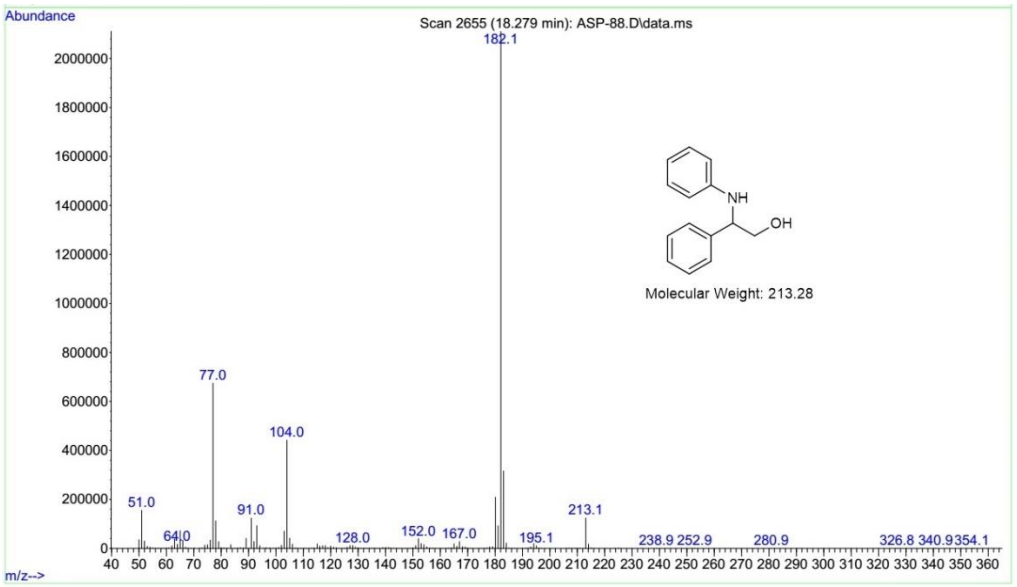

Figure 5.21 GC-MS trace of 2-phenyl-2-(phenylamino)ethan-1-ol.

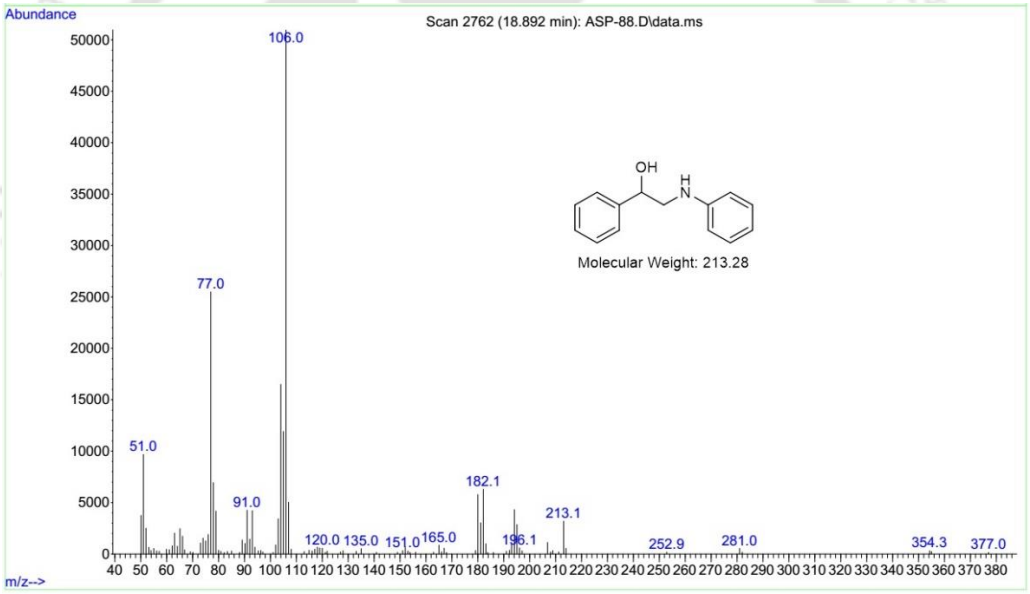

Figure 5.22 GC-MS trace of 1-phenyl-2-(phenylamino)ethan-1-ol.

TH-2604_156122006

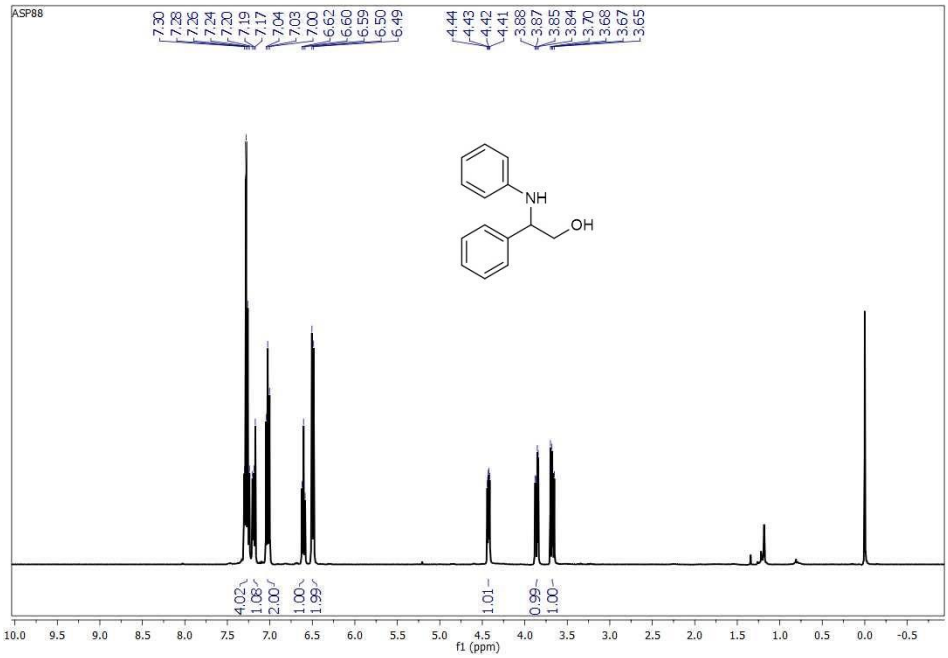

Figure 5.23 ^{1}H-NMR spectrum of 2-phenyl-2-(phenylamino)ethan-1-ol.

^{1}H NMR (400 MHz, $CDCl_3$): δ = 7.27 (q, *J* = 8.1 Hz, 4H), 7.21 – 7.17 (m, 1H), 7.07 – 6.99 (m, 2H), 6.60 (t, *J* = 7.3 Hz, 1H), 6.50 (d, *J* = 7.7 Hz, 2H), 4.43 (dd, *J* = 6.9, 4.2 Hz, 1H), 3.86 (dd, *J* = 11.1, 4.2 Hz, 1H), 3.68 (dd, *J* = 11.1, 7.0 Hz, 1H).

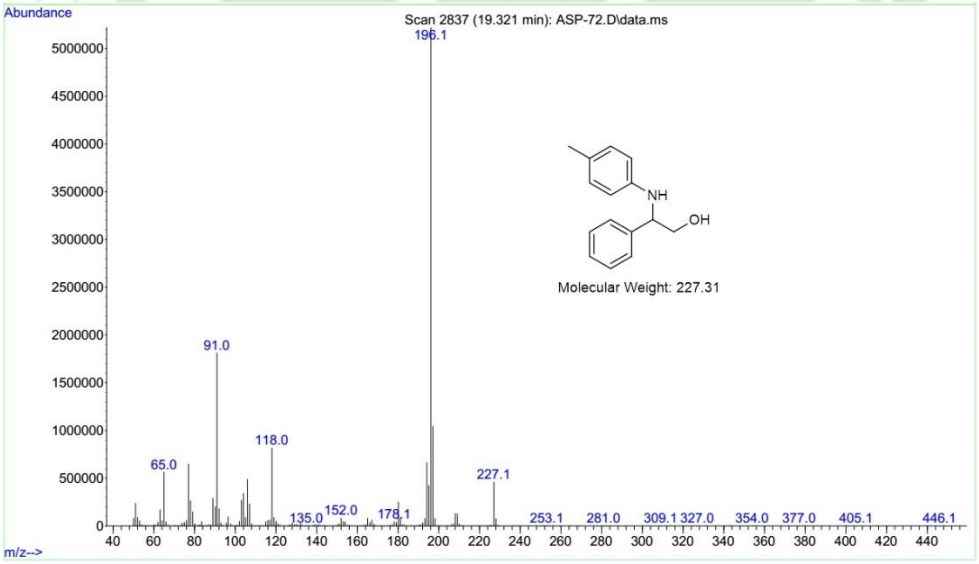

Figure 5.24 GC-MS trace of 2-phenyl-2-(*p*-tolylamino)ethan-1-ol.

TH-2604_156122006

Appendix II

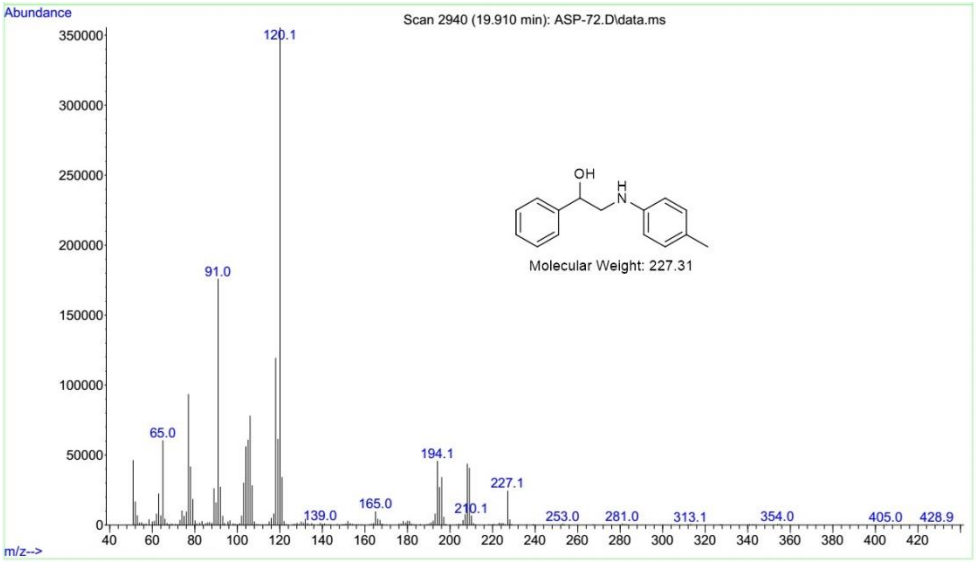

Figure 5.25 GC-MS trace of 1-phenyl-2-(*p*-tolylamino)ethan-1-ol.

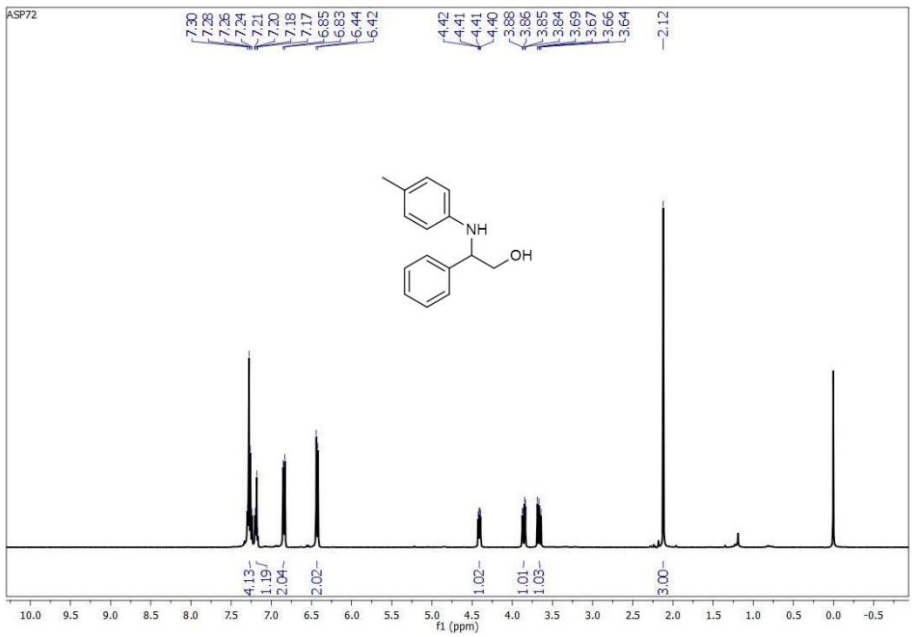

Figure 5.26 ^{1}H NMR spectrum of 2-phenyl-2-(*p*-tolylamino)ethan-1-ol.

^{1}H NMR (400 MHz, $CDCl_3$): δ = 7.27 (q, *J* = 8.0 Hz, 4H), 7.21 – 7.16 (m, 1H), 6.84 (d, *J* = 8.2 Hz, 2H), 6.43 (d, *J* = 8.4 Hz, 2H), 4.41 (dd, *J* = 7.1, 4.2 Hz, 1H), 3.86 (dd, *J* = 11.1, 4.2 Hz, 1H), 3.66 (dd, *J* = 11.1, 7.2 Hz, 1H), 2.12 (s, 3H).

TH-2604_156122006

Appendix II

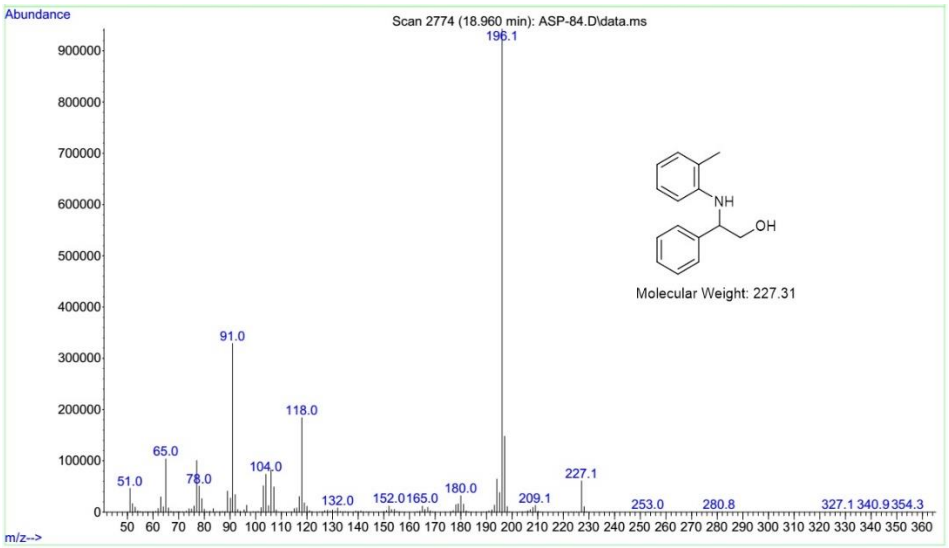

Figure 5.27 GC-MS trace of 2-phenyl-2-(*o*-tolylamino)ethan-1-ol.

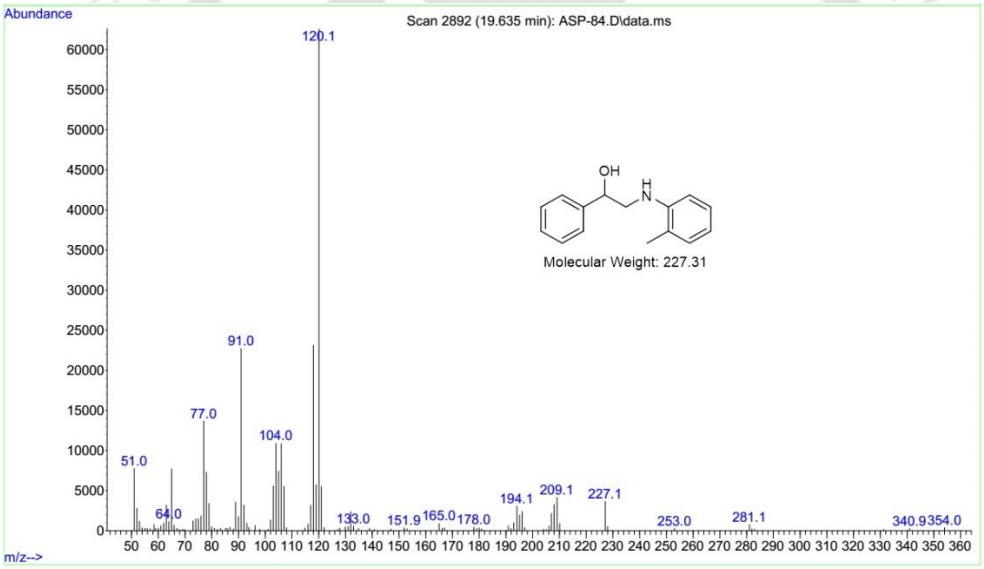

Figure 5.28 GC-MS trace of 1-phenyl-2-(*o*-tolylamino)ethan-1-ol.

TH-2604_156122006

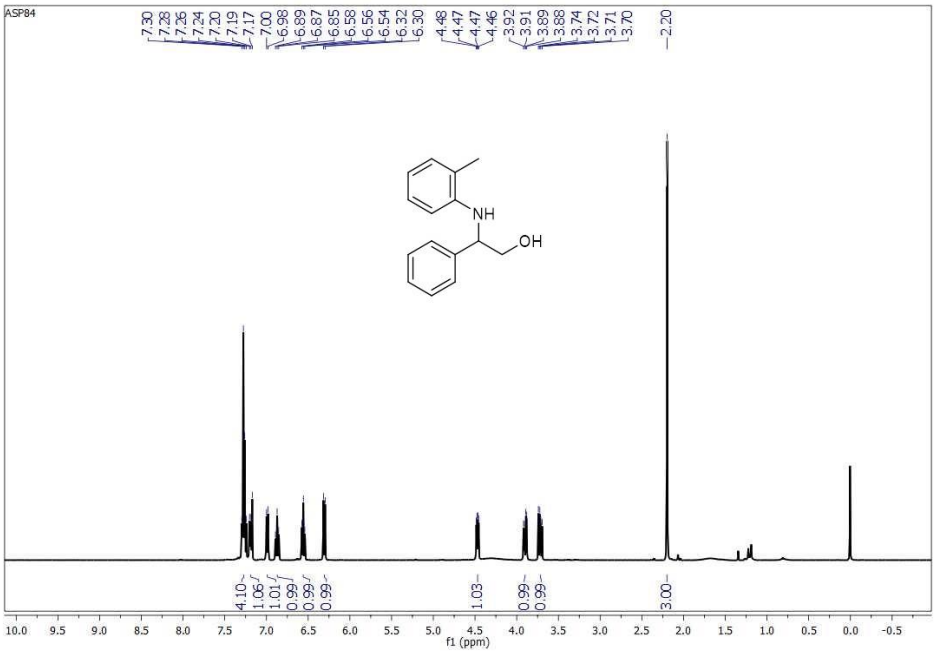

Figure 5.29 ^{1}H NMR spectrum of 2-phenyl-2-(*o*-tolylamino)ethan-1-ol.

^{1}H NMR (400 MHz, $CDCl_3$): δ = 7.31 – 7.23 (m, 4H), 7.21 – 7.17 (m, 1H), 6.99 (d, *J* = 7.2 Hz, 1H), 6.87 (t, *J* = 7.7 Hz, 1H), 6.56 (t, *J* = 7.0 Hz, 1H), 6.31 (d, *J* = 8.0 Hz, 1H), 4.47 (dd, *J* = 6.9, 4.2 Hz, 1H), 3.90 (dd, *J* = 11.1, 4.2 Hz, 1H), 3.72 (dd, *J* = 11.1, 7.0 Hz, 1H), 2.20 (s, 3H).

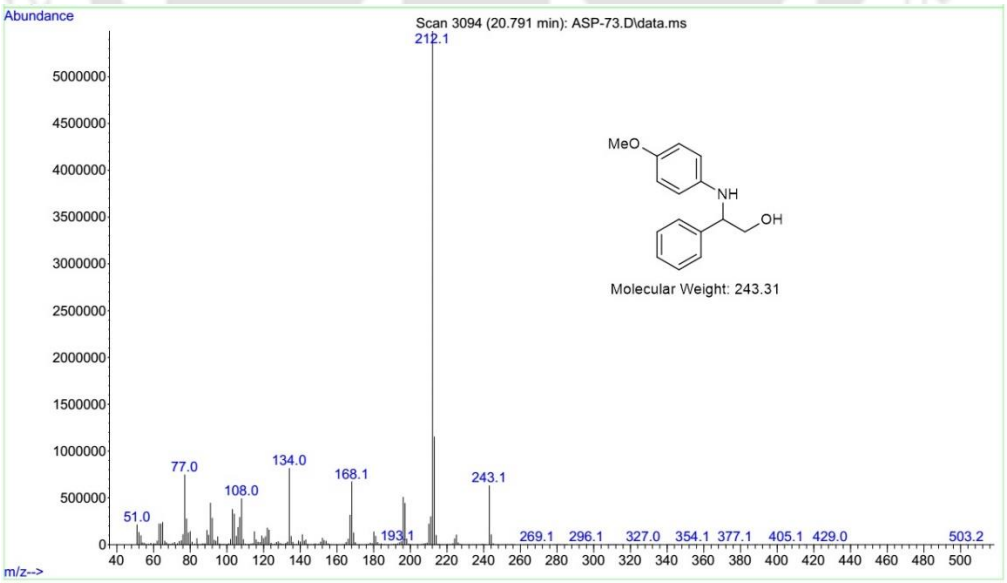

Figure 5.30 GC-MS trace of 2-((4-methoxyphenyl)amino)-2-phenylethan-1-ol.

TH-2604_156122006

Appendix II

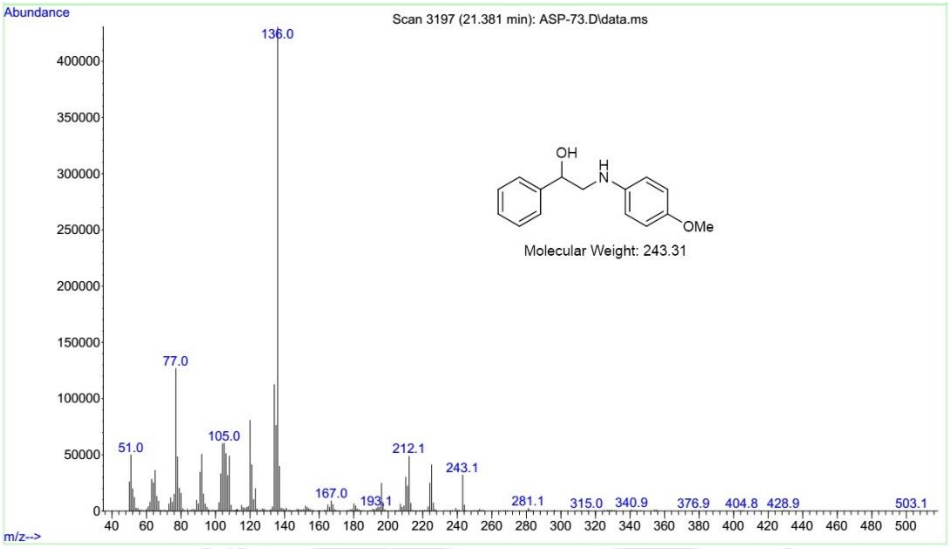

Figure 5.31 GC-MS trace of 2-((4-methoxyphenyl)amino)-1-phenylethan-1-ol.

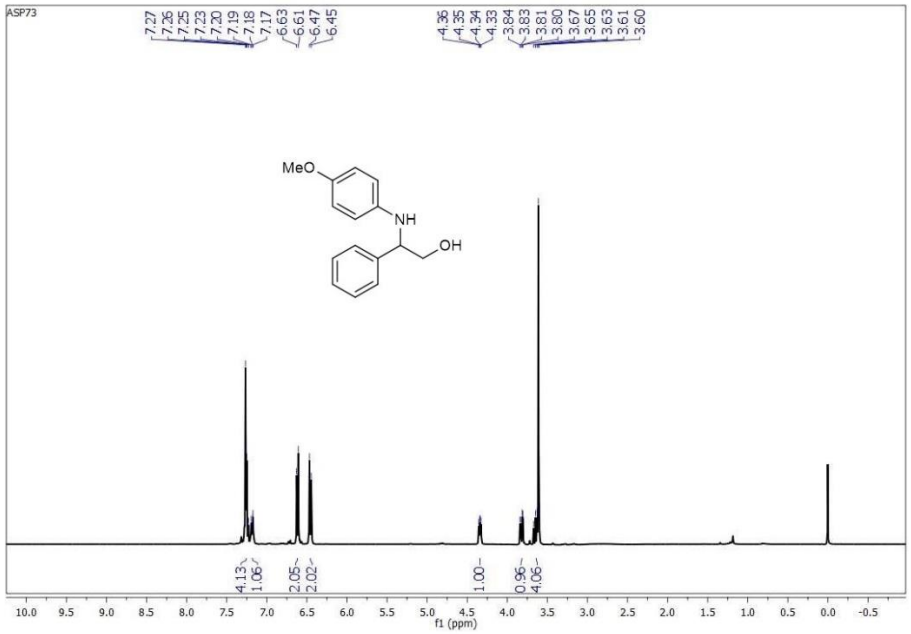

Figure 5.32 ^{1}H NMR spectrum of 2-((4-methoxyphenyl)amino)-2-phenylethan-1-ol.

^{1}H NMR (400 MHz, $CDCl_3$): δ = 7.25 (dd, *J* = 9.2, 5.1 Hz, 4H), 7.19 (dd, *J* = 8.6, 2.3 Hz, 1H), 6.62 (d, *J* = 8.9 Hz, 2H), 6.46 (d, *J* = 8.9 Hz, 2H), 4.34 (dd, *J* = 7.4, 4.2 Hz, 1H), 3.82 (dd, *J* = 11.1, 4.2 Hz, 1H), 3.68 – 3.60 (m, 4H).

TH-2604_156122006

Appendix II

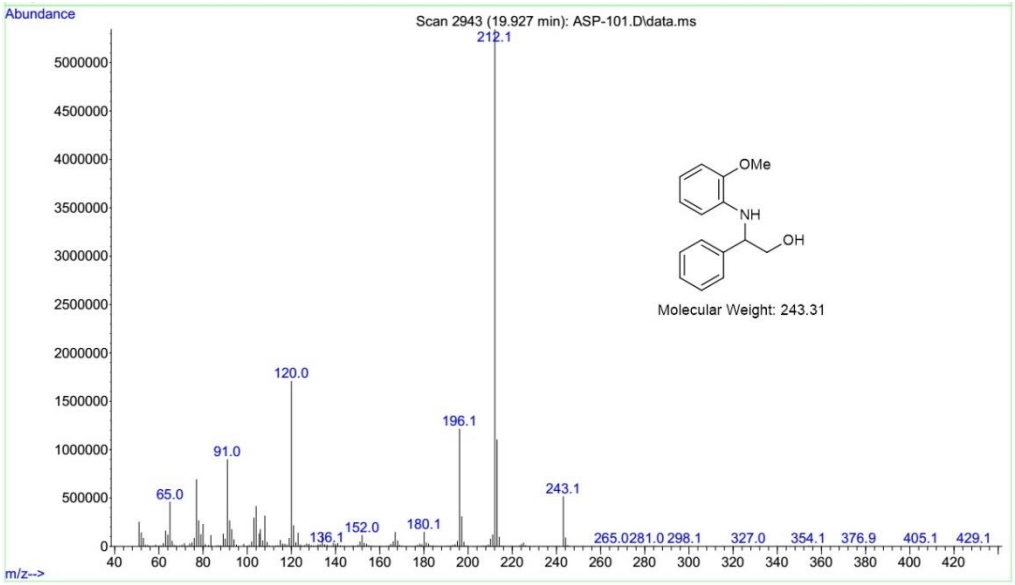

Figure 5.33 GC-MS trace of 2-((2-methoxyphenyl)amino)-2-phenylethan-1-ol.

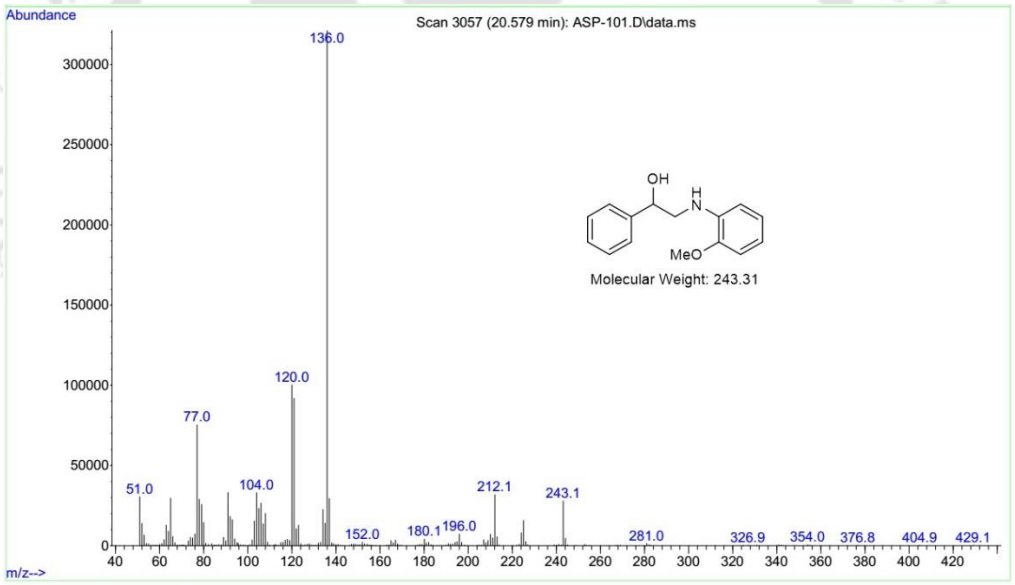

Figure 5.34 GC-MS trace of 2-((2-methoxyphenyl)amino)-1-phenylethan-1-ol.

TH-2604_156122006

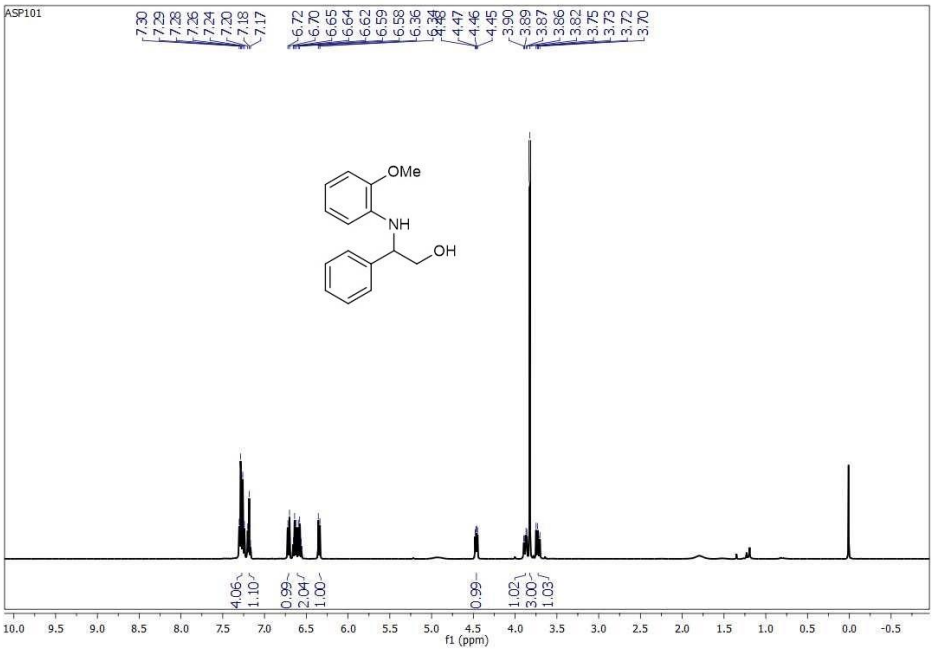

Figure 5.35 ^{1}H NMR spectrum of 2-((2-methoxyphenyl)amino)-2-phenylethan-1-ol.

^{1}H NMR (400 MHz, $CDCl_3$): δ = 7.31 – 7.23 (m, 4H), 7.18 (t, *J* = 6.9 Hz, 1H), 6.71 (d, *J* = 7.7 Hz, 1H), 6.61 (dt, *J* = 24.0, 6.9 Hz, 2H), 6.35 (d, *J* = 7.7 Hz, 1H), 4.46 (dd, *J* = 7.2, 4.4 Hz, 1H), 3.88 (dd, *J* = 11.1, 4.3 Hz, 1H), 3.82 (s, 3H), 3.73 (dd, *J* = 11.1, 7.3 Hz, 1H).

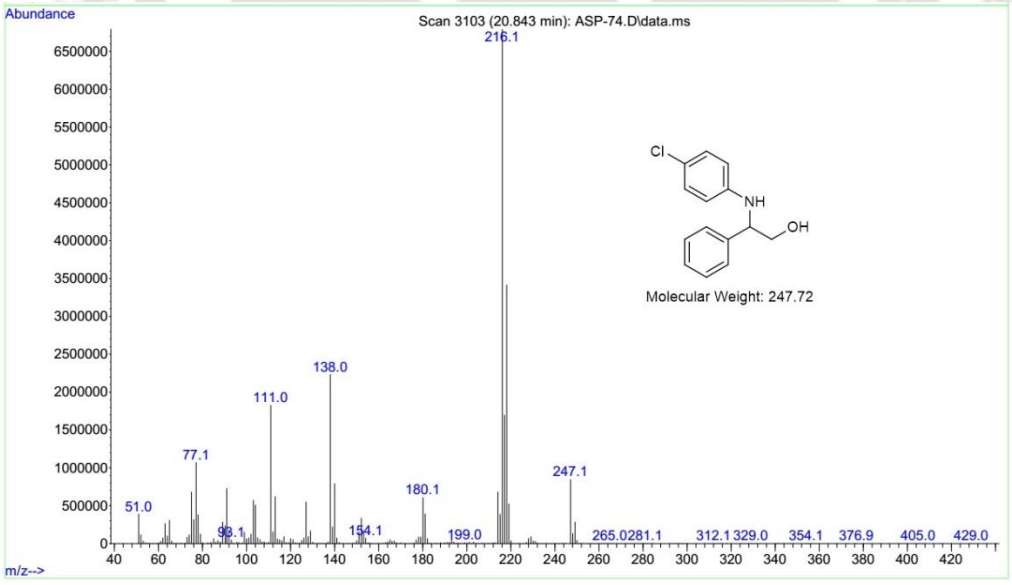

Figure 5.36 GC-MS trace of 2-((4-chlorophenyl)amino)-2-phenylethan-1-ol.

TH-2604_156122006

Appendix II

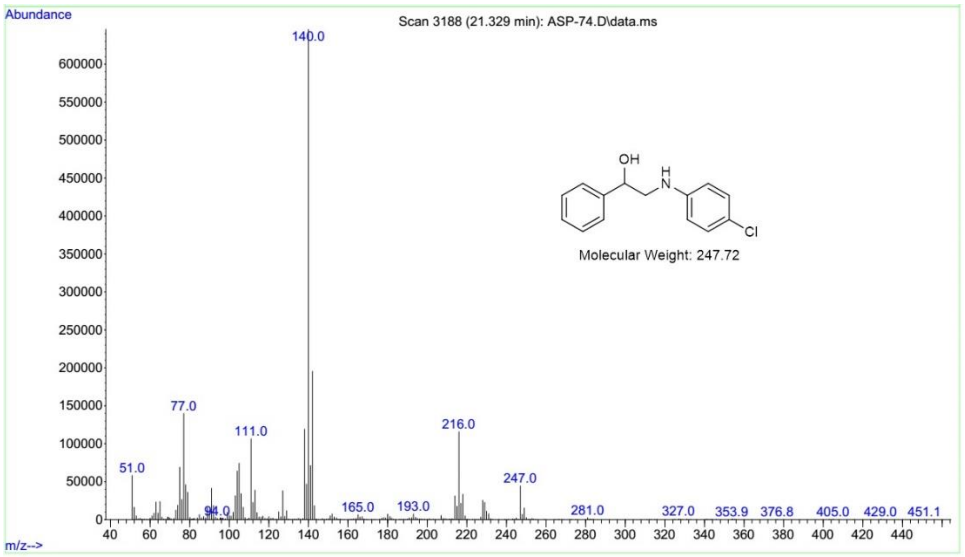

Figure 5.37 GC-MS trace of 2-((4-chlorophenyl)amino)-1-phenylethan-1-ol.

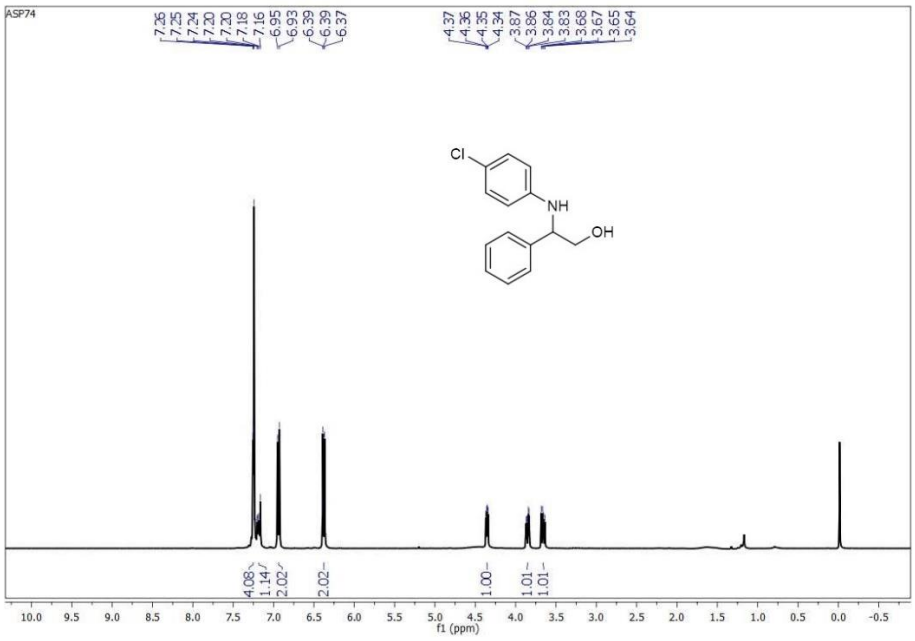

Figure 5.38 ^{1}H NMR spectrum of 2-((4-chlorophenyl)amino)-2-phenylethan-1-ol.

^{1}H NMR (400 MHz, $CDCl_3$): δ = 7.29 – 7.22 (m, 4H), 7.20 – 7.16 (m, 1H), 6.94 (d, *J* = 8.8 Hz, 2H), 6.41 – 6.34 (m, 2H), 4.36 (dd, *J* = 6.8, 4.1 Hz, 1H), 3.85 (dd, *J* = 11.1, 4.1 Hz, 1H), 3.66 (dd, *J* = 11.1, 6.8 Hz, 1H).

TH-2604_156122006

Appendix II

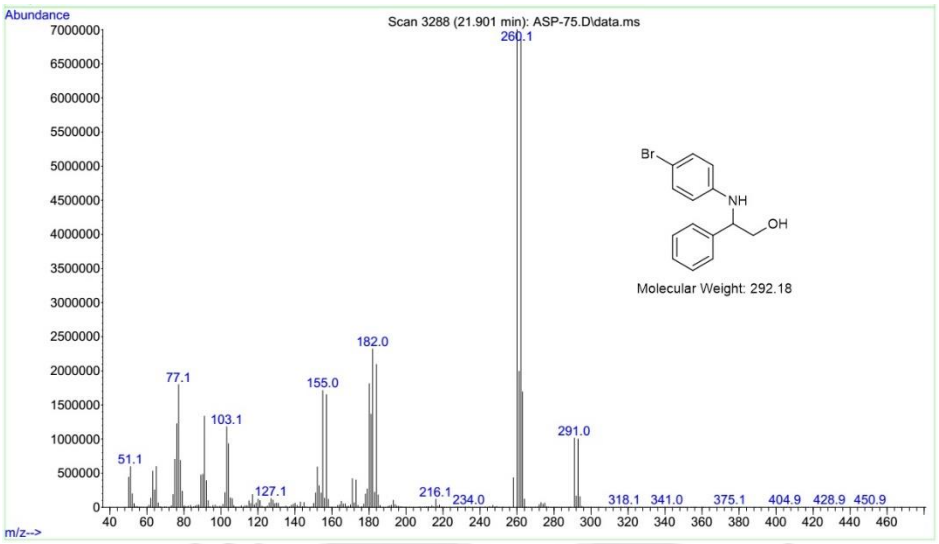

Figure 5.39 GC-MS trace of 2-((4-bromophenyl)amino)-2-phenylethan-1-ol.

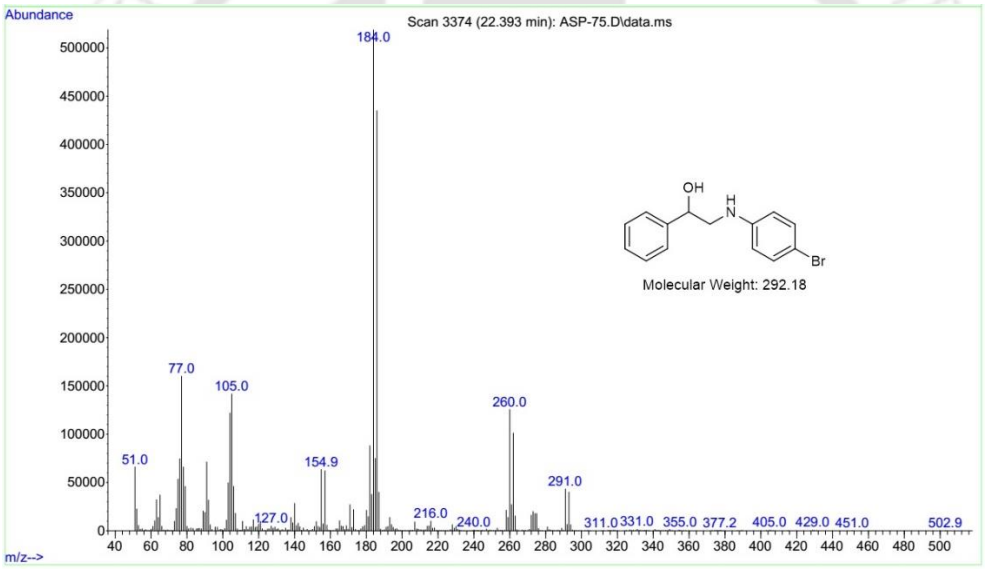

Figure 5.40 GC-MS trace of 2-((4-bromophenyl)amino)-1-phenylethan-1-ol.

TH-2604_156122006

Appendix II

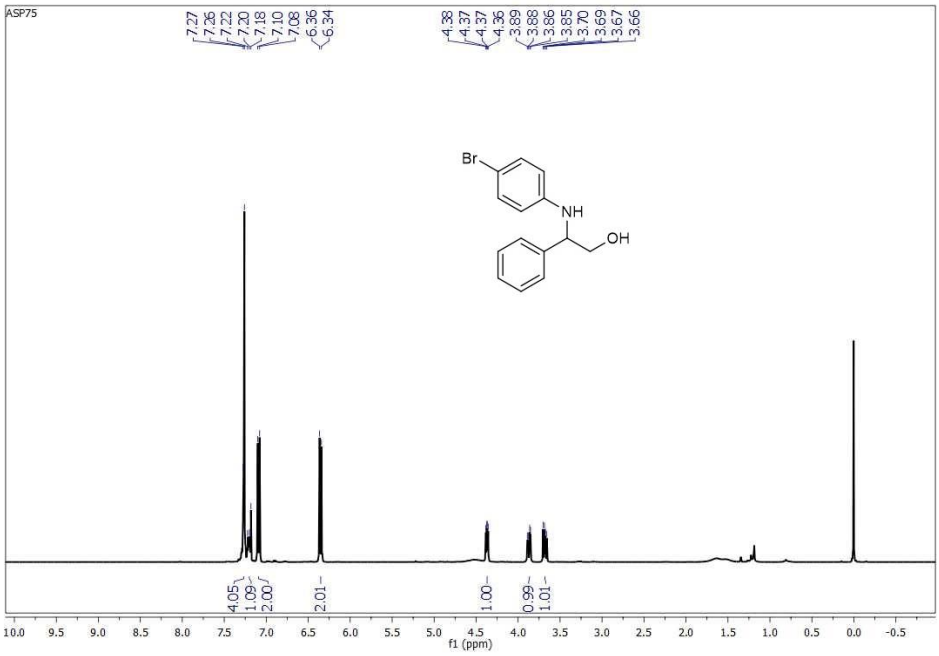

Figure 5.41 ^{1}H NMR spectrum of 2-((4-bromophenyl)amino)-2-phenylethan-1-ol.

^{1}H NMR (400 MHz, $CDCl_3$): δ = 7.27 (d, *J* = 5.6 Hz, 4H), 7.19 (d, *J* = 7.8 Hz, 1H), 7.09 (d, *J* = 8.9 Hz, 2H), 6.35 (d, *J* = 8.9 Hz, 2H), 4.37 (dd, *J* = 6.7, 4.1 Hz, 1H), 3.87 (dd, *J* = 11.1, 4.1 Hz, 1H), 3.68 (dd, *J* = 11.1, 6.8 Hz, 1H).

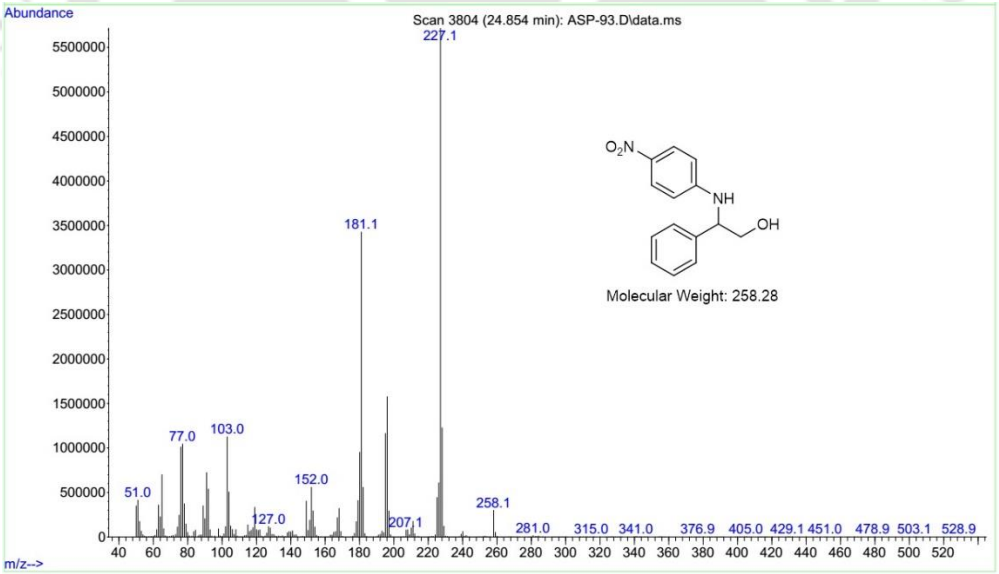

Figure 5.42 GC-MS trace of 2-((4-nitrophenyl)amino)-2-phenylethan-1-ol.

TH-2604_156122006

Appendix II

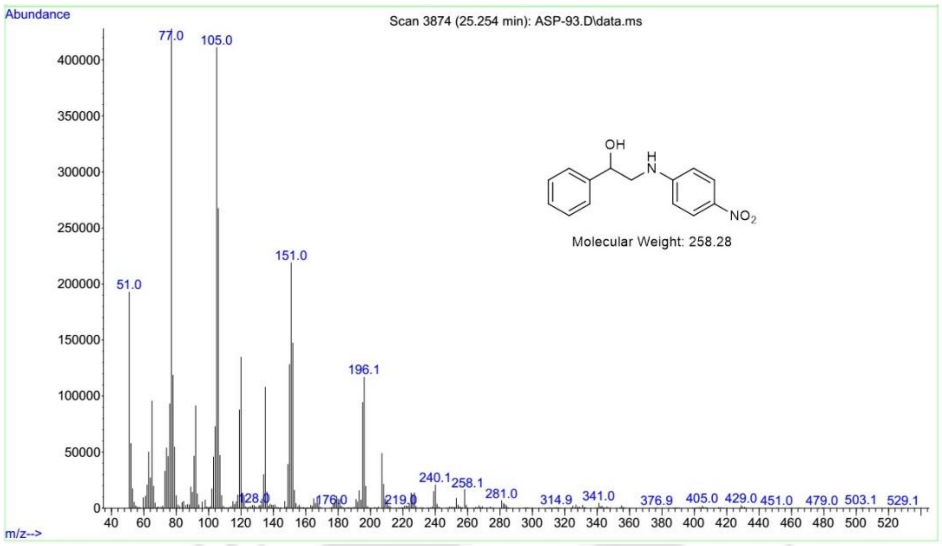

Figure 5.43 GC-MS trace of 2-((4-nitrophenyl)amino)-1-phenylethan-1-ol.

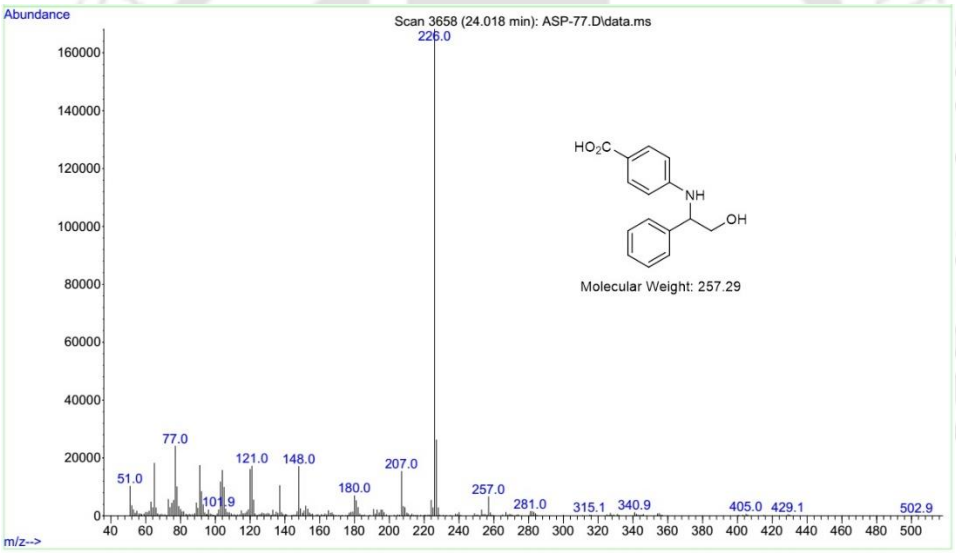

Figure 5.44 GC-MS trace of 4-((2-hydroxy-1-phenylethyl)amino)benzoic acid.

TH-2604_156122006

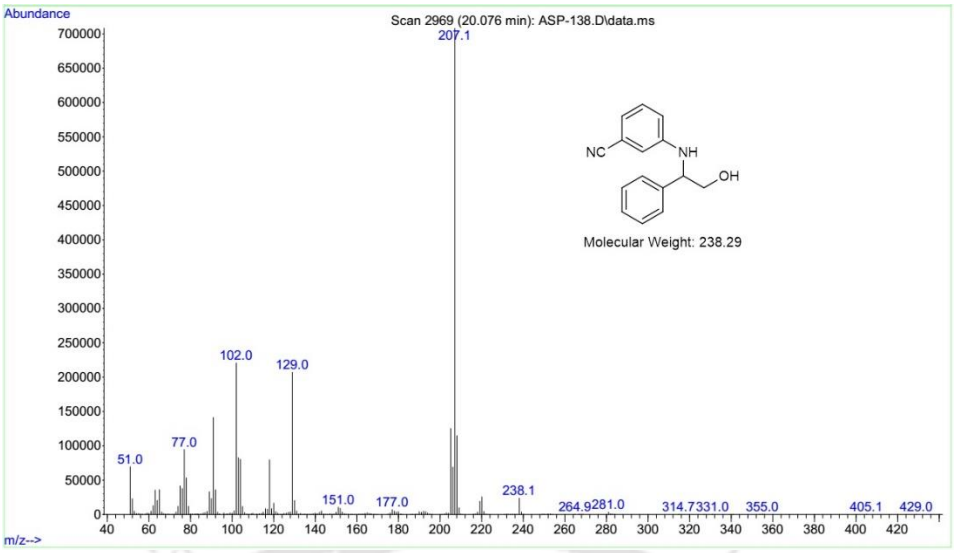

Figure 5.45 GC-MS trace of 3-((2-hydroxy-1-phenylethyl)amino)benzonitrile.

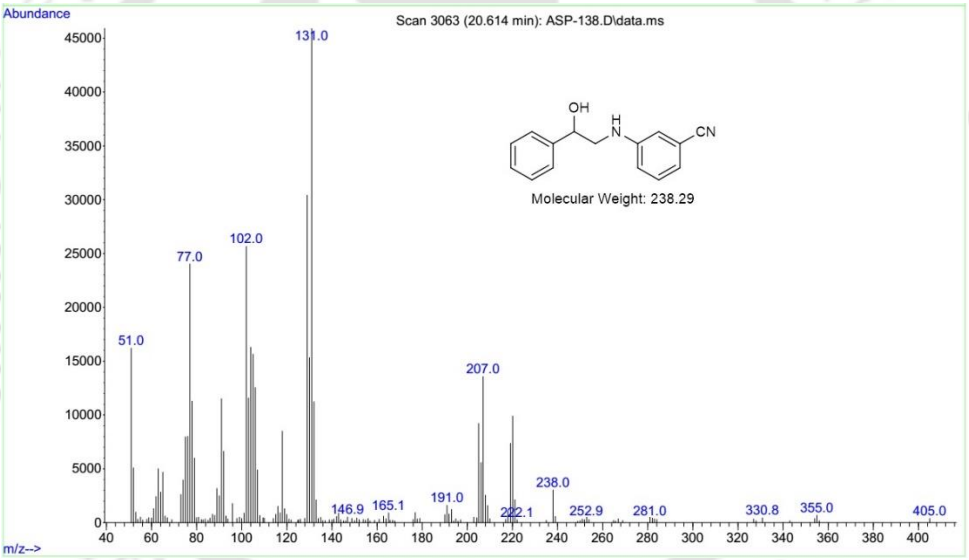

Figure 5.46 GC-MS trace of 3-((2-hydroxy-2-phenylethyl)amino)benzonitrile.

TH-2604_156122006

Appendix II

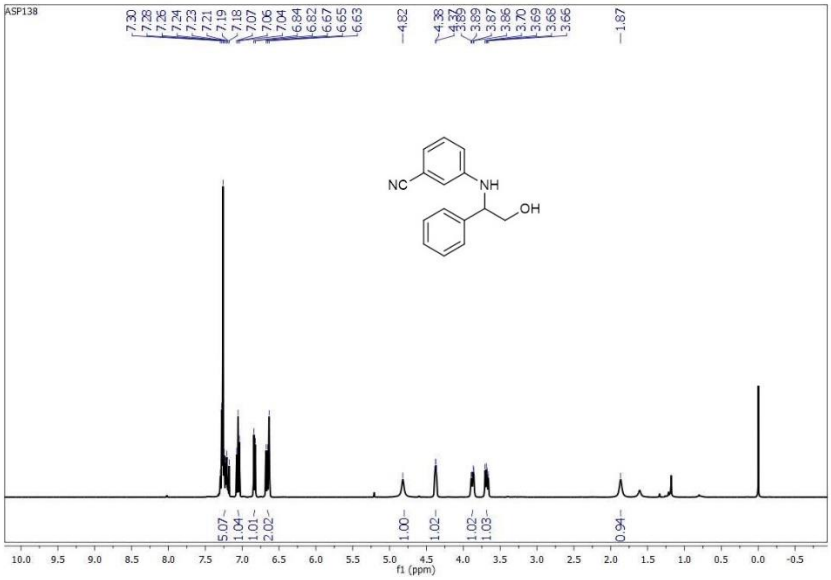

Figure 5.47 ^{1}H NMR spectrum of 3-((2-hydroxy-1-phenylethyl)amino)benzonitrile.

^{1}H NMR (400 MHz, $CDCl_3$): δ = 7.23 (dt, *J* = 14.8, 6.4 Hz, 5H), 7.06 (t, *J* = 7.9 Hz, 1H), 6.83 (d, *J* = 7.5 Hz, 1H), 6.69 – 6.62 (m, 2H), 4.82 (s, 1H), 4.38 (dd, *J* = 6.2, 4.1 Hz, 1H), 3.88 (dd, *J* = 11.1, 3.4 Hz, 1H), 3.68 (dd, *J* = 11.1, 6.8 Hz, 1H), 1.87 (s, 1H).

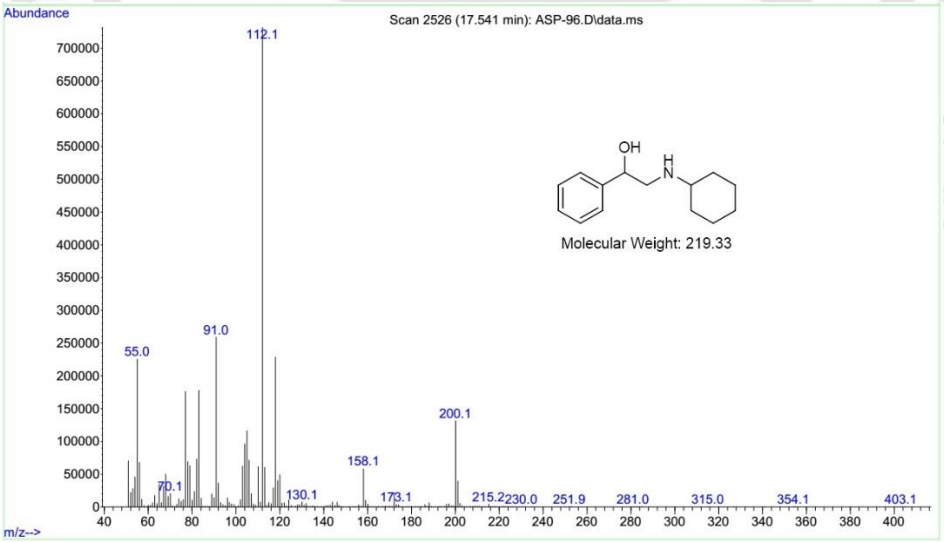

Figure 5.48 GC-MS trace of 2-(cyclohexylamino)-1-phenylethan-1-ol.

TH-2604_156122006

Appendix II

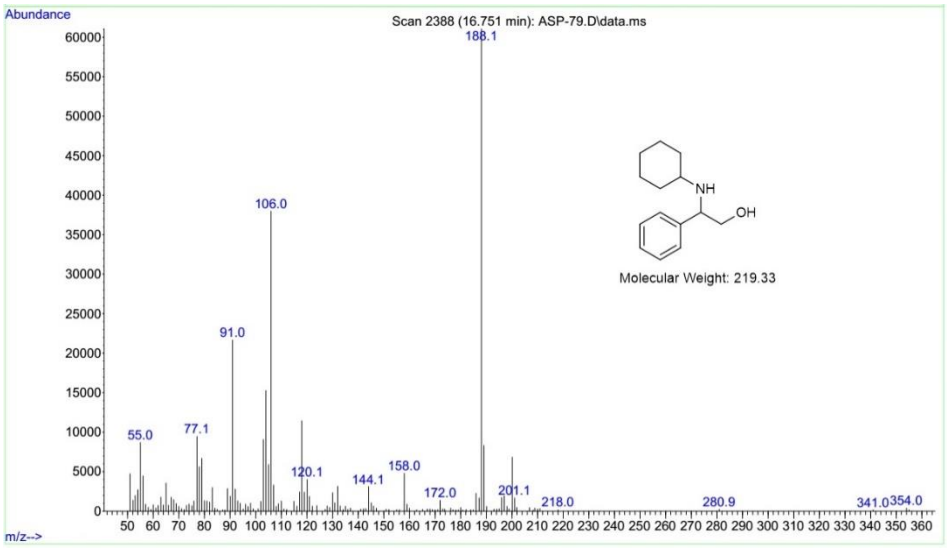

Figure 5.49 GC-MS trace of 2-(cyclohexylamino)-2-phenylethan-1-ol.

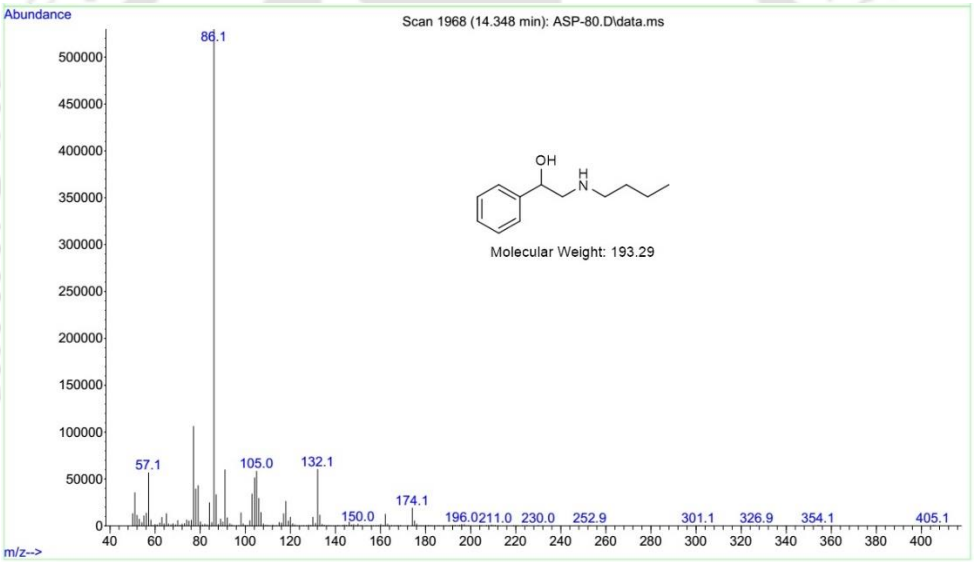

Figure 5.50 GC-MS trace of 2-(butylamino)-1-phenylethan-1-ol.

TH-2604_156122006

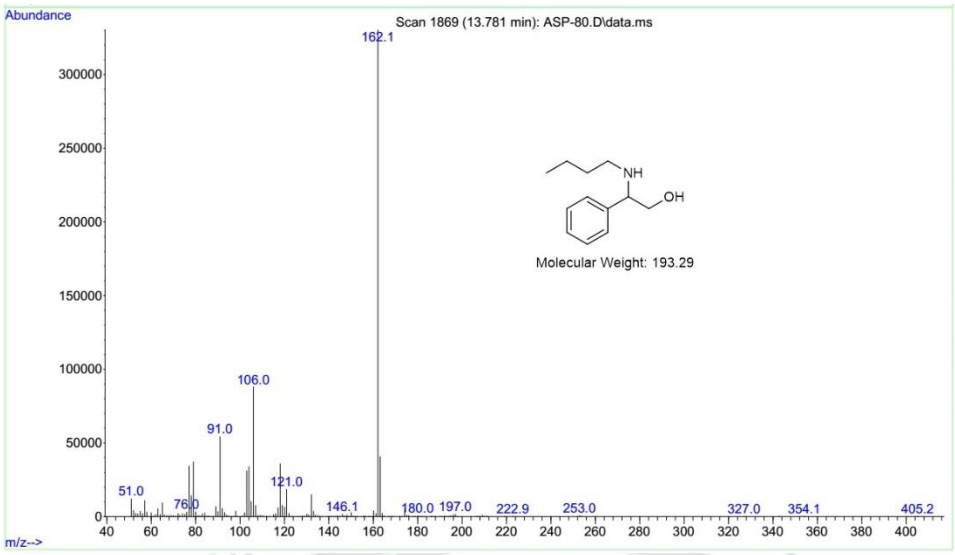

Figure 5.51 GC-MS trace of 2-(butylamino)-2-phenylethan-1-ol.

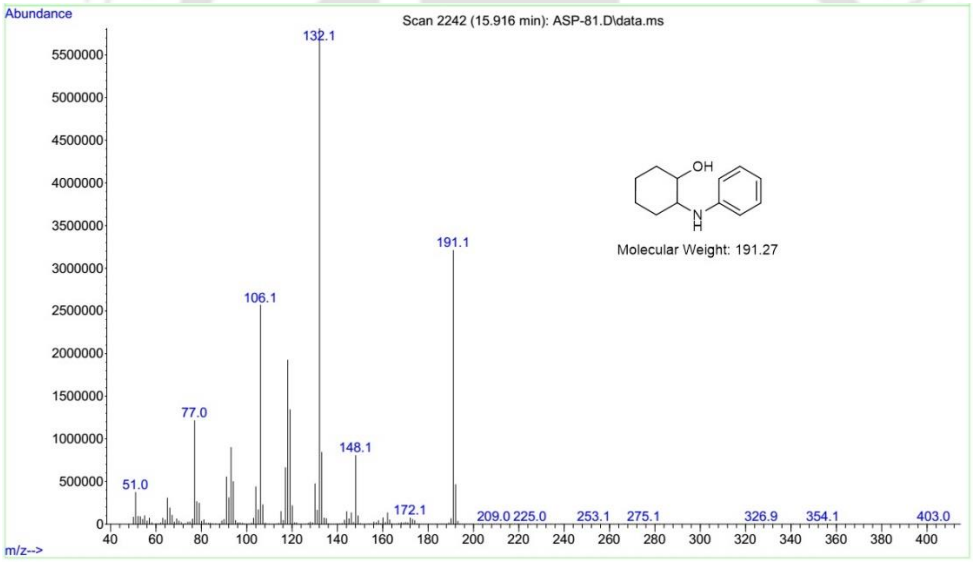

Figure 5.52 GC-MS trace of 2-(phenylamino)cyclohexan-1-ol.

TH-2604_156122006

Appendix II

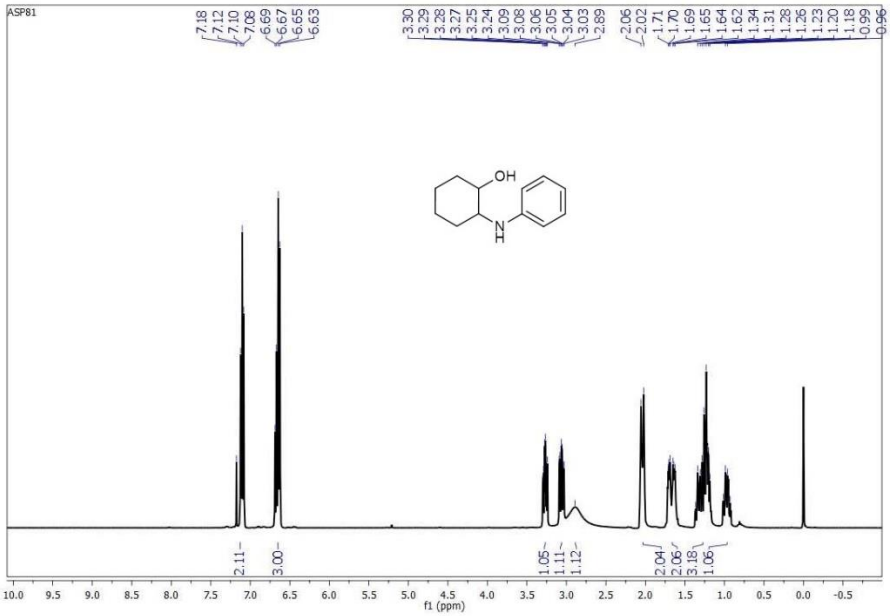

Figure 5.53 ^{1}H NMR spectrum of 2-(phenylamino)cyclohexan-1-ol.

^{1}H NMR (400 MHz, $CDCl_3$): δ = 7.12 (dd, *J* = 22.6, 14.3 Hz, 2H), 6.66 (dd, *J* = 16.9, 7.6 Hz, 3H), 3.27 (td, *J* = 10.0, 4.3 Hz, 1H), 3.10 – 3.03 (m, 1H), 2.89 (s, 1H), 2.04 (d, *J* = 13.5 Hz, 2H), 1.75 – 1.57 (m, 2H), 1.27 (dt, *J* = 23.3, 12.2 Hz, 3H), 0.97 (dd, *J* = 22.2, 10.9 Hz, 1H).

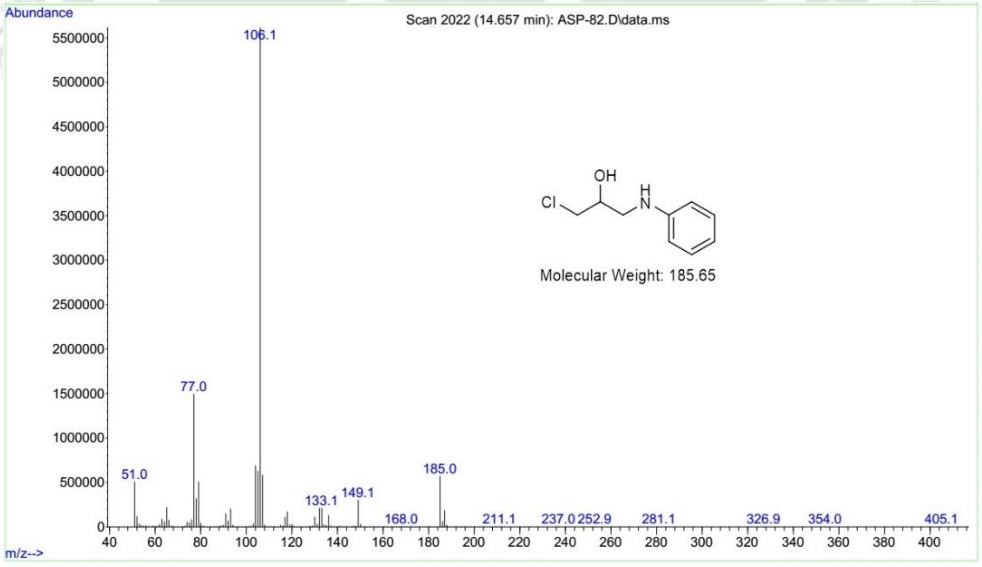

Figure 5.54 GC-MS trace of 1-chloro-3-(phenylamino)propan-2-ol.

TH-2604_156122006

Appendix II

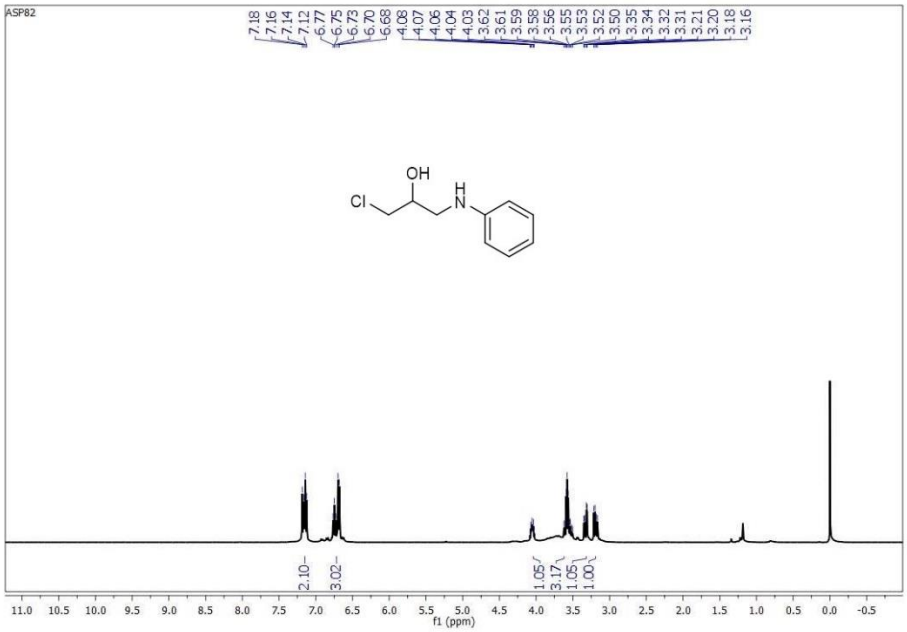

Figure 5.55 ^{1}H NMR spectrum of 1-chloro-3-(phenylamino)propan-2-ol.

^{1}H NMR (400 MHz, $CDCl_3$): δ = 7.15 (dd, *J* = 16.5, 8.3 Hz, 2H), 6.85 – 6.59 (m, 3H), 4.12 – 3.96 (m, 1H), 3.75 – 3.49 (m, 3H), 3.33 (dd, *J* = 13.2, 4.2 Hz, 1H), 3.19 (dd, *J* = 13.2, 7.4 Hz, 1H).

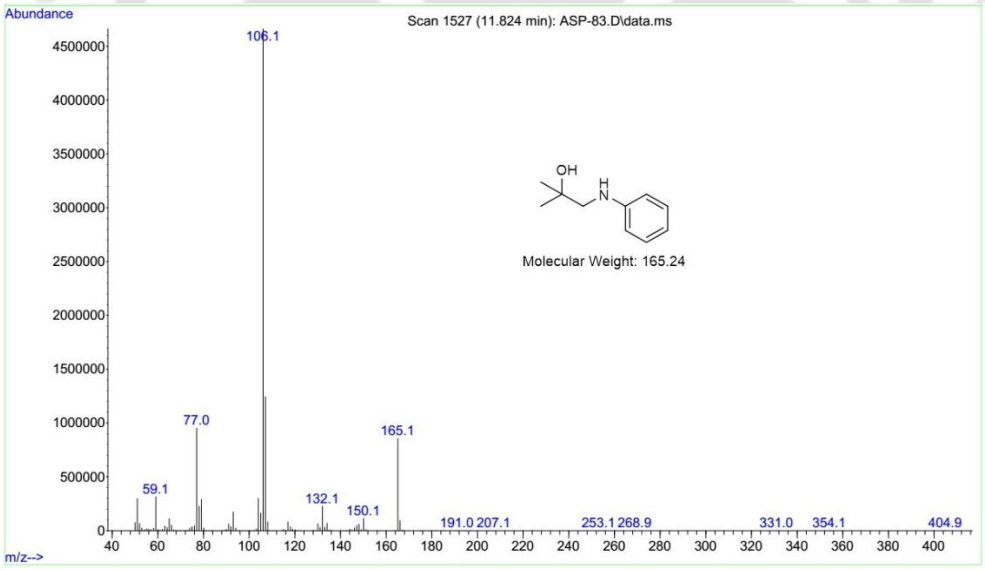

Figure 5.56 GC-MS trace of 2-methyl-1-(phenylamino)propan-2-ol.

TH-2604_156122006

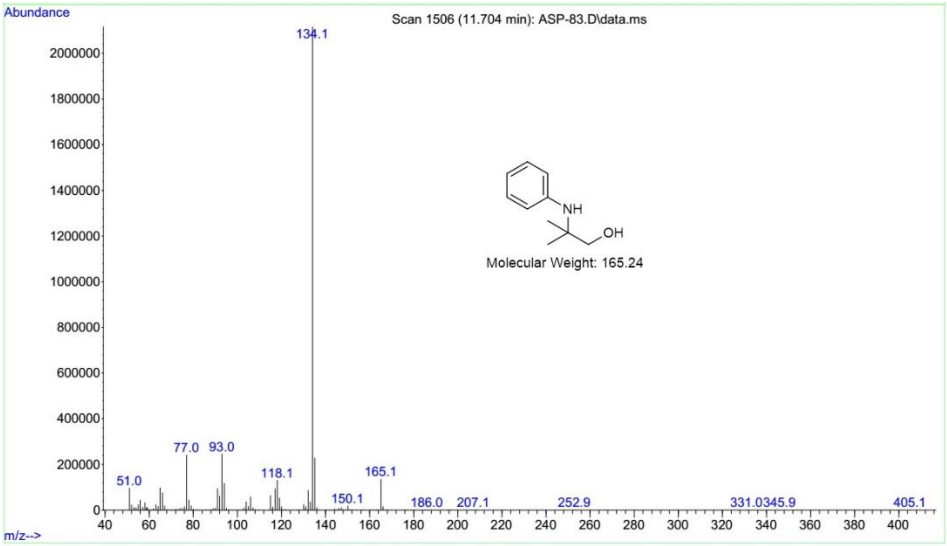

Figure 5.57 GC-MS trace of 2-methyl-2-(phenylamino)propan-1-ol.

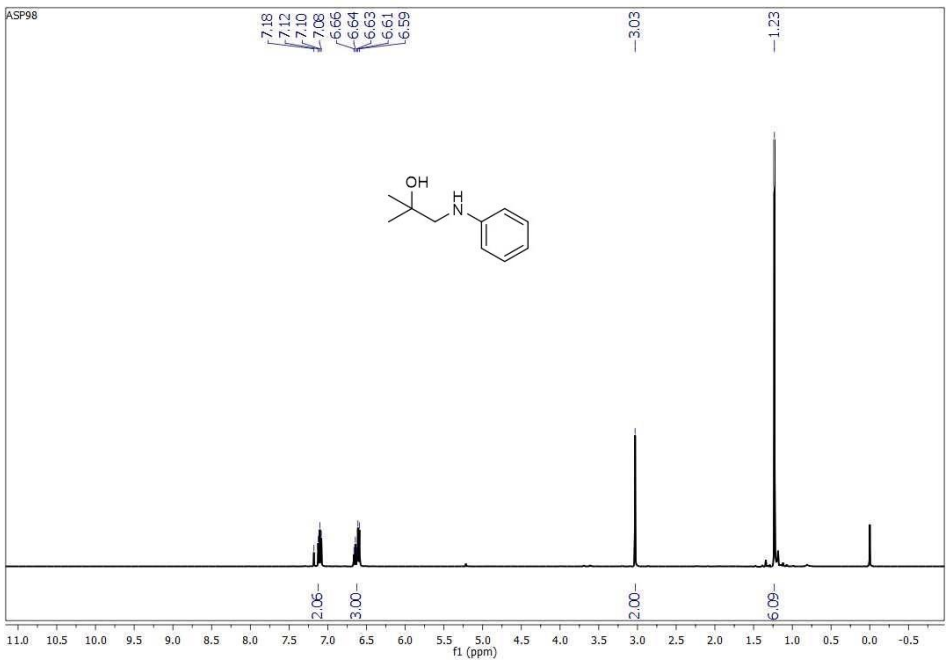

Figure 5.58 ^{1}H NMR spectrum of 2-methyl-1-(phenylamino)propan-2-ol.

^{1}H NMR (400 MHz, $CDCl_3$): δ = 7.18 – 7.07 (m, 2H), 6.68 – 6.57 (m, 3H), 3.03 (s, 2H), 1.23 (s, 6H).

TH-2604_156122006

Appendix II

TH-2604_156122006

Annexure-I

SPRINGER NATURE LICENSE
TERMS AND CONDITIONS

Mar 11, 2020

This Agreement between IIT Guwahati -- ANIRUDDHA DAS ("You") and Springer Nature ("Springer Nature") consists of your license details and the terms and conditions provided by Springer Nature and Copyright Clearance Center.

License Number	4785420190156
License date	Mar 10, 2020
Licensed Content Publisher	Springer Nature
Licensed Content Publication	Korean Journal of Chemical Engineering
Licensed Content Title	Synthesis of metal-organic frameworks: A mini review
Licensed Content Author	Yu-Ri Lee et al
Licensed Content Date	Aug 17, 2013
Type of Use	Thesis/Dissertation
Requestor type	academic/university or research institute
Format	print and electronic
Portion	figures/tables/illustrations
Number of figures/tables/illustrations	1
Will you be translating?	no

TH-2604_156122006

Annexure-I

Circulation/distribution	1 - 29
Author of this Springer Nature content	no
Title	Tuning Fluorescence Sensing and Heterogeneous Catalytic Activities of Highly Stable Metal-Organic Frameworks through Linker Design
Institution name	Indian Institute of Technology Guwahati
Expected presentation date	Jul 2020
Portions	NA
Requestor Location	IIT Guwahati IIT Guwahati Guwahati Guwahati, other 781039 India Attn: IIT Guwahati
Total	0.00 USD

Terms and Conditions

Springer Nature Customer Service Centre GmbH
Terms and Conditions

This agreement sets out the terms and conditions of the licence (the **Licence**) between you and **Springer Nature Customer Service Centre GmbH** (the **Licensor**). By clicking 'accept' and completing the transaction for the material (**Licensed Material**), you also confirm your acceptance of these terms and conditions.

1. Grant of License

1. 1. The Licensor grants you a personal, non-exclusive, non-transferable, world-wide licence to reproduce the Licensed Material for the purpose specified in your order only. Licences are granted for the specific use requested in the order and for no other use, subject to the conditions below.

1. 2. The Licensor warrants that it has, to the best of its knowledge, the rights to license reuse of the Licensed Material. However, you should ensure that the material you are requesting is original to the Licensor and does not carry the copyright of another entity (as credited in the published version).

Annexure-I

1. 3. If the credit line on any part of the material you have requested indicates that it was reprinted or adapted with permission from another source, then you should also seek permission from that source to reuse the material.

2. Scope of Licence

2. 1. You may only use the Licensed Content in the manner and to the extent permitted by these Ts&Cs and any applicable laws.

2. 2. A separate licence may be required for any additional use of the Licensed Material, e.g. where a licence has been purchased for print only use, separate permission must be obtained for electronic re-use. Similarly, a licence is only valid in the language selected and does not apply for editions in other languages unless additional translation rights have been granted separately in the licence. Any content owned by third parties are expressly excluded from the licence.

2. 3. Similarly, rights for additional components such as custom editions and derivatives require additional permission and may be subject to an additional fee. Please apply to Journalpermissions@springernature.com/bookpermissions@springernature.com for these rights.

2. 4. Where permission has been granted **free of charge** for material in print, permission may also be granted for any electronic version of that work, provided that the material is incidental to your work as a whole and that the electronic version is essentially equivalent to, or substitutes for, the print version.

2. 5. An alternative scope of licence may apply to signatories of the STM Permissions Guidelines, as amended from time to time.

3. Duration of Licence

3. 1. A licence for is valid from the date of purchase ('Licence Date') at the end of the relevant period in the below table:

Scope of Licence	Duration of Licence
Post on a website	12 months
Presentations	12 months
Books and journals	Lifetime of the edition in the language purchased

4. Acknowledgement

4. 1. The Licensor's permission must be acknowledged next to the Licenced Material in print. In electronic form, this acknowledgement must be visible at the same time as the figures/tables/illustrations or abstract, and must be hyperlinked to the journal/book's homepage. Our required acknowledgement format is in the Appendix below.

5. Restrictions on use

5. 1. Use of the Licensed Material may be permitted for incidental promotional use and minor editing privileges e.g. minor adaptations of single figures, changes of format, colour and/or style where the adaptation is credited as set out in Appendix 1 below. Any

TH-2604_156122006

Annexure-I

other changes including but not limited to, cropping, adapting, omitting material that affect the meaning, intention or moral rights of the author are strictly prohibited.

5. 2. You must not use any Licensed Material as part of any design or trademark.

5. 3. Licensed Material may be used in Open Access Publications (OAP) before publication by Springer Nature, but any Licensed Material must be removed from OAP sites prior to final publication.

6. Ownership of Rights

6. 1. Licensed Material remains the property of either Licensor or the relevant third party and any rights not explicitly granted herein are expressly reserved.

7. Warranty

IN NO EVENT SHALL LICENSOR BE LIABLE TO YOU OR ANY OTHER PARTY OR ANY OTHER PERSON OR FOR ANY SPECIAL, CONSEQUENTIAL, INCIDENTAL OR INDIRECT DAMAGES, HOWEVER CAUSED, ARISING OUT OF OR IN CONNECTION WITH THE DOWNLOADING, VIEWING OR USE OF THE MATERIALS REGARDLESS OF THE FORM OF ACTION, WHETHER FOR BREACH OF CONTRACT, BREACH OF WARRANTY, TORT, NEGLIGENCE, INFRINGEMENT OR OTHERWISE (INCLUDING, WITHOUT LIMITATION, DAMAGES BASED ON LOSS OF PROFITS, DATA, FILES, USE, BUSINESS OPPORTUNITY OR CLAIMS OF THIRD PARTIES), AND
WHETHER OR NOT THE PARTY HAS BEEN ADVISED OF THE POSSIBILITY OF SUCH DAMAGES. THIS LIMITATION SHALL APPLY NOTWITHSTANDING ANY FAILURE OF ESSENTIAL PURPOSE OF ANY LIMITED REMEDY PROVIDED HEREIN.

8. Limitations

8. 1. ***BOOKS ONLY:***Where **'reuse in a dissertation/thesis'** has been selected the following terms apply: Print rights of the final author's accepted manuscript (for clarity, NOT the published version) for up to 100 copies, electronic rights for use only on a personal website or institutional repository as defined by the Sherpa guideline (www.sherpa.ac.uk/romeo/).

9. Termination and Cancellation

9. 1. Licences will expire after the period shown in Clause 3 (above).

9. 2. Licensee reserves the right to terminate the Licence in the event that payment is not received in full or if there has been a breach of this agreement by you.

Appendix 1 — Acknowledgements:

TH-2604_156122006

Annexure-I

For Journal Content:
Reprinted by permission from [**the Licensor**]: [**Journal Publisher** (e.g. Nature/Springer/Palgrave)] [**JOURNAL NAME**] [**REFERENCE CITATION** (Article name, Author(s) Name), [**COPYRIGHT**] (year of publication)

For **Advance Online Publication papers:**
Reprinted by permission from [**the Licensor**]: [**Journal Publisher** (e.g. Nature/Springer/Palgrave)] [**JOURNAL NAME**] [**REFERENCE CITATION** (Article name, Author(s) Name), [**COPYRIGHT**] (year of publication), advance online publication, day month year (doi: 10.1038/sj.[JOURNAL ACRONYM].)

For Adaptations/Translations:
Adapted/Translated by permission from [**the Licensor**]: [**Journal Publisher** (e.g. Nature/Springer/Palgrave)] [**JOURNAL NAME**] [**REFERENCE CITATION** (Article name, Author(s) Name), [**COPYRIGHT**] (year of publication)

Note: For any republication from the British Journal of Cancer, the following credit line style applies:

Reprinted/adapted/translated by permission from [**the Licensor**]: on behalf of Cancer Research UK: : [**Journal Publisher** (e.g. Nature/Springer/Palgrave)] [**JOURNAL NAME**] [**REFERENCE CITATION** (Article name, Author(s) Name), [**COPYRIGHT]** (year of publication)

For **Advance Online Publication** papers:
Reprinted by permission from The [**the Licensor**]: on behalf of Cancer Research UK: [**Journal Publisher** (e.g. Nature/Springer/Palgrave)] [**JOURNAL NAME**] [**REFERENCE CITATION** (Article name, Author(s) Name), [**COPYRIGHT**] (year of publication), advance online publication, day month year (doi: 10.1038/sj.[JOURNAL ACRONYM])

For Book content:
Reprinted/adapted by permission from [**the Licensor**]: [**Book Publisher** (e.g. Palgrave Macmillan, Springer etc) [**Book Title**] by [**Book author**(s)] [**COPYRIGHT**] (year of publication)

Other Conditions:

Version 1.2

Questions? customercare@copyright.com or +1-855-239-3415 (toll free in the US) or +1-978-646-2777.

Annexure-I

TH-2604_156122006

Annexure-II

Luminescent transition metal–organic frameworks: An emerging sensor for detecting biologically essential metal ions

Author: Mala Pamei,Amrit Puzari
Publication: Nano-Structures & Nano-Objects
Publisher: Elsevier
Date: July 2019

© 2019 The Author(s). Published by Elsevier B.V.

Creative Commons Attribution-NonCommercial-No Derivatives License (CC BY NC ND)

This article is published under the terms of the Creative Commons Attribution-NonCommercial-No Derivatives License (CC BY NC ND).
For non-commercial purposes you may copy and distribute the article, use portions or extracts from the article in other works, and text or data mine the article, provided you do not alter or modify the article without permission from Elsevier. You may also create adaptations of the article for your own personal use only, but not distribute these to others. You must give appropriate credit to the original work, together with a link to the formal publication through the relevant DOI, and a link to the Creative Commons user license above. If changes are permitted, you must indicate if any changes are made but not in any way that suggests the licensor endorses you or your use of the work.

Permission is not required for this non-commercial use. For commercial use please continue to request permission via Rightslink.

BACK CLOSE WINDOW

© 2020 Copyright - All Rights Reserved | Copyright Clearance Center, Inc. | Privacy statement | Terms and Conditions
Comments? We would like to hear from you. E-mail us at customercare@copyright.com

TH-2604_156122006

Annexure-II

TH-2604_156122006

Annexure-III

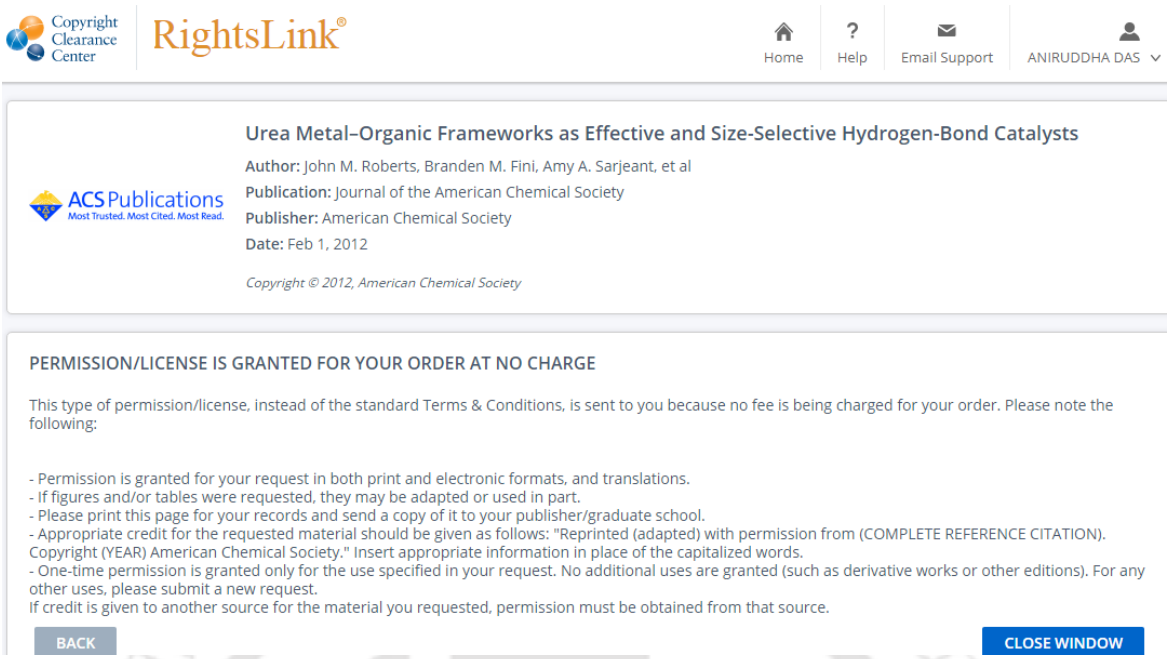

Copyright Clearance Center RightsLink®

Home | Help | Email Support | ANIRUDDHA DAS

ACS Publications
Most Trusted. Most Cited. Most Read.

Urea Metal–Organic Frameworks as Effective and Size-Selective Hydrogen-Bond Catalysts

Author: John M. Roberts, Branden M. Fini, Amy A. Sarjeant, et al
Publication: Journal of the American Chemical Society
Publisher: American Chemical Society
Date: Feb 1, 2012

Copyright © 2012, American Chemical Society

PERMISSION/LICENSE IS GRANTED FOR YOUR ORDER AT NO CHARGE

This type of permission/license, instead of the standard Terms & Conditions, is sent to you because no fee is being charged for your order. Please note the following:

- Permission is granted for your request in both print and electronic formats, and translations.
- If figures and/or tables were requested, they may be adapted or used in part.
- Please print this page for your records and send a copy of it to your publisher/graduate school.
- Appropriate credit for the requested material should be given as follows: "Reprinted (adapted) with permission from (COMPLETE REFERENCE CITATION). Copyright (YEAR) American Chemical Society." Insert appropriate information in place of the capitalized words.
- One-time permission is granted only for the use specified in your request. No additional uses are granted (such as derivative works or other editions). For any other uses, please submit a new request.

If credit is given to another source for the material you requested, permission must be obtained from that source.

BACK | CLOSE WINDOW

Indian Institute of Technology Guwahati

TH-2604_156122006

Annexure-III

TH-2604_156122006

Annexure-IV

ELSEVIER LICENSE
TERMS AND CONDITIONS

Mar 11, 2020

This Agreement between IIT Guwahati -- ANIRUDDHA DAS ("You") and Elsevier ("Elsevier") consists of your license details and the terms and conditions provided by Elsevier and Copyright Clearance Center.

License Number	4785420921526
License date	Mar 10, 2020
Licensed Content Publisher	Elsevier
Licensed Content Publication	Chinese Journal of Catalysis
Licensed Content Title	Zirconium triflate grafted on SBA-15 as a highly efficient solid acid catalyst for ring opening of epoxides by amines and alcohols
Licensed Content Author	Kamlesh N. Tayade,Lianyue Wang,Sensen Shang,Wen Dai,Manish Mishra,Shuang Gao
Licensed Content Date	Apr 1, 2017
Licensed Content Volume	38
Licensed Content Issue	4
Licensed Content Pages	9
Start Page	758
End Page	766
Type of Use	reuse in a thesis/dissertation

TH-2604_156122006

Annexure-IV

Portion	figures/tables/illustrations
Number of figures/tables/illustrations	1
Format	both print and electronic
Are you the author of this Elsevier article?	No
Will you be translating?	No
Title	Tuning Fluorescence Sensing and Heterogeneous Catalytic Activities of Highly Stable Metal-Organic Frameworks through Linker Design
Institution name	Indian Institute of Technology Guwahati
Expected presentation date	Jul 2020
Portions	NA
Requestor Location	IIT Guwahati IIT Guwahati Guwahati Guwahati, other 781039 India Attn: IIT Guwahati
Publisher Tax ID	GB 494 6272 12
Total	0.00 USD
Terms and Conditions	

INTRODUCTION

1. The publisher for this copyrighted material is Elsevier. By clicking "accept" in connection with completing this licensing transaction, you agree that the following terms and conditions apply to this transaction (along with the Billing and Payment terms and conditions established by Copyright Clearance Center, Inc. ("CCC"), at the time that you opened your Rightslink account and that are available at any time at http://myaccount.copyright.com).

Annexure-IV

GENERAL TERMS

2. Elsevier hereby grants you permission to reproduce the aforementioned material subject to the terms and conditions indicated.

3. Acknowledgement: If any part of the material to be used (for example, figures) has appeared in our publication with credit or acknowledgement to another source, permission must also be sought from that source. If such permission is not obtained then that material may not be included in your publication/copies. Suitable acknowledgement to the source must be made, either as a footnote or in a reference list at the end of your publication, as follows:

"Reprinted from Publication title, Vol /edition number, Author(s), Title of article / title of chapter, Pages No., Copyright (Year), with permission from Elsevier [OR APPLICABLE SOCIETY COPYRIGHT OWNER]." Also Lancet special credit - "Reprinted from The Lancet, Vol. number, Author(s), Title of article, Pages No., Copyright (Year), with permission from Elsevier."

4. Reproduction of this material is confined to the purpose and/or media for which permission is hereby given.

5. Altering/Modifying Material: Not Permitted. However figures and illustrations may be altered/adapted minimally to serve your work. Any other abbreviations, additions, deletions and/or any other alterations shall be made only with prior written authorization of Elsevier Ltd. (Please contact Elsevier at permissions@elsevier.com). No modifications can be made to any Lancet figures/tables and they must be reproduced in full.

6. If the permission fee for the requested use of our material is waived in this instance, please be advised that your future requests for Elsevier materials may attract a fee.

7. Reservation of Rights: Publisher reserves all rights not specifically granted in the combination of (i) the license details provided by you and accepted in the course of this licensing transaction, (ii) these terms and conditions and (iii) CCC's Billing and Payment terms and conditions.

8. License Contingent Upon Payment: While you may exercise the rights licensed immediately upon issuance of the license at the end of the licensing process for the transaction, provided that you have disclosed complete and accurate details of your proposed use, no license is finally effective unless and until full payment is received from you (either by publisher or by CCC) as provided in CCC's Billing and Payment terms and conditions. If full payment is not received on a timely basis, then any license preliminarily granted shall be deemed automatically revoked and shall be void as if never granted. Further, in the event that you breach any of these terms and conditions or any of CCC's Billing and Payment terms and conditions, the license is automatically revoked and shall be void as if never granted. Use of materials as described in a revoked license, as well as any use of the materials beyond the scope of an unrevoked license, may constitute copyright infringement and publisher reserves the right to take any and all action to protect its copyright in the materials.

9. Warranties: Publisher makes no representations or warranties with respect to the licensed material.

10. Indemnity: You hereby indemnify and agree to hold harmless publisher and CCC, and their respective officers, directors, employees and agents, from and against any and all claims arising out of your use of the licensed material other than as specifically authorized pursuant to this license.

11. No Transfer of License: This license is personal to you and may not be sublicensed, assigned, or transferred by you to any other person without publisher's written permission.

TH-2604_156122006

12. No Amendment Except in Writing: This license may not be amended except in a writing signed by both parties (or, in the case of publisher, by CCC on publisher's behalf).

13. Objection to Contrary Terms: Publisher hereby objects to any terms contained in any purchase order, acknowledgment, check endorsement or other writing prepared by you, which terms are inconsistent with these terms and conditions or CCC's Billing and Payment terms and conditions. These terms and conditions, together with CCC's Billing and Payment terms and conditions (which are incorporated herein), comprise the entire agreement between you and publisher (and CCC) concerning this licensing transaction. In the event of any conflict between your obligations established by these terms and conditions and those established by CCC's Billing and Payment terms and conditions, these terms and conditions shall control.

14. Revocation: Elsevier or Copyright Clearance Center may deny the permissions described in this License at their sole discretion, for any reason or no reason, with a full refund payable to you. Notice of such denial will be made using the contact information provided by you. Failure to receive such notice will not alter or invalidate the denial. In no event will Elsevier or Copyright Clearance Center be responsible or liable for any costs, expenses or damage incurred by you as a result of a denial of your permission request, other than a refund of the amount(s) paid by you to Elsevier and/or Copyright Clearance Center for denied permissions.

LIMITED LICENSE

The following terms and conditions apply only to specific license types:

15. **Translation**: This permission is granted for non-exclusive world **English** rights only unless your license was granted for translation rights. If you licensed translation rights you may only translate this content into the languages you requested. A professional translator must perform all translations and reproduce the content word for word preserving the integrity of the article.

16. **Posting licensed content on any Website**: The following terms and conditions apply as follows: Licensing material from an Elsevier journal: All content posted to the web site must maintain the copyright information line on the bottom of each image; A hyper-text must be included to the Homepage of the journal from which you are licensing at http://www.sciencedirect.com/science/journal/xxxxx or the Elsevier homepage for books at http://www.elsevier.com; Central Storage: This license does not include permission for a scanned version of the material to be stored in a central repository such as that provided by Heron/XanEdu.

Licensing material from an Elsevier book: A hyper-text link must be included to the Elsevier homepage at http://www.elsevier.com . All content posted to the web site must maintain the copyright information line on the bottom of each image.

Posting licensed content on Electronic reserve: In addition to the above the following clauses are applicable: The web site must be password-protected and made available only to bona fide students registered on a relevant course. This permission is granted for 1 year only. You may obtain a new license for future website posting.

17. **For journal authors:** the following clauses are applicable in addition to the above:

Preprints:

A preprint is an author's own write-up of research results and analysis, it has not been peer-reviewed, nor has it had any other value added to it by a publisher (such as formatting, copyright, technical enhancement etc.).

TH-2604_156122006

Annexure-IV

Authors can share their preprints anywhere at any time. Preprints should not be added to or enhanced in any way in order to appear more like, or to substitute for, the final versions of articles however authors can update their preprints on arXiv or RePEc with their Accepted Author Manuscript (see below).

If accepted for publication, we encourage authors to link from the preprint to their formal publication via its DOI. Millions of researchers have access to the formal publications on ScienceDirect, and so links will help users to find, access, cite and use the best available version. Please note that Cell Press, The Lancet and some society-owned have different preprint policies. Information on these policies is available on the journal homepage.

Accepted Author Manuscripts: An accepted author manuscript is the manuscript of an article that has been accepted for publication and which typically includes author-incorporated changes suggested during submission, peer review and editor-author communications.

Authors can share their accepted author manuscript:

- immediately
  - via their non-commercial person homepage or blog
  - by updating a preprint in arXiv or RePEc with the accepted manuscript
  - via their research institute or institutional repository for internal institutional uses or as part of an invitation-only research collaboration work-group
  - directly by providing copies to their students or to research collaborators for their personal use
  - for private scholarly sharing as part of an invitation-only work group on commercial sites with which Elsevier has an agreement
- After the embargo period
  - via non-commercial hosting platforms such as their institutional repository
  - via commercial sites with which Elsevier has an agreement

In all cases accepted manuscripts should:

- link to the formal publication via its DOI
- bear a CC-BY-NC-ND license - this is easy to do
- if aggregated with other manuscripts, for example in a repository or other site, be shared in alignment with our hosting policy not be added to or enhanced in any way to appear more like, or to substitute for, the published journal article.

Published journal article (JPA): A published journal article (PJA) is the definitive final record of published research that appears or will appear in the journal and embodies all value-adding publishing activities including peer review co-ordination, copy-editing, formatting, (if relevant) pagination and online enrichment.

Policies for sharing publishing journal articles differ for subscription and gold open access articles:

Subscription Articles: If you are an author, please share a link to your article rather than the full-text. Millions of researchers have access to the formal publications on ScienceDirect, and so links will help your users to find, access, cite, and use the best available version.

Theses and dissertations which contain embedded PJAs as part of the formal submission can be posted publicly by the awarding institution with DOI links back to the formal publications on ScienceDirect.

If you are affiliated with a library that subscribes to ScienceDirect you have additional private sharing rights for others' research accessed under that agreement. This includes use for classroom teaching and internal training at the institution (including use in course packs and courseware programs), and inclusion of the article for grant funding purposes.

TH-2604_156122006

Annexure-IV

Gold Open Access Articles: May be shared according to the author-selected end-user license and should contain a CrossMark logo, the end user license, and a DOI link to the formal publication on ScienceDirect.

Please refer to Elsevier's posting policy for further information.

18. **For book authors** the following clauses are applicable in addition to the above: Authors are permitted to place a brief summary of their work online only. You are not allowed to download and post the published electronic version of your chapter, nor may you scan the printed edition to create an electronic version. **Posting to a repository:** Authors are permitted to post a summary of their chapter only in their institution's repository.

19. **Thesis/Dissertation**: If your license is for use in a thesis/dissertation your thesis may be submitted to your institution in either print or electronic form. Should your thesis be published commercially, please reapply for permission. These requirements include permission for the Library and Archives of Canada to supply single copies, on demand, of the complete thesis and include permission for Proquest/UMI to supply single copies, on demand, of the complete thesis. Should your thesis be published commercially, please reapply for permission. Theses and dissertations which contain embedded PJAs as part of the formal submission can be posted publicly by the awarding institution with DOI links back to the formal publications on ScienceDirect.

Elsevier Open Access Terms and Conditions

You can publish open access with Elsevier in hundreds of open access journals or in nearly 2000 established subscription journals that support open access publishing. Permitted third party re-use of these open access articles is defined by the author's choice of Creative Commons user license. See our open access license policy for more information.

Terms & Conditions applicable to all Open Access articles published with Elsevier:

Any reuse of the article must not represent the author as endorsing the adaptation of the article nor should the article be modified in such a way as to damage the author's honour or reputation. If any changes have been made, such changes must be clearly indicated.

The author(s) must be appropriately credited and we ask that you include the end user license and a DOI link to the formal publication on ScienceDirect.

If any part of the material to be used (for example, figures) has appeared in our publication with credit or acknowledgement to another source it is the responsibility of the user to ensure their reuse complies with the terms and conditions determined by the rights holder.

Additional Terms & Conditions applicable to each Creative Commons user license:

CC BY: The CC-BY license allows users to copy, to create extracts, abstracts and new works from the Article, to alter and revise the Article and to make commercial use of the Article (including reuse and/or resale of the Article by commercial entities), provided the user gives appropriate credit (with a link to the formal publication through the relevant DOI), provides a link to the license, indicates if changes were made and the licensor is not represented as endorsing the use made of the work. The full details of the license are available at http://creativecommons.org/licenses/by/4.0.

CC BY NC SA: The CC BY-NC-SA license allows users to copy, to create extracts, abstracts and new works from the Article, to alter and revise the Article, provided this is not done for commercial purposes, and that the user gives appropriate credit (with a link to the formal publication through the relevant DOI), provides a link to the license, indicates if changes were made and the licensor is not represented as endorsing the use made of the

TH-2604_156122006

work. Further, any new works must be made available on the same conditions. The full details of the license are available at http://creativecommons.org/licenses/by-nc-sa/4.0.

CC BY NC ND: The CC BY-NC-ND license allows users to copy and distribute the Article, provided this is not done for commercial purposes and further does not permit distribution of the Article if it is changed or edited in any way, and provided the user gives appropriate credit (with a link to the formal publication through the relevant DOI), provides a link to the license, and that the licensor is not represented as endorsing the use made of the work. The full details of the license are available at http://creativecommons.org/licenses/by-nc-nd/4.0. Any commercial reuse of Open Access articles published with a CC BY NC SA or CC BY NC ND license requires permission from Elsevier and will be subject to a fee.

Commercial reuse includes:

- Associating advertising with the full text of the Article
- Charging fees for document delivery or access
- Article aggregation
- Systematic distribution via e-mail lists or share buttons

Posting or linking by commercial companies for use by customers of those companies.

20. **Other Conditions**:

v1.9

Questions? customercare@copyright.com or +1-855-239-3415 (toll free in the US) or +1-978-646-2777.

TH-2604_156122006

List of Publications and Conferences attended

List of publications

1. A Hydrazine Functionalized UiO-66(Hf) Metal-Organic Framework for the Synthesis of Quinolines by Friedlaender Condensation

A. Das, N. Anbu, P. Varalakshmi, A. Dhakshinamoorthy,* S. Biswas,* *New J. Chem.*, 2020, **44**, 10982-10988.

2. Highly Active Bisamino Functionalized Zr(IV)-UiO-67 Metal-Organic Framework for Cascade Catalysis

A. Das, N. Anbu, M. SK, A. Dhakshinamoorthy,* S. Biswas,* *Eur. J. Inorg. Chem.*, 2020, **00**, 1-6.

3. Influence of Hydrogen Bond Donating Sites in UiO-66 Metal-Organic Framework for Highly Regioselective Methanolysis of Epoxides

A. Das, N. Anbu, M. SK, A. Dhakshinamoorthy,* S. Biswas,* *ChemCatChem*, 2020, **12**, 1 – 11.

4. A Thiophene-2-carboxamide-Functionalized Zr(IV) Organic Framework as a Prolific and Recyclable Heterogeneous Catalyst for Regioselective Ring Opening of Epoxides

A. Das, N. Anbu, H. Reinsch, A. Dhakshinamoorthy,* S. Biswas,* *Inorg. Chem.*, 2019, **58**, 16581-16591.

5. A functionalized UiO-66 MOF for turn-on fluorescence sensing of superoxide in water and efficient catalysis of Knoevenagel condensation

A. Das, N. Anbu, M. SK, A. Dhakshinamoorthy,* S. Biswas,* *Dalton Trans.*, 2019, **48**, 17371-17380.

6. A phthalimide functionalized UiO-66 metal-organic framework for the fluorogenic detection of hydrazine in live-cells

M. SK, M. R. Uz Zama Khan, **A. Das**, S. Nandi, V. Trivedi and S. Biswas,* *Dalton Trans.*, 2019, **48**, 12615- 12621.

7. A highly catalytically active Hf(IV) metal-organic framework for Knoevenagel condensation

TH-2604_156122006

List of Publications and Conferences attended

A. Das, N. Anbu, A. Dhakshinamoorthy,* S. Biswas,* *Microporous Mesoporous Mater.*, 2019, **284**, 459-467.

8. Highly Active Urea Functionalized Zr(IV)-UiO-67 Metal-Organic Framework as Hydrogen Bonding Heterogeneous Catalyst for Friedel-Crafts Alkylation

A. Das, N. Anbu, M. SK, A. Dhakshinamoorthy,* S. Biswas,* *Inorg. Chem.*, 2019, **58**, 5163-5172.

9. A dual functional MOF-based fluorescent sensor for intracellular phosphate and extracellular 4-nitrobenzaldehyde

A. Das, S. Das, V. Trivedi, S. Biswas,* *Dalton Trans.*, 2019, **48**, 1332-1343.

10. Extraordinary sensitivity for H_2S and Fe(III) sensing in aqueous medium by Al-MIL-53-N_3 metal-organic framework: in vitro and in vivo applications of H_2S sensing

A. Das, S. Banesh, V. Trivedi, S. Biswas,* *Dalton Trans.*, 2018, **47**, 2690-2700.

11. A multi-responsive carbazole-functionalized Zr(IV)-based metal-organic framework for selective sensing of Fe(III), cyanide and *p*-nitrophenol

A. Das, S. Biswas,* *Sens. Actuators, B.*, 2017, **250**, 121-131.

List of Conferences

1. Modern Trends in Inorganic Chemistry, 2019, IIT Guwahati.
2. Frontiers in Chemical Sciences, 2018, IIT Guwahati.
3. 5th International Conference on Advanced Nanomaterials & Nanotechnology, 2017, IIT Guwahati.
4. 20th CRSI National Symposium in Chemistry, 2017, Gauhati University.
5. Frontiers in Chemical Sciences, 2016, IIT Guwahati.

TH-2604_156122006